Fuel Performance Experiments and Modeling: Fission Gas Bubble Nucleation and Growth in Alloy Nuclear Fuels

Fuel Cycle R&D

Dr. Sean M. McDeavitt

Texas A&M University

In collaboration with:

Idaho National Laboratory
University of Tennessee, Knoxville

Frank Goldner, Federal POC
Steve Marschman, Technical POC

NEUP | Nuclear Energy University Programs

U.S. Department of Energy

Fuel Performance Experiments and Modeling: Fission Gas Bubble Nucleation and Growth in Alloy Nuclear Fuels

**Battelle Energy Alliance — U.S. Department of Energy
Project No. CFP-09-0816**

FINAL TECHNICAL REPORT

April 4, 2014

Consortium Institutions:
Texas A&M University (through TEES)
University of Tennessee, Knoxville
Idaho National Laboratory

Contact:
Dr. Sean M. McDeavitt, Associate Professor
Prepared by Allison Cosgrove, FCML Program Manager
Department of Nuclear Engineering, Texas A&M University
MS 3133 TAMU, 337 Zachry, College Station, TX, 77843-3133
E-mail: mcdeavitt@tamu.edu or acosgrove@tamu.edu
Phone: 979/865-4106, Fax: 979/845-6443

Collaborating Investigators:

Texas A&M University (through TEES)
    Dr. Sean M. McDeavitt, Associate Professor
    Dr. Lin Shao, Assistant Professor
    Dr. Pavel Tsvetkov, Associate Professor

University of Tennessee, Knoxville
    Dr. Brian Wirth, Professor
    (Formerly with UC Berkeley)

Idaho National Laboratory
    Dr. Rory Kennedy

1.0   Project Overview

Advanced fast reactor systems being developed under the DOE's Advanced Fuel Cycle Initiative are designed to destroy TRU isotopes generated in existing and future nuclear energy systems. Over the past 40 years, multiple experiments and demonstrations have been completed using U-Zr, U-Pu-Zr, U-Mo, and other metal alloys. As a result, multiple empirical and semi-empirical relationships have been established to develop empirical performance modeling codes. Many mechanistic questions about fission gas mobility, bubble coalescence, and gas release have been answered through industrial experience, research, and empirical understanding. The advent of modern computational materials science, however, opens new doors of development such that physics-based multi-scale models may be developed to enable a new generation of predictive fuel performance codes that are not limited by empiricism.

This project had the following objectives:

1. Develop and customize *in situ* ion beam analysis tools to observe and characterize the nucleation and growth of gas bubbles in advanced U-TRU-Zr alloy fuel materials.

2. Quantify and model the fundamental phenomena relevant to fission gas induced swelling in advanced U-TRU-Zr alloy fuel materials.

3. Validate and benchmark the new multi-scale fuel swelling models using critical experiments performed using new *in situ* ion beam methods and post-test analysis.

To achieve this objective, a comprehensive strategy is being implemented to provide insight and validation for the fundamental models that will enable multi-scale fuel performance predictions from first principles. The development experiments will focus on fission gas bubble nucleation and swelling in uranium–zirconium alloys containing transuranic (TRUs); however, the fundamental models developed for diffusion and fission gas mobility in the various phases present in U-TRU-Zr nuclear fuels will enable the modeling of other critical fuel performance phenomena in the future such as creep, component redistribution, and fuel-cladding mechanical or chemical interactions.

2.0   Technical Report

Texas A&M University (TAMU) is the lead institution, under the administration of the Texas Engineering Experiment Station (TEES), and is examining sample fabrication and characterization, and methods development; ion beam irradiation and implementation and methods development; and system model development and data integration. The University of Tennessee is leading the atomistic model development and methods development. Idaho National Laboratory is examining sample fabrication and characterization, methods development and program relevance.

In this report, brief summaries and bibliographies of papers produced by this work are provided to describe the work performed. The appendices contain extended details with reports and dissertations to provide complete summary of the research.

2.1   Highlights from Texas A&M University-Uranium Metallurgy and Ion Irradiation
        (Dr. Sean McDeavitt, Sangjoon Ahn, and Sandeep Irukuvarghula with Dr. Lin Shao)

    The research began with a survey of the U-Zr alloy system and it quickly became obvious that the existing knowledge in literature was insufficient to enable a fast track toward project objective #1 of ion implantation studies. Therefore, detailed metallurgical studies were completed and a much more complete

understanding of the U-Zr metallurgical system was created. At the end of the project, helium ion irradiations were indeed completed and bubble morphologies and densities were estimated for two dose. Figure 1. Shows an image from one of these samples.
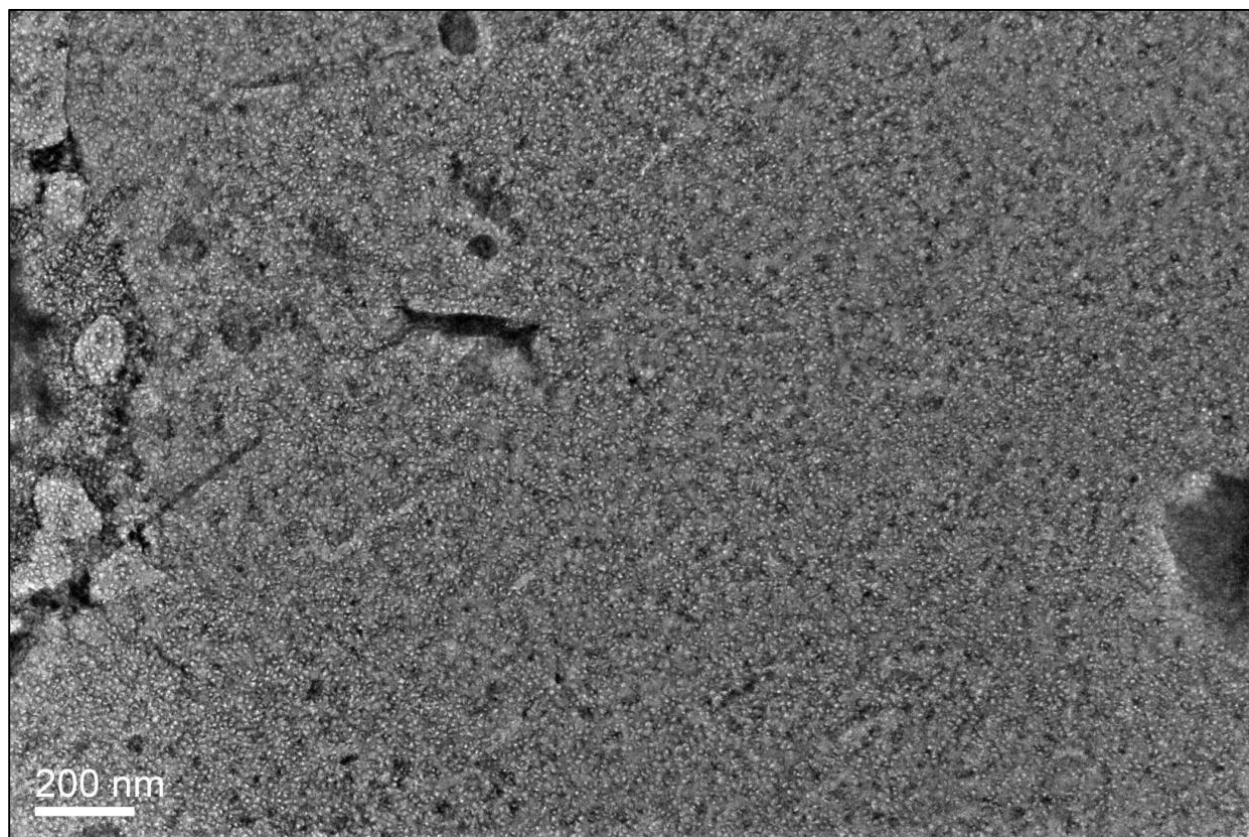

Figure1.   Transmission electron image of helium bubbles induced from 140 keV He$^+$ ion-beam irradiation in U-40Zr (ion dose ~5x10^{16} ions/cm^2).

The following sections provide summaries of the findings that are detailed in the appendices.

2.1.1   *Thermophysical Properties, Phase Characterization and Ion Implantation (Appendix A & B)*

Uranium-zirconium (U-Zr) alloys comprise a class of metallic nuclear fuel that is regularly considered for application in fast nuclear energy systems. The U-10wt%Zr alloy has been demonstrated to very high burnup without cladding breach in the Experimental Breeder Reactor-II (EBR-II). This was accomplished by successfully accommodating gaseous fission products with low smear density fuel and an enlarged cladding plenum. Fission gas swelling behavior of the fuel has been experimentally revealed to be significantly affected by the temperature gradient within a fuel pin and the multiple phase morphologies that exist across the fuel pin. However, the phase effects on swelling behavior have not been yet fully accounted for in existing fuel performance models which tend to assume the fuel exists as a homogeneous single phase medium across the entire fuel pin.

Phase effects on gas bubble nucleation and growth in the alloy were investigated using transmission electron microscopy (TEM). To achieve this end, a comprehensive examination of the alloy system was carried out. This included the fabrication of uranium alloys containing 0.1, 2, 5, 10, 20, 30, 40, and 50 wt% zirconium by melt-casting. These alloys were characterized using electron probe micro-analysis (EPMA), differential scanning calorimetry (DSC), and thermogravimetric analysis (TGA). Once

the alloys were satisfactorily characterized, selected U-Zr alloys were irradiated with 140 keV He$^+$ ions at fluences ranging from 1×10^{14} to 5×10^{16} ions/cm^2.

Metallographic and micro-chemical analysis of the alloys indicated that annealing at 600°C equilibrates the alloys within 168 h to have stable α-U and δ-UZr$_2$ phase morphologies. This was in contrast to some reported data that showed kinetically sluggish δ-UZr$_2$ phase formation.

Phase transformation temperatures and enthalpies were measured using DSC-TGA for each of the alloys. Measured temperatures from different time annealed alloys have shown consistent matches with most of the features in the current U-Zr phase diagram which further augmented the EPMA observed microstructural equilibrium. Nevertheless, quantitative transformation enthalpy analysis also suggests potential errors in the existing U-Zr binary phase diagram. More specifically, the (β-U, γ2) phase region does not appear to be present in Zr-rich (> 15 wt%) U-Zr alloys and so further investigation may be required.

To prepare TEM specimens, characterized U-Zr alloys were mechanically thinned to a thickness of ~150 μm, and then electropolished using a 5% perchloric acid/95% methanol electrolyte. Uranium-rich phase was preferentially thinned in two phase alloys, giving saw-tooth shaped perforated boundaries; the alloy images were very clear and alloy characterization was accomplished.

During *in-situ* heating U-10Zr and U-20Zr alloys up to 810°C, selected area diffraction (SAD) patterns were observed as the structure evolved up to ~690°C and the expected α-U → β-U phase transformation at 662°C was never observed. For the temperature range of the (α-U, γ2) phase region, phase transformation driven diffusion was observed as uranium moved into Zr-rich phase matrix in U-20Zr alloy; this was noted as nonuniform bridging of adjacent phase lamellae in the alloy.

From the irradiation tests, nano-scale voids were discovered to be evenly distributed over several micrometers in U-40Zr alloys. For the alloys irradiated at the fluences of 1×10^{16} and 5×10^{16} ions/cm^2, estimated void densities were proportional to the irradiation doses, (250 ± 40) and (1460 ± 30) /μm^2, while void sizes were fairly constant, (6.0 ± 1.5) and (5.2 ± 1.2) nm, respectively. Measured data could be foundational inputs to the further development of a semi-empirical metal fuel performance model.

2.1.2   Solid State Phase Transformations in Uranium-Zirconium Alloys (Appendix C & D)

Uranium-10wt% zirconium (U-10Zr) alloy nuclear fuels have been used for decades and new variations are under consideration ranging from U-5Zr to U-50Zr. As a pre- cursor to understanding the fission gas behavior in U-Zr alloys using ion implantation, a basic study on the U-Zr metallurgy was completed using EPMA, DSC, XRD, optical microscopy, and TEM with a focus on solid state phase transformations in alloys containing 2, 5, 10, 20, 30, and 50wt% zirconium. Alloys were cast by crucible melting using high temperature furnace under argon atmosphere in yttrium oxide crucibles and various thermal profiles were used to study phase transformations in these alloys.

Using TEM, XRD, and DSC data, it was ascertained that athermal-ω, along with martensitic α', formed in all alloys quenched from γ phase. XRD could detect the presence of athermal-ω only in U-20, 30 and 50wt%Zr alloys. BSE images for as-cast alloys of 2, 5, 10, 20, and 30wt%Zr had lamellar microstructure with lamellae rich in zirconium. All alloy samples clearly showed a heating transformation pertaining to δ→γ in DSC data while XRD could only confirm the presence of δ phase in U-20, 30, and 50wt%Zr alloys. An explanation is offered for the absence of δ phase peaks in uranium-rich alloys based on it's formation mechanism.

Alloy samples of U-2, 5, and 10wt%Zr were step-cooled from γ phase by annealing in the (α + δ) phase field before cooling to room temperature revealed broad peaks for δ phase indicating incomplete collapse of {111}$_γ$ planes. Both as cast and γ-quenched alloys were annealed at 600°C, in the (α + δ) phase field for 1, 3, 7, and 30 days. Microstructures of the samples in both cases contained uranium-rich

matrix and zirconium-rich precipitates and WDS analyses were consistent with their being α-U and δ phase, respectively. However, XRD data for annealed alloys never showed peaks for δ phase even though its area fraction was within the detection limits. Moreover, the peaks which were present in U-20wt%Zr vanished after annealing for 7 days. Based on the data obtained, it is suggested that it is more appropriate to consider the presence of metastable diffusional-ω instead of a stable δ in the as-cast alloys and that it is not stable at 600ºC.

2.1.3   Bibliography of publications from this portion of the research

Journal Articles
1. J.T. McKeown, S. Irukuvarghula, S. Ahn, M.A. Wall, L.L. Hsiung, S. McDeavitt, P.E.A. Turchi, Coexistence of the α and δ phases in an as-cast uranium-rich U-Zr alloy, Journal of Nuclear Materials, 436 (2013) 100-104.
2. S. Ahn, S. Irukuvarghula, S. M. McDeavitt, Thermophysical investigation of the uranium-zirconium alloy system, Journal of Alloys and Compounds (*accepted for publication*)

Under Review

1. S. Ahn, S. Irukuvarghula, and S. M. McDeavitt, "Investigation of uranium-zirconium alloy phase transformations based on the evolution of selected-area electron diffraction patterns from U-10Zr and U-20Zr alloys during in-situ heating." (submitted to the Materials Letters)
2. S. Irukuvarghula, S. Ahn, and S. M. McDeavitt, "Decomposition of the phase in as-cast and quenched U-Zr alloys" (*in preparation*)

Papers presented at professional meetings

1. J.T. McKeown, S. Ahn, M.A. Wall, L.L. Hsiung, S.M. McDeavitt, and P.E.A. Turchi, Thermal Stability of Uranium-rich U-Mo Alloys for Advanced Nuclear Fuels," TMS Annual Meeting, San Diega, CA, Feb. 16-20, 2014.
2. S. Ahn, S.M. McDeavitt, "An investigation of U-Zr alloy phase diagram using in-situ heating electron diffractometry," ANS Winter Meeting, Washington, DC, November 10-14, 2013, Transactions of the American Nuclear Society 109 (2013) 608-611
3. J.T. McKeown, S. Irukuvarghula, S. Ahn, M. Wall, L.L. Hsiung, S. McDeavitt, P.E.A. Turchi, "Microstructural assessment of U-rich U-Zr alloys for advanced nuclear fuels," TMS Annual Meeting, San Antonio, TX, March 3-7, 2013.
4. S. Ahn, S.M. McDeavitt, "Transformation enthalpies of uranium-zirconium alloy system," ANS Annual Meeting, Chicago, IL, June 24-28, 2012, Transactions of the American Nuclear Society 106 (2012) 239-241.
5. S. Ahn, S.M. McDeavitt, "Thermophysical investigation of uranium-zirconium alloy phase diagram," KNS Spring Meeting, Jeju, Korea, May 17-18, 2012, Transactions of the Korean Nuclear Society Spring Meeting (2012) 462-463.
6. S. Ahn, S. Irukuvarghula, S.M. McDeavitt, "Thermodynamic assessment of the uranium-zirconium alloy system for nuclear energy applications," TMS Annual Meeting, Orlando, FL, March 11-14, 2012.
7. S. Irukuvarghula, S. Ahn, S.M. McDeavitt, "Metallurgical characterization of the delta phase formation in uranium-zirconium alloy fuels," TMS Annual Meeting, Orlando, FL, March 11-14, 2012.
8. J.T. McKeown, S. Ahn, S. Irukuvarghula, M. Wall, L.L. Hsiung, S. McDeavitt, P.E.A. Turchi, "Characterization of U-Zr alloys for ultrahigh burn-up nuclear fuels," MS & T 2012, Pittsburgh, PA, October 7-11, 2012.

2.2   Highlights from Texas A&M University-Fuel Performance Modeling (Appendix E)
       (Dr. Pavel Tsvetkov and Hyocheol Lee)

Fuel performance analysis is indispensable for the development of new fuel designs and the reliable operation of fuels at high burnup and power density. Many analysis codes have been developed to evaluate the irradiation behavior of metallic fuels for sodium-cooled fast reactors (SFR). However, some of them such as LIFE-METAL [1] and SESAME [2] contain many empirical correlations and cannot be extrapolated beyond the narrow database for which they were developed [3]. The newer codes, ALFUS [4] and MACSIS [5], have more physics-based models, but they are limited to steady state conditions. FEAST-METAL [3] is the newest code and adopted the most advanced and mechanistic models. Nonetheless, it depends on simplifications which are different from real phenomena. Therefore, in this research, development of a new fuel performance code has been pursued to more accurately simulate thermo-mechanical responses of metallic SFR fuels under irradiation. The scope of research in this project has been focused mainly on establishing basic code structures and numerical algorithms to incorporate brand-new physics-based models. The data from the project experimental efforts support the macro-scale model and the code development efforts serving both as a property database foundation as well as a validation databank. The focus is on developing an approach to describe swelling behavior in a real alloy pin. This involves simulating a thermal profile and coupling the fundamental diffusion data into theoretical models, such as those developed for swelling and hot pressing by creep cavitation mechanisms. This will be an important first step toward combining fundamental computational methods, experimental data, and theoretical models into a meaningful fuel performance code system for metal alloy fuels. Thus, for describing specific fuel behaviors such as transient creep fracture and fuel-cladding chemical interaction, relevant phenomenological models should be implanted into the platform developed here in the future research.

Based on the experimentally appraised fundamental physics of gas atom migration, bubble nucleation, and bubble growth, new mechanistic models are being developed to describe and predict fission gas release and fission gas induced swelling in sodium-cooled fast reactor fuels. Especially, the new models will consider both the homogeneous bubble nucleation and the heterogeneous bubble nucleation. In the case of the heterogeneous nucleation, the equivalent diffusion area like the Booth sphere is the grain lattice, and the bubbles are nucleated only in the grain boundaries. Thus, the behaviors of fission gas atoms and bubbles will be formulated by diffusion-controlled kinetics [8]. On the other hand, in the homogeneous nucleation, the equivalent diffusion area is the phase precipitate lattice, and the bubbles are homogeneously nucleated in the phase boundaries and the grain boundaries. Therefore, reaction-rate-controlled kinetics [8] is being implemented. The new models developed in this research are incorporated as a module in a SFR fuel performance code.

References for Section 2.2
[1]   M.C. Billone, Y.Y. Liu, "Status of the fuel element modeling codes for metallic fuels", Proceedings of the International Conference Reliable Fuels for Liquid Metal Reactors, American Nuclear Society Tucson, Arizona 1986.
[2]   T. Kobayashi, M. Kinoshita, S. Hattori, T. Ogawa, Y. Tsuboi, M. Ishida, S. Ogawa, H. Saito, "DEVELOPMENT OF THE SESAME METALLIC FUEL PERFORMANCE CODE", Nuclear Technology 89 (1990) 183–193.
[3]   Aydın Karahan, Jacopo Buongiorno, "A new code for predicting the thermo-mechanical and irradiation behavior of metallic fuels in sodium fast reactors", Journal of Nuclear Materials 396 (2010) 283–293.
[4]   T. Ogata, T. Yokoo, "DEVELOPMENT AND VALIDATION OF ALFUS: AN IRRADIATION BEHAVIOR ANALYSIS CODE FOR METALLIC FAST REACTOR FUELS", Nuclear Technology 128 (1999) 113–123.
[5]   W. Hwang, N. Cheol, B.S. Thak, Y.C. Kim, "MACSIS: A METALLIC FUEL PERFORMANCE ANALYSIS CODE FOR SIMULATING IN-REACTOR BEHAVIOR UNDER STEADY-STATE CONDITIONS", Nuclear Technology 123 (1998) 130–141.
[6]   James H. Rust, "Nuclear Power Plant Engineering", Haralson Publishing Company, 1979.
[7]   Henri BAILLY, "The Nuclear fuel of Pressurized Water Reactors and Fast Neutron Reactors", CEA, 1999.
[8]   Donald R. Olander, "Fundamental Aspects of Nuclear Reactor Fuel Elements", Technical Information Center, 1976.

2.3   Highlights from the University of Tennessee, Knoxville (Appendix F)
         (Dr. Brian Wirth)

At the time of report preparation, no overall report was available. However, the following information summarizes some of the progress made during the course of this project. A summary is presented below regarding the activies undertaken in this portion of the project.

Ab-initio calculations were performed using the VASP code to calculate the behavior of vacancy and self-interstitial atom defects in alpha U-Zr alloys, as well as the energetics of small Xe-vacancy clusters and the mechanisms of xenon diffusion in alpha uranium. A comprehensive analysis of xenon – vacancy cluster formation and binding energy calculated by ab-initio modeling was completed. A manuscript describing these results is being finalized for submission, and should be submitted to the Journal of Physics: Condensed Matter (Appenix F). A cluster dynamics modeling approach was implemented to evaluate the nucleation stage of fission gas bubbles in the outer periphery of metallic U-Zr nuclear fuel.

Abstract from Appendix F

"Metallic uranium–zirconium alloys are of interest for a variety of fast reactor designs, and there is substantial experience with the behavior of metallic fuels. Yet, there remain a number of questions regarding the mechanisms controlling fission-gas-driven swelling in these alloys. Here we present results of ab initio calculations of the diffusion behavior of interstitial and vacancy point defects in α U–Zr alloys. The formation energy and migration barrier of vacancy and interstitial defects, and the influence of Zr on these values, is obtained and compared with experimental results. Our results confirm that self-diffusion in pure α U is via a simple vacancy mechanism, and shows anisotropic character. The calculated values of activation energy are consistent with the experimental results in the literature. For interstitial diffusion, the kick-out mechanism was found to have the smallest energy barrier. The calculations of point defects, and later Xe, in U–Zr alloys will provide a foundation for computational modeling of fission gas bubble nucleation and growth."

APPENDICES

Appendix A – **DOCTORAL DISSERTATION:** S. Ahn, *Comprehensive Investigation of the Uranium-Zirconium Alloy System: Thermophysical Properties, Phase characterization and Ion Implantation Effects*, Doctoral Dissertation, Texas A&M University, August 2013. (Page 9)

Appendix B - **ORAL DEFENSE PRESENTATION:** S. Ahn, *Comprehensive Investigation of the Uranium-Zirconium Alloy System: Thermophysical Properties, Phase characterization and Ion Implantation Effects*, Doctoral Dissertation, Texas A&M University, May 2013. (Page 355)

Appendix C - **DOCTORAL DISSERTATION:** S. Irukuvarghula, *Solid State Phase Transformations in Uranium Zirconium Alloys*, Doctoral Dissertation, Texas A&M University, August 2013. (Page 432)

Appendix D - **ORAL DEFENSE PRESENTATION:** S. Irukuvarghula, *Solid State Phase Transformations in Uranium Zirconium Alloys*, Doctoral Dissertation, Texas A&M University, June 2013. (Page 582)

Appendix E - **SUMMARY REPORT:** Fuel Performance Experiments and Modeling: Fission Gas Bubble Nucleation and Growth in Alloy Nuclear Fuels: Macro Model Development (Pavel V. Tsvetkov, Hyocheol Lee), April 2015.(Page 640)

Appendix F - G. Huang and B.D. Wirth,First-principles study of diffusion of interstitial and vacancy in α U–Zr," J. Phys: Condens. Matter 23 (2011) 205402. (Page 667)

All Appendices are available through the NEUP Integration Office. Please contact neup@inl.gov to request a copy.

Appendix A – **DOCTORAL DISSERTATION:** S. Ahn, *Comprehensive Investigation of the Uranium-Zirconium Alloy System: Thermophysical Properties, Phase characterization and Ion Implantation Effects*, Doctoral Dissertation, Texas A&M University, August 2013.

COMPREHENSIVE INVESTIGATION OF THE URANIUM-ZIRCONIUM

ALLOY SYSTEM: THERMOPHYSICAL PROPERTIES, PHASE

CHARACTERIZATION AND ION IMPLANTATION EFFECTS

A Dissertation

by

SANGJOON AHN

Submitted to the Office of Graduate Studies of
Texas A&M University
in partial fulfillment of the requirements for the degree of

DOCTOR OF PHILOSOPHY

Chair of Committee,	Sean M. McDeavitt
Committee Members,	Lin Shao
	Pavel V. Tsvetkov
	Xinghang Zhang
Head of Department,	Yassin A. Hassan

August 2013

Major Subject: Nuclear Engineering

ABSTRACT

Uranium-zirconium (U-Zr) alloys comprise a class of metallic nuclear fuel that is regularly considered for application in fast nuclear energy systems. The U-10wt%Zr alloy has been demonstrated to very high burnup without cladding breach in the Experimental Breeder Reactor-II (EBR-II). This was accomplished by successfully accommodating gaseous fission products with low smear density fuel and an enlarged cladding plenum. Fission gas swelling behavior of the fuel has been experimentally revealed to be significantly affected by the temperature gradient within a fuel pin and the multiple phase morphologies that exist across the fuel pin. However, the phase effects on swelling behavior have not been yet fully accounted for in existing fuel performance models which tend to assume the fuel exists as a homogeneous single phase medium across the entire fuel pin.

Phase effects on gas bubble nucleation and growth in the alloy were investigated using transmission electron microscopy (TEM). To achieve this end, a comprehensive examination of the alloy system was carried out. This included the fabrication of uranium alloys containing 0.1, 2, 5, 10, 20, 30, 40, and 50 wt% zirconium by melt-casting. These alloys were characterized using electron probe micro-analysis (EPMA), differential scanning calorimetry (DSC), and thermogravimetric analysis (TGA). Once the alloys were satisfactorily characterized, selected U-Zr alloys were irradiated with 140 keV He$^+$ ions at fluences ranging from 1×10^{14} to 5×10^{16} ions/cm^2.

Metallographic and micro-chemical analysis of the alloys indicated that annealing at 600 °C equilibrates the alloys within 168 h to have stable α-U and δ-UZr$_2$ phase morphologies. This was in contrast to some reported data that showed kinetically sluggish δ-UZr$_2$ phase formation.

Phase transformation temperatures and enthalpies were measured using DSC-TGA for each of the alloys. Measured temperatures from different time annealed alloys have shown consistent matches with most of the features in the current U-Zr phase diagram which further augmented the EPMA observed microstructural equilibrium. Nevertheless, quantitative transformation enthalpy analysis also suggests potential errors in the existing U-Zr binary phase diagram. More specifically, the (β-U, γ$_2$) phase region does not appear to be present in Zr-rich (> 15 wt%) U-Zr alloys and so further investigation may be required.

To prepare TEM specimens, characterized U-Zr alloys were mechanically thinned to a thickness of ~150 μm, and then electropolished using a 5% perchloric acid/95% methanol electrolyte. Uranium-rich phase was preferentially thinned in two phase alloys, giving saw-tooth shaped perforated boundaries; the alloy images were very clear and alloy characterization was accomplished.

During *in-situ* heating U-10Zr and U-20Zr alloys up to 810 °C, selected area diffraction (SAD) patterns were observed as the structure evolved up to ~690 °C and the expected α-U → β-U phase transformation at 662 °C was never observed. For the temperature range of the (α-U, γ$_2$) phase region, phase transformation driven diffusion

was observed as uranium moved into Zr-rich phase matrix in U-20Zr alloy; this was noted as nonuniform bridging of adjacent phase lamellae in the alloy.

From the irradiation tests, nano-scale voids were discovered to be evenly distributed over several micrometers in U-40Zr alloys. For the alloys irradiated at the fluences of 1×10^{16} and 5×10^{16} ions/cm^2, estimated void densities were proportional to the irradiation doses, (250 ± 40) and (1460 ± 30) /μm^2, while void sizes were fairly constant, (6.0 ± 1.5) and (5.2 ± 1.2) nm, respectively. Measured data could be foundational inputs to the further development of a semi-empirical metal fuel performance model.

DEDICATION

To Hyunsook

ACKNOWLEDGEMENTS

NOMENCLATURE

BF	Bright Field
BSE	Back-Scattered Electron
DBA	Design Basis Accident
DF	Dark Field
DP	Diffraction Pattern
DSC	Differential Scanning Calorimetry/Calorimeter
DTA	Differential Thermal Analysis
EBR-I	Experimental Breeder Reactor-I
EBR-II	Experimental Breeder Reactor-II
EDS	Energy Dispersive Spectroscopy
EPMA	Electron Probe Micro-Analysis/Analyzer
FBR	Fast Breeder Reactor
FIB	Focused Ion Beam
FCCI	Fuel-Cladding Chemical Interaction
FCMI	Fuel-Cladding Mechanical Interaction
FF	Fission Fragment
FMS	Ferritic Martensitic Steel
FOLZ	First Order Laue Zone
FP	Fission Product
GFP	Gaseous Fission Product

GIF	Generation IV International Forum
HLW	High Level Waste
HOLZ	Higher Order Laue Zone
HRTEM	High Resolution Transmission Electron Microscopy/e
IFR	Integral Fast Reactor
LN$_2$	Liquid Nitrogen
LOFA	Loss of Flow Accident
LWR	Light Water Reactor
MA	Minor Actinide
NIH	National Institutes of Health
NNWS	Non-Nuclear Weapon State
NPP	Nuclear Power Plant
OM	Optical Microscopy/e
R&D	Research and Development
RT	Room Temperature
SAD	Selected Area Diffraction
SFP	Solid Fission Product
SFR	Sodium-cooled Fast Reactor
SNF	Spent Nuclear Fuel
SOLZ	Second Order Laue Zone
TEM	Transmission Electron Microscopy/e
TGA	Thermogravimetric Analysis/Analyzer

TRU	Transuranic element
U-Zr	Uranium-Zirconium
U-Pu-Zr	Uranium-Plutonium-Zirconium
XEDS	X-ray Energy Dispersive Spectroscopy
XRD	X-ray Diffraction
WDS	Wavelength Dispersive Spectroscopy
ZOLZ	Zeroth Order Laue Zone

TABLE OF CONTENTS

Page

LIST OF FIGURES

xvii

1. INTRODUCTION

1.1 Motivation

Uranium-zirconium (U-Zr) alloys are metallic nuclear fuels. The U-10Zr alloy has demonstrated excellent performance up to ~20 at% burnup in Experimental Breeder Reactor-II (EBR-II) [1, 2], and other higher Zr and lower Zr alloys are being considered for advanced nuclear applications [3, 4]. Metallic alloy nuclear fuel is a key feature for fast breeder reactor (FBR) systems where the fast neutron spectrum enables effective destruction of minor actinides (MA) that are bred into spent nuclear fuel (SNF) [5-7]. The presence of all of the actinides in spent nuclear fuel is a challenge for direct disposal because the actinides have long half-lives that necessitate long term monitoring and deep geological disposal, which dramatically increasing the disposal cost and public anxiety on the issue [8, 9].

Accommodating voluminous gaseous fission products (GFP) within nuclear fuels and claddings has been a critical challenge for nuclear fuel performance since the onset of nuclear energy [10]. However, fuel swelling due to insoluble fission gases, i.e. xenon and krypton, is more severe in metallic fuels than in its oxide counterparts because, in part, fast nuclear systems are driven to higher burnup and the metallic fuel alloys readily allow diffusion of the fission gas atoms to sinks such as grain and phase boundaries [11-13]. Fission gas bubbles formed in the fuels cause significant volumetric swelling, thus requiring the design of lower smear density fuels [14]. "Smear density" is a commonly

1

used term, defined as the ratio between the theoretical planar fuel density and the internal planar cladding dimension [15], in order to evaluate allowed fuel swelling before fuel-cladding mechanical interaction (FCMI).

In highly swollen fuel pins above ~1 at% burnup [16], fission gas in interconnected bubbles may be released into the fuel-cladding gap and plenum through the open pore structures connected to the surface of the fuel pin. Released gas increases the pressure inside the cladding tube, creating another challenge that is overcome by an enlarged plenum to accommodate the fission gas without significant cladding deformation which could result cladding rupture.

Fission gas bubble behavior in metallic fuels is a key phenomenon of interest which needs to be thoroughly understood to enable effective fuel performance modeling. Therefore extensive studies on and related to the issue have been carried out for U-Zr alloy fuels [17-47], and referred for the development of current fuel performance models. Most of the studies were, however, focused on single zirconium composition alloys, U-10Zr and U-Pu-10Zr, due to the historical importance of these alloys to the EBR-II and Integral Fast Reactor (IFR) systems [48, 49]. The U-10Zr alloy was used in EBR-II for 30 years [50]. A higher Zr-content alloy was not desired for that program, but it was not technically feasible either since the softening point of fused quartz mold used for containing the molten alloy mixture in the casting process was far below the liquidus temperatures of U-Zr alloys containing more than 10 wt% of zirconium [51]. In more recent applications, high Zr alloys have been considered for the transmutation fuels bearing MAs.

Current fuel performance models are highly empirical and validation is primarily limited to the database established from U-10Zr alloys, in part owing to the historical application alluded to above. Moreover, those models commonly adopt a homogeneous medium assumption [52-63], which is in contrast to the true structures observed in fuel as noted in published post-irradiation examinations (PIE) of spent U-10Zr alloy fuels discharged from EBR-II.

The PIEs consistently indicate that two or three distinct phase zones exist in the fuel corresponding to high fuel centerline temperatures and the temperature gradient within the fuel pin [1, 2, 15, 16, 64, 65]. In addition, each phase zone is typically a two phase mixture except for the central high temperature zone in the hottest fuel pins, which is comprised of the single γ phase. It was further revealed from the examinations that fission gas bubble behavior and fuel constituent redistribution are significantly affected by the properties and morphologies of the solid phase(s) within the fuel pins.

The incorrect homogeneous medium assumption adopted in the models has been justified mainly by considering the small dimensions of phase precipitates and matrix phase lamellae, which results in nearly random phase boundary distributions. However due to radial redistribution of fuel constituents, the volume fraction of each phase within a concentric phase zone may be significantly varied with pin power level and position within the reactor core. Thus the reliability and conservativeness of the assumption is questionable, particularly in the case where the models need to be extrapolated beyond the existing experimental data.

Although the current empirical fuel performance models are still applicable for U-10Zr alloy fuels, the model validated for Zr-rich U-Zr alloys and extended burnup is potentially beneficial for mainly two reasons; 1) there are design requirements under development that may extend fuel applications to Zr-rich U-Zr alloys which can now be fabricated using advanced methods [66] and 2) the high burnup potential of U-Zr fuel is clearly evident since the latest EBR-II cladding never failed in operation up to 19.9 at% [4, 50].

It is thus desirable that the reliability of the models based on U-10Zr alloy fuels be ensured for extended burnup. Zr-rich U-Zr alloys are expected to yield numerous benefits in terms of fuel performance, e.g. enhanced irradiation tolerance, higher temperature operability, long-term mechanical integrity, and mitigated fuel-cladding chemical interaction (FCCI) [67]. The cost, however, is that there will be a lower heavy metal density in the fuel. In addition, it might be worthwhile to emphasize that the zirconium composition of the U-Zr alloys has never been optimized with respect to fuel performance, but it was capped by the limitation of historical fuel fabrication method as noted above.

A more accurate metal fuel performance model may be developed by incorporating the actual thermophysical properties and behavior of U-Zr alloys [68-73]. To do this, the fundamentals of fission gas behavior must be characterized in order to model the reliability and effectiveness for higher burnup fuel designs. In order to find the first principles, atomic-scale observation on gas bubble behavior in U-Zr alloys is

4

thought to be the first step prior to the development of the models, since little data is currently available in open literature.

1.2 Overview of the Investigation of U-Zr Alloys

The objective of this research is to experimentally evaluate the effects of the solid phases on gas bubble nucleation and behavior in U-Zr alloys. As a first study, helium was used in place of krypton or xenon. The experiments and analyses described below may be divided into two main parts. For the first part, the metallurgical and thermophysical characterization of U-Zr alloys was completed using electron probe micro-analysis (EPMA), differential scanning calorimetry (DSC), and thermogravimetric analysis (TGA). This was completed to characterize the nature of the fabricated alloys, upon comparing the data with the existing U-Zr binary phase diagram. Some inconsistencies were noted from the quantitative analysis on measured transformation enthalpies (described in Section 5.2.4). More specifically, the (β, γ_2) phase region does not appear to be present in Zr-rich (> 15 wt%) U-Zr alloys and so further investigation will be required to validate the accuracy of the U-Zr binary phase diagram.

For the second part of this work, the nano-scale metallographic characterization of helium ion-beam irradiated U-Zr alloys was completed using transmission electron microscopy (TEM). This was carried out to estimate how the phases affect gas bubble morphology in the alloys. As an additional study, U-10Zr and U-20Zr alloys were examined in the TEM with *in-situ* heating to further investigate the phase transformation

behavior of the alloys. These measurements revealed the same inconsistencies with the binary U-Zr phase diagram that were evident in the DSC-TGA measurements.

The data generated in this work is designed to be foundational for the further development of a semi-empirical metal fuel performance model accounting the solid phase effects on the restructuring of U-Zr alloy fuel. It is essential to correlate the experimental observations with the underlying physical principles in order to establish an extendable fuel performance model over very high burnup (> 20 at%) and Zr-rich (> 15 wt%) U-Zr alloy nuclear fuels while overcoming the drawbacks of current empirical models based on limited experimental data mostly obtained from U-10Zr alloy fuels.

In the light of the historical context and future directions for U-Zr fuels noted above, the following sections present a comprehensive study on the uranium-zirconium alloy system along with a nascent study on the behavior of gas bubbles within the system. The academic background that is indispensable to comprehend the study is briefly summarized in Section 2. Section 3 depicts the experimental procedures and methods used for various aspects of this study. The observed experimental data from the alloy characterization and advanced alloy behavior studies along with the calculations for ion-beam irradiation conditions and parameters are fully described in Section 4 along with brief descriptions and explanations. The acquired data is discussed with a thorough literature review in Section 5. Finally, the overall summary and conclusions are given in the last section with recommended future work. The appendices include additional metallurgical and thermophysical characterization data that were gathered alongside of this work for the uranium-molybdenum (Appendix A) and uranium-titanium (Appendix

B) alloy systems. Selected additional experimental results related to the U-Zr alloys are given at the last in Appendix C.

2. BACKGROUND

The broad range of academic fundamentals required to comprehend this study are included in this section; the nature of spent nuclear fuel is reviewed in Section 2.1 with emphases on describing the closed fuel cycle, sodium-cooled fast reactor (SFR), and metallic nuclear fuels. Following that, alloy details are discussed for U-Pu-Zr (Section 2.2) and U-Zr (Section 2.3) metallic alloy nuclear fuels. The final two sections describe relevant information regarding U-Zr alloy fuel restructuring and phases effects (Section 2.4) and the ion-beam irradiation method used to simulate void and fission gas bubble formation inside the alloys (Section 2.5).

2.1 Spent Nuclear Fuel

Public interests and concerns about potential risks of spent nuclear fuel were recently renewed due to the nuclear incident at Fukushima Dai-ich nuclear power plant provoked by catastrophic natural disasters beyond design basis accident (DBA); the magnitude 9.0 earthquake followed by 14 meters-high tsunami [74, 75]. Spent nuclear fuel is an unavoidable critical challenge to the continued use of nuclear energy for long-term electricity generation, especially since other viable renewable energy sources are not soon to be applicable at commercial scale. However, since the dawn of the *"Atoms for Peace"* program [76], decisive solutions for nuclear waste management have been challenging to select and implement due to fluctuating pressures and motivations from

political, social, economic, and even international driving forces. In other words, spent nuclear fuel is a challenge waiting to be solved and a challenge that must be solved even though consensus is difficult to achieve.

Fresh nuclear fuel typically starts as pure uranium dioxide, but spent nuclear fuel is an complex compound comprised of about 95 % of valuable resources, uranium and plutonium, can be recycled as fresh nuclear fuel [77], and trace amount of extremely long-term radioactivity sources (e.g. minor actinides whose half-lives are ~10^6 years) [78, 79]. Therefore there are severe objections to construction of underground geologic repositories for quasi-permanent disposal of spent nuclear fuel from both sides of nuclear communities and general public around the world. On the other hand, concerns regarding the potential scarcity of naturally occurring fissionable materials, uranium and thorium, keep the idea of reprocessing and transmutation of spent nuclear fuel as an active alternative solution being developed internationally.

2.1.1 Closed Fuel Cycle

In an open, or once-through, fuel cycle, once-used nuclear fuel will be eventually disposed in underground repository sites which ought to be monitored for over a million years until its radioactivity has decayed to at least below that of natural uranium. This comes with concern regarding the integrity and potential breach of the casks which could potentially leak radioactive materials into underground water. This extremely long term monitoring is required mainly due to long half-lives of MAs contained in spent nuclear

fuel principally discharged from light water reactors (LWR), a workhorse of electricity production worldwide.

The closed nuclear fuel cycle, in contrast, enables the repeated reprocessing of spent nuclear fuel to create feed material as fresh fuel for fast reactors to maximize the utilization of the potential energy stored in uranium, plutonium and other transuranic elements (TRU). Through the closed fuel cycle, the effective half-life and volume of spent nuclear fuel is expected to be reduced by a factor of 1/1000 and 1/100, respectively [80].

Despite these tremendous foreseen benefits of recycling spent nuclear fuel in the standpoints of environment, public safety, and natural resource utilization, the closed fuel cycle is, however, not yet very attractive commercially or to governments due to its cost [81]. Economic aspects of the nuclear fuel cycle ought to be considered for the sustainability of the nuclear industry and public acceptance to extended deployment of nuclear power reactors. Hence, commercial scale advanced fast reactor systems including integrated reprocessing facilities could be developed to lower the costs for construction and operation of the system. The anticipated expense for research and development (R&D) and performance demonstration of commercial scale advanced FBR with an associated fuel cycle facility is a barriers to the realization of the benefits of a closed fuel cycle [82], even though EBR-II, a metallic U-Zr and U-Pu-Zr alloy fueled sodium-cooled fast breeder reactor, successfully demonstrated superior performance decades ago [50].

2.1.2 Sodium-cooled Fast Reactor

The sodium-cooled fast reactor (SFR) is one of the advanced fast reactor concepts suggested from the Generation IV international forum (GIF). The SFR typically employs U-Zr alloy fuels with sodium coolant to generate a fast neutron spectrum to effectively burn out the long living radioactive isotopes in spent nuclear fuel [5, 83].

Sodium has many excellent material properties that make it suitable as a coolant for a fast reactor embedding metallic fuels, e.g. neutron transparency, relatively high atomic number, high thermal conductivity, low melting temperature, applicably high boiling temperature, and high compatibility with metals. Therefore sodium coolant facilitates the reactor operation with fast neutron spectrum, ambient operating pressure, high operating temperature, and passive core cooling in loss of flow accident (LOFA) [84-86]. This eliminates one of the main causes of the incident in Fukushima Dai-ich NPP other than tremendous natural disasters [74].

However, the flammability of sodium in contact with water and activation of ^{23}Na to ^{24}Na do necessitate unique safety design features into SFR, most notably, an intermediate sodium loop. Typical SFR design has three loops, primary and secondary sodium loops and a water/steam loop, as shown in Fig. 2-1. This is used to minimize radioactive environmental contamination through water/steam loop during accident conditions that can potentially be initiated by leaked sodium contacted with water/steam/air; this happened at the incident in the MONJU SFR facility in Japan [87,

88]. Alternative inactive gaseous secondary coolants, for example supercritical carbon dioxide (S-CO$_2$), are now being considered inplace of water to minimize the concerns on the flammability of sodium coolant [89, 90].
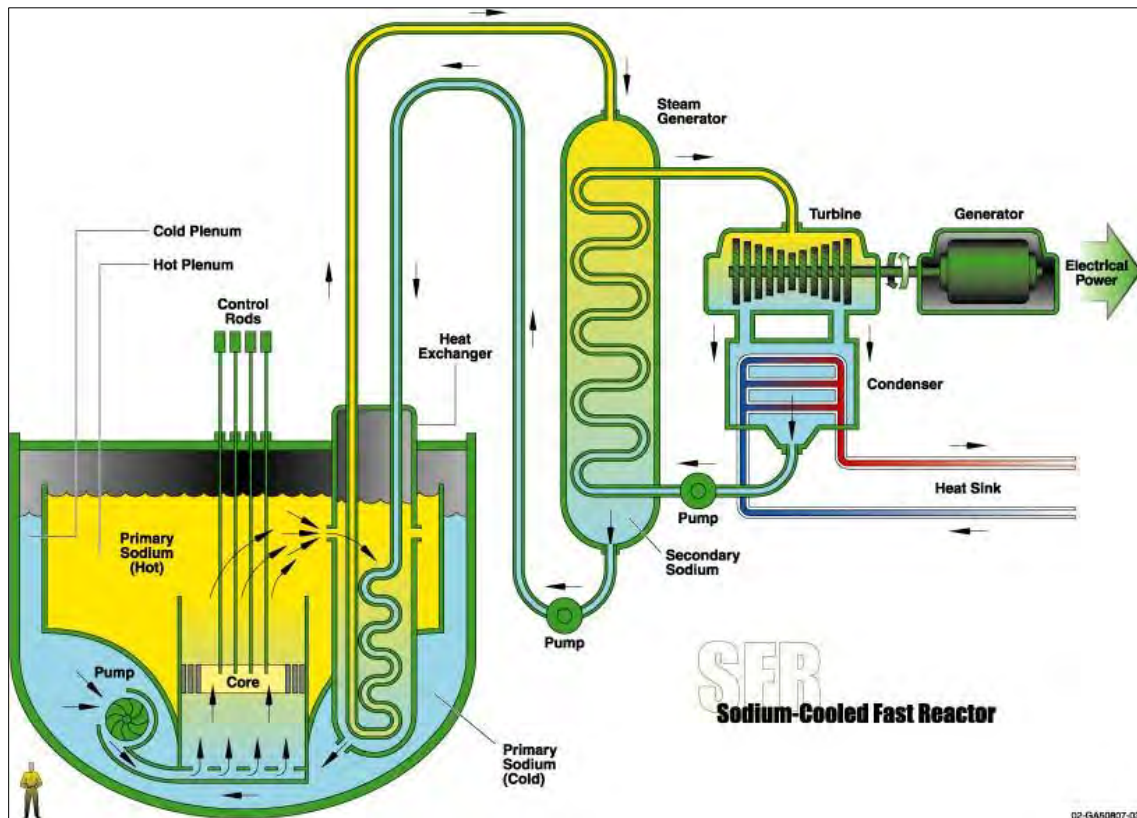
Figure 2-1: Schematic diagram of sodium-cooled fast reactor [5].

2.1.3 Metallic Nuclear Fuels

The first electricity generating nuclear reactor, Experimental Breeder Reactor-I (EBR-I) was fueled with metallic nuclear fuels [91]. Metallic fuels have been also widely used for many other FBRs because of their excellent breeding performance compare to oxide or any other types of ceramic nuclear fuels. Higher fissile atom density, thermal conductivity and burnup potential of metallic fuels than any other type fuels have strengthened the rationale for the material selection [92-94].

Additional benefit of importance obtained from using metallic fuels is to facilitate a novel reprocessing technique for closed fuel cycle, i.e. pyroprocessing utilizing electrorefining [95-97]. In contrast, reprocessing oxide fuels into a metal fuel requires a chemical reduction process before electrorefining may be used. Diversion of nuclear materials and proliferation of nuclear weapons from any stage of pyro-processing is virtually inconceivable, since cathode products in electrorefining process contains highly radioactive fission products (FP) with uranium, plutonium and MAs [98, 99]. Throughout the recycling process of the fuels, it is conceivable that all actinides may be retained within the fuel cycle to be fissioned in a fast reactor system instead of participated in high level radioactive waste (HLW), which is a crucial benefit ought to be emphasized. Consequently, radioactive waste separated from spent nuclear fuel in a closed fuel cycle utilizing electrorefining of metallic fuel has several hundred years of effective half-life which is ~1/1000 of that of spent nuclear fuel generated from once-through fuel cycle without reprocessing [80].

13

2.2 U-Pu-Zr Alloy Fuel

The ternary uranium-plutonium-zirconium (U-Pu-Zr) alloy was selected as the fuel for EBR-II, amongst many considerable metallic alloy systems because of outstanding performance [50]. Fissionable actinide elements are necessary by the nature of FBR. Uranium is recovered from spent nuclear fuel and the presence of plutonium is indispensable in breeder reactor using ^{238}U as the fertile material. On the other hand, zirconium was chosen in order to elevate solidus temperature of the fuel, therefore, increasing operating temperature and safety margin, since solidus temperature of U-Pu binary alloy is unfeasibly low for a practical reactor design. Zirconium was selected over several other neutron transparent refractory metals, i.e. chromium, molybdenum, and titanium which can all satisfactorily increase solidus temperatures of U-Pu alloys, because it enhances compatibility of the fuel with austenitic stainless steel claddings (D9) used at the time the fuel was being developed [100].

At the periphery of the alloy fuel pin, minor interstitial elements of the cladding, e.g. nitrogen and oxygen, diffused into the fuel pin, formed zirconium nitride and oxide layer which hindered the diffusion of major constituents of the cladding, e.g. ion and nickel, into the fuel. Therefore, the zirconium formed a ceramic interlayer that prevented the formation of low meting temperature phases in both of uranium-ion (U-Fe) and uranium-nickel (U-Ni) binary alloy systems where eutectic melting occurs below 800 °C [101-103], limiting fuel performance [104-108].

Anisotropic fuel swelling was still a crucial issue even after alloying zirconium with U-Pu [109]. The issue has been successfully resolved by lowering smear density of the fuel down to 75 % to accommodate about 30 % volumetric swelling [14, 110, 111]. Cladding dimensions were correspondently enlarged to have larger plenum and diameter to shelter released fission gas without significant increase of internal pressure could breach the cladding. After all design modification were made, U-Pu-Zr fuel achieved 18.4 at% burnup with D9 cladding and later it was extended up to 19.9 at% with a ferritic martensitic steel (FMS) cladding (HT9) without cladding breach [1, 2]. Hence U-Pu-Zr fuel is one of the most promising fuels due to demonstrated outstanding performance during several decades of EBR-II operation [112, 113].

2.3 U-Zr Alloy Fuel

The U-Zr alloy is the centerpiece material of this present study because of two reasons. First, the U-Zr binary alloy system is an excellent representative for the U-Pu-Zr ternary alloy system at the low plutonium contents alloys commonly utilized in an SFR. The solubility of plutonium in all allotropic phases of uranium, i.e. 15, 20, and 100 wt% (complete) solubility respectively for α-, β- and γ-U [114-116], is comparable to the maximum plutonium contents (19 wt%) of U-Pu-Zr fuel used in EBR-II. Therefore, the U-Zr binary phase diagram has been often referred for phase analysis of the ternary fuel behavior [117]. Second, affirmative understanding on polymorphic modifications in U-Zr sub-binary system is vital to the construction of ternary phase diagram of U-Pu-Zr

alloy. Research in this area should begin with U-Zr and expand from there. Interestingly, the data reported in this document (Sections 4 and 5) indicate that the "well-established" U-Zr binary system still has many inconsistencies and potential errors to sort out.

U-Zr alloy fuel was used extensively as a driver fuel in EBR-II, and it showed comparable performance with U-Pu-Zr alloy. Furthermore, U-Zr alloys are more suitable for non-nuclear weapon states (NNWS) in both aspects of politics and procurement to start up a fast reactor which could eventually use reprocessed U-TRU-Zr fuel, unless the given political circumstance is exceptionally extraordinary. Thus, complete material property database of U-Zr alloy is mandatory to establish the safety, operability, and, therefore, licensability of any future SFR system.

For the commercial deployment of a U-Zr fueled SFR, crucial keys include the more extensive demonstration of the fuel performance and the development of a fuel performance model that will reliably predict the fuel behavior and cladding failure for long-term operation. It is the assertion of this author that predictive modeling will be more effective if it is based on first principles and materials properties and performances. The importance of fuel performance demonstration and modeling is more intensified in recent trend seeking very high burnup (> 20 at%) [3, 81, 118].

Unfortunately, currently available material database are significantly limited on U-10Zr alloys and correlated fuel performance models are empirically based on the limited data. This bias was due to a simple historical reason, i.e. zirconium concentration of U-Zr alloy nuclear fuel was limited up to 10 wt% for the fuel fabrication method used when the fuel was being developed, i.e. injection casting. Liquidus temperature of the

16

fuel including more than 10 wt% of zirconium exceeded the softening point of quartz mold containing liquefied fuel mixture, hence fabrication was physically impossible [51]. This limitation may be overcome by utilizing other fuel fabrication methods, for instance, hot-extrusion and metal powder sintering [66, 119].

2.3.1 U-Zr Binary Phase Diagram

U-Zr alloy system (Figs. 2-2 and 2-3) has seven solid phases; α-U (orthorhombic), β-U (tetragonal), γ (body-centered cubic), γ_1 (body-centered cubic, uranium rich), γ_2 (body-centered cubic, zirconium rich), α-Zr (hexagonal close-packed), and intermediate intermetallic δ-UZr_2 phase (hexagonal, C32) whose long-term stability as stable phase had been questioned [120-130]. The binary phase diagram of U-Zr alloy has been developed and improved over several decades but there are essentially two types of distinctively different phase diagrams present in the literature, as shown in Figs. 2-2 and 2-3.

The U-Zr phase diagram published by Sheldon and Peterson shown in Fig. 2-2 (hereinafter referred to as Sheldon's phase diagram) is currently widely used and more recent diagrams have been published that mimic its basic features. Sheldon's phase diagram was constructed by selecting a set of data [131-136] among conflicting experimental results that were separately reported in open literatures by the end of 1980's [127]. The other type of U-Zr phase diagram is shown in Fig. 2-3 suggested by

Rough and Bauer (hereinafter referred to as Rough' phase diagram), mainly based on available experimental data at late 1950's [120, 121, 123, 124, 137-141].
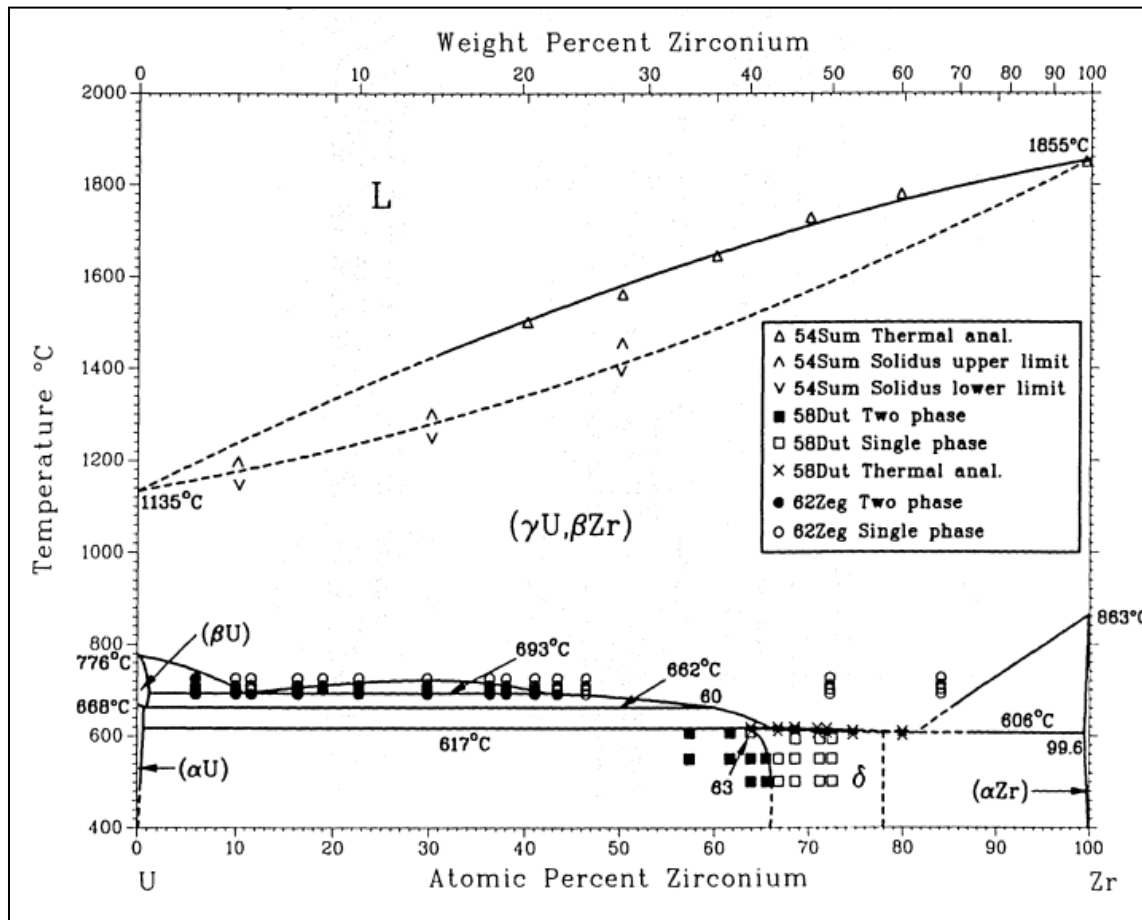
Figure 2-2: U-Zr binary phase diagram constructed by Sheldon and Peterson [127].
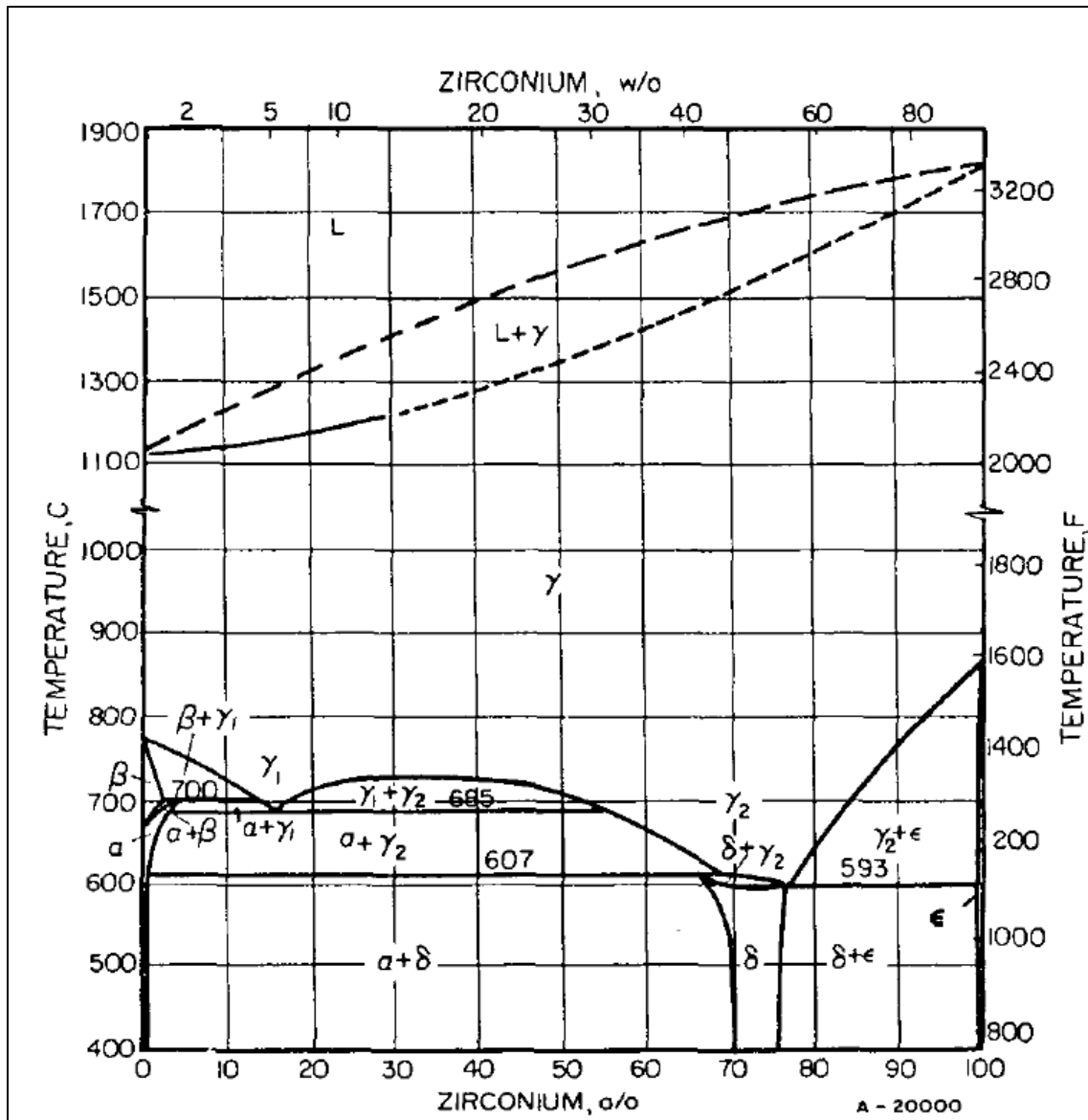
Figure 2-3: U-Zr binary phase diagram constructed by Rough and Bauer [124].
(Note ε phase in the figure is α-Zr phase in Fig. 2-2.)

There are several mismatches between the two phase diagrams. The major distinction is aroused from whether adopting eutectoid decomposition of β-U phase into (α-U, γ_2) phase or peritectoid formation of α-U phase from (β-U, γ_1) phase. Although Sheldon's phase diagram has been widely referred as the nearly constitutional U-Zr phase diagram without significant modification over the other phase diagrams, Rough's phase diagram is more matched with DSC-TGA measurements given in Section 4.2 of this particular study. Further discussion in detail is given in Section 5.2 with literature review concluded that current U-Zr phase diagram may need to be experimentally revisited.

2.4 Phase Effects on U-Zr Alloy Fuel Restructuring

As-cast fuel structures begin evolving immediately once reactor operation begins, mainly due to fission of heavy metal atoms, increasing fuel temperatures (and a reasonably broad temperature profile), and simultaneously occurring radiation damage cascades. Fissioned heavy metal atoms leave vacancies at its original sites and split into two or three energetic ionized fission fragments (FF), sharing ~85 % of fission energy. Each FF trigger radiation damage cascades to pristine fuel structure until being stationed in a lattice site after transmitting most of its kinetic energy to fuel constituents, in the form of aggrandized vibration within crystal lattice, therefore elevated fuel temperature. A steep temperature gradient is established within the fuel pin at the generated heat is removed by the coolant on the external side of the cladding. Consequently for U-Zr alloy

20

fuel pins, two or three distinctive radial zones having different phases are developed. Specific number of phase zones in each fuel pin is primarily depending on centerline temperature and fuel composition.

2.4.1 Gaseous Fission Product Swelling

Interstitial and vacancy pairs generated by fission damage cascades tend to be instantly recombined and annihilated, however, various types of defect structures, i.e. vacancy, dislocation, phase boundary, and grain boundary, acting as preferential sinks for interstitial atoms consequently leave unbalanced remnant vacancies which will gather to form voids due to expedited diffusion at elevated temperature and increased defect density. At low burnup, voids are typically small and empty, i.e. internal pressure of those would be remarkably low near absolute vacuum. Along the burnup increase, voids will grow to a certain extent and be gradually filled with gaseous FPs causing significant fuel swelling.

After irradiation, it has been observed that the in-pile U-Zr fuel pin has two or three distinctive concentric phase zones corresponding to radial temperature distribution; cylindrical γ phase zone around centerline, very thin (β, γ_2) phase zone annularly encapsulating the central γ phase zone, and (α-U, δ) phase zone at periphery of the fuel pin [15, 142]. Each phase boundary position can be estimated by referring U-Zr phase diagram with known distributions of temperature and composition within the fuel pin.

Therefore single γ phase zone would be absent from the fuel pin where fuel centerline temperature is below ~700 °C.

Post-irradiation examination (PIE) of spent U-10Zr alloy fuel pins discharged from EBR-II at low burnup (~0.5 at%) has revealed that central γ phase zone exhibits instant swelling due to coarsely interconnected large gas bubbles, i.e. voids filled with insoluble gaseous fission products (GFP), maybe due to high temperature and bcc crystal structure [143]. This hotter swollen central region applies hydrostatic mechanical stress on colder periphery of the fuel pin inducing anisotropic swelling of the fuel pin where radial elongation is approximately two fold larger than axial elongation. Specific proportion between radial and axial swelling can be affected by various driving forces such as fuel temperature, axial temperature gradient, and swelling due to solid fission products (SFP) [16].

2.4.2 Fuel Constituent Redistribution

Fission and diffusion of the fuel constituents not only leads the formation and growth of voids and bubbles, but also severely alters the zirconium composition of the fuel pin in the radial direction, likely due to temperature dependency of diffusion rate and dissimilar chemical potential of each fuel constituent in each solid phase [144-146]. Post-irradiation examinations on spent U-10Zr alloy fuel discharged from EBR-II at 5 at% burnup discovered that zirconium depletion from intermediate β-U phase zone and zirconium enrichment at the center and periphery of the fuel pin [15]. Temperature

22

gradient driven zirconium depletion in the U-10Zr alloy was observed in elevated temperature zone above 662 °C [147], isothermal phase transformation temperature between α-U and β-U phase following Sheldon's phase diagram. Hence the argument that β-U phase is relevant to zirconium depletion in intermediate annular region of the fuel pin was strengthened.

Zirconium-depleted intermediate β-U phase region could pose a potential challenge to reactor safety during transient operation, since melting temperature of the zone including only ~2 wt% zirconium lower than the bulk alloy [1]. If Rough's phase diagram is correct, this issue can be straightforwardly avoided by using Zr-rich U-Zr alloys, since no β-U phase formation would occur in Zr-rich (> 15 wt%) U-Zr fuel pin, even considering possible extension of the (β, γ_1) phase zone due to oxygen and nitrogen.

This measure is neutronically impractical if Sheldon's phase diagram is factual because zirconium contents of the fuel pin needs to exceed ~40 wt%, however the compositions of U-Zr alloy, corresponding to the composition range of single δ-UZr$_2$ phase, could have extra benefit in the standpoint of suppressing fuel swelling, since the fuel pin would be subjected under single phase zones, periphery δ-UZr$_2$ and central γ phase zones, eliminating the presence of phase boundary.

2.4.3 Homogeneous Medium Assumption in Fuel Performance Models

Most of existing fuel performance models are based on a homogeneous medium assumption, despite the empirical observations of anisotropic swelling and constituent

23

redistribution in U-Zr alloy fuel in EBR-II which clearly shows phase effects on fission gas bubble behavior in the fuel [70]. This is done, in part, because the established models did not have the basis for or the computational capability to include the complex features that accompany the multi-phase structures observed in real fuel. The previous models have successfully been able to capture trends and basic phenomena, but new data and new computational tools are creating the opportunity to introduce a more physical representation of the fuel's performance.

The existing empirical models may be usable for U-10Zr alloy fuel at low to intermediate burnup, but the reliability of the models is suspicious at higher burnup or for alloy compositions far from U-10Zr because fuel constituent redistribution significantly changes local fuel composition. Since volumetric fraction of α-U and δ-UZr$_2$ phase are varying in conjunction with alloy composition, the density of phase boundaries in each concentric phase zone may not stay within the range where the homogeneous medium assumption for entire fuel pin can still be effective.

Zirconium-rich U-Zr alloy fuels should exhibit different constituent redistribution behavior. The lowest temperatures for γ phase formation in U-Zr binary system are approximately constant with zirconium composition increase. However, the presence of β-U phase zone can be questioned in Zr-rich (> ~15 wt%) alloys if Rough's phase diagram is more reliable than Sheldon's phase diagram likewise DSC-TGA and *in-situ* heated TEM experiments indicated in Sections 4.2 and 4.4. Rough's phase diagram was particularly well matched with the measured phase transformation properties of Zr-rich U-Zr alloys.

2.5 Ion-beam Irradiation

Ion-beam irradiation techniques are commonly used in order to study radiation interactions with matter in relatively short time scale [148]. Ion beam methods were used to simulate fission gas bubbles in U-Zr alloys by implanting helium ions into thin alloy foils using a 140 keV accelerator.

The method was chosen over other available irradiation methods (i.e. high energy cyclotron or low power research reactor) due to its extreme handiness to promptly induce radiation damage and simultaneously deposit helium atoms in nearby irradiated surface. More specifically, two significant benefits were obtained from using the method. First, relatively high fluence (1×10^{16} ions/cm^2) was achievable during approximately 1 h of irradiation. Second, the irradiation induced radioactivity was negligible; therefore the irradiated specimens could be handled at the university-level. However, ion-beam irradiation method was improbable to accurately match the radiation damage with the fission gas concentration for a burnup so as to consider the sample as a replica of spent nuclear fuel at particular burnup, even aside from the absence of FPs.

3. EXPERIMENTAL

Various compositions of U-Zr alloys were melt-cast under inert atmosphere using a high temperature vacuum furnace. As-cast and annealed U-Zr alloys were metallographically and thermophysically examined, often after being irradiated with helium ions as needed, using EPMA, energy dispersive spectroscopy (EDS), wavelength dispersive spectroscopy (WDS), DSC-TGA, and TEM in the purposes as listed below;

- Electron probe micro-analysis (EPMA) assisted with EDS and WDS
  - ■ To confirm the quality of as-cast and annealed alloys, e.g. intended chemical compositions and acceptable impurity concentration.
  - ■ To measure compositions of phase precipitates and matrix phases of the alloys, therefore chemically confirm the formation of room temperature (RT) stabilized phases and identify unknown secondary phase particles in the alloys.

- Differential scanning calorimetry and thermogravimetric analysis (DSC-TGA)
  - ■ To verify the EPMA characterization that short-term (168 h) annealing is enough to equilibrate the alloys at RT.
  - ■ To measure transformation temperatures and enthalpies of different time period annealed alloys, hence reexamining the U-Zr phase system.

- Transmission electron microscopy (TEM)

  ■ To observe gas bubble nucleation and growth in helium ion-beam irradiated alloys.

  ■ To observe evolution of selected area electron diffraction patterns of U-10Zr and U-20Zr alloys along the temperature increase, and therefore document the phase transformation behavior of the alloys appeared in DSC-TGA measurements, which was partially not in accordance with current U-Zr phase diagram.

3.1 Fabrication and Processing of U-Zr Alloys

3.1.1 Melt-casting

High purity zirconium crystal bars and depleted uranium chunks were cut into small (~3 g) pieces using a low speed diamond blade equipped on Leco VC-50 [149]. The oxidized layers on the uranium pieces were reduced before melting using nitric acid. Matched amounts of both metal pieces were prepared for the desired compositions of U-Zr alloys (i.e. U-0.1, 2, 5, 10, 20, 30, 40, and 50wt%Zr) and were placed separately in cylindrical yttrium oxide crucibles as shown in Fig. 3-1. The outer larger crucible was used to protect the furnace from the possible failure of inner crucibles could leak liquid phase uranium. Each alloy composition was selected due to the reasons given in Table 3-1.

Table 3-1: Classification of melt-cast U-Zr alloys.

Category		Alloy	Comment
Single α-U phase alloy		U-0.1Zr	Zr-saturated α-U
Two phase alloy	α-U phase matrix	U-2Zr	Zr-depleted zone composition of spent U-10Zr alloy fuel
		U-5Zr	Monotectoid invariant point composition in U-Zr phase diagram
		U-10Zr	Most commonly-used U-Zr alloy fuel composition [142]
	δ-UZr$_2$ phase matrix	U-20Zr	Metallurgical counterpart of U-10Zr alloy
		U-30Zr	Near periphery zone composition of spent U-10Zr alloy fuel pin [15]
Single δ-UZr$_2$ phase alloy		U-40Zr	Lower end of single δ-UZr$_2$ phase at elevated temperature (~600 °C)
		U-50Zr	Single δ-UZr$_2$ phase for entire RT range
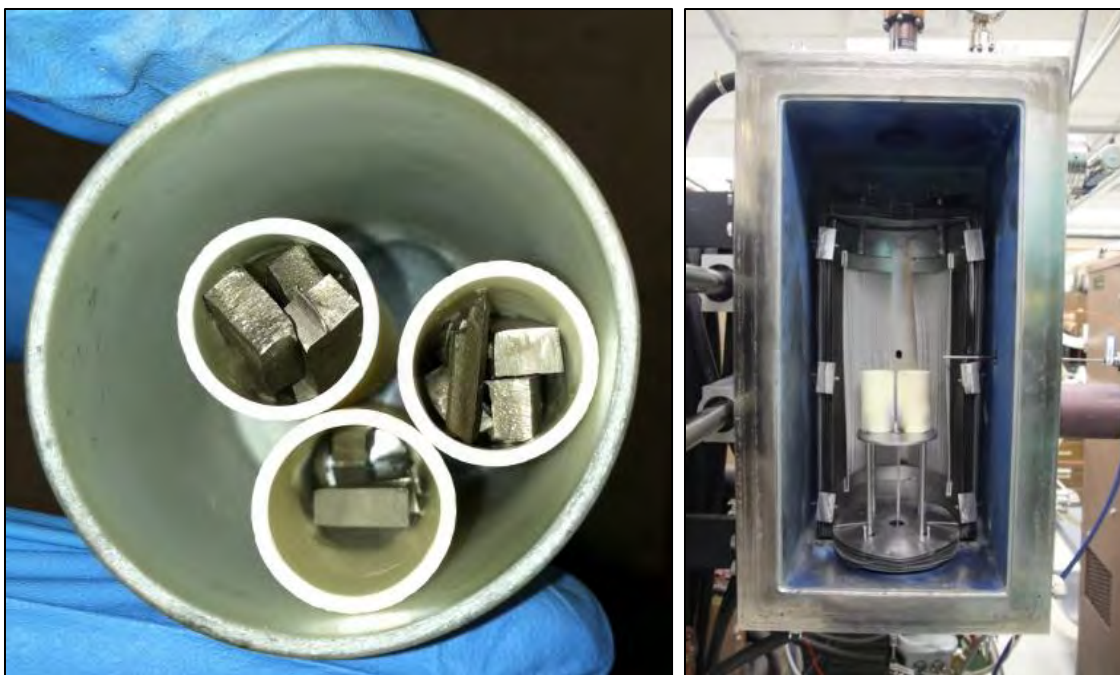
Figure 3-1: Uranium and zirconium metal pieces placed in yttrium oxide crucibles (left) to be melt-cast in vacuum chamber (right) of a high temperature furnace.

Uranium and zirconium metal pieces were melted at ~1900 ℃ under argon atmosphere for 1 h and then cooled down to RT at 30 °C/min rate. The cooling rate was chosen to avoid potential cracking by thermal shock on the crucibles. Once cast, alloy slugs were then flipped and placed in slightly larger yttrium oxide crucibles and re-melted under identical conditions in order to improve alloy homogeneity. The amount of uranium and zirconium metal used for each U-Zr alloys are listed in Table 3-2 with resulted heights of the alloy slugs whose diameter was approximately 15.5 mm fitting the radial dimension of the crucible used for the final melting.

Table 3-2: Specification of melt-cast U-Zr alloys.

Alloy	Uranium (g)	Zirconium (g)	Composition (wt%Zr)	Estimated height (mm)
U-0.1Zr	30.9548	0.0382	0.1	9
U-2Zr	40.6069	0.8472	2.0	12
U-5Zr	54.3520	2.8808	5.0	16
U-10Zr	41.2332	4.5680	10.0	14
U-20Zr	33.1530	8.3121	20.0	13
U-30Zr	28.5021	12.0757	29.8	14
U-40Zr	11.2247	7.4814	40.0	7
U-50Zr	9.4666	9.5024	50.1	8

The alloy heights of the slugs were intended to range from 7 mm to 16 mm because longer slugs would have more axial drift of alloy compositions and shorter slugs would include more impurities per unit volume due to excessive surface to volume ratio.

3.1.2 Annealing

Melt-cast U-Zr alloy slugs were commonly transversely sectioned as ~0.5 mm to ~1 mm thick circular buttons to minimize compositional drift within a sample. However, one alloy slug of U-20Zr was axially sectioned and examined using EPMA as a representative, shown excellent microstructural homogeneity across the alloy slug from the top to the bottom.

Sectioned buttons were further cleaved into half-buttons to be annealed in a cylindrical quartz tube (10 mm diameter). Half buttons of the alloys were tightly wrapped with tantalum foil and then placed in a quartz tube. One end of the quartz tube

was connected to roughing pump decreasing the pressure inside the tube down to $\sim 10^{-3}$ Torr, and the other end of the tube were simultaneously heated using acetylene torch and manually twisted to be sealed as shown in Fig. 3-2.

Figure 3-2: Tantalum foil wrapped U-Zr alloy buttons sealed in a quartz tube connected to a roughing pump for further annealing; before (left), during (center), and after (right) the sealing.

A small concave dent appeared in upper part of sealed quartz tube shown in Fig. 3-2(right) shows the validity of the low pressure inside the tube tested by slightly heating an intact spot on the tube until atmospheric pressure made the dent on the heated spot.

31

Quartz tubes passing the vacuum test were then annealed at temperatures of 500, 550, and 600 °C for 1, 3, 7, and 28 day(s) as needed. The annealed alloy surfaces were as shiny as they were in their as-cast state, regardless of annealing conditions.

3.2 Electron Probe Micro-analysis

Micro-scale metallographic examination was conducted to check the quality of as-cast and annealed U-Zr alloys using EPMA. Room temperature stabilized phase formation in the alloys was chemically examined utilizing WDS after EDS confirmed the absence of peaks corresponding to the possible impurities, e.g. yttrium, zirconium, carbon, nitrogen, and oxygen.

3.2.1 EPMA Sample Preparation

U-Zr alloy buttons were cut into appropriate sizes and fixed in epoxy resin using a cylindrical plastic mold. After the resin was fully hardened, the surface of the alloys was polished on a MiniMet 1000, a semi-auto grinder-polisher manufactured by Buehler, by using gradually finer sizes of SiC papers from 180 grit to 1200 grit with ethanol lubricant. Polishing was continued by consecutively using smaller sizes (i.e. 3, 1, and 0.25 μm) of polycrystalline diamond suspensions on microcloth. The polished surface was often examined using optical microscopy during and after polishing to ensure the flat and smooth metallic surface applicable for EPMA observation.

Prepared samples were carried to the Electron Microprobe Laboratory, Texas A&M University and then carbon coated after repeating the final polishing using the diamond suspensions in order to remove the oxide layer that formed during the transport. A typical EPMA sample embedding multiple alloy pieces is shown in Fig. 3-3.
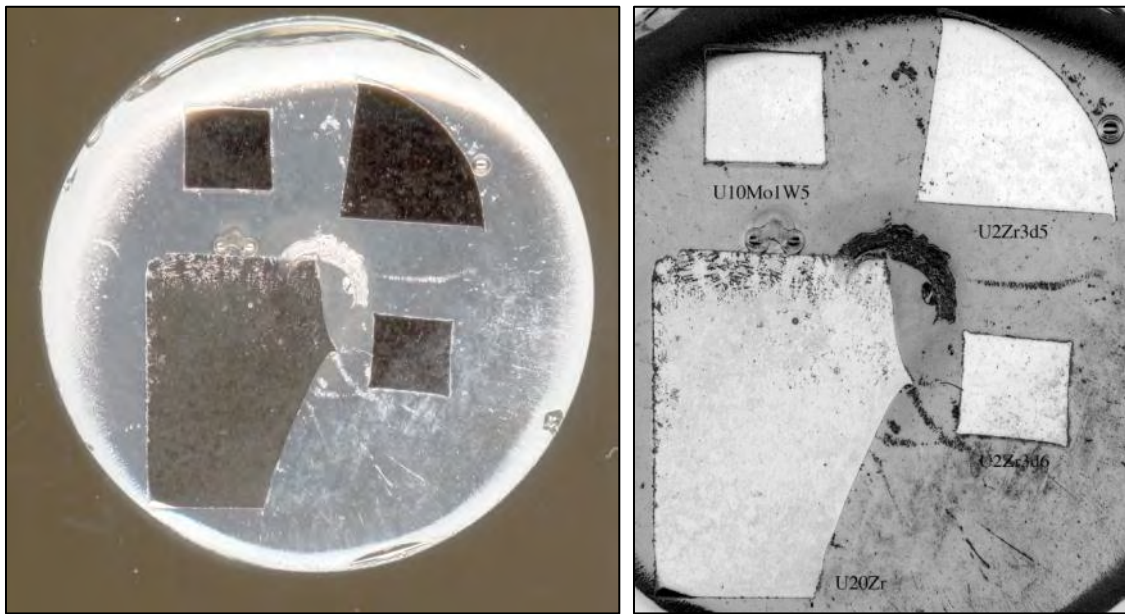
Figure 3-3: Photo (Left) and optical scan (right) of an EPMA sample embedding multiple uranium-based alloys.

3.2.2 Metallography

The Cameca SX-50 electron microprobe was used for back-scattered electron (BSE) imaging at several magnifications ranging from 90X to 4000X, to visualize metallographic features at various scales. To estimate actual compositions of the cast

alloys, at least ten BSE images were taken without scale bar, and ImageJ, an image processing program developed at the National Institutes of Health (NIH), was used to measure the area fractions of matrix and precipitate phases in each BSE image of the alloys. Magnifications were adjusted depending on average phase precipitate size in the alloys to mitigate systematic errors in the estimated alloy compositions.

3.2.3 Micro-chemical Analysis

Chemical compositions of precipitates and matrix phases in the alloys were measured using PGT energy dispersive system and dedicated Sun workstation annexed with Cameca SX-50. The WDS method was used to measure chemical compositions of the areas in the alloys after EDS was used to quantify the elements that comprise the regions. Measured compositions were referred to assess that actual composition of each annealed U-Zr alloy was homogeneously matched with intended composition within acceptable range.

Metallic uranium and zirconium EPMA sample were produced and utilized as an alternative reference for U-0.1Zr alloy including only trace amount of zirconium, therefore demanding higher accuracy for its chemical analysis, since standard reference materials available for WDS were in oxide forms of uranium and zirconium. However, WDS measurements using metallic reference sample yielded statistically identical results with those using oxide references.

3.3 Differential Scanning Calorimetry and Thermogravimetric Analysis

Phase transformation enthalpies and temperatures of the alloys from 25 °C to 1000 °C were measured using a DSC-TGA, NETZSCH STA-409PC. Schematic of the device is shown in Fig. 3-4.
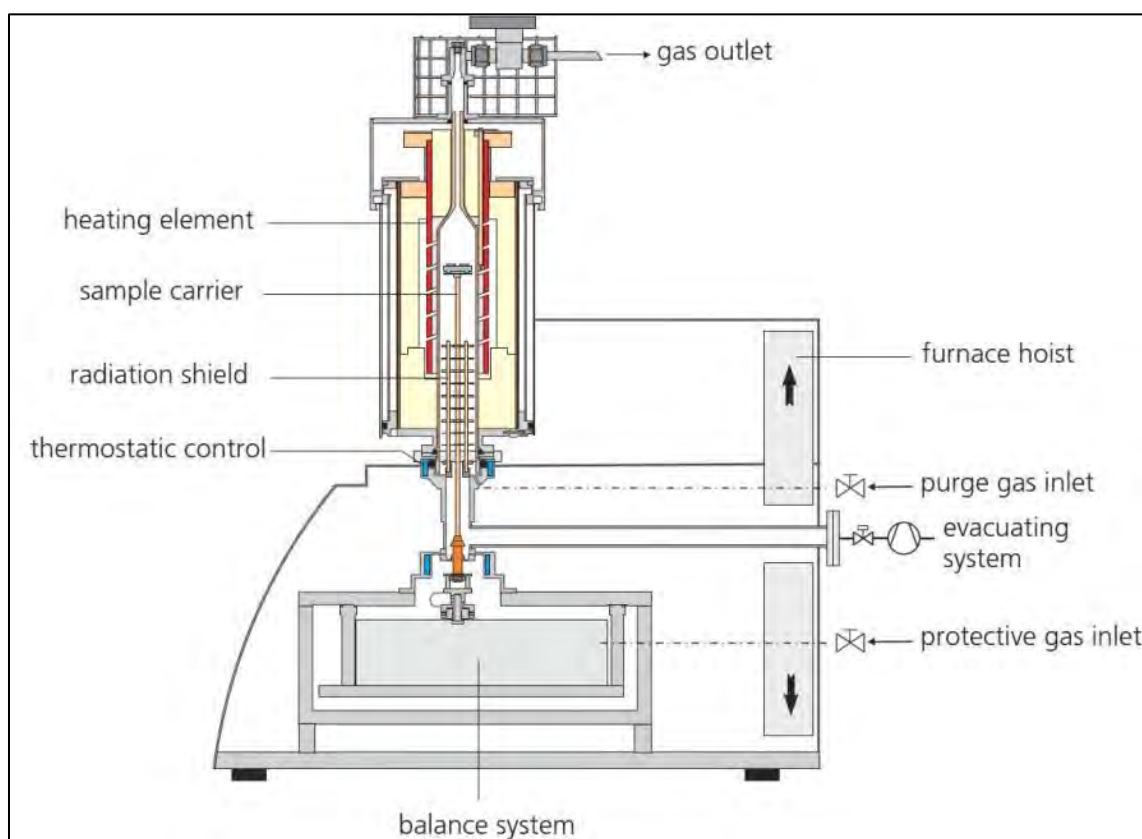
Figure 3-4: Schematic of STA-409PC (figure courtesy of NETZSCH).

3.3.1 Calibration and Baseline Measurements

The DSC-TGA was calibrated multiple times by simultaneously measuring the melting temperatures and the heats of fusion of seven standard materials, indium (In), tin (Sn), bismuth (Bi), zinc (Zn), aluminum (Al), silver (Ag), and gold (Au), also supplied by NETZSCH. Two separate calibration files for temperature and sensitivity calibration were generated from the ratios between the measured data from the standard reference materials and the thermophysical data of the materials in open literatures [136, 150]. Calibrations were reassured by referring repeated measurements from uranium and zirconium metals using the calibration files.

Baseline measurements were conducted prior to sample measurements by loading a set of empty crucibles. Baseline and calibration measurements were conducted under identical conditions, e.g. temperature ramping rate and purge gas, with sample measurements.

3.3.2 DSC Sample Preparation

EPMA characterized U-Zr alloy buttons (~1 mm thick) were cut into small pieces ranging from 10 mg to 100 mg. All surfaces of each sectioned sample were mechanically polished using coarse grit SiC papers to remove the oxide layers until shiny metallic surface was observed. Alloy samples were prudently carved to have a flat surface so to fully contact with the bottom of the crucible during the measurements to minimize

sample exposure to purge gas, therefore limiting the growth of oxidation film on the surface which would potentially affect the accuracy of the measurements. Polished samples were loaded on an aluminum oxide crucible covered with a lid after cleaned using ethanol and ultrasonic vibrator. The crucibles were placed on the sample carrier of DSC-TGA head as shown in Fig. 3-4. Each sample mass was measured and recorded before the loading.

3.3.3 Sample Measurements

After loading a prepared U-Zr alloy sample in the crucible placed on the DSC-TGA head vertically installed in the furnace area surrounded by heating element as shown in Fig. 3-4, furnace area was immediately evacuated using a roughing pump and then repeatedly backfilled with 99.9 % argon gas. In order to minimize sample oxidation, the purge gas was further purified through moisture and oxygen trap system before circulating the DSC system.

The initial heating rate was 50 °C/min up to 500 °C, which was the maximum capability of the DSC. The rate was decreased down to 5 °C/min for further heating up to 1000 °C. The heating rate was controlled in order to minimize sample oxidation and simultaneously obtain reasonable phase transformation data. In addition, slower heating rate (1 °C/min) was tested in regards to the concern on resolution of the DSC to distinguish multiple transformations occurring at similar temperatures. However, the

decreased heating rate merely intensified systematic fluctuation of the measured data and sample oxidation due to long term heating, while not improving the resolution.

The mass increase of each sample was recorded along with DSC curve using TGA for entire measurements. The first DSC heating curves were solely assumed as to represent phase transformations of the alloys, since hysteresis and kinetically sluggish transformations of some alloy phases often change the locations of corresponding peaks in the DSC cooling curves [151].

3.4 Helium Ion-beam Irradiation

Mechanically thinned foils of U-Zr alloys were irradiated with helium ions using a 140 keV accelerator to simulate fission gas bubble nucleation and growth in the alloys.

3.4.1 Alloy Foil Preparation

Alloy buttons were sectioned from the alloy slugs to have ~0.5 mm thickness. Sectioned buttons were mechanically thinned from both sides down to ~150 μm thick foils using gradually smaller grit size SiC papers in similar manner with EPMA sample preparation. The applied force on the samples during the thinning was stepwisely decreased from 3 lb to 1 lb with decreasing the grit size. Particularly, no force was applied on both sides of foils for the later stages of polishing using 3, 1, and 0.25 μm

diamond suspensions to relieve mechanical damage accumulated on the alloy foil surface during the thinning.

3.4.2 Ion-beam Irradiation

Prepared thin foils of characterized U-0.1 10, 20, 30, 40, and 50Zr alloys were placed on the wall of the target chamber, vertically against the path of the ion-beam, using carbon adhesive. The foils were then irradiated with ionized helium gas from a Danfysik ion source equipped with a 140 keV accelerator. A well-defined monotonic energy ion-beam was achieved by applying a magnetic field to refine the beam utilizing the mass to charge ratio of helium ions under high vacuum (10^{-7} Torr). Schematic of the accelerator is shown in Fig. 3-5.

The ion-beam flux was typically near 1×10^{16} ions/cm$^2 \cdot$h. Irradiation doses were calculated by integrating the ion-beam flux over a period of time for irradiation. The tested fluences were 1×10^{14}, 1×10^{15}, 1×10^{16}, and 5×10^{16} ions/cm^2, conveniently referred as to 0.01, 0.1, 1, and 5, respectively, for the notation of TEM specimens. The experimental matrix of ion-beam irradiation is given in Section 4.4.

Maximum dose was limited by pseudo maximum duration (5 h) of ion-beam irradiation regarding the concerns on thin foil oxidation and *in-situ* loss of implanted helium atoms from the foil. The irradiated alloy surface was often tinted with very dim yellow color at the highest doses ($> 1 \times 10^{16}$ ions/cm^2), indicating the formation of a thin oxide layer on the foil surface. The metallic surface was swiftly recovered via

39

electropolishing. Less than 2 s with applied 40 V was commonly enough to mark a circle (~2 mm diameter) on the irradiated foil surface. Specific recovery time for metallic surface was subjected to the applied electric potential.
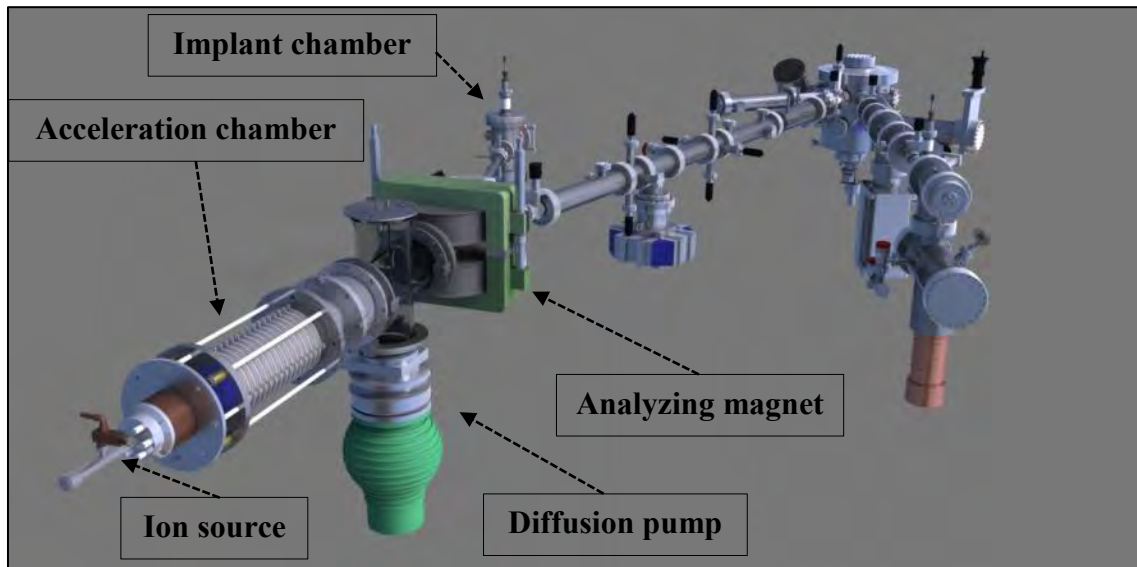
Figure 3-5: Schematic of a 140 keV accelerator used for He$^+$ ion-beam irradiation (figure courtesy of Michael Justinn General, Texas A&M University).

3.4.3 Irradiation Damage and Implanted Ion Distribution

Implanted helium ion distribution and induced radiation damage profile in the various compositions of U-Zr alloys was calculated (Section 4.3.1) using Stopping and Range of Ions in Matter (SRIM), a simulation program based on Monte Carlo method assuming sequential binary collisions between implanted ions and target atoms [152]. The program can be used to estimate the projection of implantation profile for the

bombarding atoms, thus estimating the concentration from the foil surface to the maximum penetration depth. The atom concentration peak was targeted to also be within the electron transparent areas during electro-chemical thinning of U-Zr alloy TEM specimens. Radiation damage distributions were also calculated utilizing the profiles of two types of collision, i.e. vacancy collision and replacive collision.

However, the distributions of radiation induced defect structures and implanted helium ions are not supposed to exactly follow the calculations. Nonetheless the samples were not intentionally heated in the irradiation chamber, stationed implanted atoms and induced voids are still mobile at slightly elevated temperature due to the energy from ion-beam irradiation itself. Degree of ion-beam heating for the alloy foil during the irradiation was assessed in Section 4.3.2 in terms of saturated elevated temperature. Estimated sample temperature was below 200 °C, with extremely conservative assumptions, which was negligible following the EPMA observation on low temperature (500 °C) annealed U-Zr alloys and *in-situ* heated TEM observation on as-cast two phase U-Zr alloys (U-10Zr and U-20Zr).

3.5 Transmission Electron Microscopy

*3.5.1 TEM Specimen Preparation*

Several 3 mm diameter disks were punched out from irradiated foils by using FISCHIONE Model 130 specimen punch, manually or with a hydraulic pressure. No

observable mechanical damage was found from the central region of the punched disks. Thicker disks often had a concave unirradiated side, i.e. this implies that the convex side was the irradiated side since irradiated side of the foils was constantly placed to face the base of the puncher. However, no mechanical force was directly applied on the irradiated surface of punched disk throughout punching due to conical dimple on the puncher base.

The centers of the punched disks were electro-chemically thinned to have electron transparent areas (< ~100 nm thick) using South Bay Technology Model 550D single vertical jet electropolisher. The apparatus of the electro-jet-polisher is presented in Fig. 3-6(a). A punched 3 mm disk was placed on top of the electrode of the polisher as shown in Fig. 3-6(b) and was then subjected under the slowest possible flow of 5% perchloric acid/95% methanol electrolyte. Flow speed was adjusted to barely maintain exact cylindrical pillar shape whose diameter was corresponding to that of the jet nozzle, 1.5 mm. Broad ranges of electric potentials between 1 V to 150 V were tested for U-0.1, 10, 20, and 40Zr alloys to prepare wide electron transparent areas representing the bulk of each alloy. The specimen disk was under observation through attached magnifier on the electrode during electropolishing. Applied voltages were often slightly adjusted to not oxidize the specimen surface.

(a) Apparatus of the electropolisher (figure courtesy of South Bay Technology)
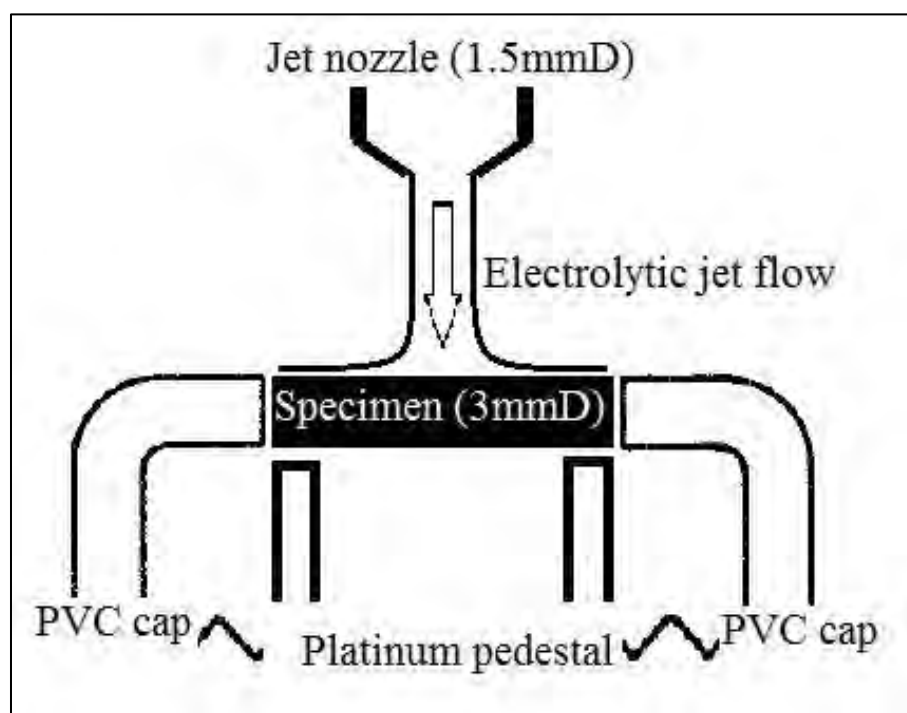
(b) Schematic of specimen arrangement under electrolyte flow (not to scale)

Figure 3-6: Schematic of Model 550D single vertical jet electropolisher.

The commonly applied electric potential for the single phase alloys, U-0.1Zr and U-40Zr, was 40 V with induced current varying typically within 30 mA to 35 mA. The induced current was varied depending on various reasons, e.g. voltage adjustment, alloy composition, specimen thickness, specimen/electrode contact, electrolyte temperature, and electrolyte flow rate. For the two phase alloys, U-10Zr and U-20Zr, higher voltages around 100 V were successful to prepare numerous large transparent areas ($> \sim 100~\mu m^2$) for 200 keV electron beam. The induced current was more or less linearly proportional to the applied voltage over entire voltage range have been tested.

The electrolyte temperature was maintained below 0 °C by directly mixing liquid nitrogen (LN_2) mainly to increase the viscosity of the electrolyte and simultaneously suppress potential chemical reaction between resolved uranium and zirconium ions with the electrolyte which could redeposit various compounds as artifacts on the specimen surface. Due to the inaccessibility to the electrolyte bath as shown in Fig. 3-6(a), additive liquid nitrogen was unable to be supplied into the electrolyte bath during electropolishing. Hence, the electrolyte temperature increased during electropolishing time due to pump work, applied voltage, and natural air circulation in the fume hood where the electropolisher was operated. Additional LN_2 was supplied during intermission when the temperature was approaching to 0 °C. The starting temperature of the electrolyte was controlled below -40 °C.

The prepared specimen quality was fairly insensitive to the monotonic increase of electrolyte temperature as long as it was maintained at sub-zero temperatures. The electrolyte temperature was also relevant for maintaining the cylindrical pillar shape of

electrolyte flow with slow to intermediate flow rate. Obtaining stable and slow flow of the electrolyte was critical to obtain a metallic surface with the least degree of surface oxidation. The distance between the nozzle tip and the specimen was maintained within 3 mm to 4 mm to be approximately 2.2 times of the jet flow thickness, as recommended by the manufacturer. Accurately adjusted flow often generated stable concentric wave ridges on the loaded specimen disk throughout the electropolishing.

Electropolishing was terminated immediately after the perforation was recognized. The thinned area of the specimen under slow and viscous flow was typically circular (~1.5 mm diameter) and had one or more perforated hole(s) close to the center of the disk. Perforated holes (< 1 mm) were often observable with the naked eyes. Prepared specimens were indirectly rinsed using methanol to dilute remnant perchloric acid and then immediately preserved in a plastic vial filled with acetone. TEM specimens were often inspected using an optical microscope, during and after the electropolishing. Thin, flat and wide metallic surfaces of well-prepared specimens were clearly observed. Major portions of the perforated circumference in those specimens were transparent under 200 keV electron beam.

3.5.2 Imaging and Electron Diffractometry

Nano-scale metallographic characterization of the alloys was conducted using a TEM, JEOL JEM-2010. Specimens were loaded either on a double tilt holder for RT observation or on a single tilt heating stage holder for *in-situ* heated diffractometry.

Numerous numbers of bright field (BF) and dark field (DF) images and selected area diffraction (SAD) patterns were obtained from the prepared alloy specimens.

X-ray energy dispersive spectroscopy (XEDS) was supportively used for chemical analysis. However, the usage of XEDS was significantly limited because minimum size of electron beam was larger than the dimensions of nano-size particles and defect structures discovered from the alloys. Therefore, using the method, measured chemical compositions had impractically large error and implanted helium atoms were undetectable due to low atomic mass of the element. Electron diffractometry was preferentially used for element identification and phase characterization.

As-cast U-10Zr and U-20Zr alloy specimens irradiated at the dose of 5×10^{16} ions/cm^2 were *in-situ* heated using the TEM to reinvestigate the numbers of phase transformations observed in the DSC-TGA of the two compositions of U-Zr alloys; the results in Section 4.4 disagree with Sheldon's phase diagram but do agree with the DSC data in Section 4.2. Selecting the dose, it was required to be low enough not to change the stabilized equilibrium phase of the alloys and high enough to polycrystalize the phase medium to give a clear ring type diffraction pattern (DP). Polycrystalline medium was preferred not only because only single tilt holder was available for *in-situ* heating but also thermal expansion and vibration of heated alloy TEM specimens were anticipated.

4. RESULTS

The experimental data and theoretical evaluations are presented in this section, which contains with four sections segregated according to the nature of the experimental tools applied in this study; EPMA, DSC-TGA, ion-beam irradiation, and TEM. Microstructures of the U-Zr alloys revealed using EPMA are presented in Section 4.1. The phase transformation temperatures and enthalpies of the alloys measured using DSC-TGA are presented in Section 4.2. In Section 4.3, SRIM estimates for ion-beam irradiation induced radiation damage and helium distribution are discussed, but the revelation of irradiated structures are presented in Section 4.4, which contains the TEM data regarding the observed nano-scale structures of the irradiated alloys. For the sake of brevity, only selected images and data essential to derive following discussions and conclusions are included.

4.1 Microstructures of As-cast and Annealed U-Zr Alloys

A list of alloys characterized using EPMA methods is given as Table 4-1, showing the various compositions and thermal histories examined for this study. Representative back-scattered electron (BSE) images of all as-cast and annealed alloys are presented in this section with brief descriptions. More detailed explanations are provided with the images if necessary, although the complete discussion of the data is integrated in Section 5, cross-linked with the other experimental results.

Table 4-1: EPMA experimental matrix.

Alloy	As-cast	Annealing time (day)					
		1		3		7	
		Annealing temperature (°C)					
		500	600	500	600	550	600
U-0.1Zr	-	-	-	-	-	-	O
U-2Zr	O	-	O	O	O	O	O
U-5Zr	O	-	O	-	O	-	O
U-10Zr	O	-	O	-	O	-	O
U-20Zr	O	-	O	-	O	-	O
U-30Zr	O	-	O	-	O	-	O
U-40Zr	O	-	-	-	-	-	O
U-50Zr	O	O	O	-	O	O	O

A shorthand notation was created to identify all of the U-Zr alloy samples according to the various compositions and thermal histories. The notation is simply the alloy composition followed by a thermal designation (i.e. AC for "as-cast" and xd for 1, 3, or 7 day annealed) and the annealing temperature in Celsius. As an example, U-0.1ZrAC denotes the as-cast U-0.1wt%Zr alloy and U-50Zr28d550 stands for U-50wt%Zr alloy annealed for 28 days at 550 °C. Note that this shorthand notation is expanded for TEM and irradiated specimens used in later sections to seek further convenience in denoting the entire matrix of TEM experiments.

4.1.1 Uranium-rich Alloys (< 15 wt%Zr)

Based on the observed microstructures, the U-rich U-Zr alloys (U with 0.1, 2, 5,

and 10 wt%Zr) were classified as having an α-U matrix phase. Following Sheldon's phase diagram (Fig. 2-2), theoretical volumetric fraction of two RT stable phases (α-U and δ-UZr$_2$) of U-Zr binary system is being equivalent in U-14.4Zr alloy at 600 °C.

4.1.1.1 U-0.1Zr

This alloy was the lowest zirconium content alloy fabricated for this study and it was created to establish a Zr-saturated α-U structure without a significant intermetallic presence. A representative featureless α-U medium forming the bulk of U-0.1Zr alloy is shown in Fig. 4-1(a) with very narrow straight lines evident as artifacts from mechanical polishing. In contrast, numerous number of secondary phase particles, i.e. oxygen or nitrogen fixed zirconium dendrites and yttrium oxide (Y$_2$O$_3$) precipitates formed during melt-casting, were found to be scattered in the alloy as shown in Fig. 4-1(b).

The contrast of Fig. 4-1(b) is significantly exaggerated to visualize very small compositional fluctuation within the matrix phase. Although two distinguishable regions have different contrast are shown in the BSE image, WDS was used to confirm that the zirconium content were similar and negligible (< 0.01 wt%) for both regions. Measured values were consistently below the detection limit (~0.14 %) for commonly used analytical conditions. The chemical composition of the alloy was reaffirmed due to the concern on the usage of the oxide standard materials for uranium and zirconium by using metallic references in the forms of EPMA samples. Measured alloy compositions were again below the detection limit using metallic references of uranium and zirconium.
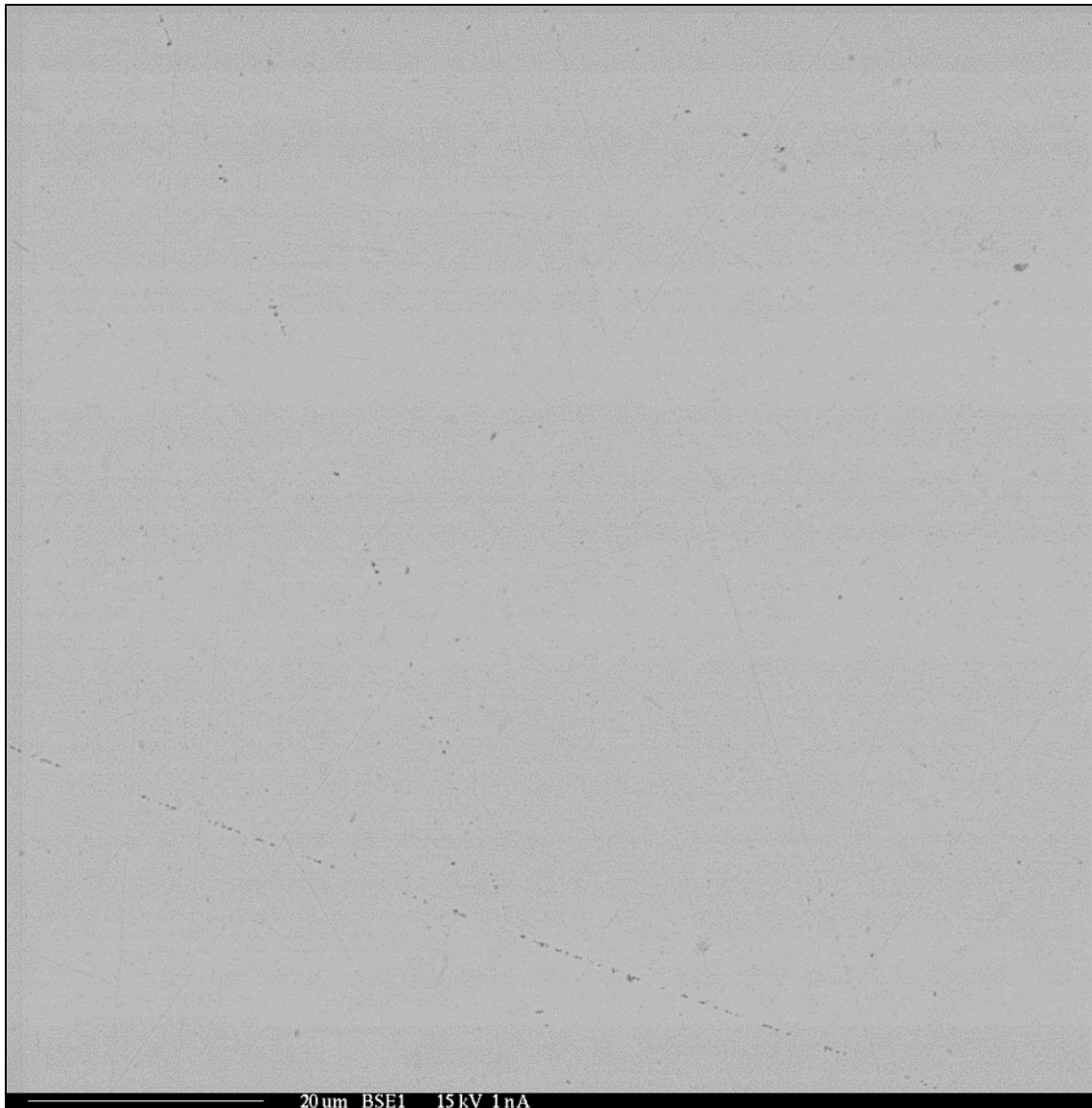
(a) Featureless bulk of U-0.1Zr7d600 (1000X)

Figure 4-1: Microstructure of U-0.1Zr7d600.
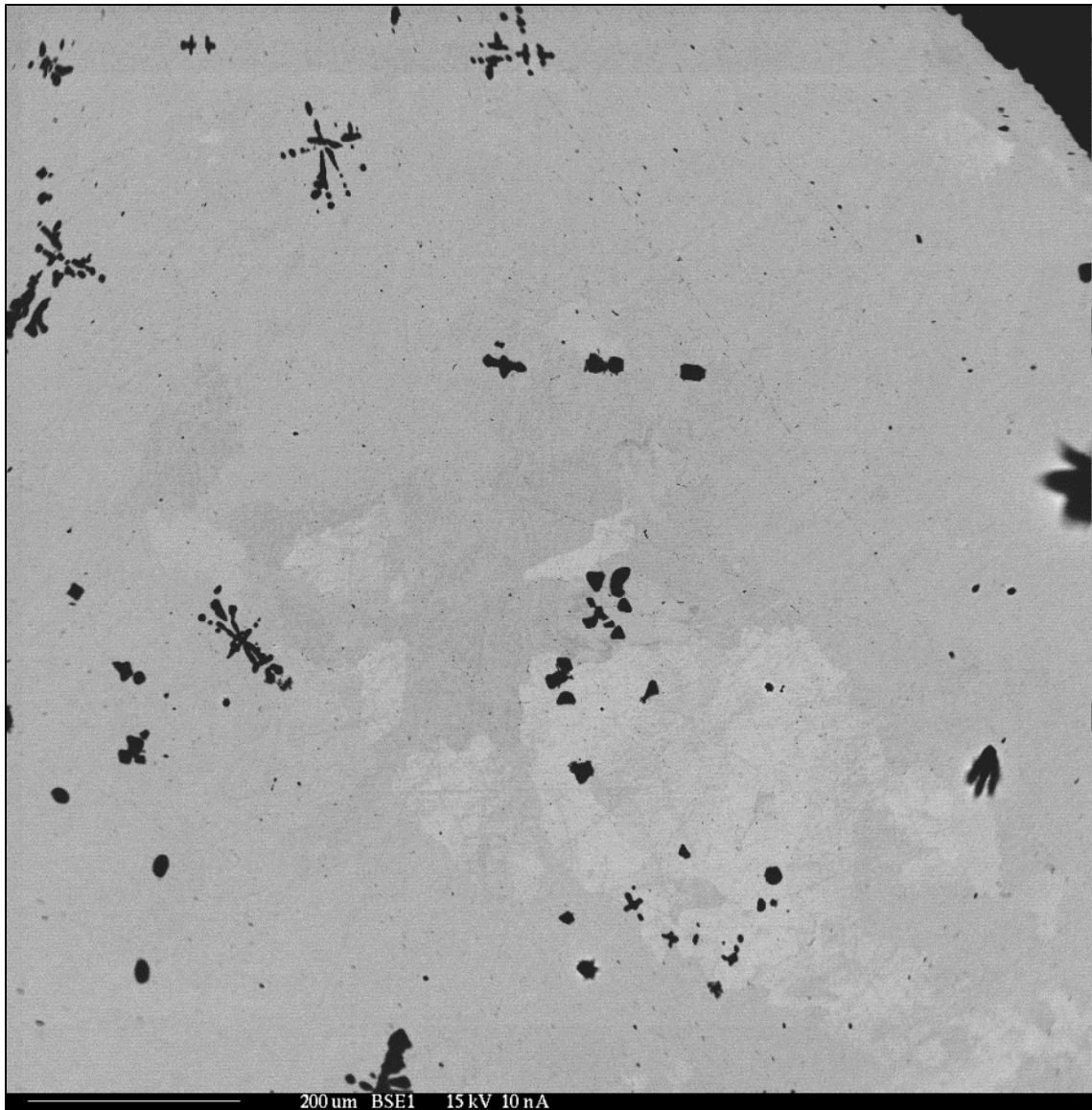
(b) Secondary phase particles (black precipitates) in U-0.1Zr7d600 (90X)

Figure 4–1: Continued.

4.1.1.2 U-2Zr

The EPMA methods were unable to clearly resolve the composition or the distinct shapes of the very fine lamellar features shown in Fig. 4-2 because the widths of characteristic lamellae structure of as-cast U-2Zr alloy were narrower than electron beam diameter (1 μm). However, contrast difference indicates significantly biased zirconium distribution was initiated during slow cooling of alloy melt-casting at 30 °C/min rate for ~1 h. Limited resolution was more severe with WDS, since high energy electrons interact with spherical bulb shape zone of the alloy, potentially including different phases with observed facial phase.

Although the sample was not electrochemically etched but mechanically polished, grains of parent bcc γ phase are evident in Fig. 4-2(a) due to 1) different orientation of lamellae structure in each grain and 2) dark Zr-rich secondary phase particles alongside grain boundaries. This structure indicates that zirconium diffusion within grains was anisotropic, maybe due to orthorhombic crystal structure of α-U [153, 154]. Even using the highest available magnification in EPMA, fine lamellae structure of the as-cast alloy was still difficult to resolve as shown in Fig. 4-2(b).

Figure 4-3(b) highlights two different impurity phases. The WDS data confirmed that the brighter gray particles are α-Zr including (0.70 ± 0.16) at% uranium and darker black particles are yttrium oxide. Note different types of impurities are clearly contrasted in Fig. 4-3(a), while the fine lamellar structure shown in Fig. 4-2 is indistinct against the smeared white background in the figure.
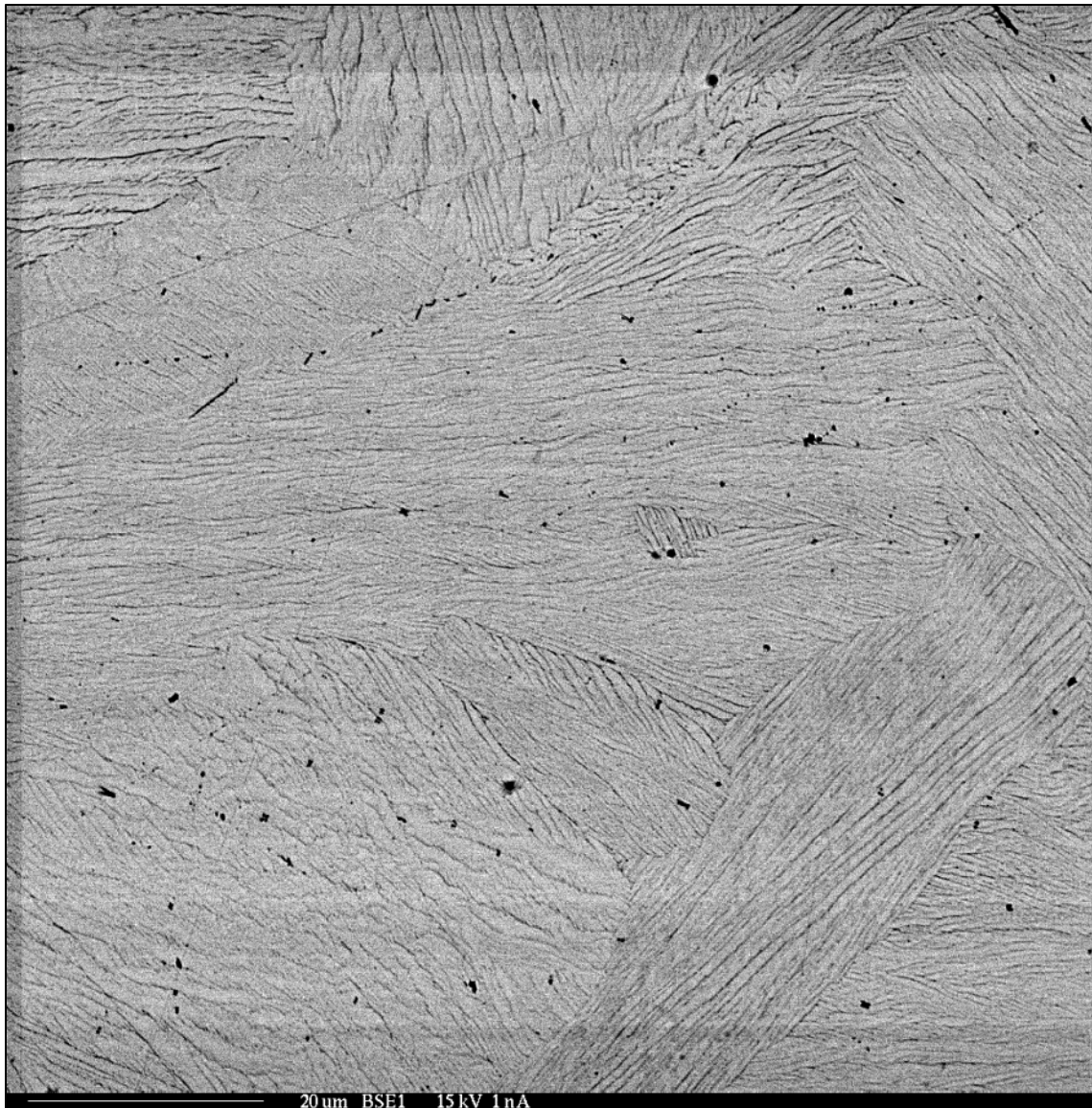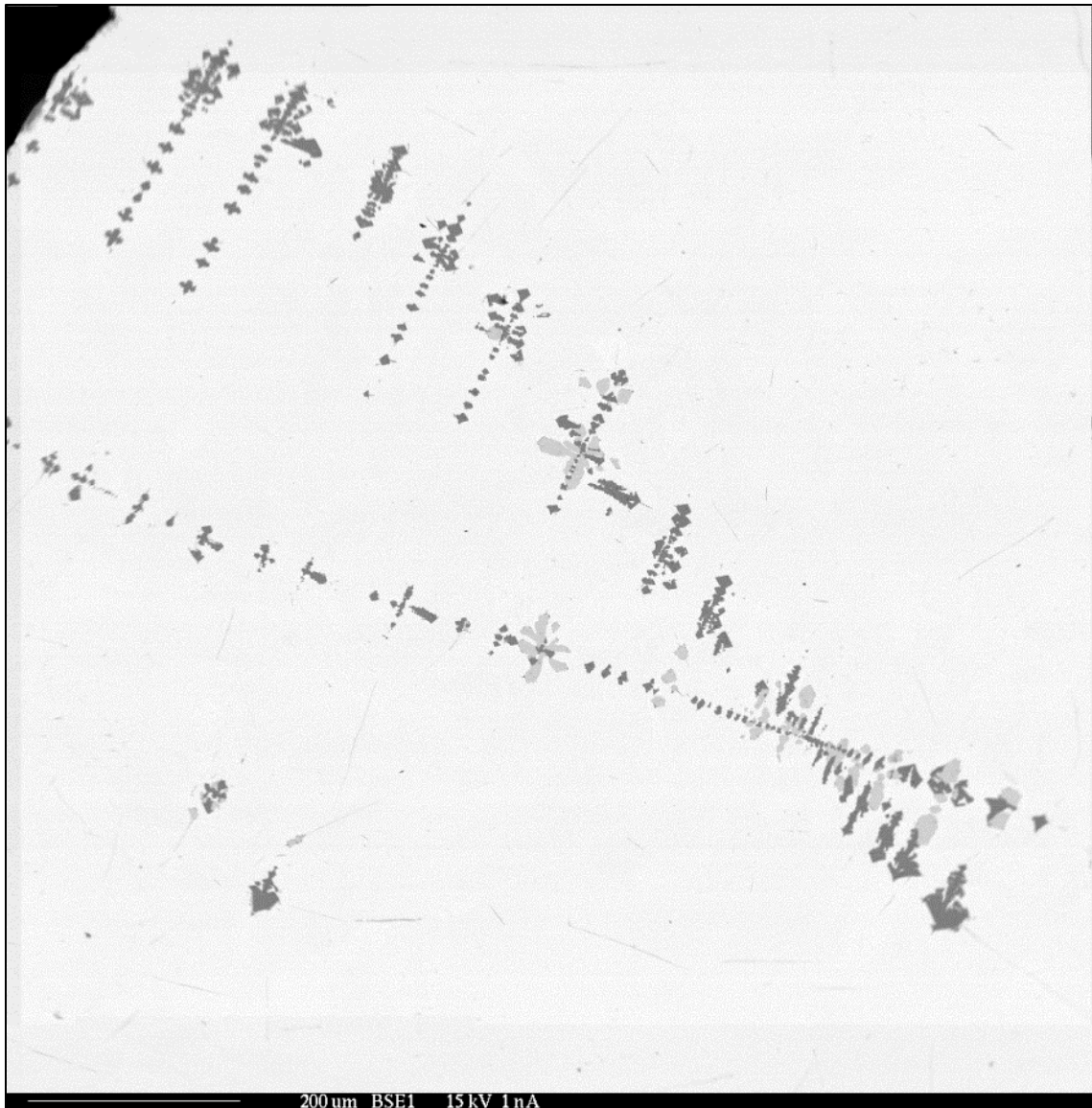
(a) Fine lamellae structure and grain boundaries within U-2ZrAC (1000X)

Figure 4-2: Fine lamellae structure of U-2ZrAC.
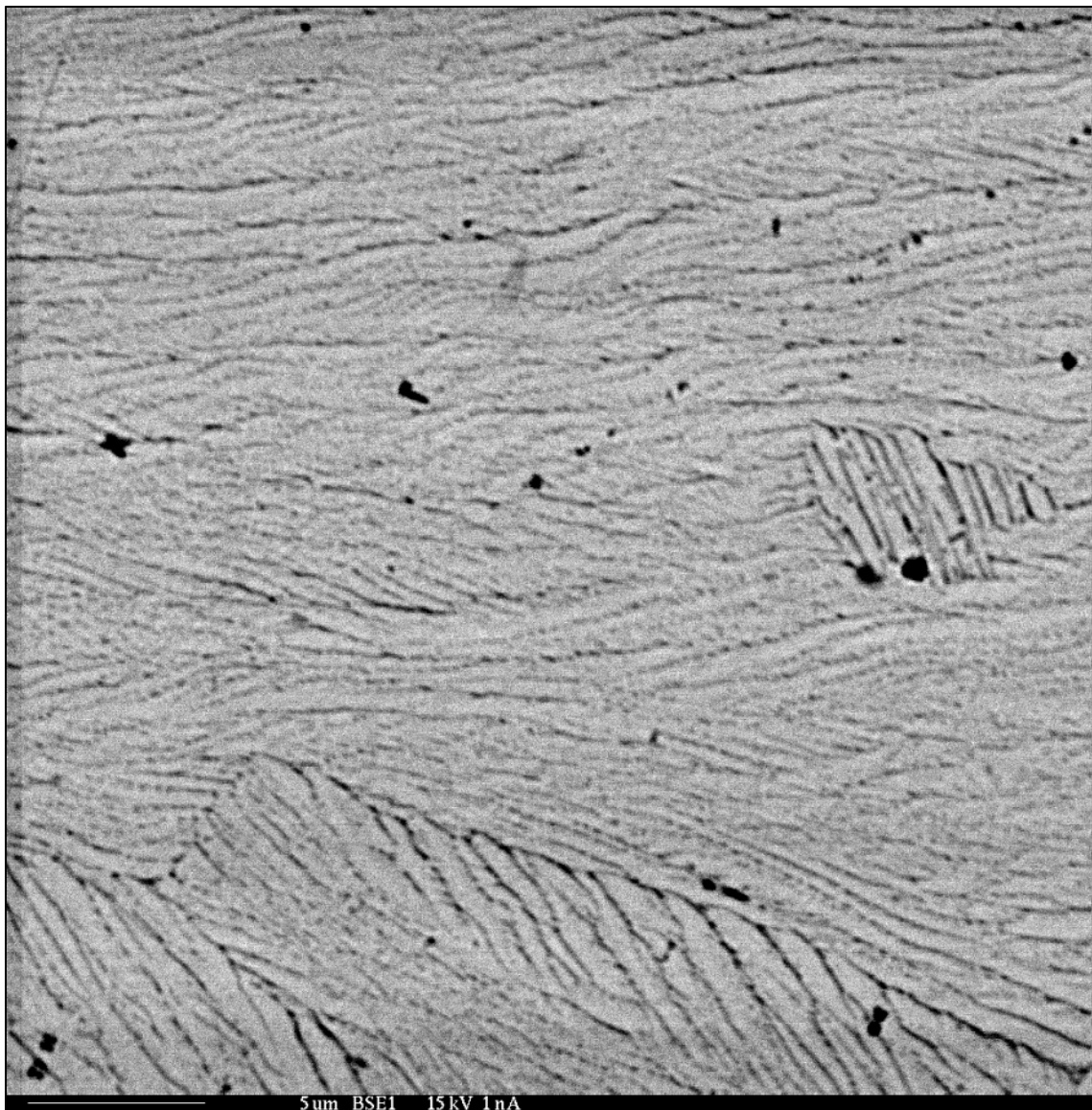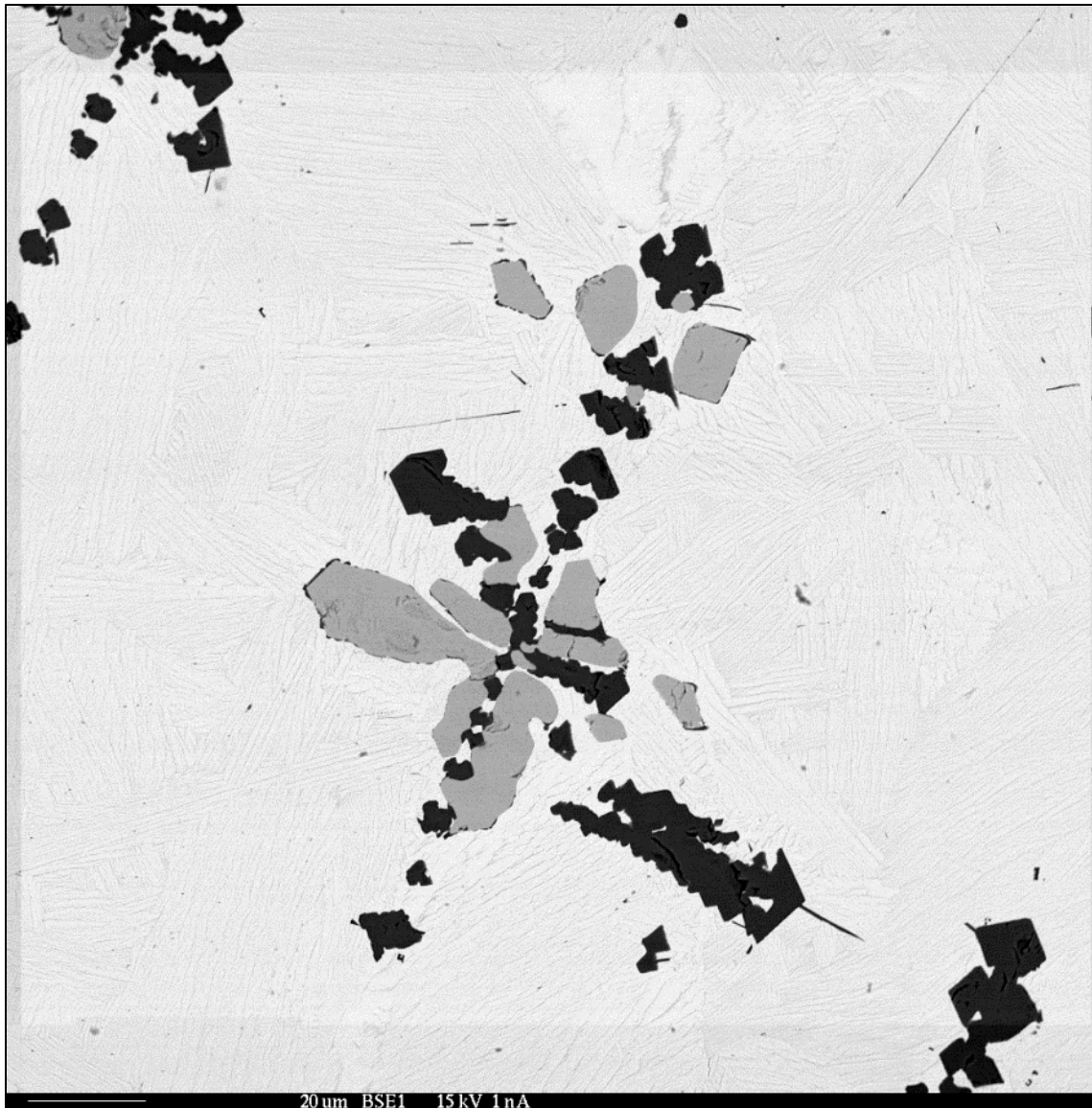
(b) Magnified irresolvable fine lamellae structure of U-2ZrAC (3000X)

Figure 4–2: Continued.

(a) Parallel secondary phase precipitates at periphery of U-2ZrAC (90X)

Figure 4-3: Secondary phase particles in U-2ZrAC.

(b) Magnified secondary phases within fine lamellae structure of U-2ZrAC (500X)
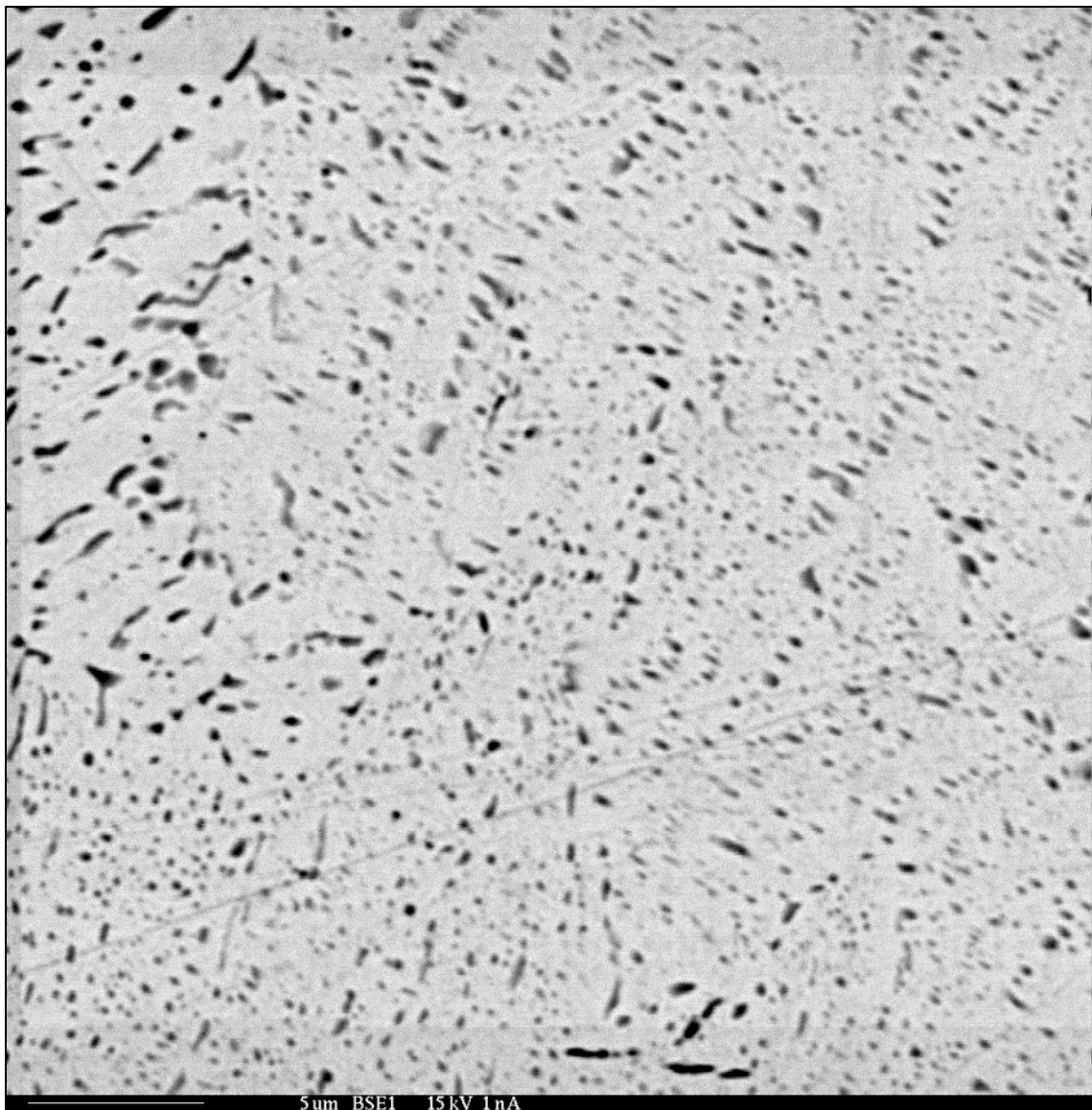
Figure 4–3: Continued.

56

The microstructural evolution of U-2Zr alloy from the as-cast condition to the annealed structures for 1d600, 3d500, 3d600, and 7d600 is shown in Figs. 4-4 and 4-5. All alloys annealed at 600 °C have shown a distinctive difference with the as-cast alloy, even for U-2Zr1d600, as shown in Fig. 4-4(a). The zirconium begins to gather into a uniform dispersion of second phase precipitates almost immediately. However, U-2Zr3d500 conserved more of the as-cast features than U-2Zr1d600, as shown in Fig. 4-5. On the other hand, U-2Zr1d600, 3d600, and 7d600 are indistinguishably similar; it is not clear that much coarsening of the phases occurs between 1 day and 7 days. This observation may lead to two hypotheses: 1) Diffusion rate of zirconium within α-U medium is highly temperature dependent between 500 °C and 600 °C and the rate at 500 °C is conducive to a sluggish transformation and 2) the rate at 600 °C enable rapid, near complete, transformation within 1 day, at least in metallurgical standpoint.

For annealed U-2Zr alloys, while WDS was able to confirm the bright matrix phase shown in the annealed alloys is α-U including solubility limit of zirconium, darker phase precipitates were too small (< 1 μm) and having dispersed phase boundary, even after 28 days of annealing at 600 °C. Therefore measured compositions of the phases using WDS was not decisive for many small dark precipitates. However, measured zirconium compositions from several of the larger dark precipitates (~1 μm × ~1 μm) were consistently ranged from 62 at% to 66 at% which corresponds to low end of unstoichiometric δ-UZr_2 phase. Note that the measured zirconium contents were systematically underestimated since those precipitates were surrounded by U-rich medium yielding some extra uranium counts to the measurements.
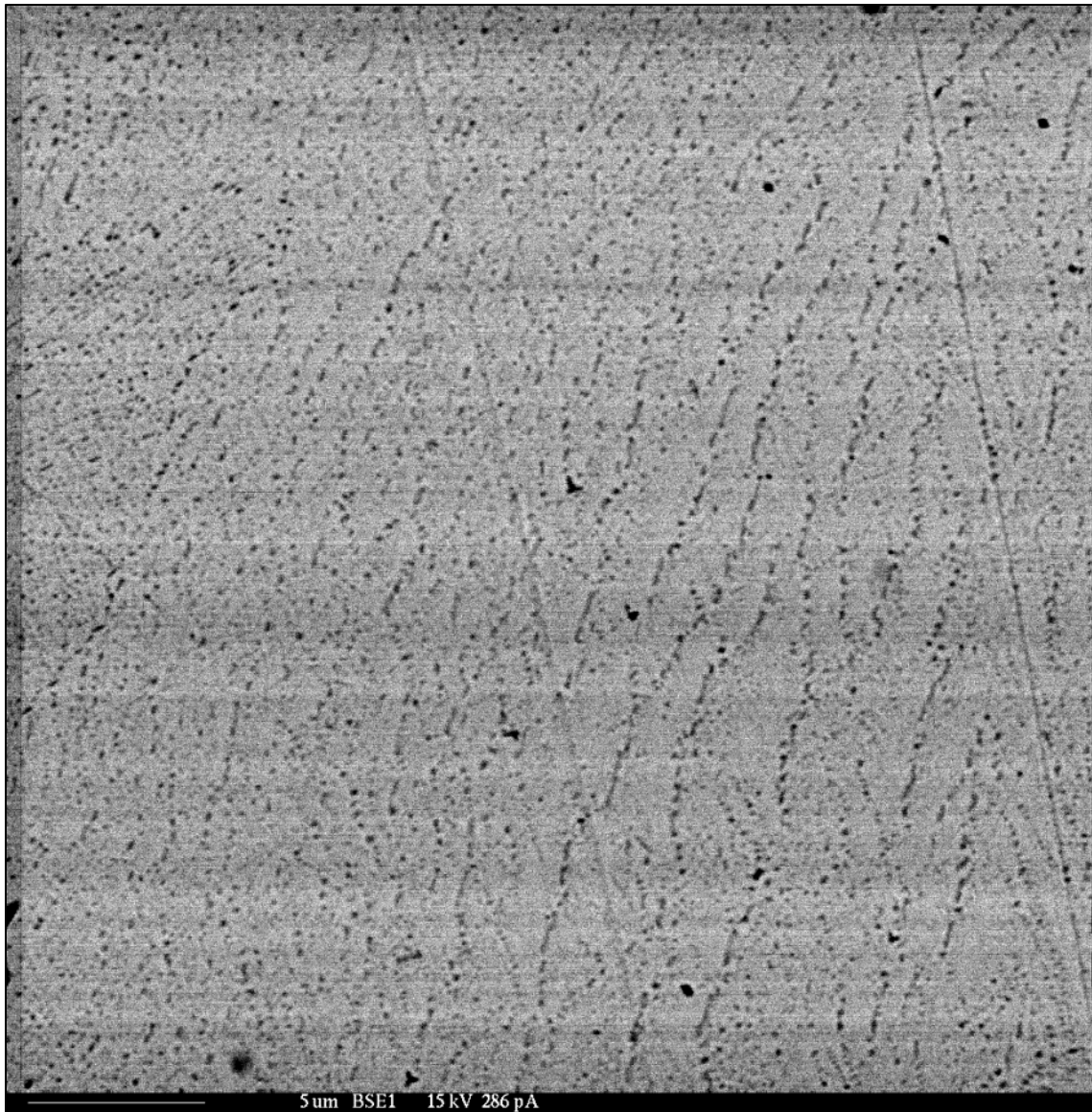
(a) Two phase precipitate structure of U-2Zr1d600 (1000X)

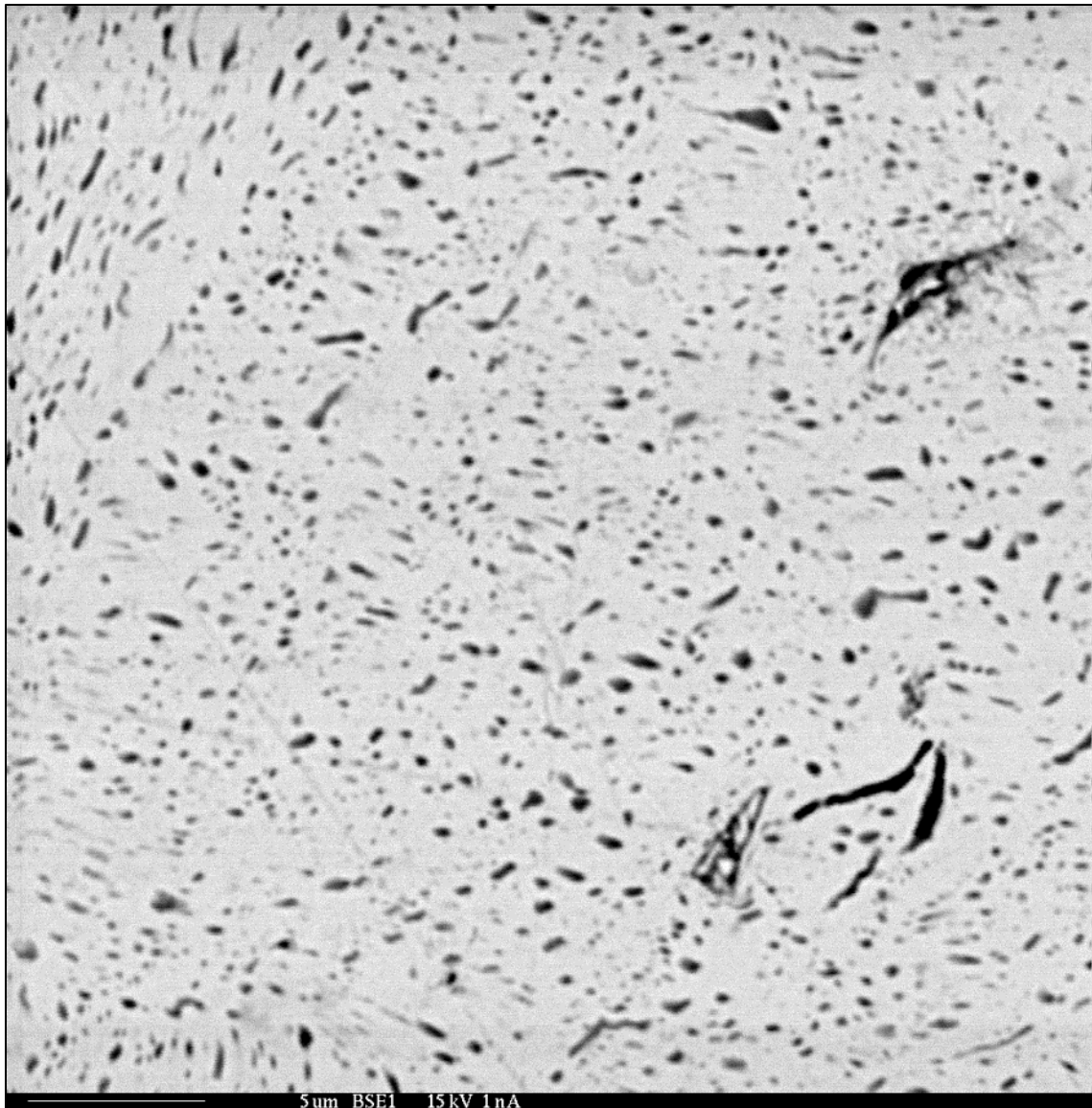**Figure 4-4: Microstructure evolution of U-2Zr1d600.**

(b) Magnified bulk of U-2Zr1d600 (3000X)
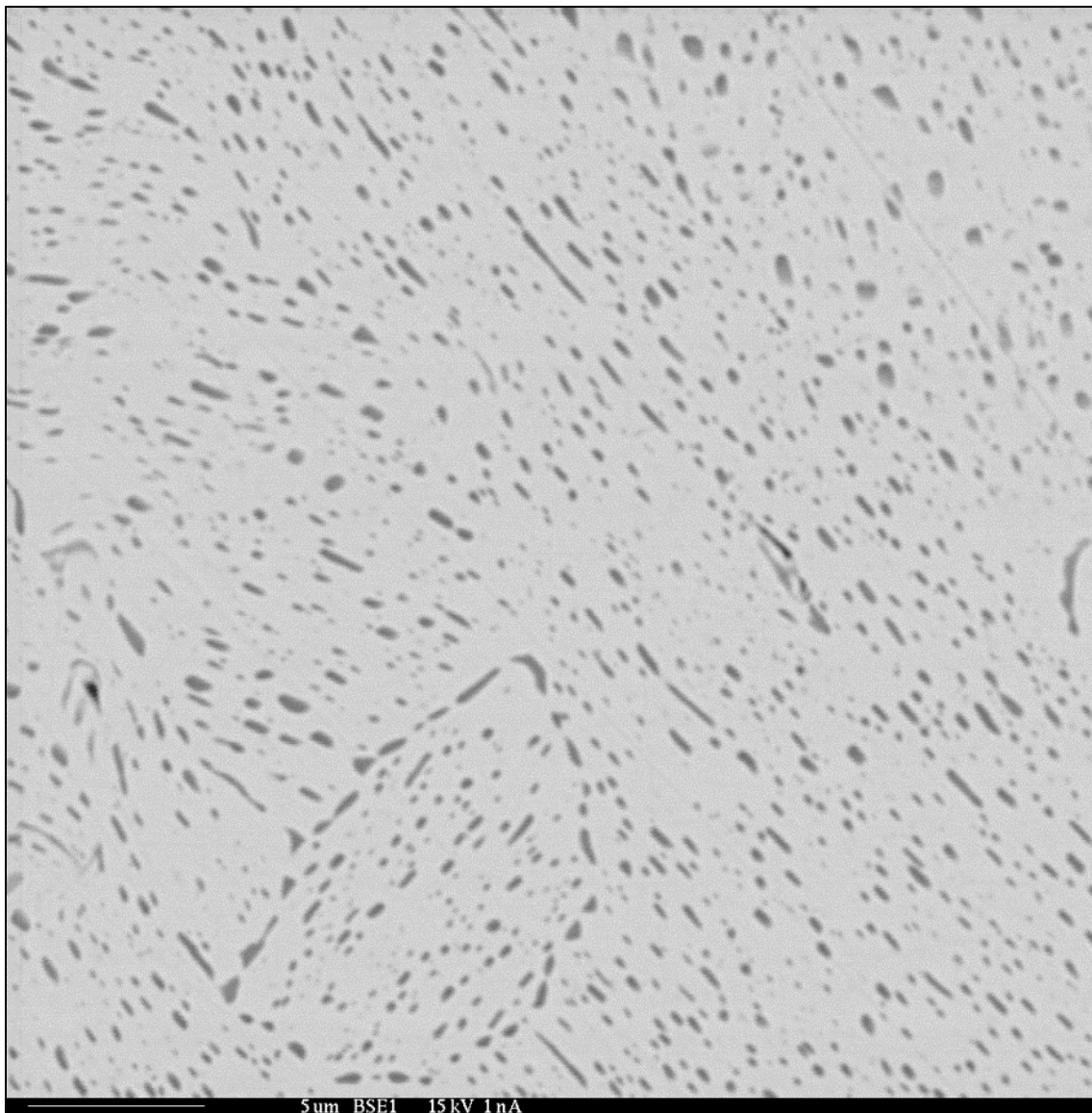
Figure 4–4: Continued.

(a) Low temperature annealed morphology of U-2Zr3d500 (3000X)

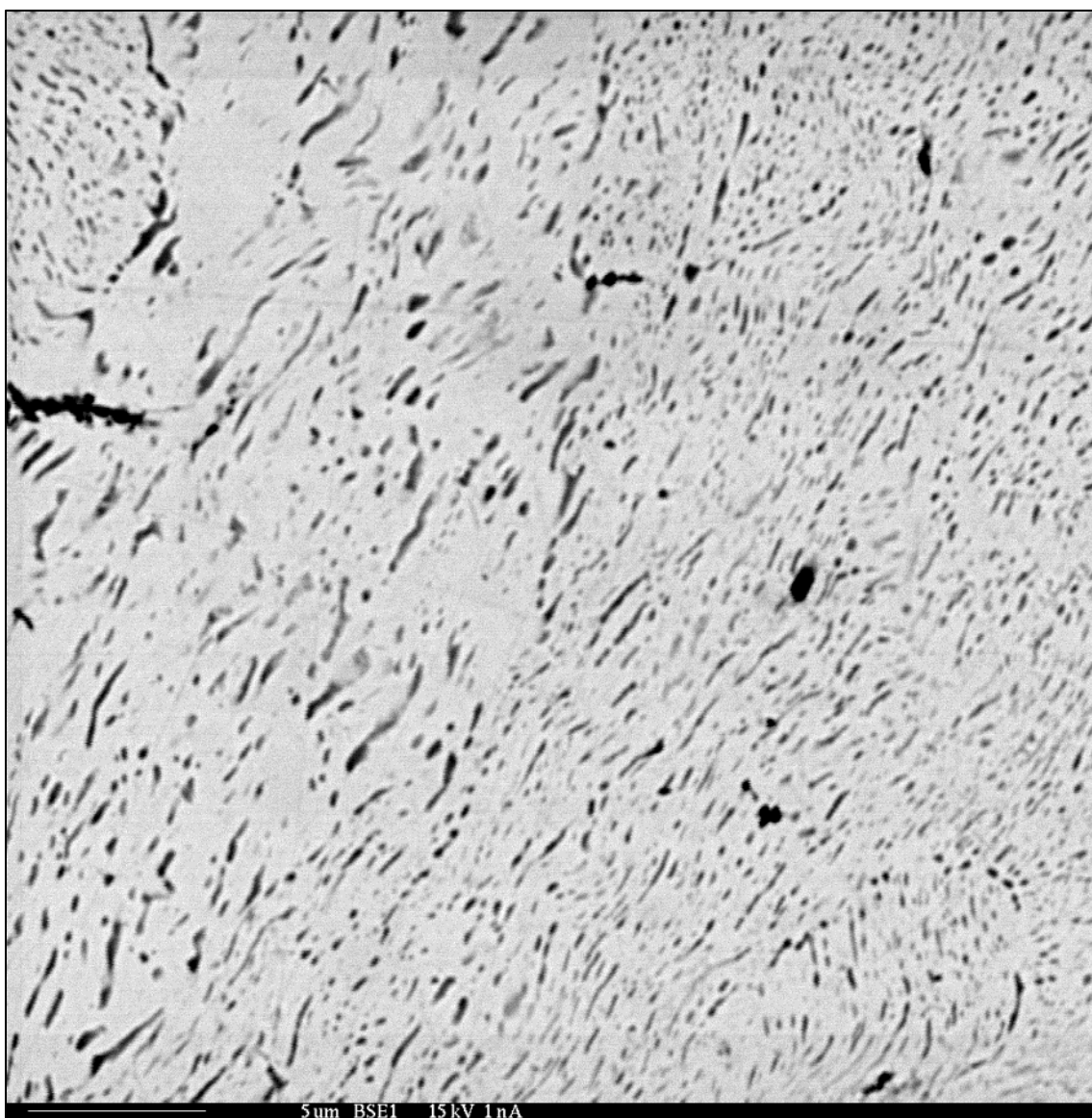**Figure 4-5: Temperature dependent microstructure evolution of annealed U-2Zr alloys.**

(b) U-2Zr3d600 (3000X)

Figure 4–5: Continued.

(c) U-2Zr7d600 (3000X)

Figure 4–5: Continued.

(d) Intermediate temperature annealed structure of U-2Zr7d550 (3000X)
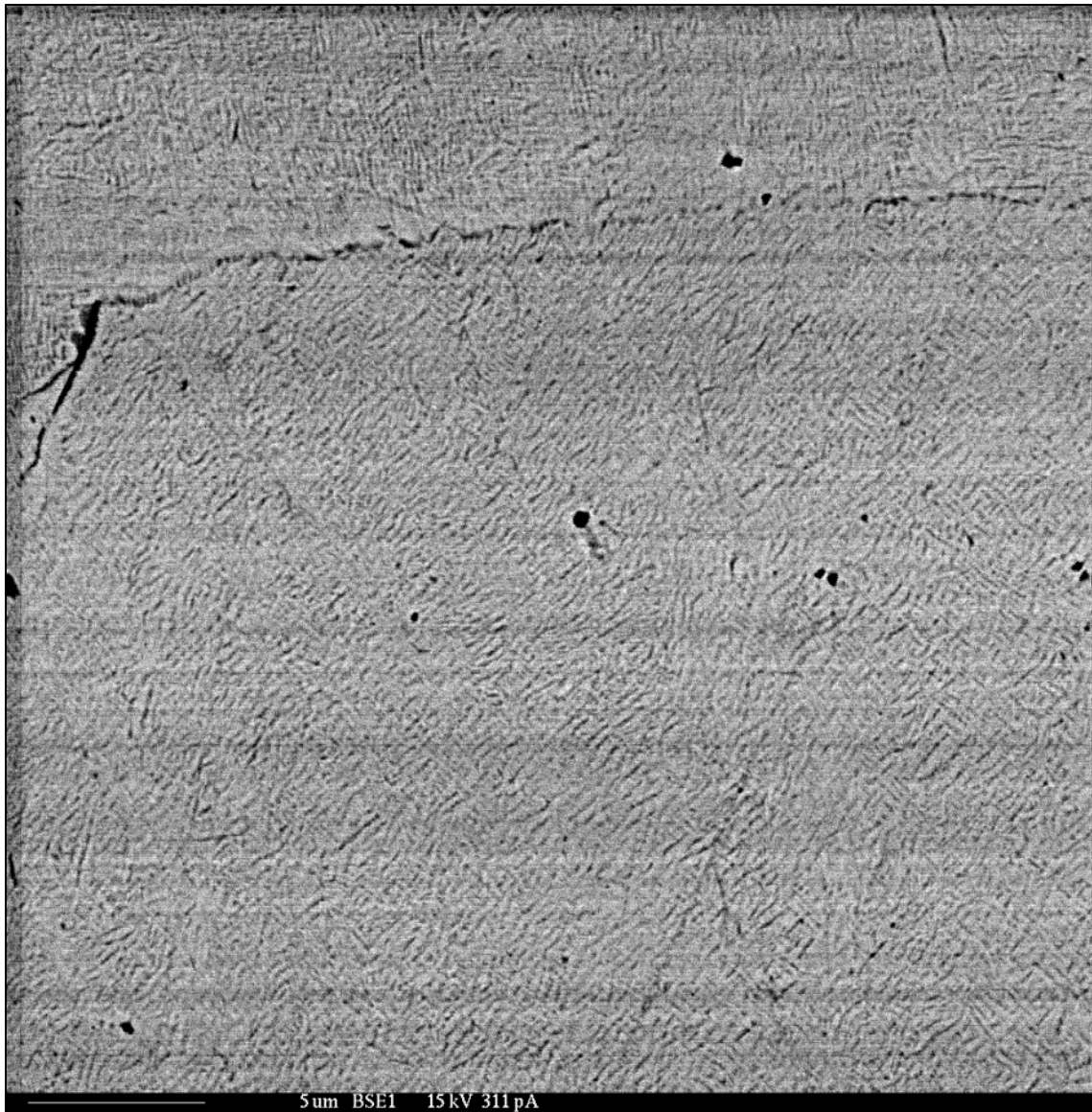
Figure 4–5: Continued.

4.1.1.3 U-5Zr

Figure 4-6 shows the structural evolution of U-5Zr alloy from the as-cast condition to the 7 day annealed condition. The remnant boundaries of parent γ phase grains in the as-cast alloy are shown in Fig. 4-6(a). Note fairly large grain sizes (> ~100 μm) of the as-cast alloy, which was beneficial for TEM specimen preparation. In Fig. 4-6(b), two phase lamellae are clearly hinted from highly magnified as-cast structure. The growth of the two phase lamellae structure is evident in Fig. 4-6(c), (d) and (e), alongside the annealing for 1, 3 and 7 day(s), respectively.

In annealed U-5Zr alloys, the area fraction of presumptive δ-UZr$_2$ phase is increased compared to U-2Zr alloy (Fig. 4.4) is clearly shown to be coarsening. However, precipitate growth was sluggish after 3 days of annealing, which is apparent upon comparing the last three BSE images of Fig. 4-6. It seems that the alloy achieved chemical equilibrium for 1 day annealing, and then is approaching microstructural equilibrium for additive 2 days of annealing at 600 °C.
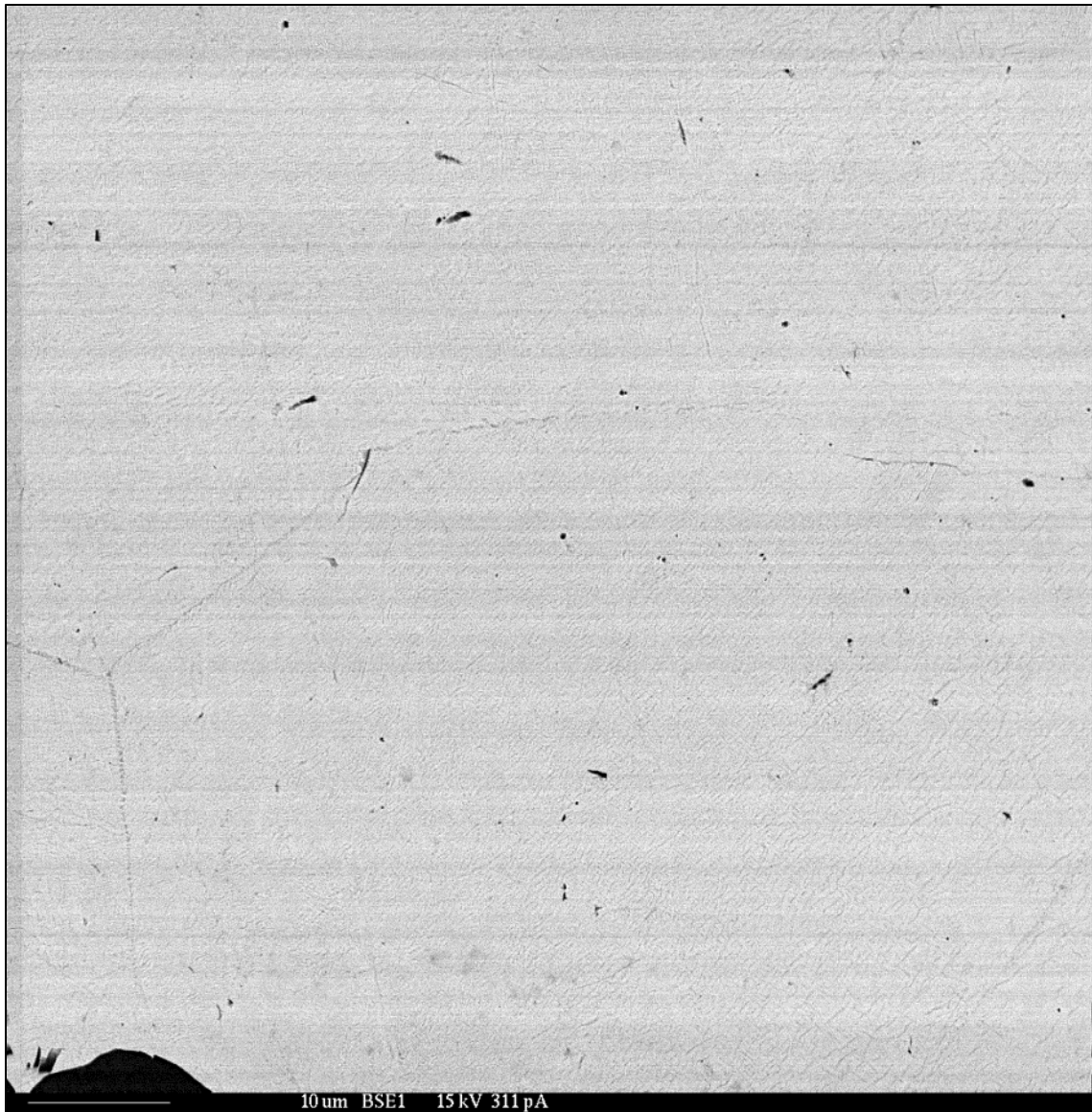
(a) Remnant grain boundaries of parent γ phase in U-5ZrAC (1200X)

Figure 4-6: Microstructure evolution of U-5Zr alloy from as-cast to 7d600.

(b) High magnification of the irresolvable fine structure of U-5ZrAC (3000X) (figure

courtesy of Sandeep Irukuvarghula, Texas A&M University)

Figure 4–6: Continued.

66
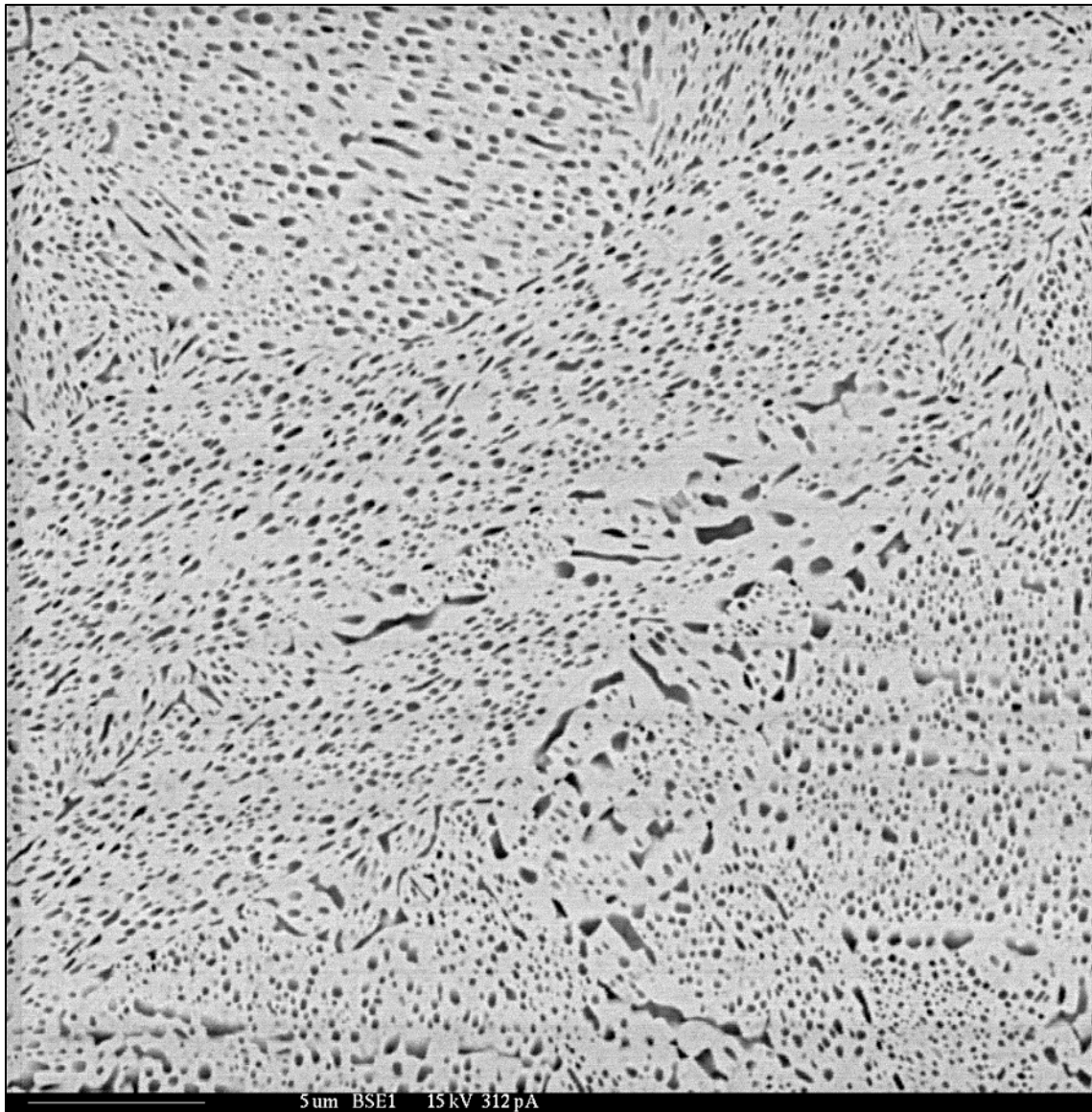
(c) Two phase precipitate structure of U-5Zr1d600 (3000X) (figure courtesy of Sandeep

Irukuvarghula, Texas A&M University)

Figure 4–6: Continued.
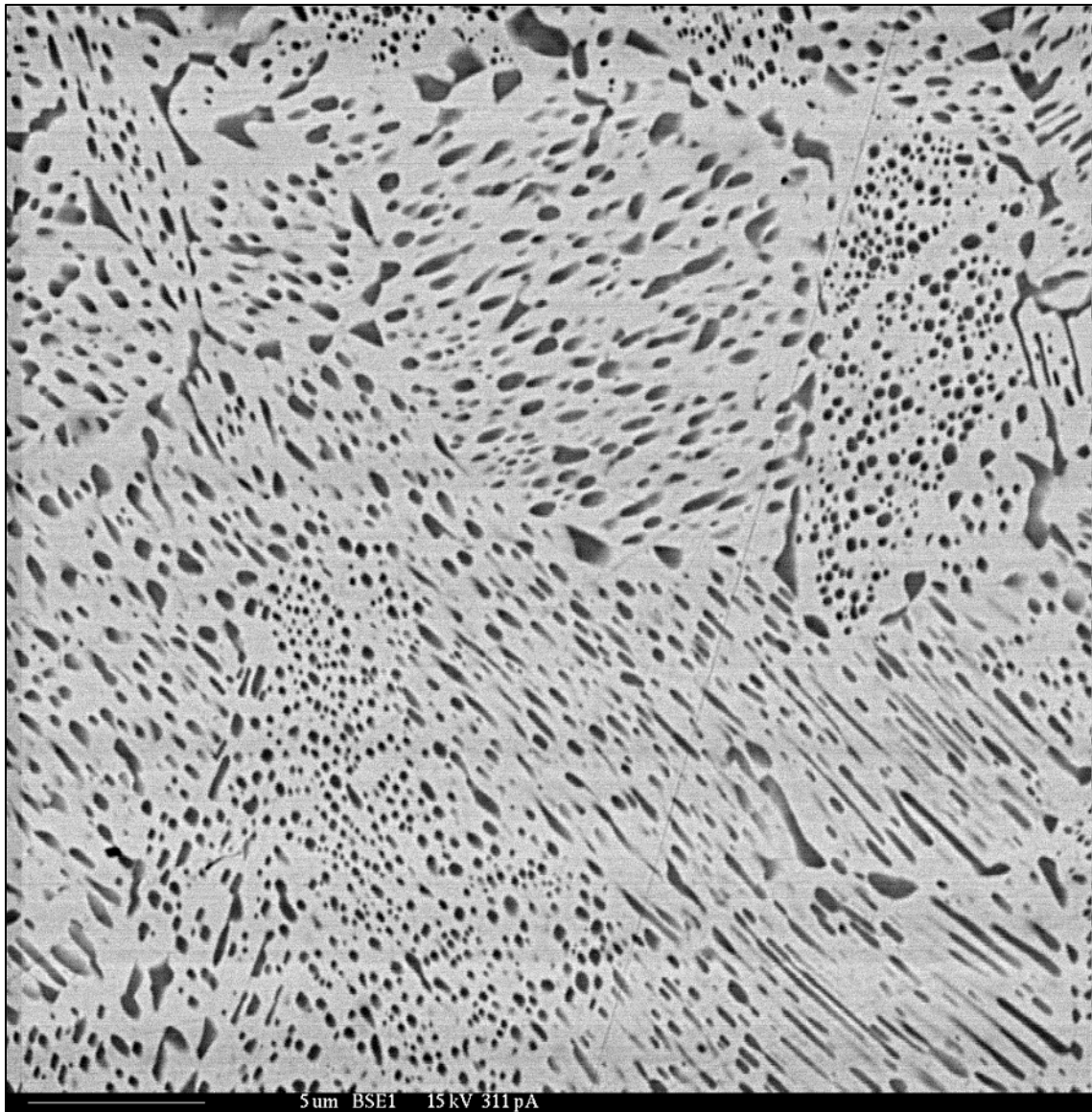
(d) U-5Zr3d600 (3000X) (figure courtesy of Sandeep Irukuvarghula, Texas A&M University)

Figure 4–6: Continued.

(e) U-5Zr7d600 (3000X)

Figure 4–6: Continued.

4.1.1.4 U-10Zr

The microstructural evolution of U-10Zr alloy from the as-cast condition to the 7 day annealed condition is sequentially displayed in Fig. 4-7. The very fine texture of as-cast U-10Zr alloy was again irresolvable, although sub-micrometer scale phase segregation is apparent. A group of zirconium and yttrium oxide precipitates were again observed to be aligned parallel to each other, often decorating the grain boundaries. In annealed U-10Zr alloys, Zr-rich phase precipitates began elongated and interconnected to each other forming eutectic lamellae structure. Zirconium-rich phase lamellae growth in the alloy was halted after 3 day annealing similarly with the Zr-rich precipitates growth in U-5Zr alloy.

It may be worthwhile to highlight that, following Sheldon's phase diagram, U-2, 5, and 10Zr alloys each transform in a different manner during cooling, being in hyper-, near-, and hypo-peritectoid reactions, respectively. Along the cooling of as-cast U-2Zr alloy, the γ phase alloy first decomposes into β-U and γ_1 phase, both have low zirconium compositions, ~1 and ~10 at%, respectively [127]. Then γ_1 phase is further transformed into Zr-rich γ_2 phase and α-U. On the other hand, the γ phase in U-5Zr alloy directly transforms into β-U and γ_2 phase. The zirconium composition of γ_2 phase is comparable to δ-UZr$_2$ phase. Therefore once formed γ_2 phase could be more handily transformed into δ-UZr$_2$ phase after cooling below 617 °C. In U-10Zr alloy, γ phase would be expected to decompose into γ_1 and γ_2 phases through the miscibility gap prior to β-U

phase formation owing to positive mixing enthalpy of uranium and zirconium which originates U-rich and Zr-rich phase separation.

(a) Irresolvable sub-micrometer structure of U-10ZrAC (1000X)
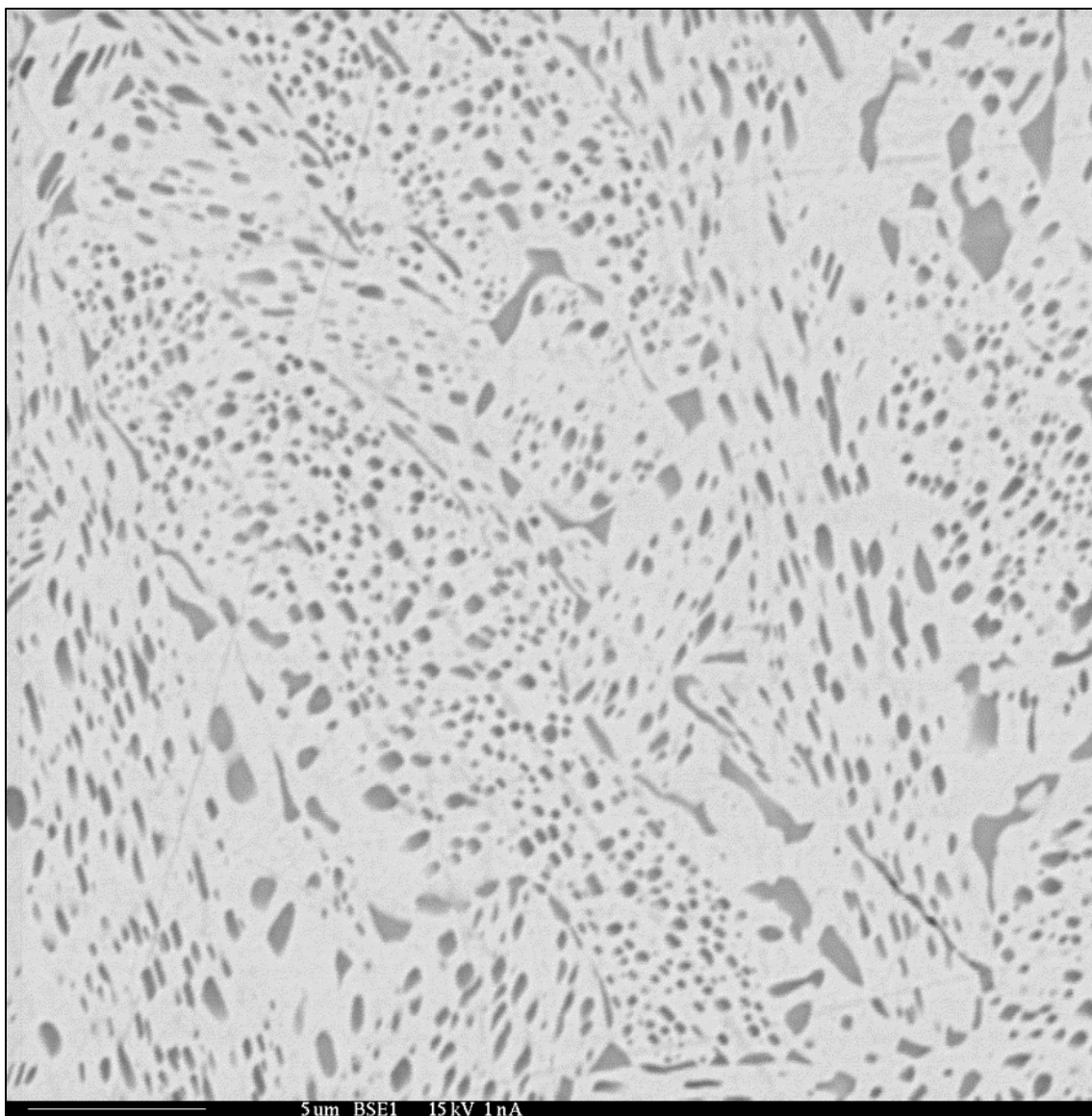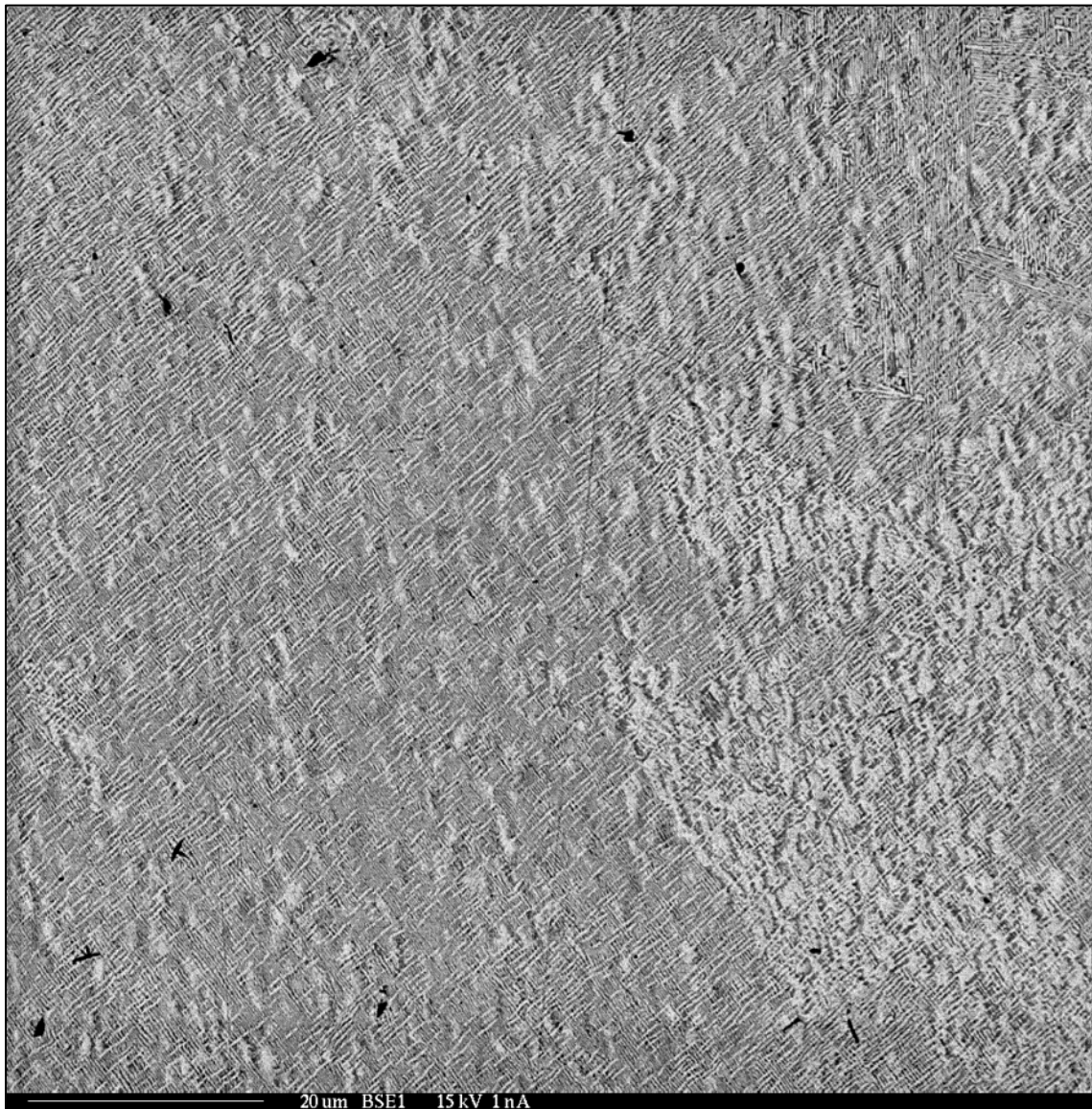
Figure 4-7: Microstructure evolution of U-10Zr alloy from as-cast to 7d600.
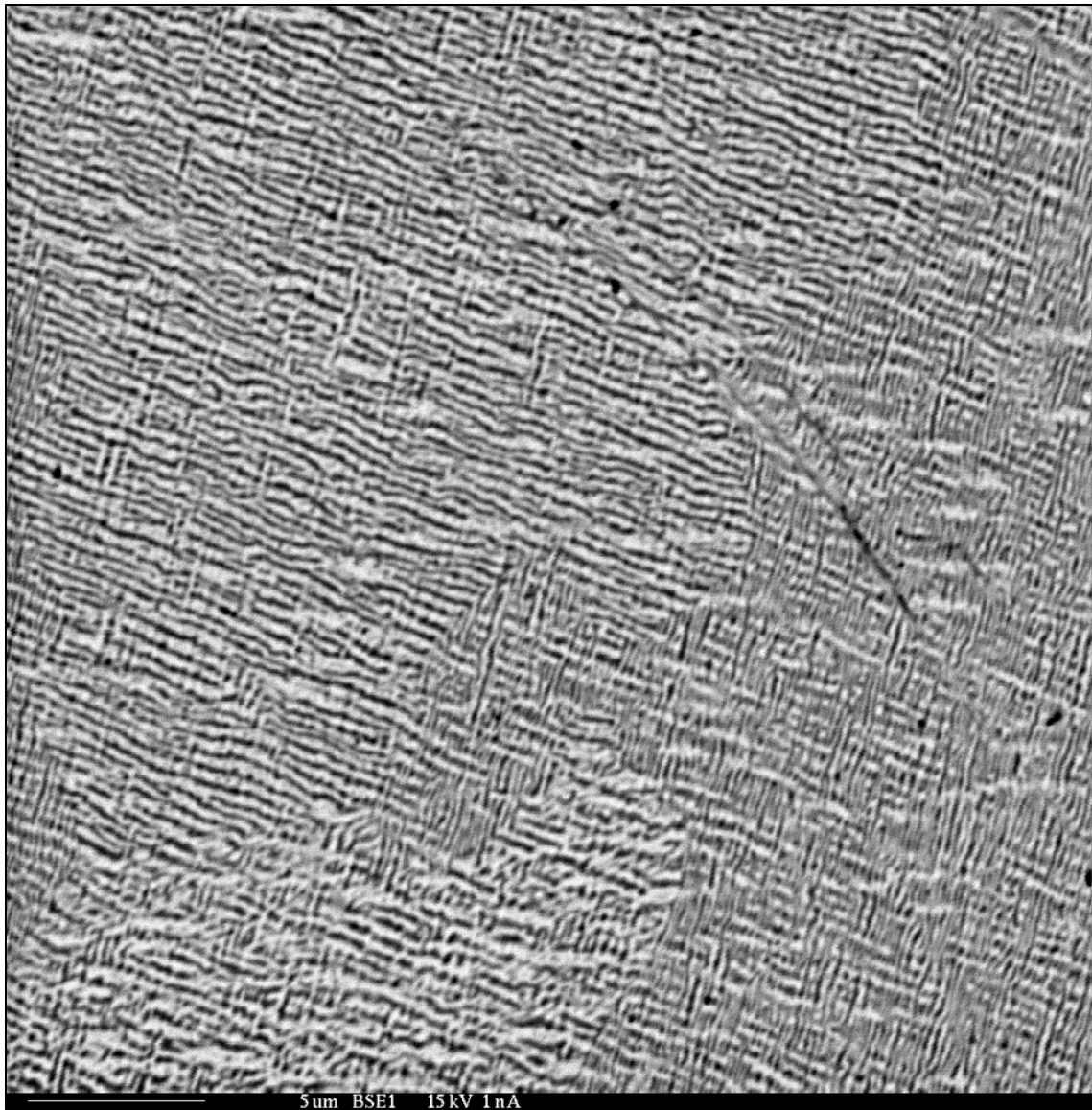
(b) Nano-scale two phase lamellae structure of U-10ZrAC (3000X) (figure courtesy of

Sandeep Irukuvarghula, Texas A&M University)

Figure 4–7: Continued.
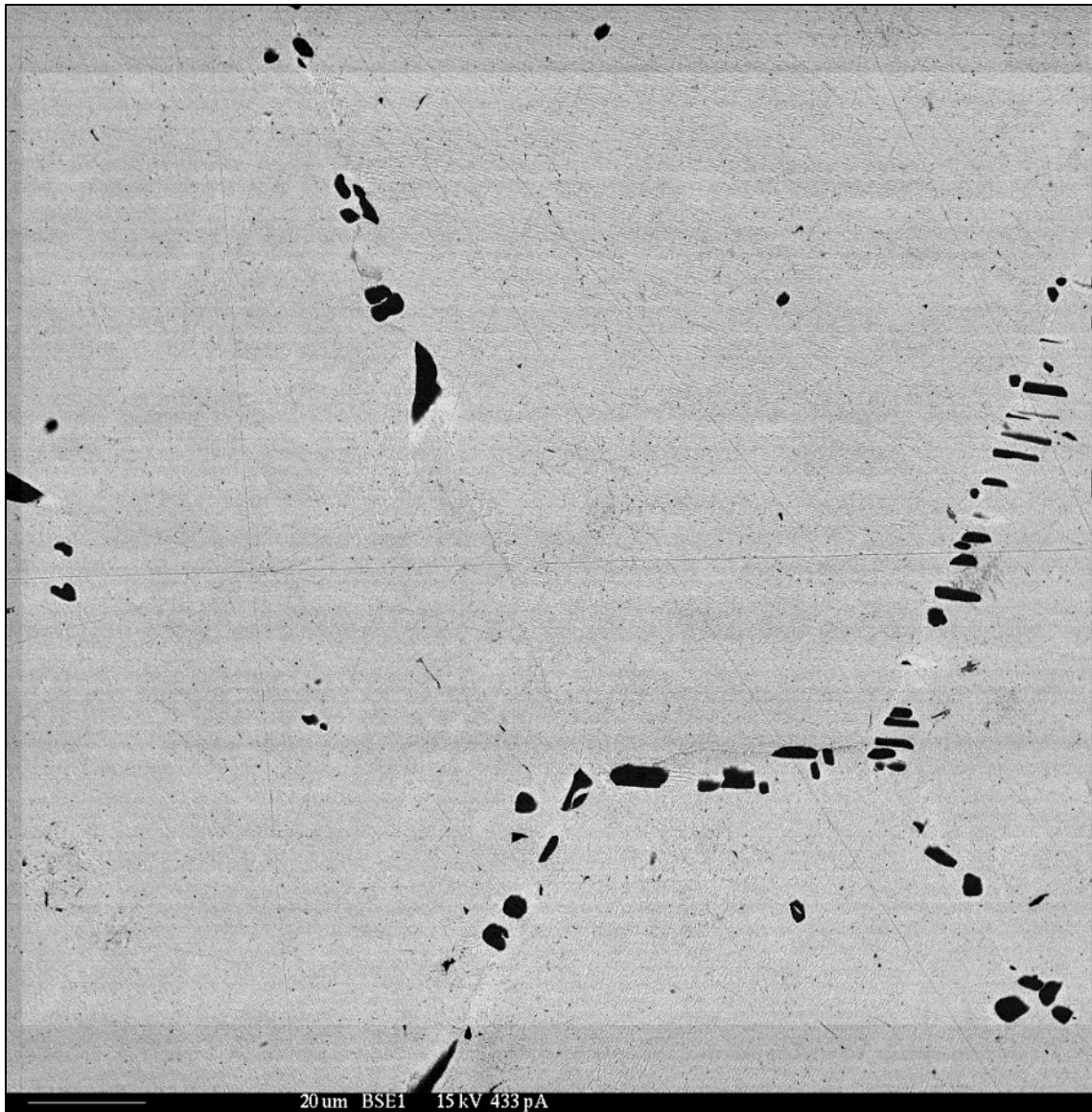
(c) Secondary phase particles alongside grain boundaries in U-10ZrAC (500X) (figure

courtesy of Sandeep Irukuvarghula, Texas A&M University)

Figure 4–7: Continued.
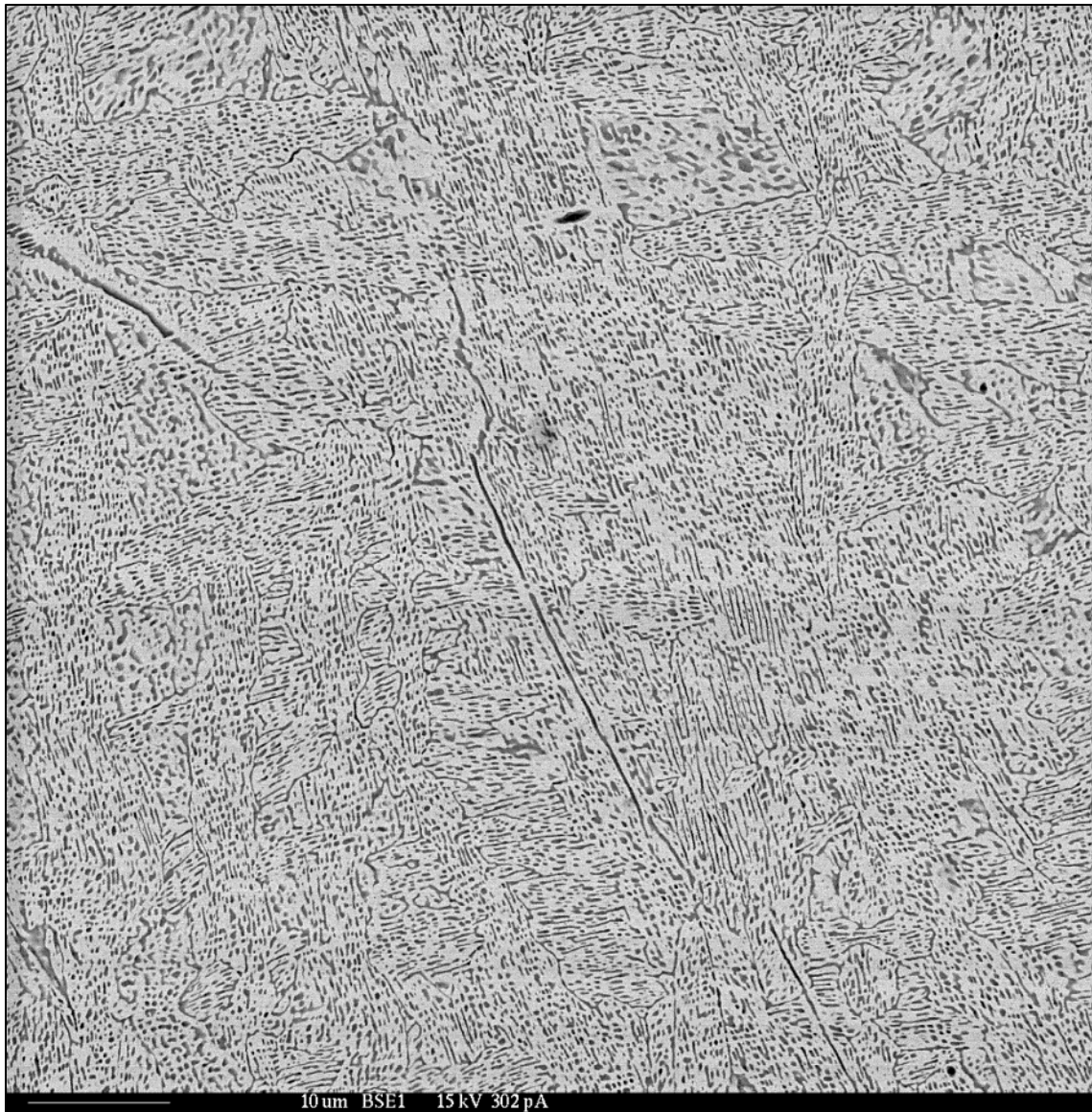
(d) Two phase lamellae of U-10Zr1d600 (1200X)

Figure 4–7: Continued.
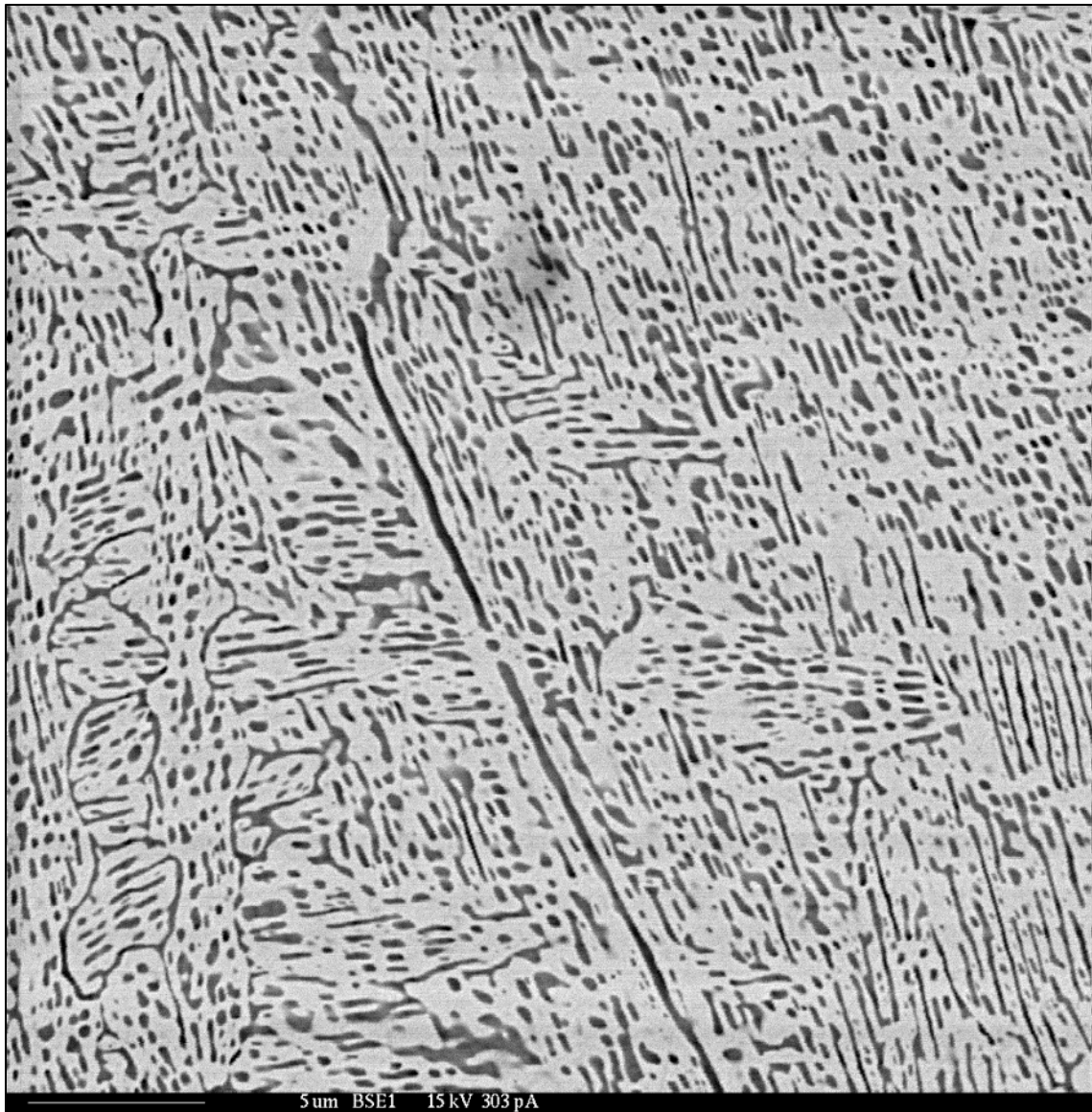
(e) Zirconium-rich phase packing former grain boundary in U-10Zr1d600 (3000X)

Figure 4–7: Continued.
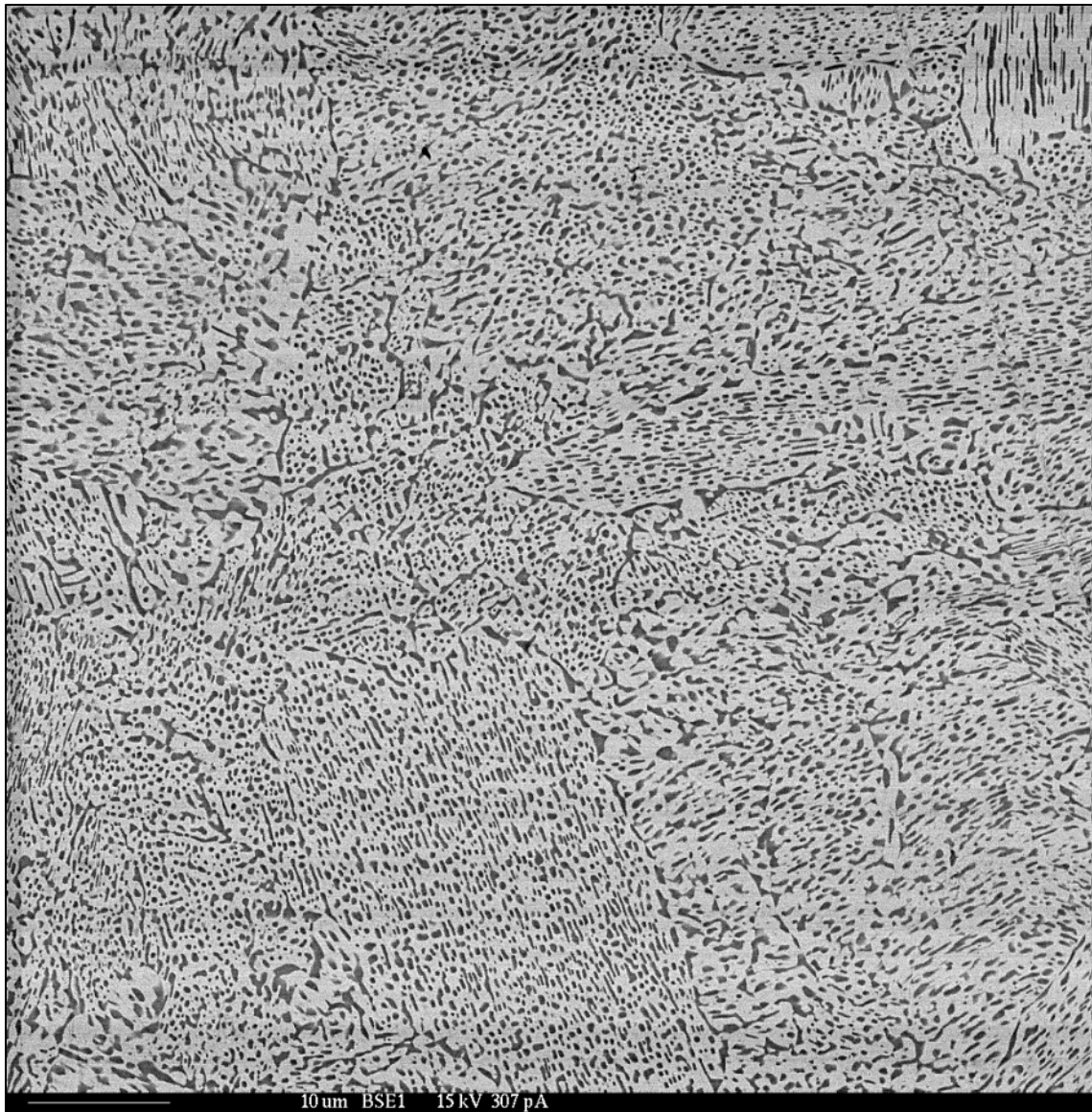
(f) U-10Zr3d600 (1200X)

Figure 4–7: Continued.
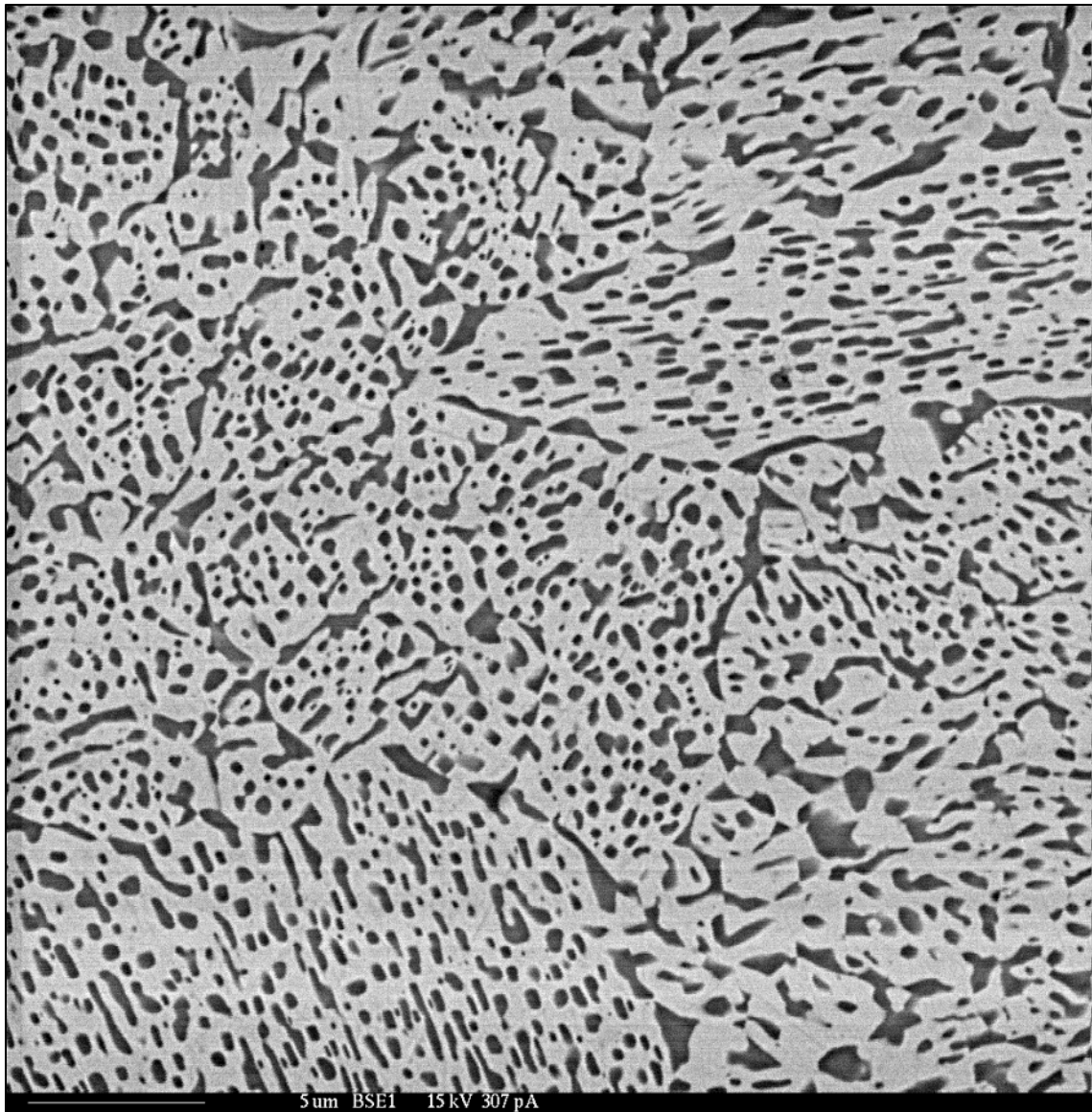
(g) U-10Zr3d600 (3000X) (figure courtesy of Sandeep Irukuvarghula, Texas A&M University)

Figure 4–7: Continued.

77
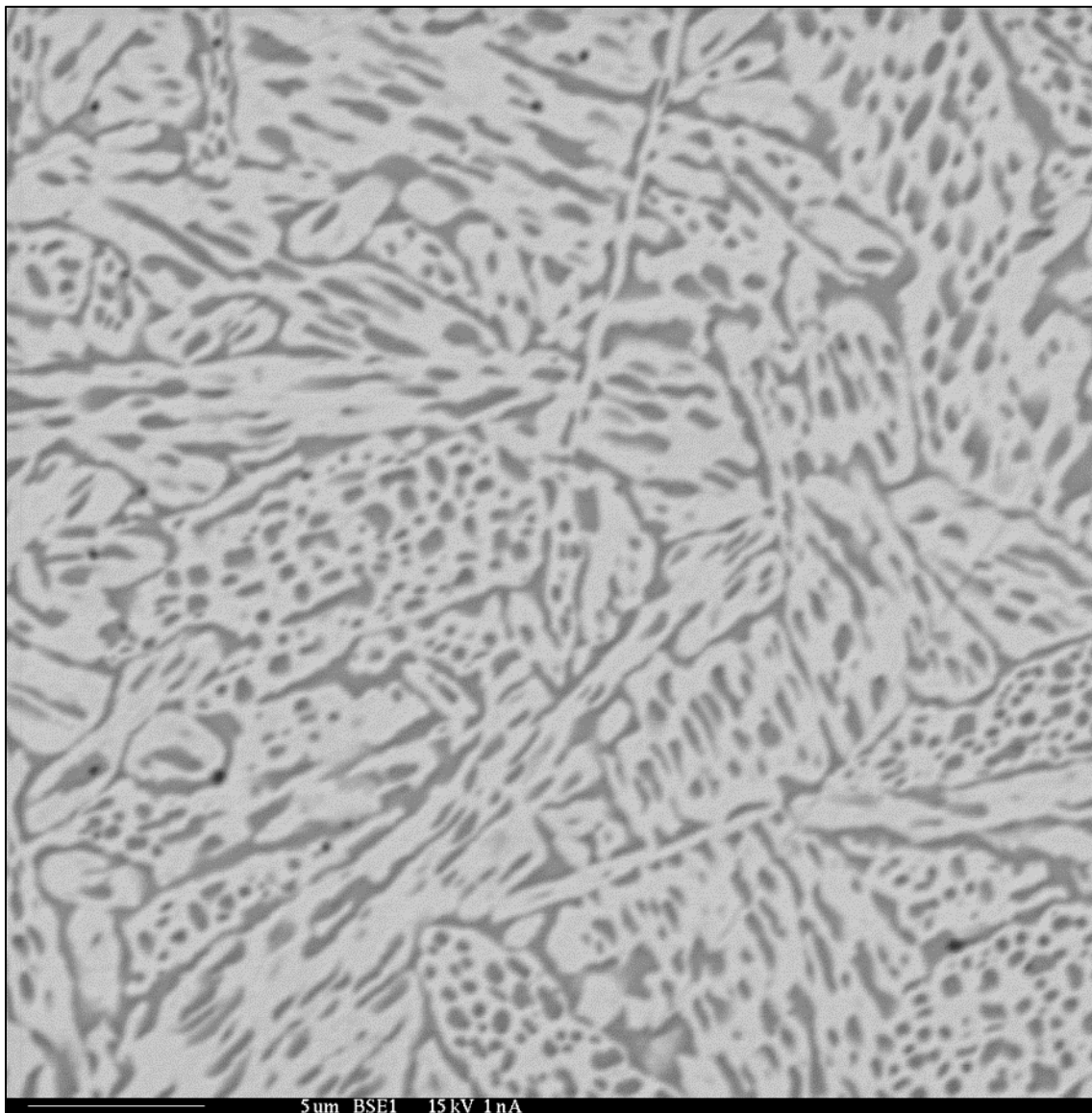
(h) U-10Zr7d600 (3000X)

Figure 4–7: Continued.

4.1.2 Zirconium-rich Alloys (> 15 wt%Zr)

The zirconium-rich U-Zr alloys (U-20, 30, 40, and 50Zr) are presented in this section. The demarcation between U-rich and Zr-rich was established based on the observed alloy structures. The U-rich alloys in Section 4.1.1 exhibited α-U as a dominant matrix phase with varying amounts of an apparent δ-UZr$_2$ precipitate phase of varying quantity. The Zr-rich alloys in this section exhibit an apparent δ-UZr$_2$ matrix phase.

4.1.2.1 U-20Zr

The images collected for annealed U-20Zr alloy may be considered in contrast to the U-10Zr alloy images in the previous section. The morphologies of the apparent α-U and δ-UZr$_2$ phases are reversed with a δ-UZr$_2$ matrix and α-U precipitates, as shown in Fig. 4-8. The WDS data confirmed the long, bright, rectangular particles with angular boundaries in annealed U-20Zr alloys are α-U precipitates, in contrast to the rounded δ-UZr$_2$ phase precipitates in U-rich U-Zr alloys.

The growth of α-U phase precipitates in Zr-rich U-Zr alloys also appeared to be stagnant (or negligibly slow) after 3 days of annealing, similar to that of δ-UZr$_2$ phase particle in U-rich alloys. The measured compositions of the precipitates and matrix phase in Zr-rich U-Zr alloys were in good agreement with expected α-U and δ-UZr$_2$ phase compositions, respectively.

(a) U-20ZrAC (4000X) (figure courtesy of Sandeep Irukuvarghula, Texas A&M University)

Figure 4-8: Microstructure evolution of U-20Zr alloy from as-cast to 7d600.
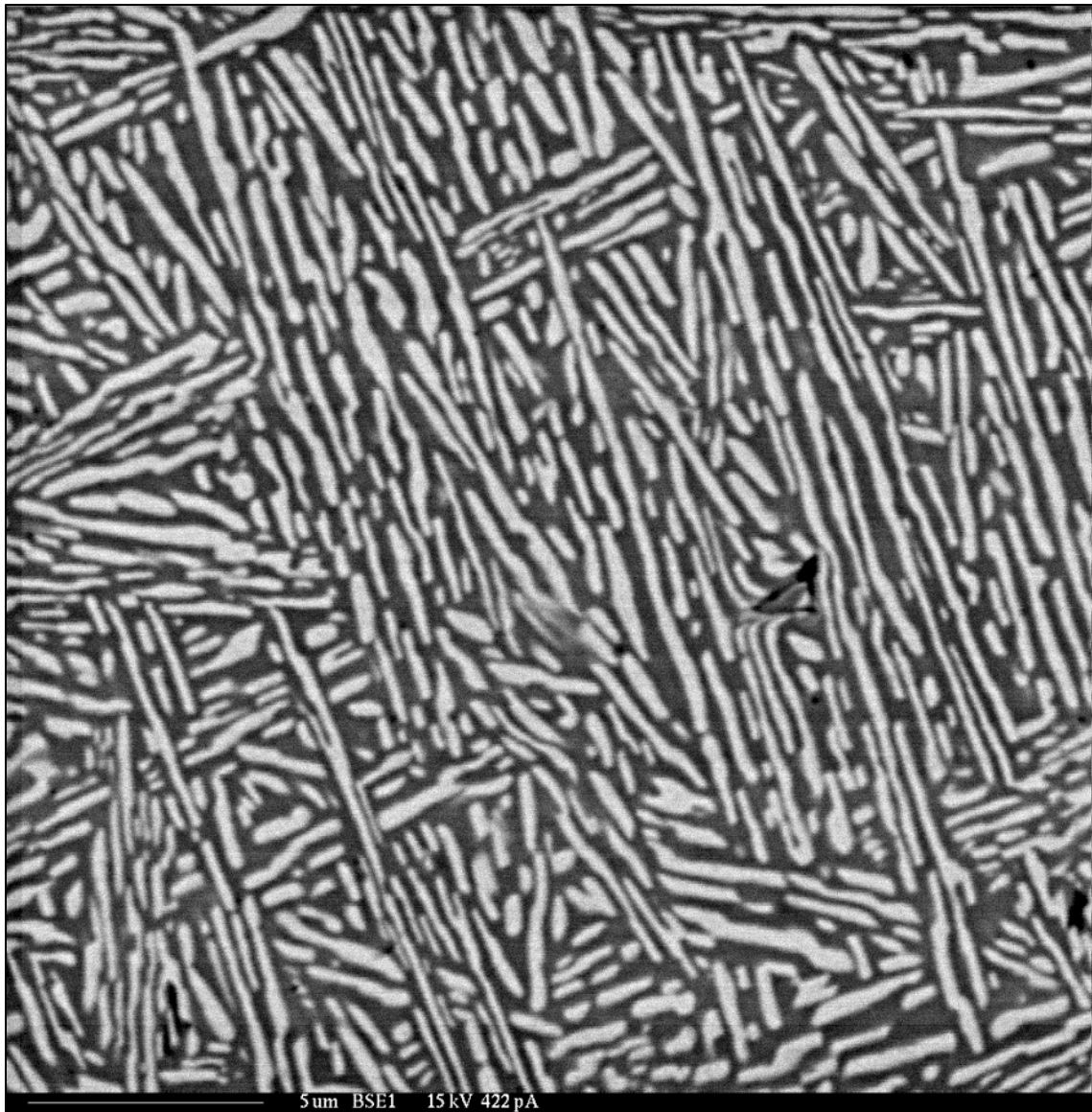
(b) δ-UZr$_2$ phase matrix and α-U phase precipitates in U-20Zr1d600 (4000X) (figure

courtesy of Sandeep Irukuvarghula, Texas A&M University)

Figure 4–8: Continued.
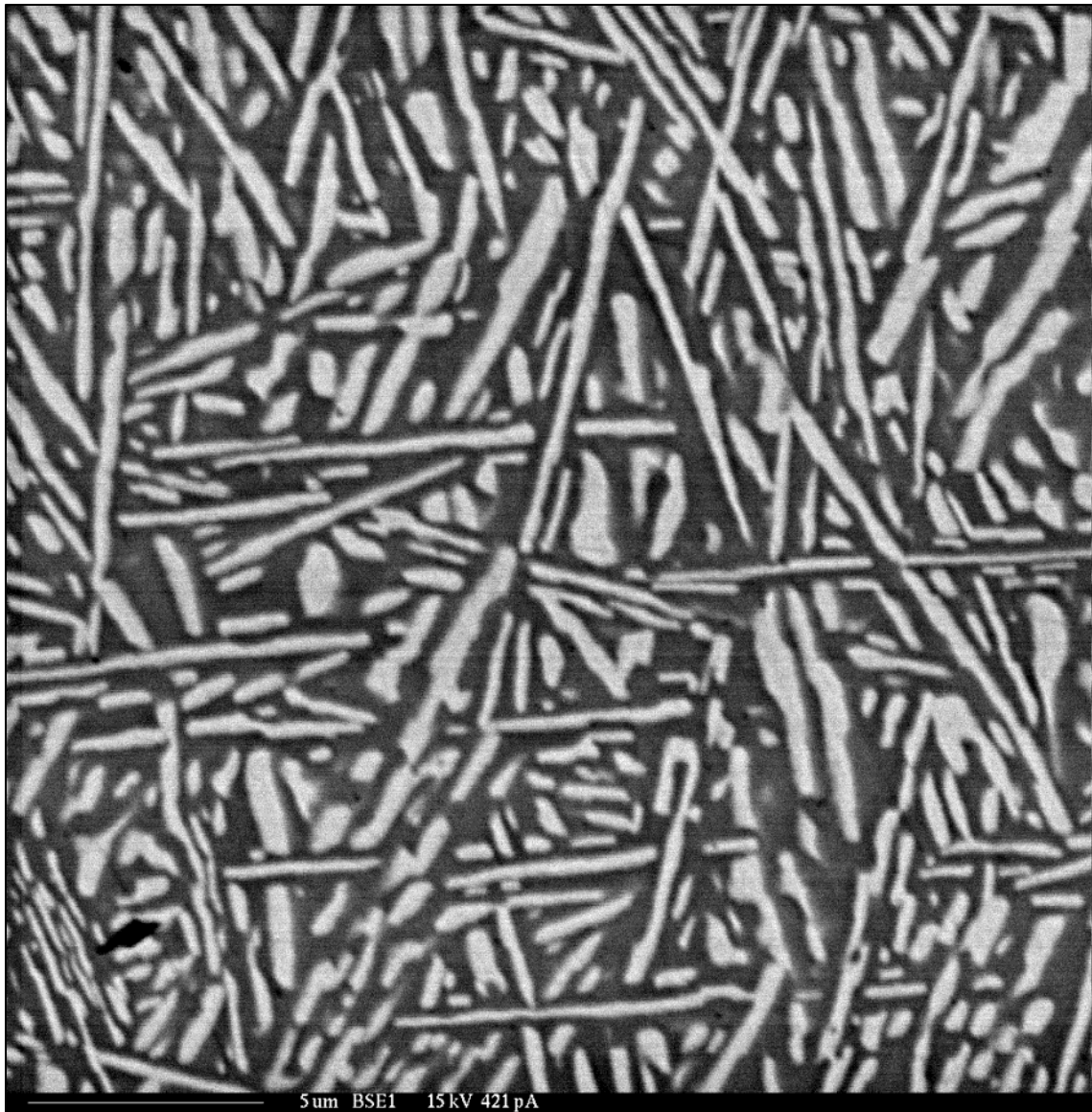
(c) U-20Zr3d600 (4000X)
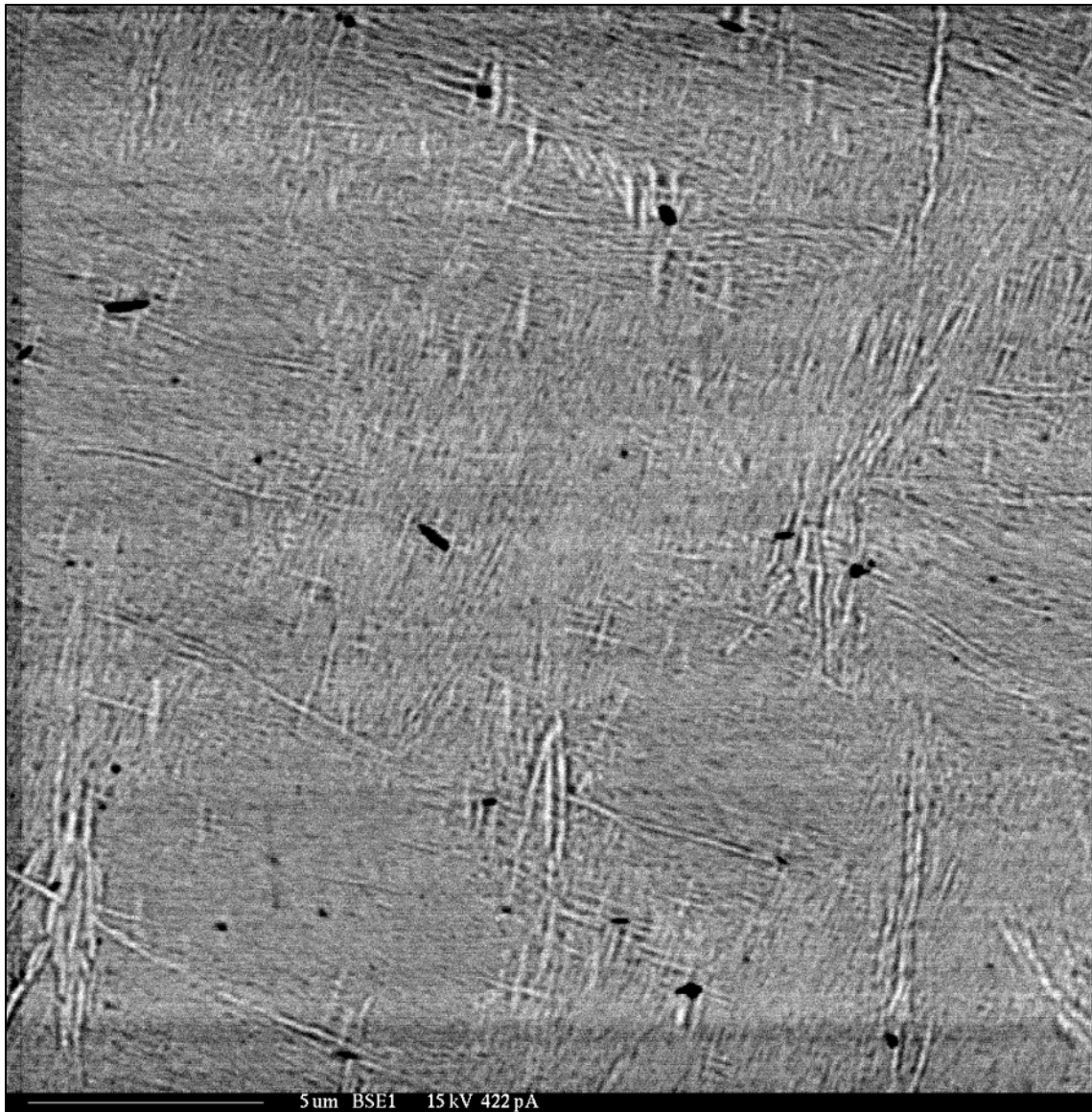
Figure 4–8: Continued.
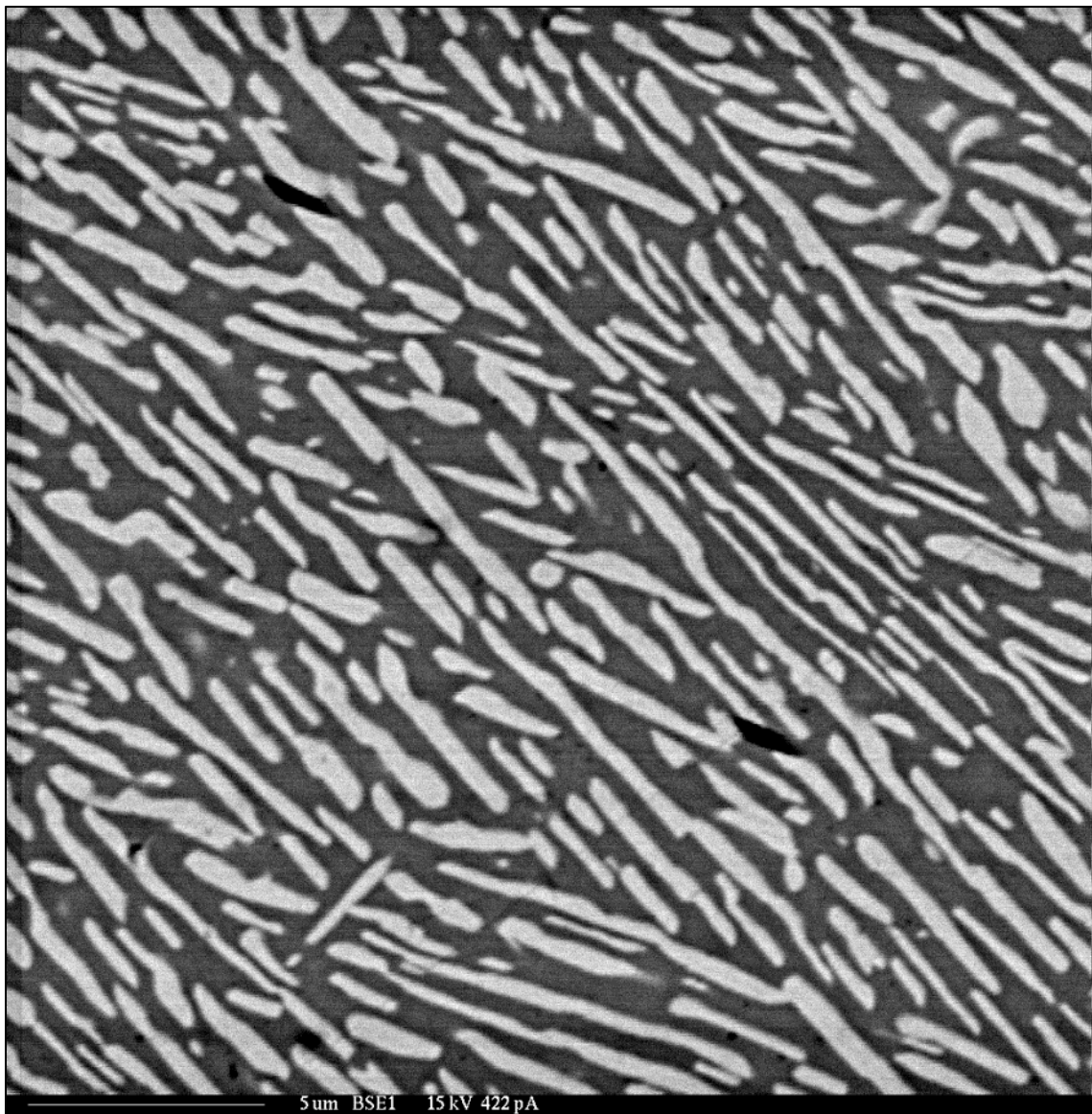
(d) U-20Zr7d600 (4000X)

Figure 4–8: Continued.

4.1.2.2 U-30Zr

The BSE images from U-30Zr alloy are presented here showing the evolution from the as-cast structure to the 7 day annealed structure. As-cast two phase structure of U-30Zr alloy is more clearly shown in Fig. 4-9(a) than as-cast U-20Zr alloy shown in Fig. 4-8(a), likely indicating in the more Zr-rich U-Zr alloy the faster formation of Zr-rich δ-UZr$_2$ phase. The α-U phase precipitates are smaller and less dense (in number) in annealed U-30Zr alloy, also compared to U-20Zr alloy, as shown in Fig. 4-9(b), (c) and (d).

Remnant grain boundaries from the parent γ phase were not distinctively visualized in the annealed U-20Zr or U-30Zr alloy (Figs. 4-8 and 4-9), in contrast with annealed U-rich U-Zr alloys where the long δ-UZr$_2$ phase lamellae would preferably align parallel to boundaries as shown in Fig. 4-7(e). This was assumed to be due to nucleated δ-UZr$_2$ phase filled in grain boundaries during annealing, since free space between incoherent adjacent grains attracts relatively voluminous solid phases, e.g. δ-UZr$_2$ and α-Zr in U-Zr alloy system.

(a) U-30ZrAC (2000X) (figure courtesy of Sandeep Irukuvarghula, Texas A&M University)

Figure 4-9: Microstructure evolution of U-30Zr alloy from as-cast to 7d600.
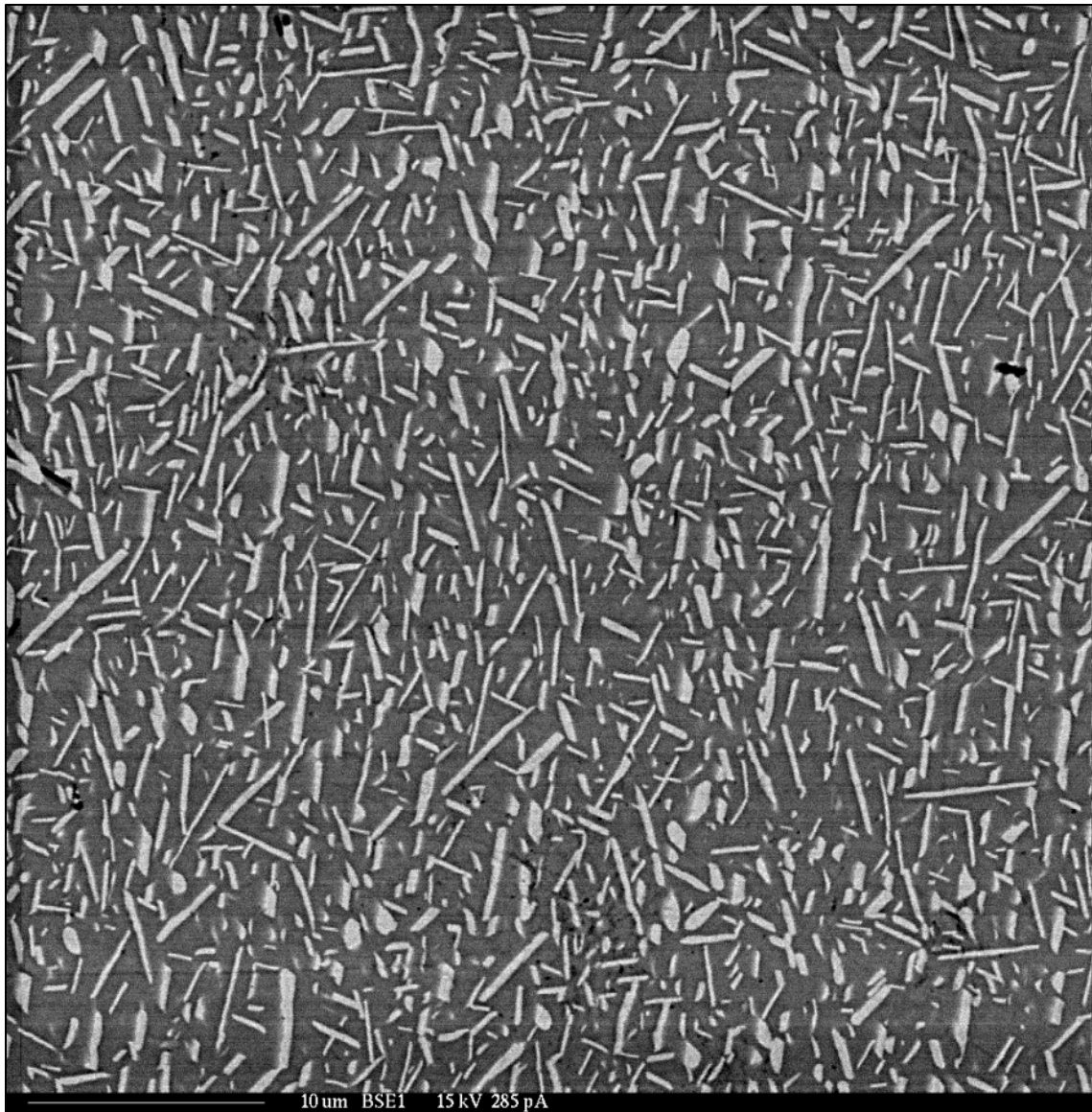
(b) U-30Zr1d600 (2000X)

Figure 4–9: Continued.
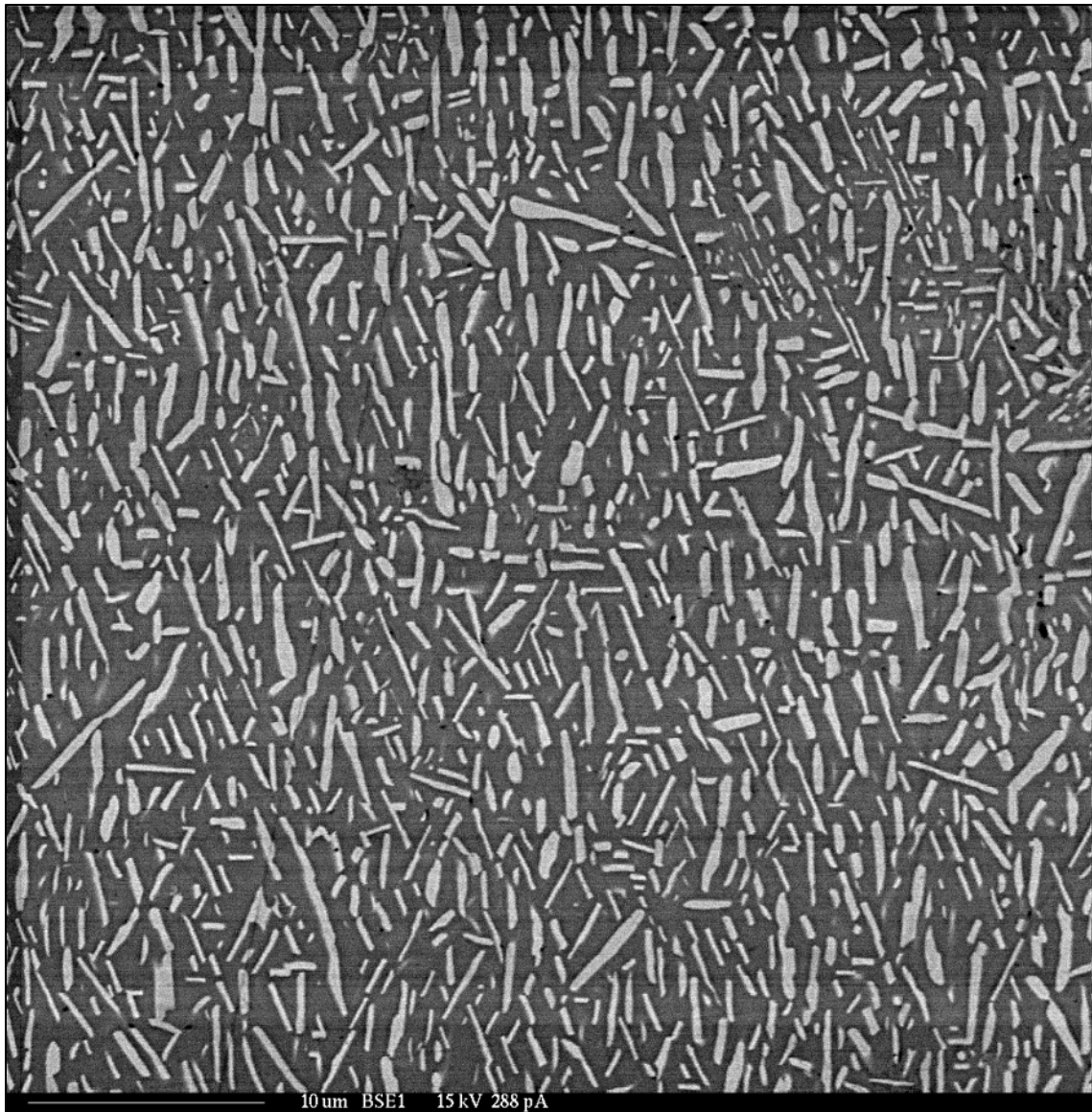
(c) U-30Zr3d600 (2000X)

Figure 4–9: Continued.
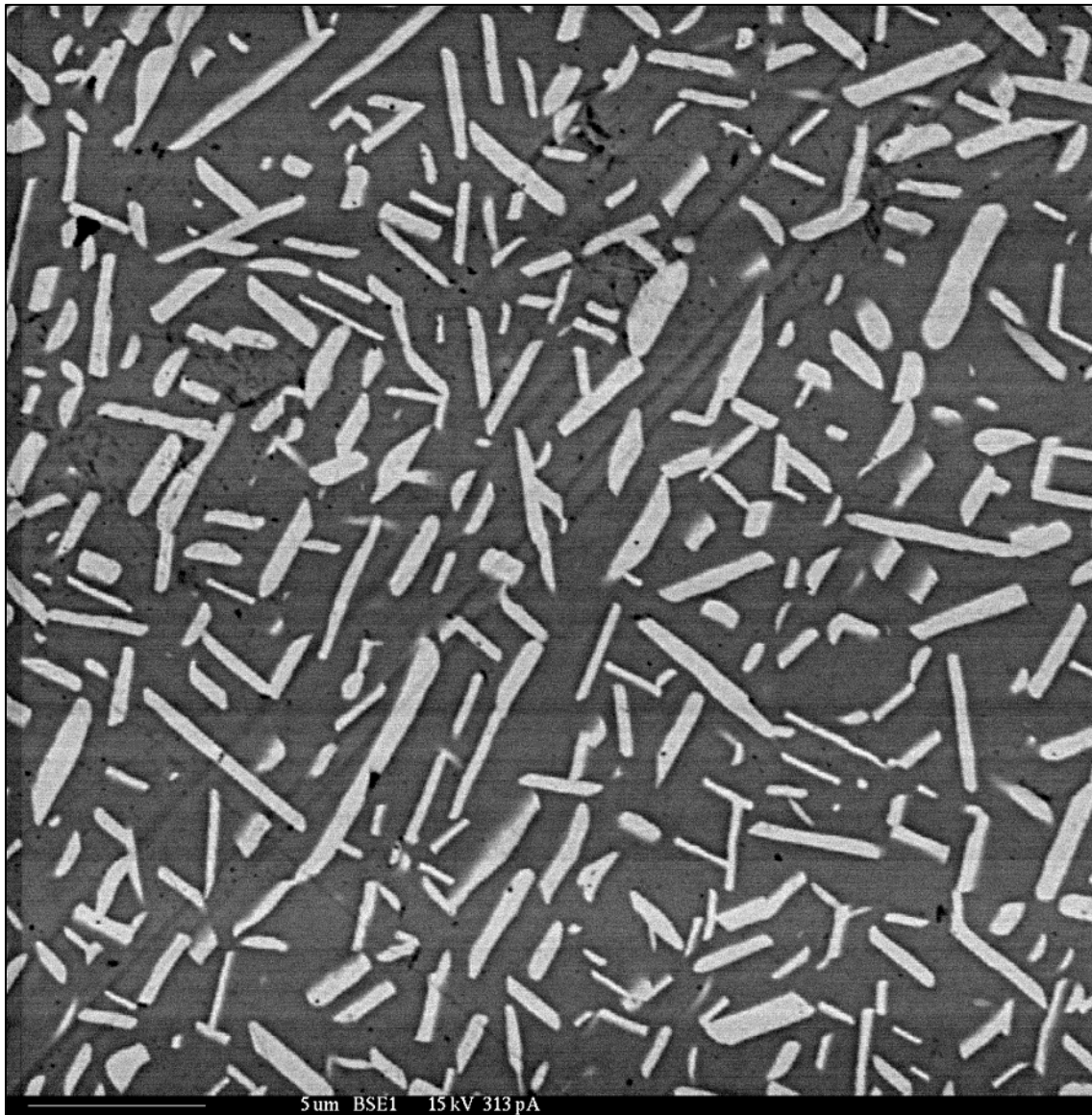
(d) U-30Zr7d600 (3000X) (figure courtesy of Sandeep Irukuvarghula, Texas A&M University)

Figure 4–9: Continued.

The precipitate sizes of α-U have not shown remarkable change during the course of annealing. (Note the magnification difference in Fig. 4-9.)

4.1.2.3 U-40Zr

A representative area of as-cast U-40Zr alloy is shown in Fig. 4-10(a). Following Sheldon's phase diagram and Akabori *et al*. [127, 155], U-40Zr alloy should have single δ-UZr$_2$ phase. However, numerous α-Zr phase precipitates have been generally formed within δ-UZr$_2$ phase matrix in the as-cast U-40Zr alloy. Furthermore, the coexistence of all three low temperature phases of U-Zr binary system, α-U, δ-UZr$_2$ and α-Zr phases, are observed in annealed U-40Zr alloy, as shown in Fig. 4-10(d).

Figure 4-10(a) shows zirconium (dark gray) precipitates along grain boundaries and within grains. The round (black) particles are yttrium oxide inserted from the crucible used for melt-casting. The matrix (gray) phase shown in Fig. 4-10(b) includes (64.7 ± 0.4) at% zirconium, which corresponds to low end of δ-UZr$_2$ phase and also the gross composition of the alloy.

Although the presence of α-U phase was not clearly observed in as-cast U-40Zr alloy, the annealed U-40Zr alloy for 7 days at 600 °C clearly exhibits U-rich (white) precipitates including less than 0.8 at% zirconium as shown in Fig. 4-10(d), likely α-U saturated with zirconium. In the annealed alloy, U-rich precipitates were concentrated near zirconium precipitates, however, scattered precipitates were also observed within presumptive δ-UZr$_2$ phase medium as shown in Fig. 4-10(e).
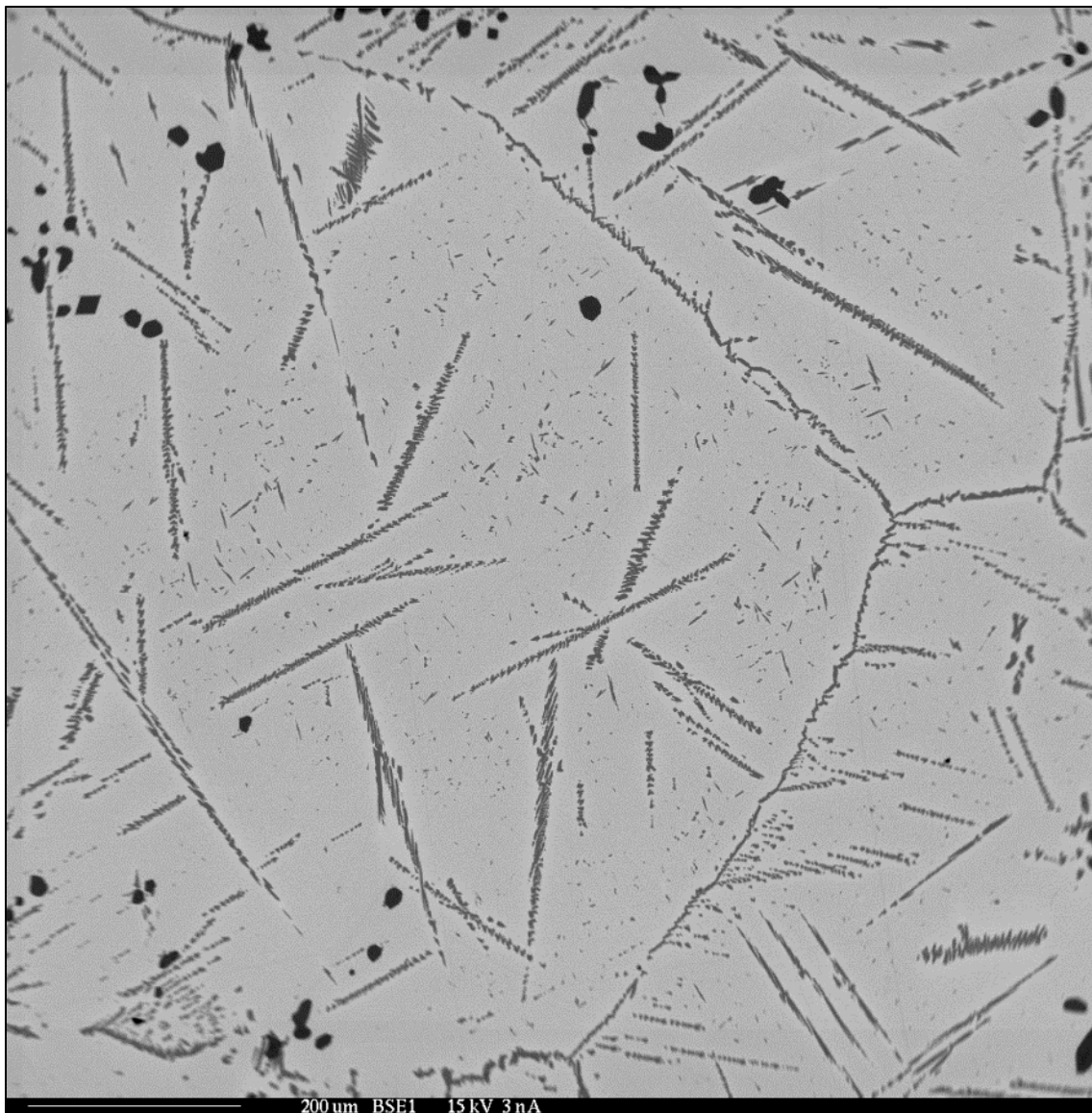
(a) Zirconium precipitates in U–40ZrAC (90X)

Figure 4-10: Microstructure evolution of U–40Zr alloy from as-cast to 7d600.
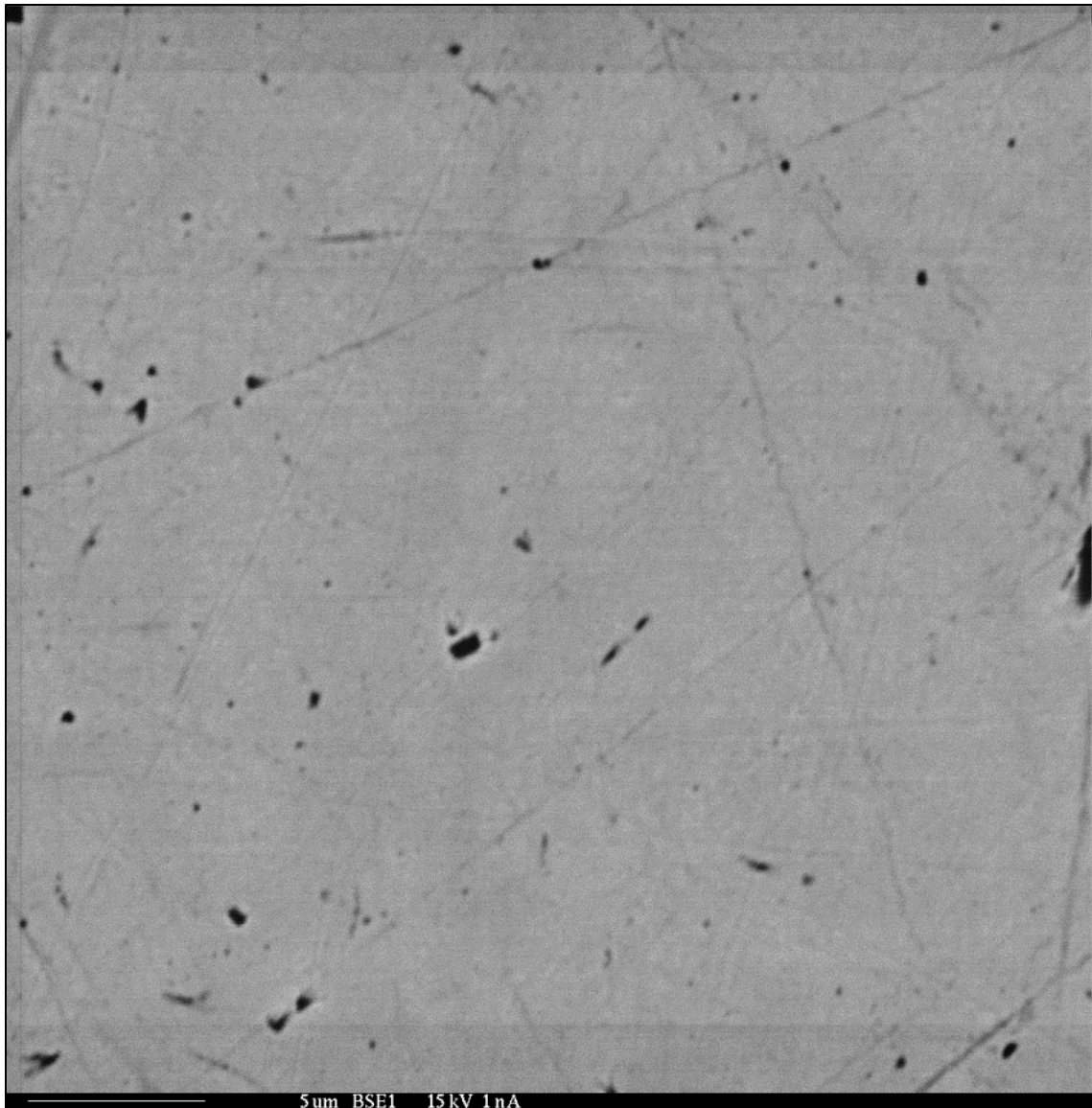
(b) δ-UZr$_2$ phase medium of U-40ZrAC (3000X)

Figure 4–10: Continued.

91
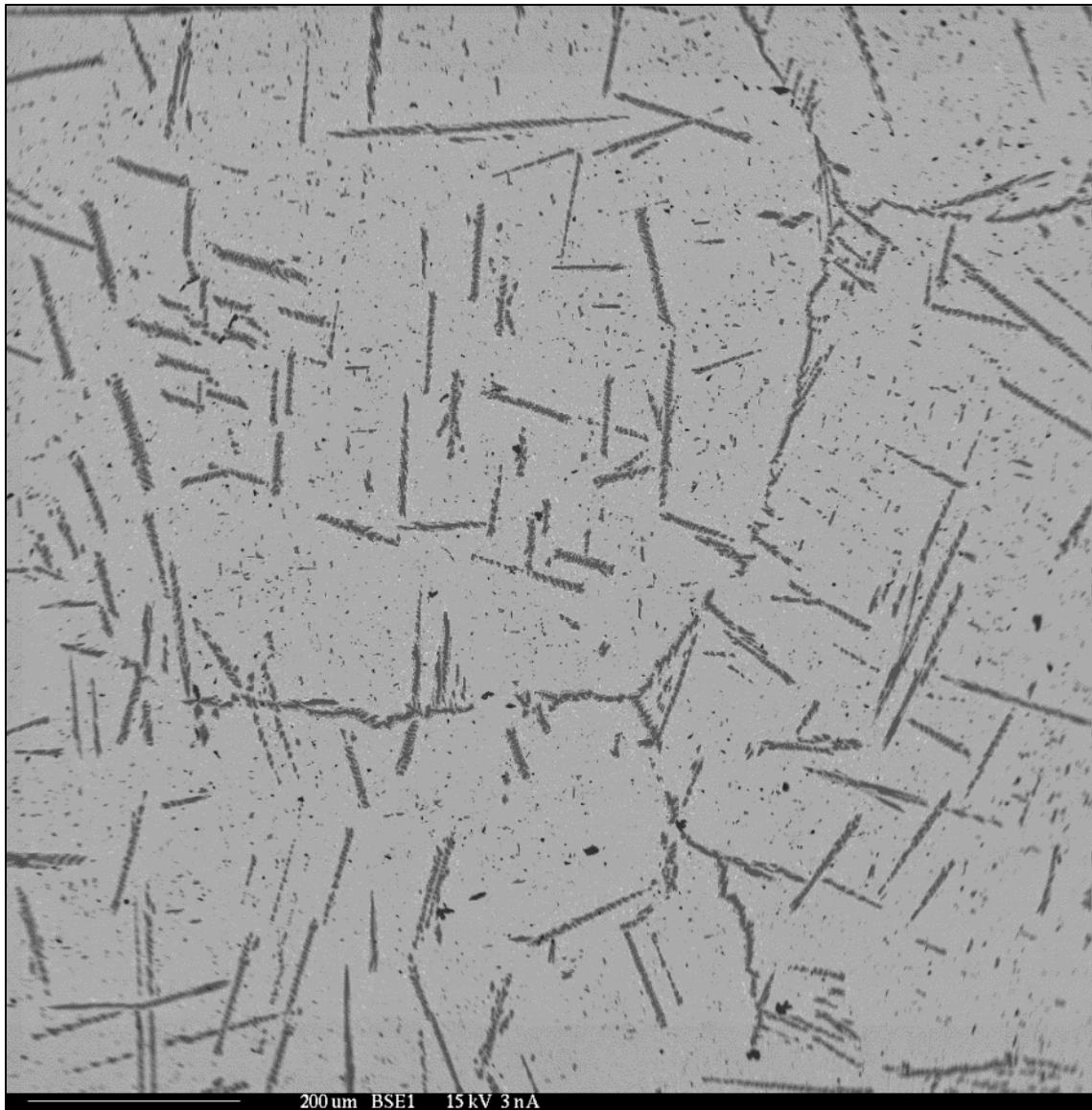
(c) Grain boundaries combined with zirconium precipitates in U-40Zr7d600 (90X)

Figure 4–10: Continued.

92
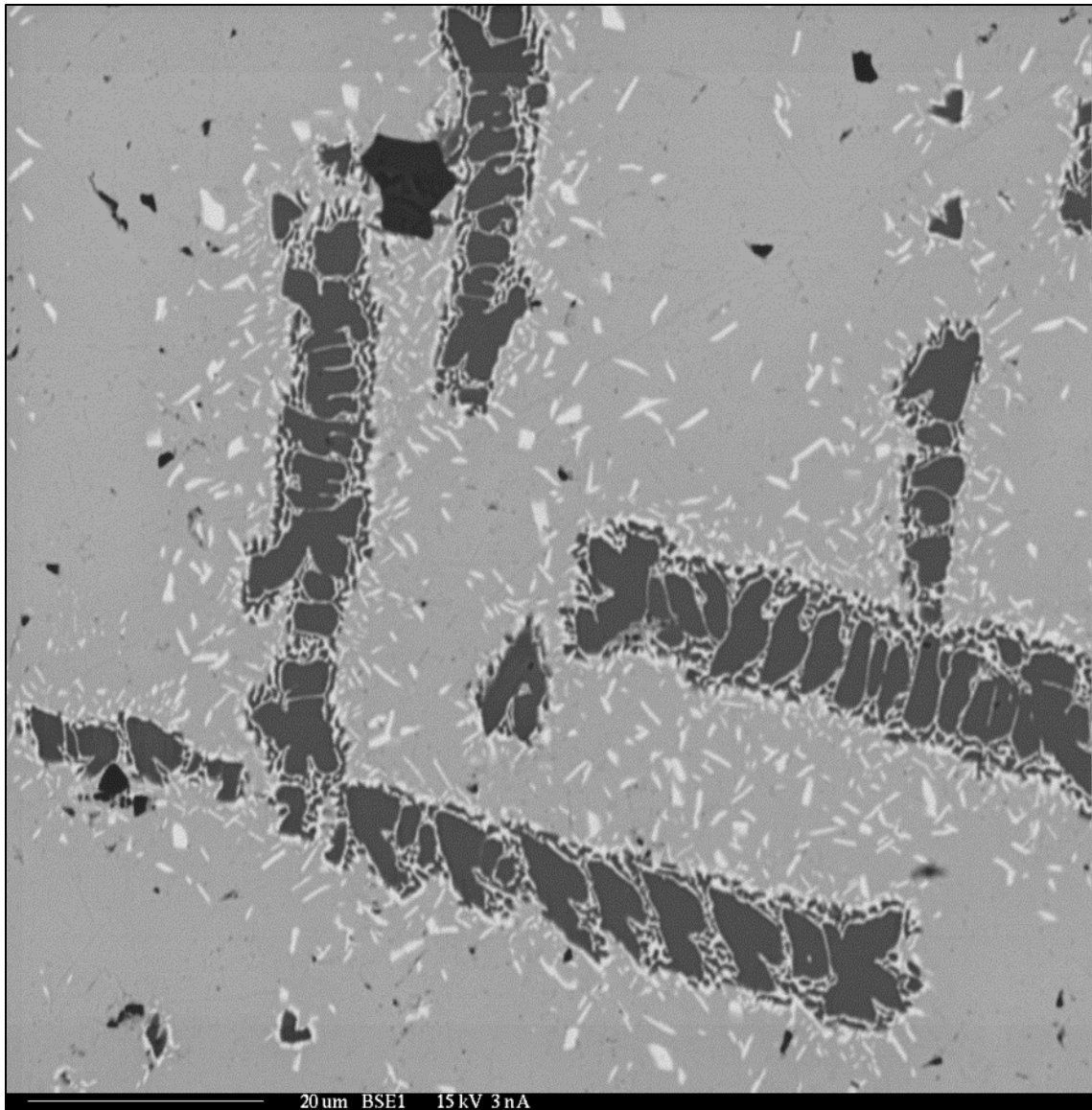
(d) Uranium precipitates adjacent to zirconium precipitates in U-40Zr7d600 (1000X)

Figure 4–10: Continued.
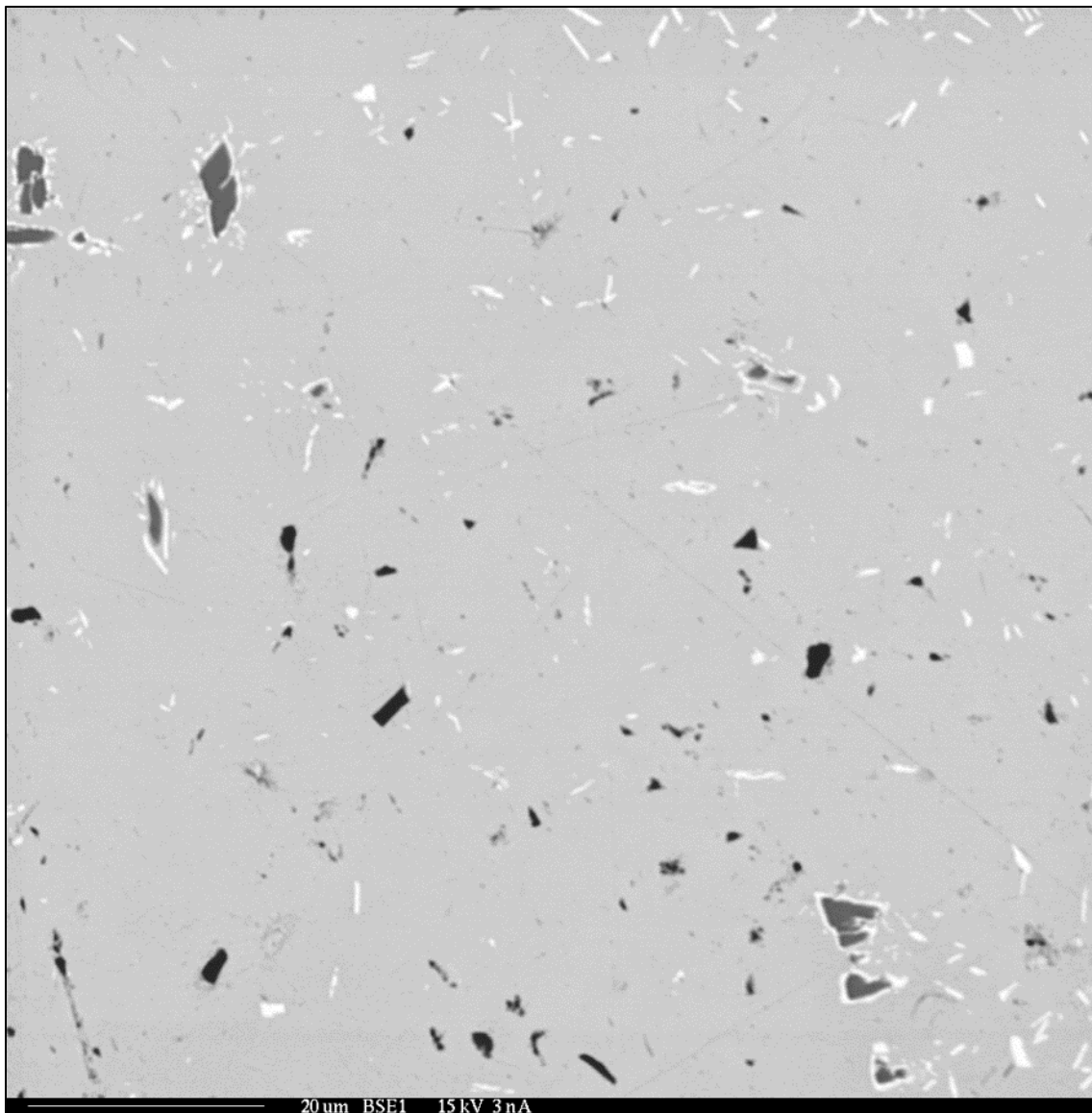
(e) Uranium precipitates apart from zirconium precipitates in U-40Zr7d600 (1000X)

Figure 4–10: Continued.

4.1.2.4 U-50Zr

The BSE images from U-50Zr alloy are presented here (Fig. 4-11) showing the evolution from the as-cast structure to the 7 day annealed structure. The U-50Zr alloy should exhibit a single δ-UZr$_2$ phase following Akabori *et al*. [155], however, it has very similar morphologies to the U-40Zr alloy structures reported in the previous section. A representative area of as-cast U-50Zr alloy is shown in Fig. 4-11(a) and (b). Numerous α-Zr phase precipitates were generally found within δ-UZr$_2$ phase matrix, regardless of the alloy thermal history. The coexistence of α-U, δ-UZr$_2$ and α-Zr phases are also observed in annealed U-50Zr alloy likewise in U-40Zr alloy, as shown in Fig. 4-11(d).

The average composition of the matrix (gray) δ-UZr$_2$ phase measured using WDS was (50.1 ± 1.6) wt% zirconium which almost exactly corresponds to the alloy composition. However, considering the presence of α-Zr phase precipitates, observed alloy samples were obviously sectioned from Zr-enriched part of the cast alloy slug. Uranium-rich (white) precipitates including trace amount of zirconium ($< \sim 1$ at%) were appeared in U-50Zr7d600, likely α-U saturated with zirconium. The precipitates were, however, found only near zirconium precipitates. In other words, scattered precipitates were not independently observed within presumptive δ-UZr$_2$ phase medium, unlike were in U-40Zr. This may be due to the farther compositional distance in U-Zr binary phase diagram between U-50Zr and the (α-U, δ-UZr$_2$) phase region, which extends only up to around stoichiometric composition of δ-UZr$_2$ phase, i.e. ~ 66.7 at% (~ 43.4 wt%) zirconium at low temperatures ($< \sim 400$ °C), following Sheldon's phase diagram.

95
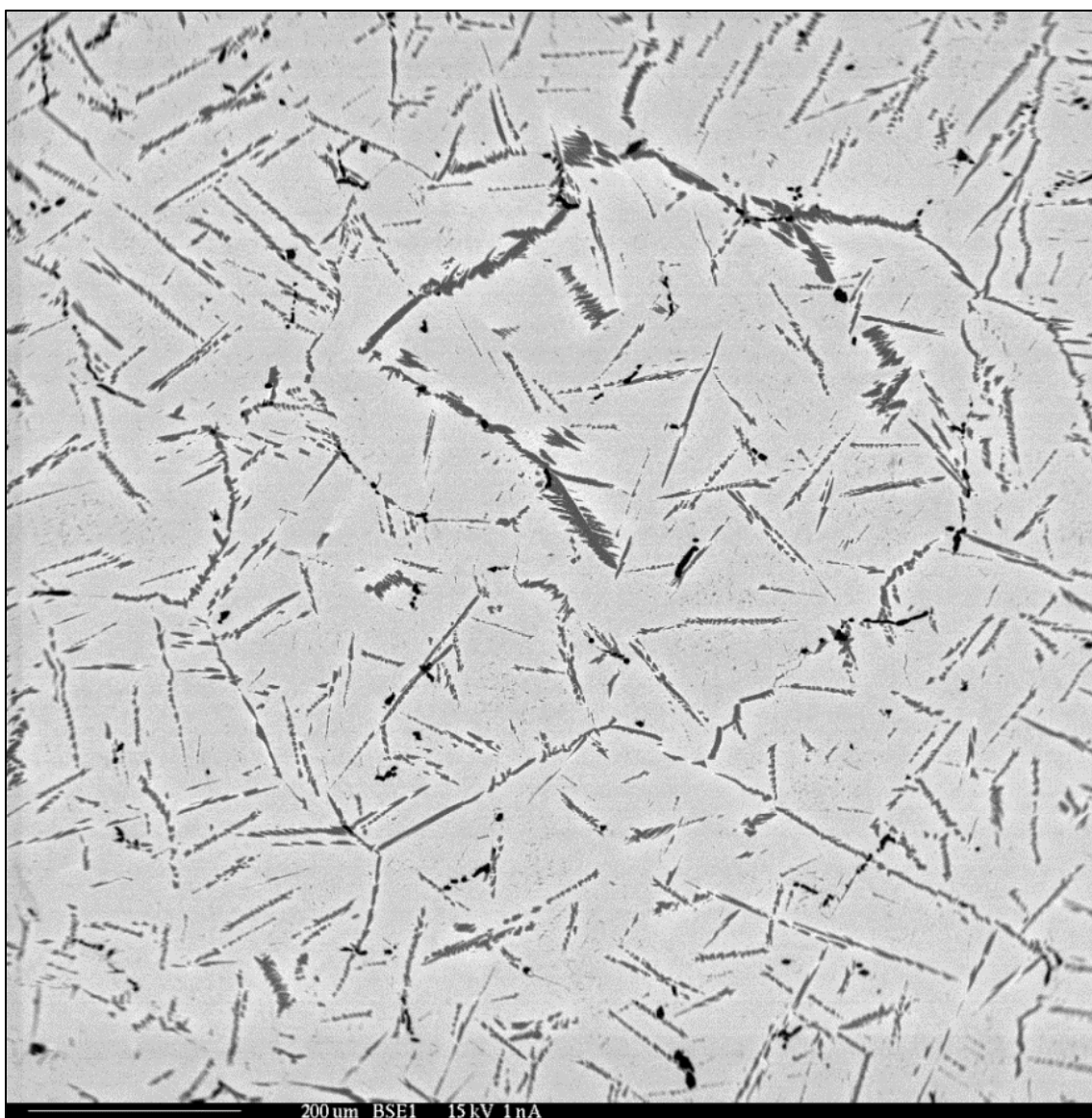
(a) Zirconium precipitates in the bulk of U-50ZrAC (90X)

Figure 4-11: Microstructure evolution of U-50Zr alloy from as-cast to 7d600.
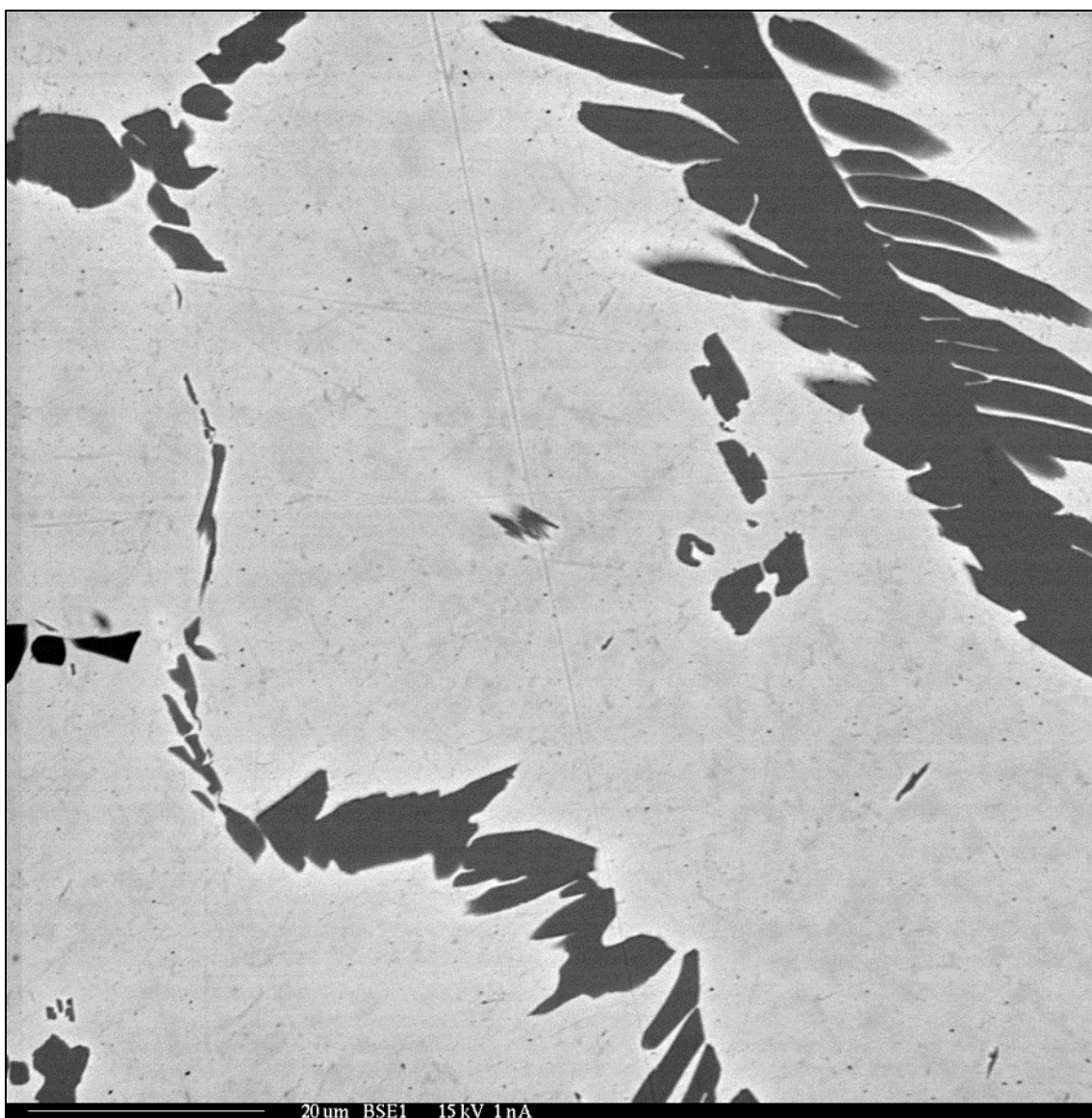
(b) Zirconium dendrites within δ-UZr$_2$ matrix phase in U-50ZrAC (1000X)

Figure 4–11: Continued.
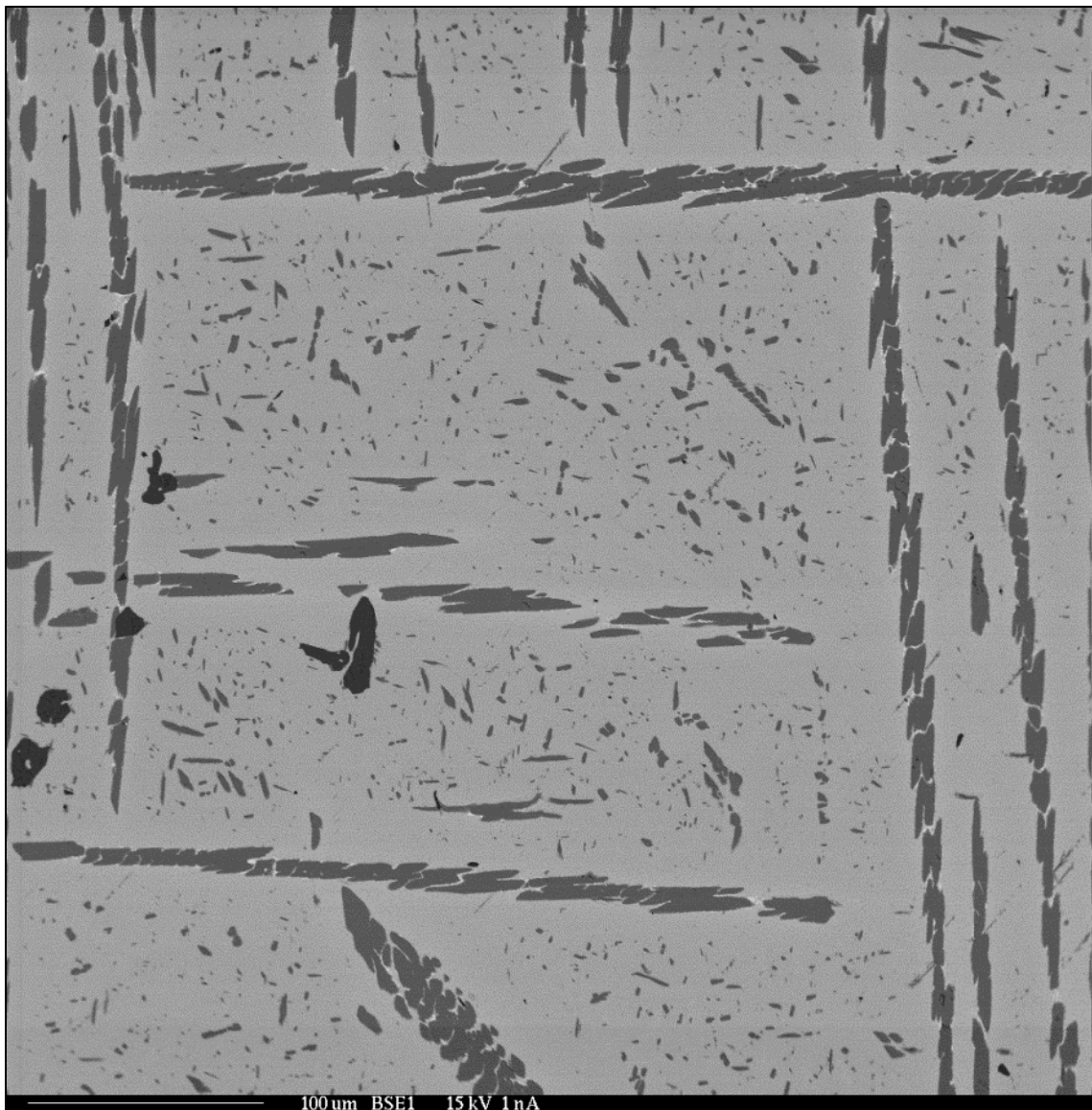
(c) U-50Zr7d600 (200X)

Figure 4–11: Continued.
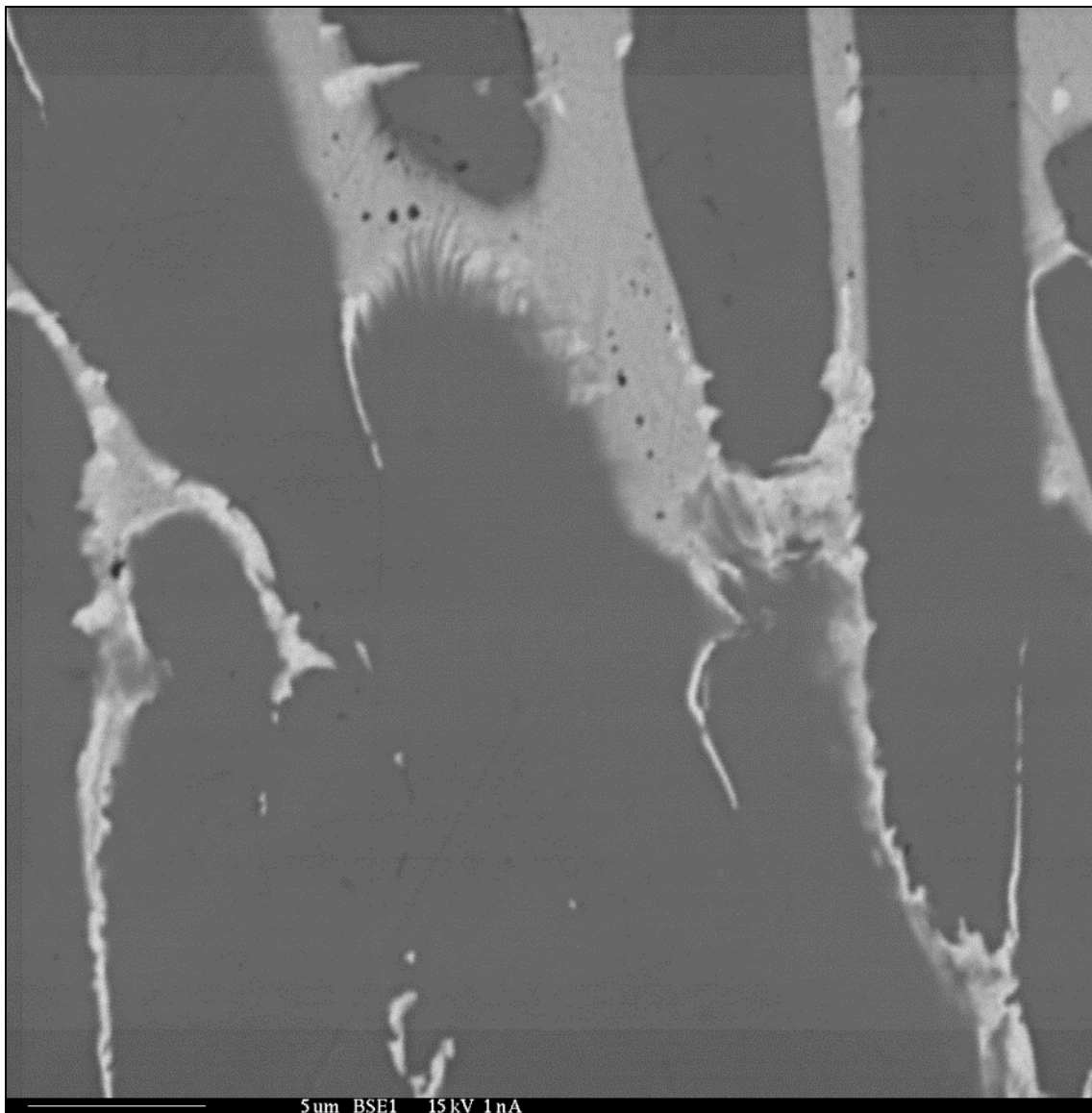
(d) Uranium-haloed zirconium precipitates in U-50Zr7d600 (3000X)

Figure 4–11: Continued.

4.2 Phase Transformation Properties of U-Zr Alloys

The phase transformation behavior of the fabricated U-Zr alloys was investigated up to 1000 °C using DSC-TGA. The results from this study are presented in this section. The alloy specifications of the examined samples are given in Table 4-2. It is noteworthy that an additional set of samples was annealed to 28 days at 600 °C to attempt to achieve reasonably-complete equilibrium.

Table 4-2: DSC-TGA experimental matrix.

Metal / Alloy	As-cast	Annealing time (day)									
		1			3			7			28
		Annealing temperature (°C)									
		500	550	600	500	550	600	500	550	600	600
Uranium	O	-	-	-	-	-	-	-	-	-	-
U-0.1Zr	O	-	-	-	-	-	-	-	-	-	-
U-2Zr	O	-	-	O	O	-	O	-	O	O	O
U-5Zr	O	-	-	O	-	-	O	-	-	O	O
U-10Zr	O	-	-	O	-	-	O	-	-	O	O
U-20Zr	O	-	-	O	-	-	O	-	-	O	O
U-30Zr	O	-	-	O	-	-	O	-	-	O	-
U-40Zr	-	-	-	-	-	-	-	-	-	O	-
U-50Zr	O	O	-	O	-	-	O	-	O	O	O
Zirconium	O	-	-	-	-	-	-	-	-	-	-

4.2.1 DSC Calibration

The melting temperatures and heats of fusion for standard materials whose melting points range from 157 °C to 1064 °C were measured to generate temperature and sensitivity calibration files. The phase transformation temperatures and enthalpies of unalloyed uranium and zirconium samples were also measured using the calibration files to confirm their reliability.

4.2.1.1 Standard Materials

The measured DSC data from seven standard materials are given in Fig. 4-12; the standards used were materials indium, tin, bismuth, zinc, aluminum, silver, and gold. The dashed lines in the figures represent differential DSC (DDSC) curves, essentially the derivative of the directly measured DSC changes that are used to ascertain the temperature ranges of the transformations. The measured melting temperatures and heats of fusion for the standards are summarized in Table 4-3 along with comparisons to reference values. Calculated sensitivity values used for further sample measurements are also included in the table.
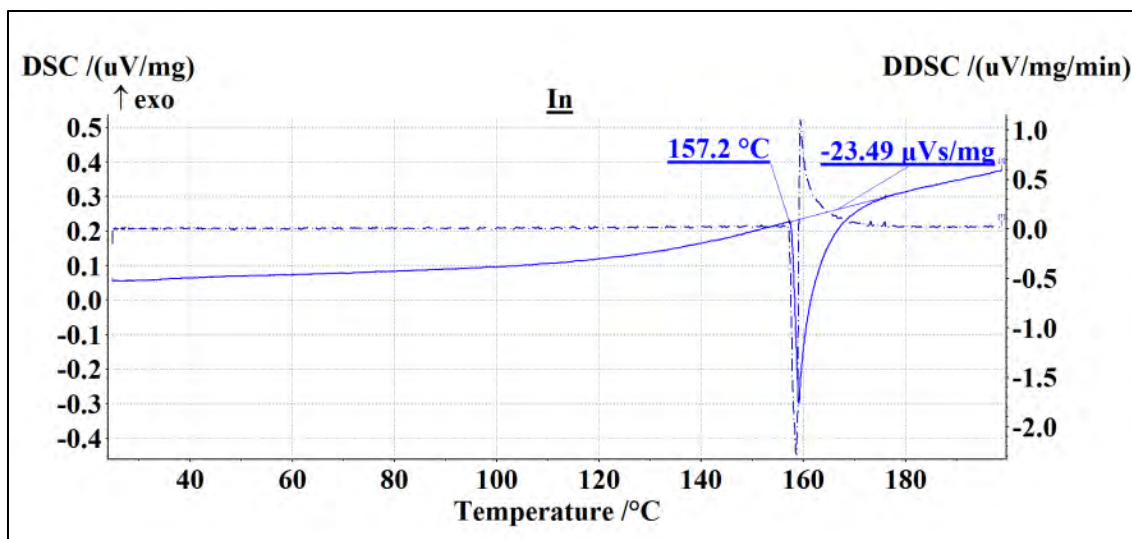
(a) Indium
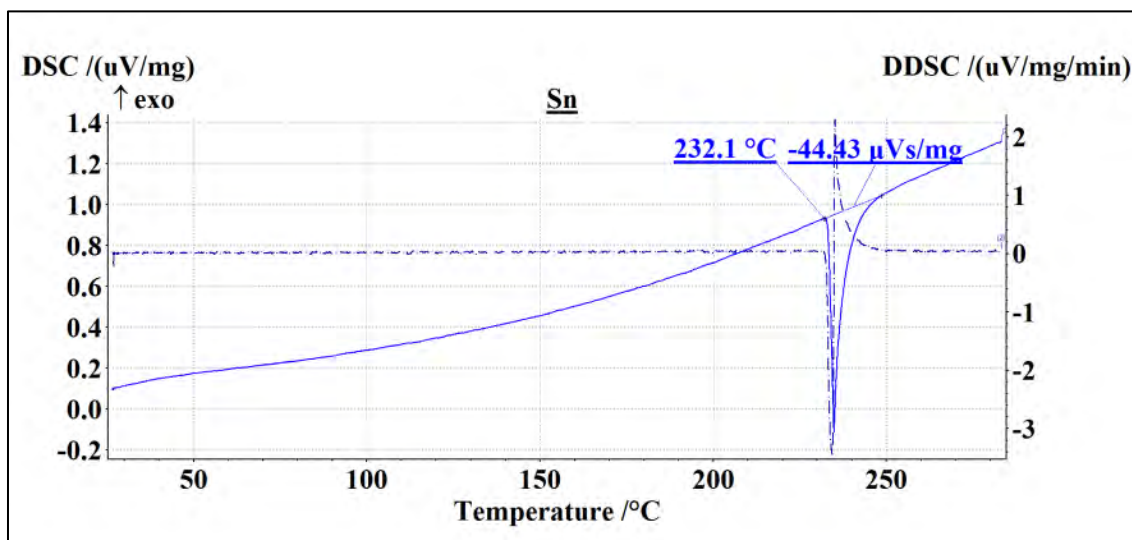
(b) Tin

Figure 4-12: Calibration measurements of seven standard materials (In, Sn, Bi, Zn, Al, Ag, and Au).
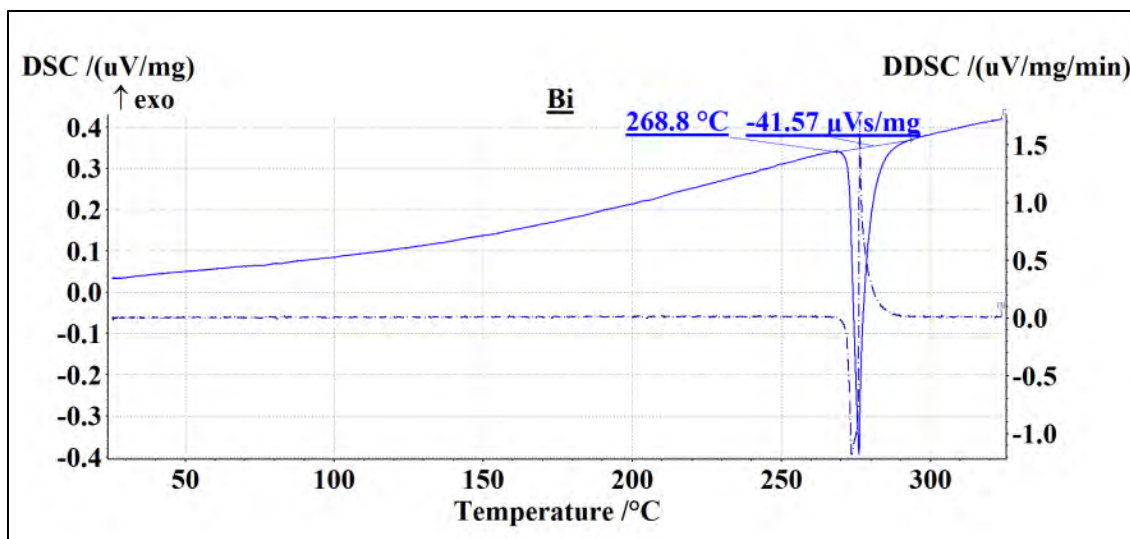
(c) Bismuth
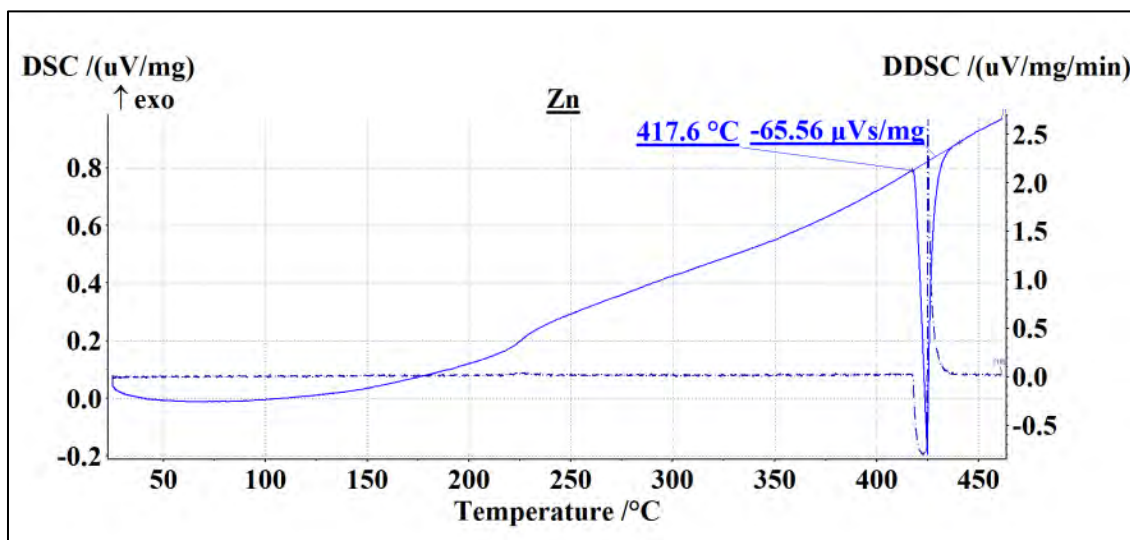
(d) Zinc

Figure 4-12: Continued.
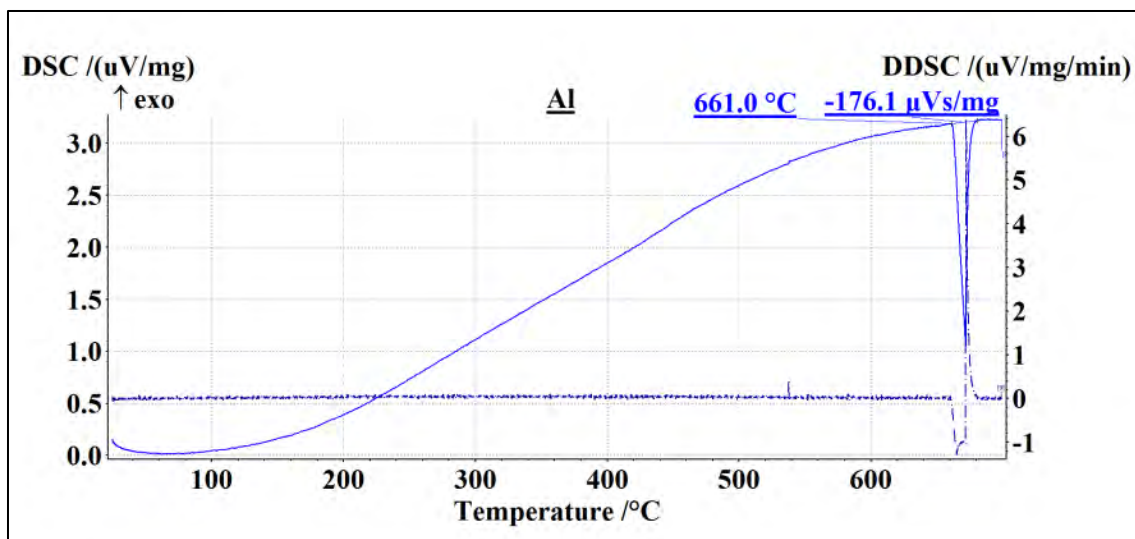
(e) Aluminum
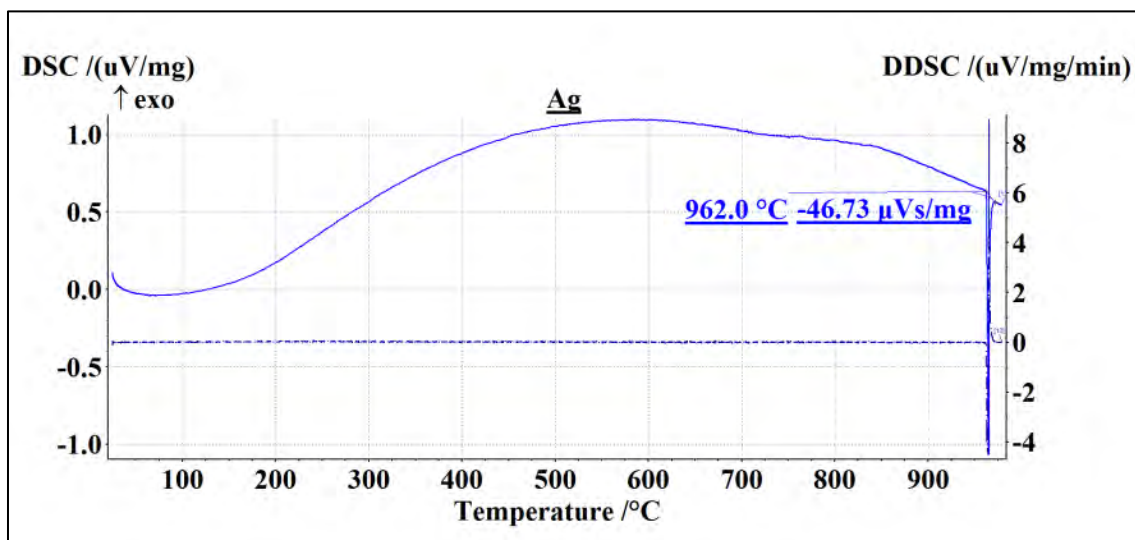
(f) Silver

Figure 4-12: Continued.
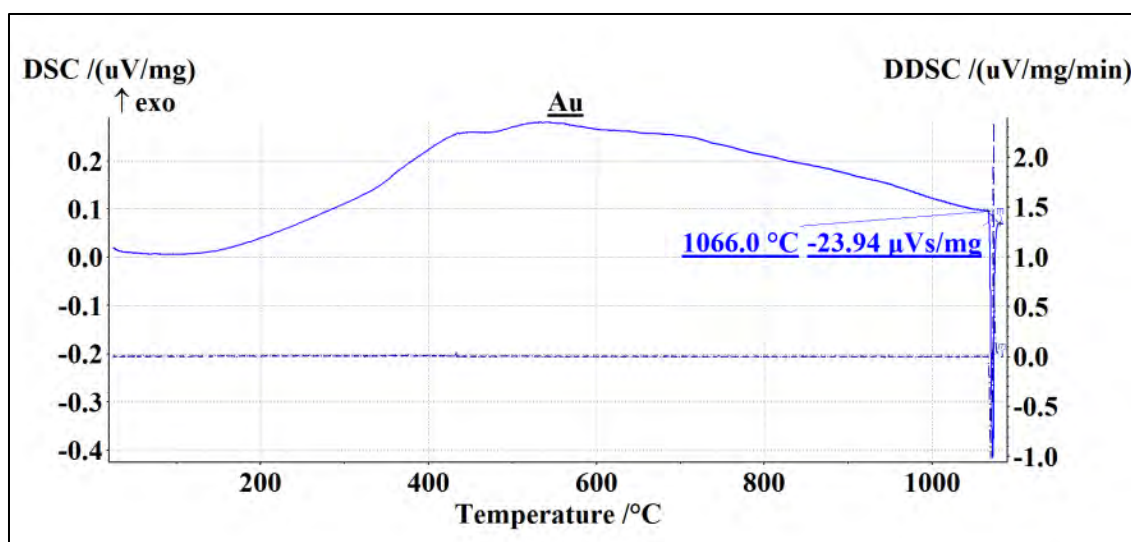
(g) Gold

Figure 4-12: Continued.

Table 4-3: DSC calibration data for STA-409PC.

Element	Atomic Weight (g/mol)	Melting point		Heat of fusion (ΔH)			Sensitivity
		Ref. (°C)	Exp. (°C)	Reference [136]		Exp.	
				(J/mol)	(J/g)	(µVs/mg)	(mVs/J)
In	114.82	156.6	157.2	3280	28.57	23.49	0.82
Sn	118.71	232.0	232.1	7195	60.61	44.43	0.73
Bi	208.98	271.4	268.8	11300	54.07	41.57	0.77
Zn	65.39	419.6	417.6	7320	111.94	65.56	0.59
Al	26.98	660.5	661.0	10700	396.56	176.1	0.44
Ag	107.87	961.9	962.0	11300	104.76	46.73	0.45
Au	196.97	1064.4	1066.0	13000	66.00	23.94	0.36

4.2.1.2 Uranium and Zirconium

The heat of fusion of aluminum whose melting temperature (660 °C) corresponds to the majority of solid phase transformations in U-Zr binary alloy system are over tenfold larger than transformation enthalpies in U-Zr binary system. Therefore uranium was considered as an ideal and necessary alternative standard measurement to give better reference enthalpy values than aluminum. The DSC heating curves from uranium and zirconium are shown in Figs. 4-13 and 4-14.

As shown in Table 4-4, the transformation enthalpies of uranium, measured using the calibration files generated from the standard reference materials, are well matched with the reference values published in literatures [136, 150]. On the other hand, the transformation enthalpy for zirconium was ~65 % of the reference value, most likely due to aggravated sample oxidation at the transformation temperature (~860 °C) indicated by mass increase measured using TGA.

Sample oxidation at relatively higher temperatures such as 860 °C were of a lesser concerned for this study, since all transformations observed later in the U-Zr binary alloy system occurred below 720 °C. However, oxidation effect was accounted by considering effective sample mass calculated by subtracting oxidized fraction of sample from initial sample mass. Compensated enthalpies still underestimated to a degree because an oxidized sample surface will partially absorb transformation heat. The oxide layer may also hinder heat transfer from the sample to the crucible. Therefore, partial transformation heat could escape the system not being measured.

106
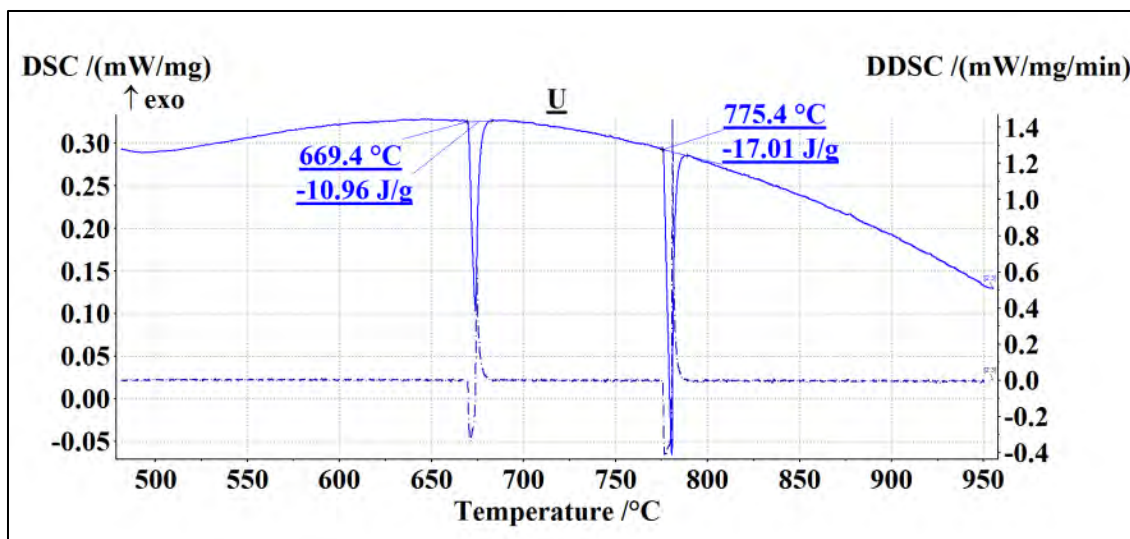
Figure 4-13: Transformation temperatures and enthalpies of uranium (measured using standard calibration files).
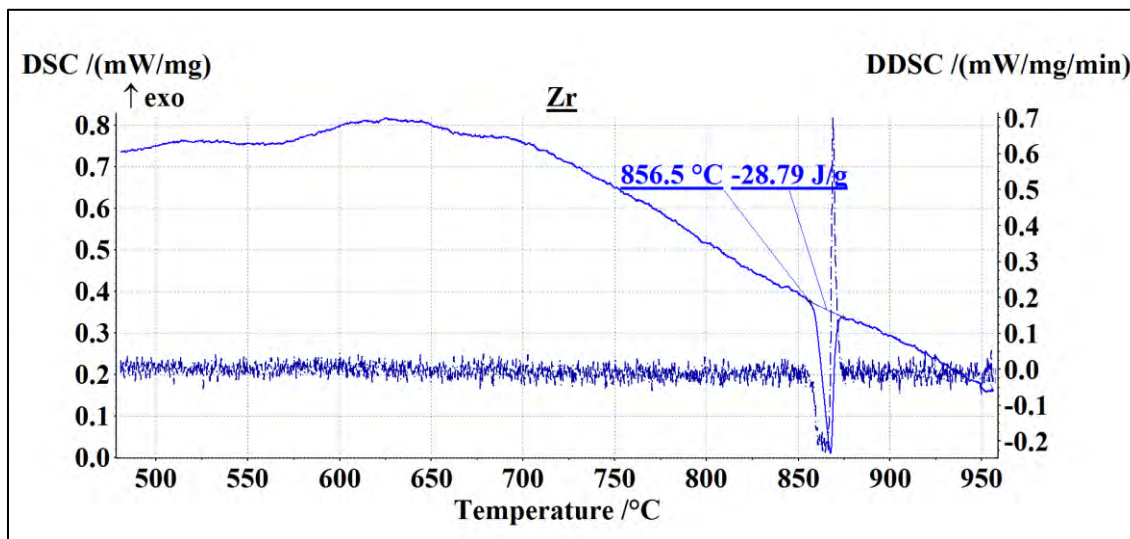
Figure 4-14: Transformation temperatures and enthalpies of zirconium (measured using standard calibration files).

Table 4-4: Phase transformation temperatures and enthalpies of uranium and zirconium.

Element	Atomic Weight (g/mol)	Trans. temp. (T_s)			Trans. enthalpy (ΔH)			$\dfrac{\Delta H_{exp}}{\Delta H_{ref}}$
		No.	Ref. (°C)	Exp. (°C)	Reference [136]		Exp.	
					(J/mol)	(J/g)	(J/g)	(%)
U	238.03	1	669	669	2791	11.73	10.96	94
		2	776	775	4757	19.98	17.01	85
Zr	91.22	1	863	857	4015	44.01	28.79	65

4.2.2 As-cast Alloys

As-cast alloys were first measured to be references for annealed alloys; nevertheless those alloys would have non-equilibrium phases except for single phase alloys, U-0.1, 40, and 50ZrAC. Considering the degree of DSC curve evolution from as-cast alloys to different time period annealed alloys, it was decided whether longer annealing brings further change, or not, in alloy crystal structure in thermophysical standpoint. All "first" (initial heating ramp) DSC heating curves obtained from as-cast alloys are shown in Fig. 4-15.
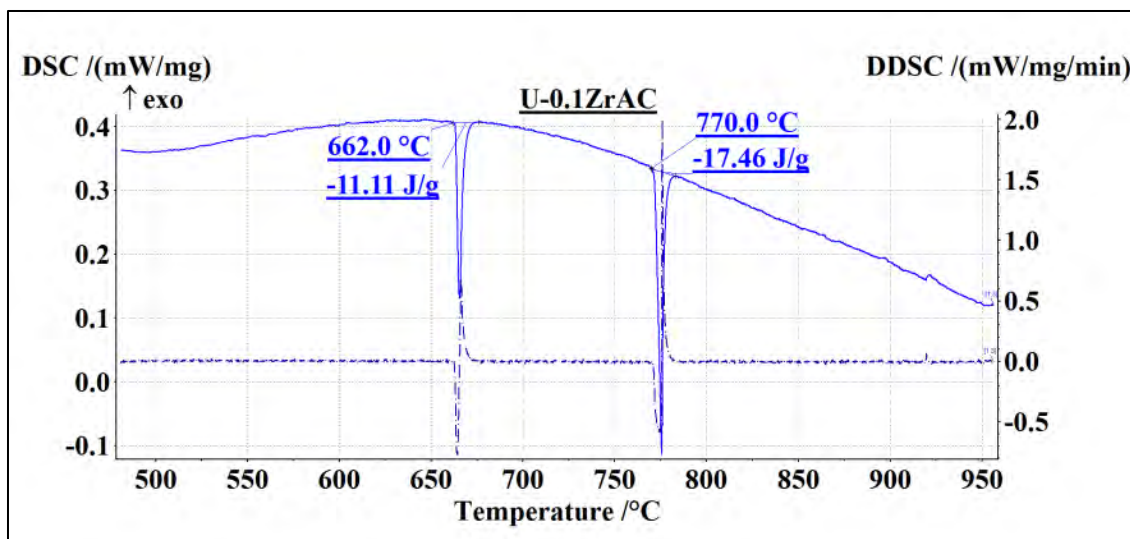
(a) U-0.1ZrAC
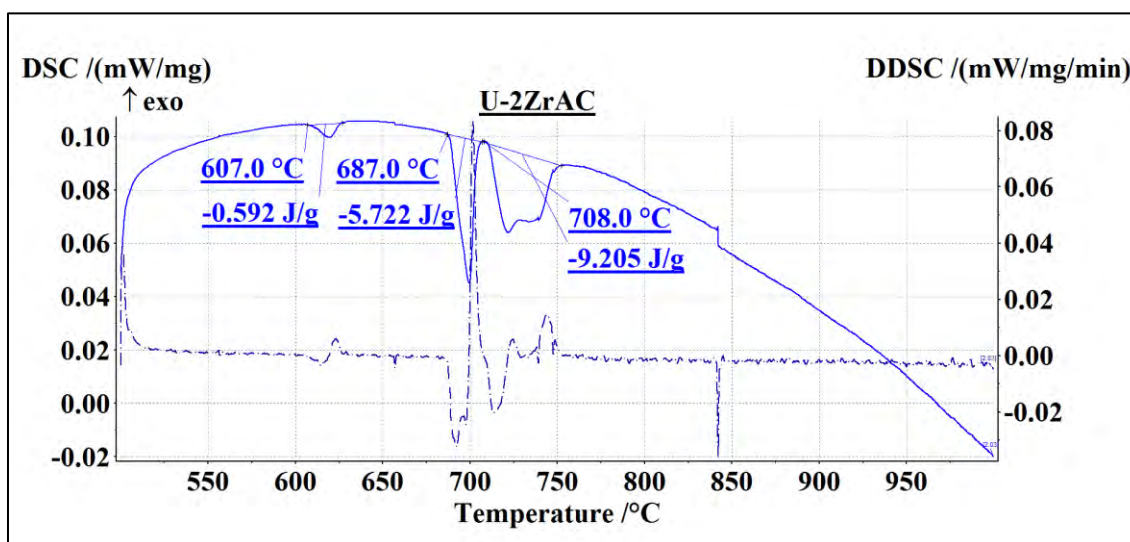
(b) U-2ZrAC

Figure 4-15: DSC heating curves from as-cast U-Zr alloys.
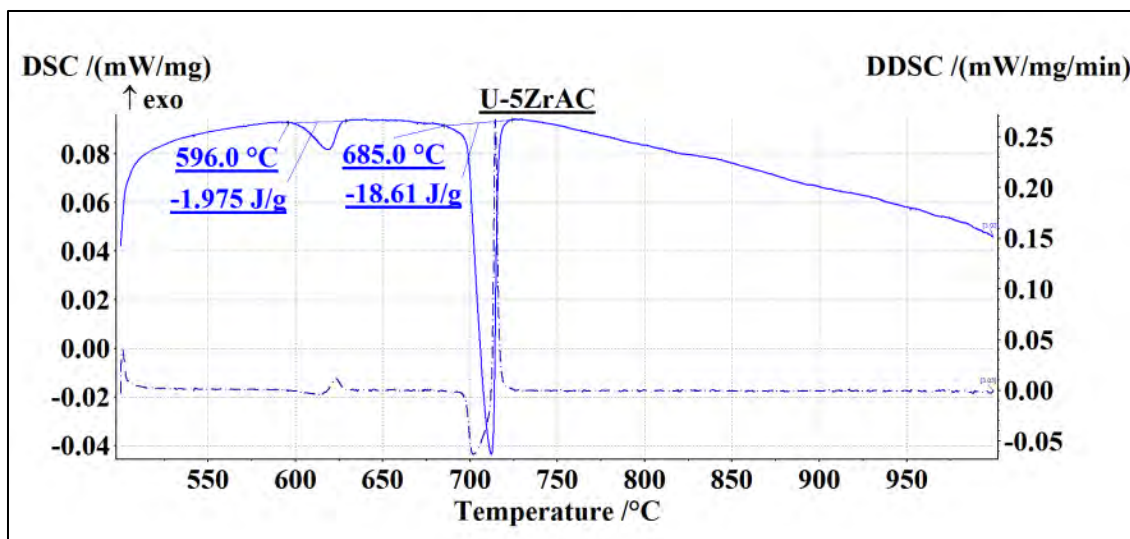
(c) U-5ZrAC
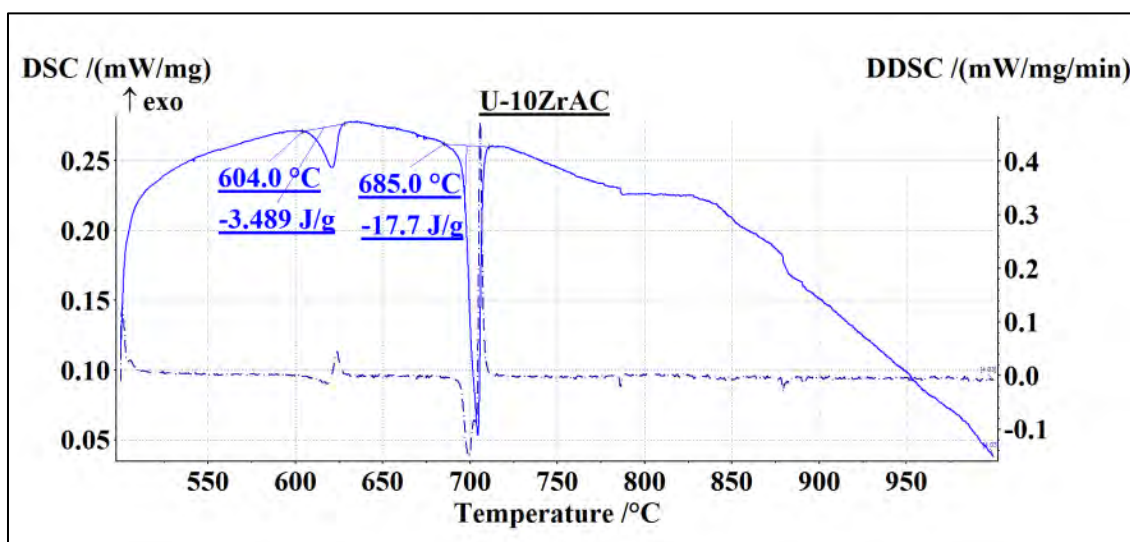
(d) U-10ZrAC

Figure 4-15: Continued.
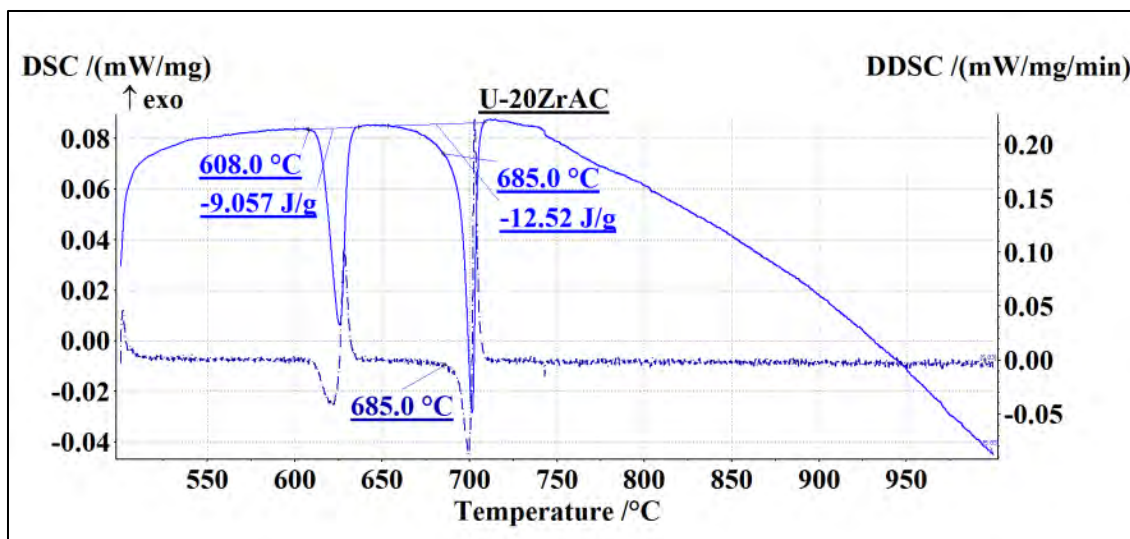
(e) U-20ZrAC

(f) U-30ZrAC

Figure 4-15: Continued.

111

DSC /(mW/mg)   U-50ZrAC   DDSC /(mW/mg/min)

↑ exo

612.0 °C
-25.32 J/g
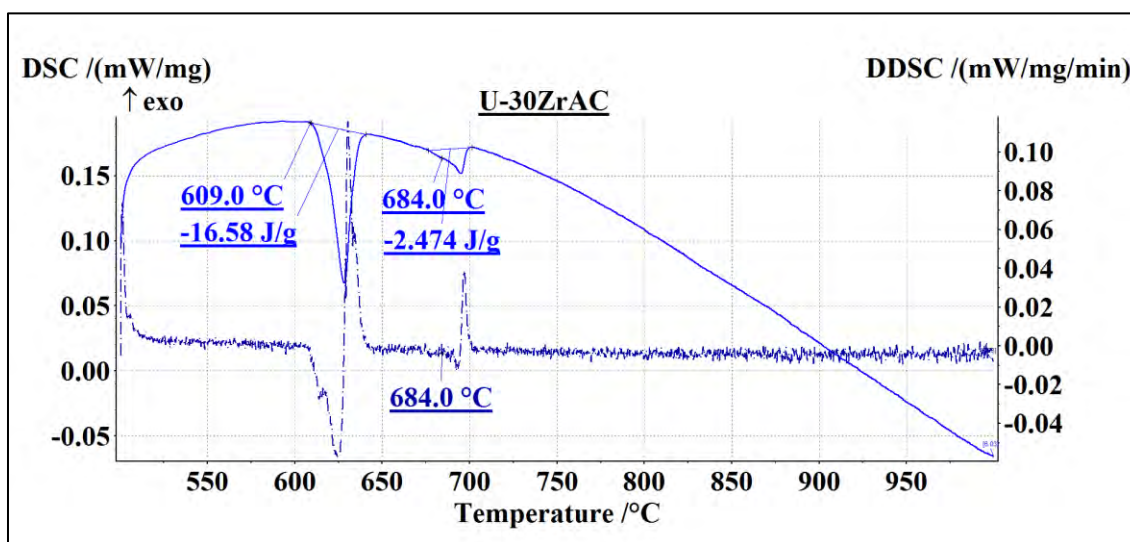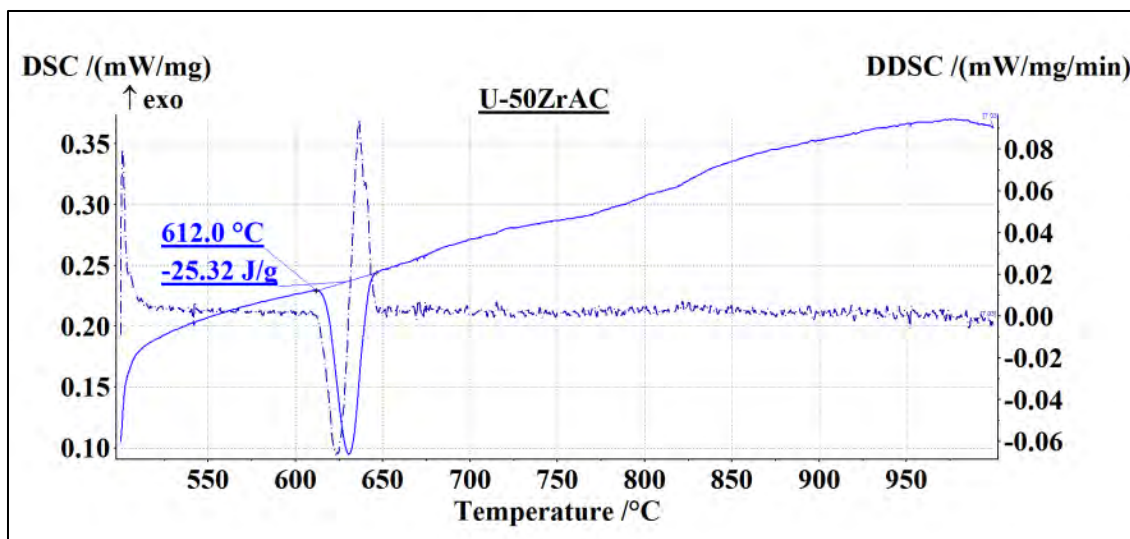
Temperature /°C

(g) U-50ZrAC

Figure 4-15: Continued.

4.2.3 Annealed Alloys

U-Zr alloys annealed for 1, 3, 7, and 28 day(s) at 600 °C were measured to trace the evolution of transformation temperatures and enthalpies verses annealing time. Other annealing temperatures, 500 and 550 °C were also tested for selected alloys. However, it became apparent that those temperatures are too low to achieve equilibrium changes within 7 days.

Only the initial heating DSC curves are displayed for each composition per thermal history from 500 °C to 1000 °C are given in this section, although some selected alloy samples were repeatedly cycled within the temperature range to observe oxidation effects and cooling behavior.

112

The given DSC curves in this section were selected among multiple measurements of alloys having identical composition and thermal history after at least two independent DSC samples exhibited reasonably accurate matches in terms of numbers, temperatures and enthalpies of phase transformations.

4.2.3.1 U-2Zr

The DSC heating curve for U-2Zr1d600 is given in Fig. 4-16. A combined peak near 720 °C was apparent indicating that 1 day annealing is not enough to achieve equilibrium. From some U-2Zr3d600 samples, the first peak often appeared at ~547 °C, as shown in Fig. 4-17(a). This peak at abnormal temperature was only obtained from three samples taken from a particular button of annealed U-2Zr alloy. Otherwise the first peak in DSC heating curves from the alloy was consistently obtained near 600 °C as shown in Fig. 4-17(b). Since the temperatures were slightly below the annealing temperature, U-2Zr3d500 and 550 were also tested after regenerating the calibration files. However, the obtained transformation temperatures were unchanged, regardless of annealing temperature, as shown in Fig. 4-18. Also in the figure, the ineffectiveness of annealing temperatures below 600 °C to fully anneal the as-cast alloy is clearly shown from the third peak at ~720 °C.

The combined peak feature disappeared from the alloys annealed for longer periods, U-2Zr7d600 and 28d600, as shown in Fig. 4-19. It is interesting to note from the TEM experiments in Section 4.4 that 7 days of annealing was assumed as enough to

113

fully anneal the alloys at RT, since the two DSC curves in Fig. 4-19 are practically identical.
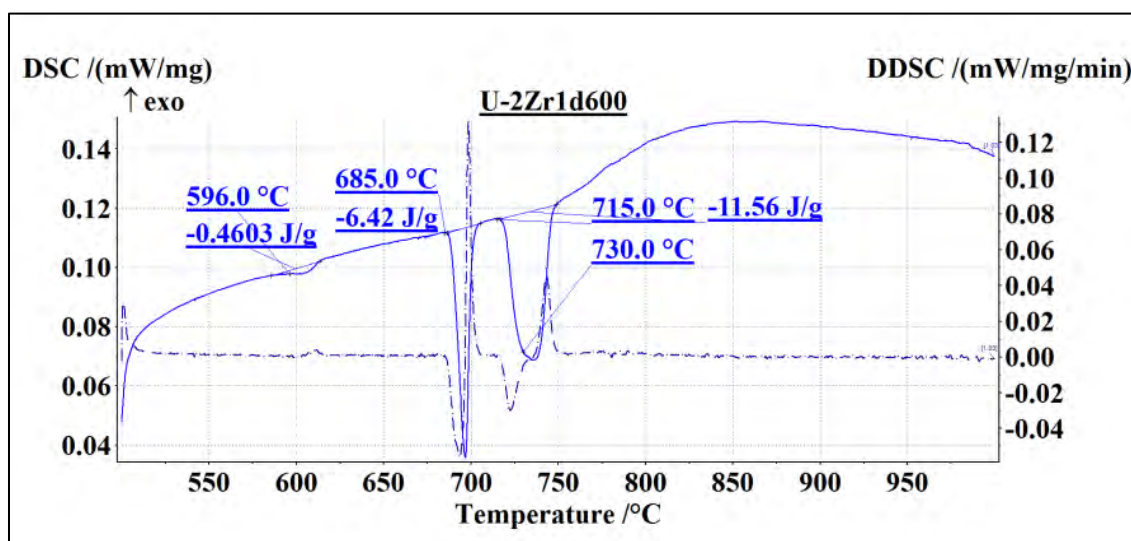
Figure 4-16: DSC heating curve from U-2Zr1d600.
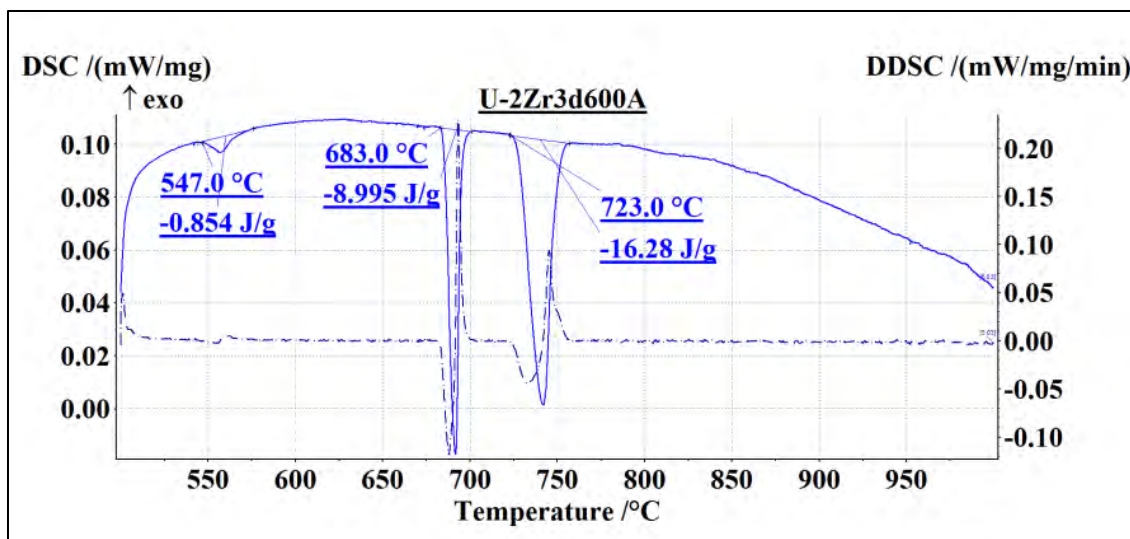
(a) U-2Zr3d600A (aberration)
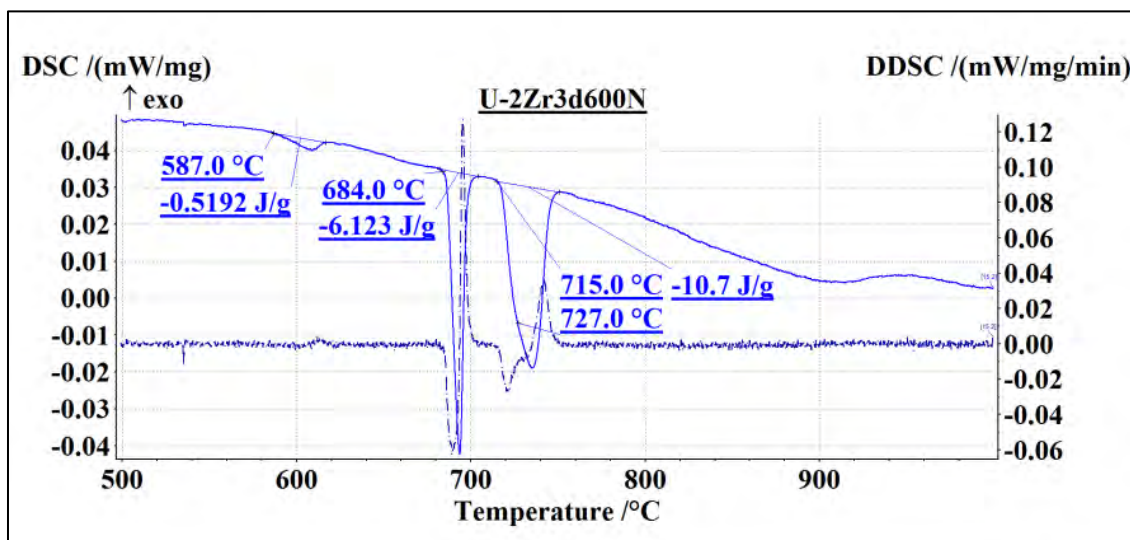
(b) U-2Zr3d600N (normal)

Figure 4-17: DSC heating curves from U-2Zr3d600.
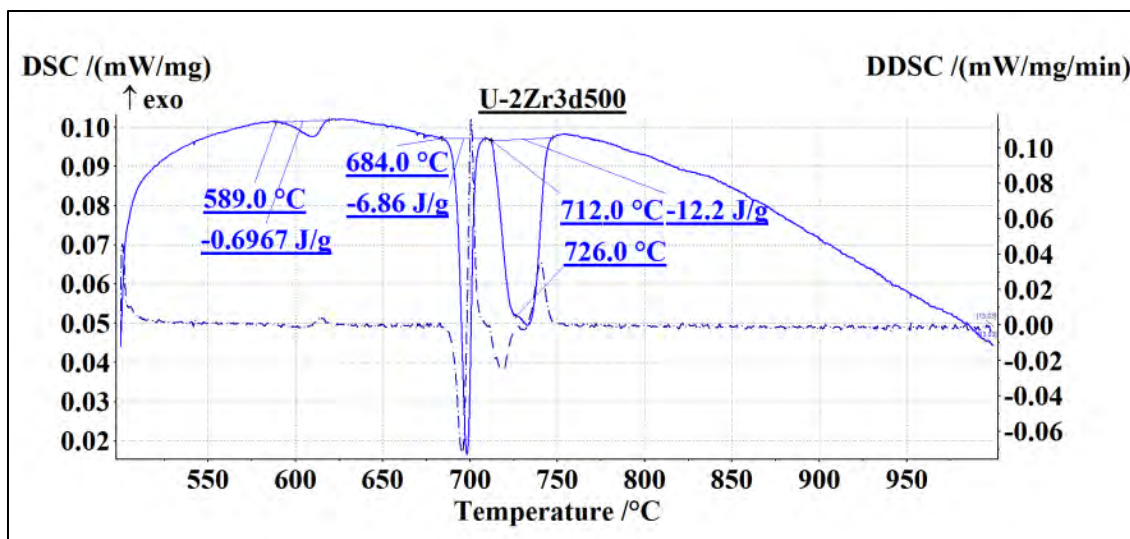
(a) U-2Zr3d500
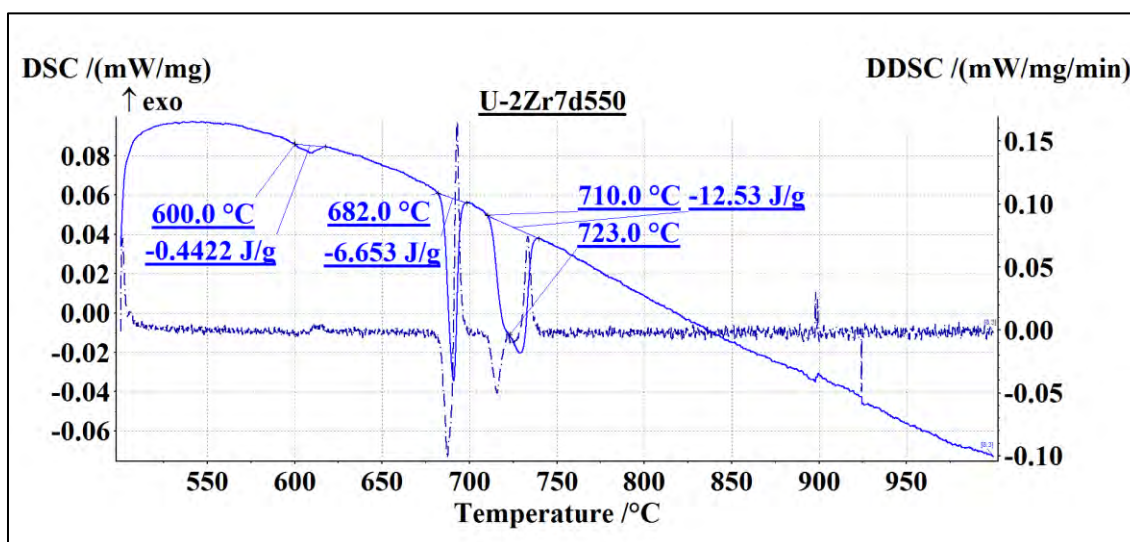
(b) U-2Zr7d550

Figure 4-18: DSC heating curves from low temperature annealed U-2Zr alloys.

116
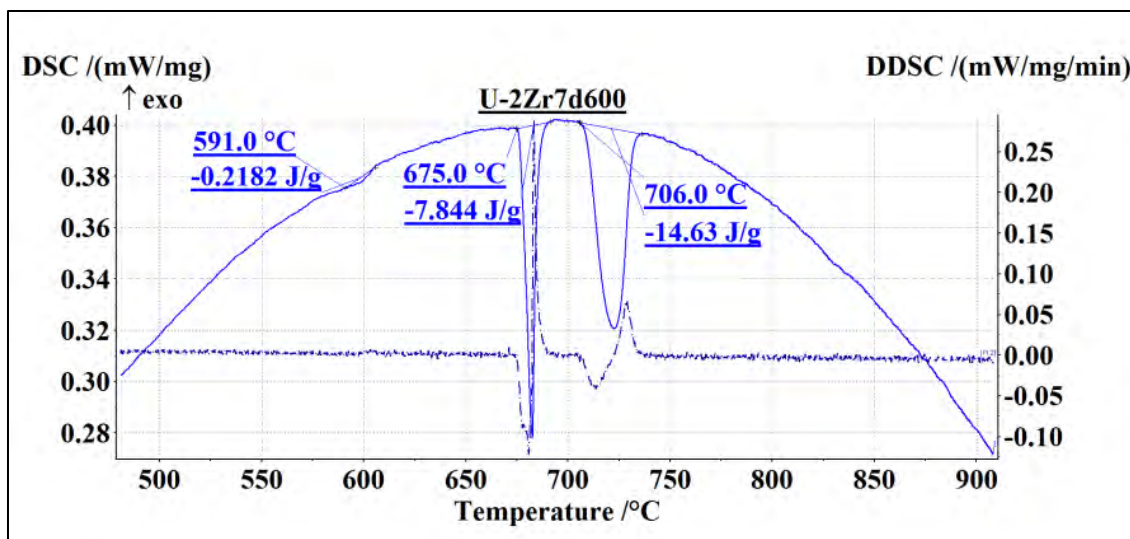
(a) U-2Zr7d600
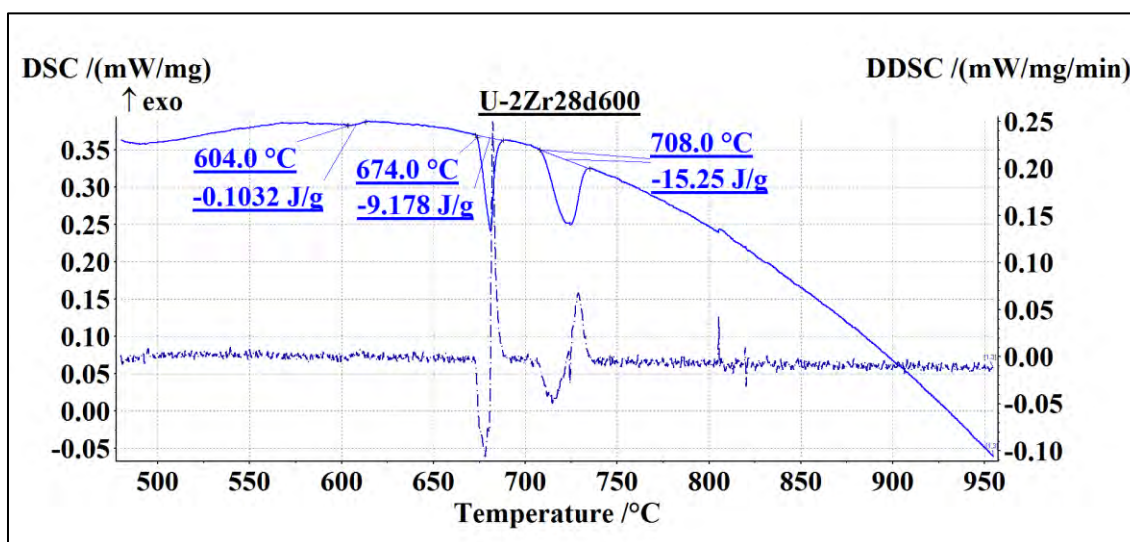
(b) U-2Zr28d600

Figure 4-19: DSC heating curves from long term annealed U-2Zr alloys.

4.2.3.2 U-5Zr

Figure 4-20 shows that the DSC heating curves from the annealed U-5Zr alloys, which exhibit basically identical behavior with the annealed U-2Zr alloys, except the sizes of the peaks, i.e. phase transformation enthalpies. The consistent matches between the phase transformation temperatures and the number of phase transformations for the two alloys affirm that the presence of the three isotherms in U-rich part of U-Zr binary phase diagram, even though the measured second phase transformation temperatures are not matched with both of the two U-Zr binary phase diagrams given in Figs. 2-2 and 2-3.
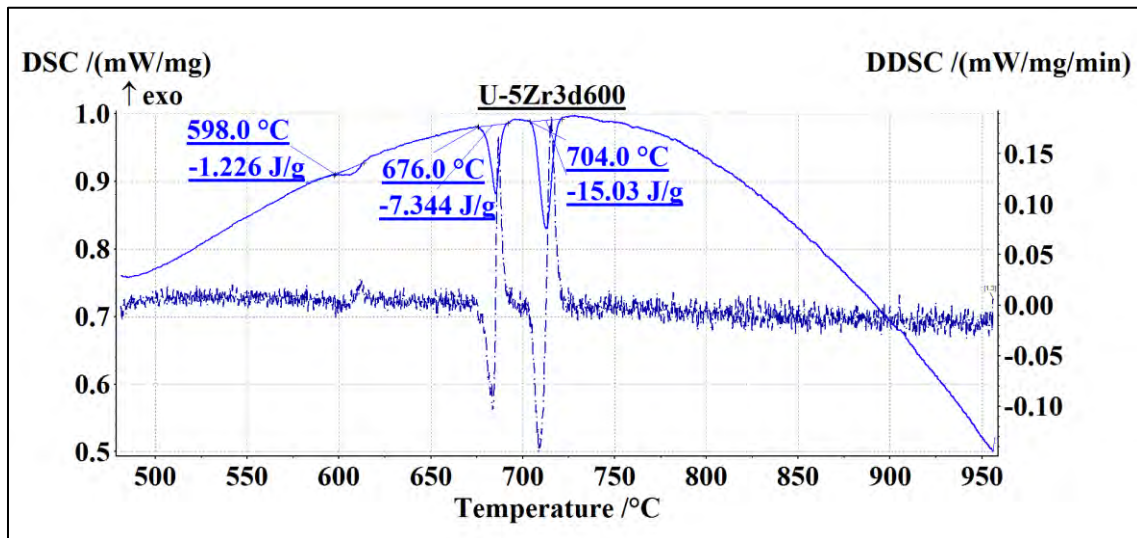
(a) U-5Zr3d600

Figure 4-20: DSC heating curves from annealed U-5Zr alloys.
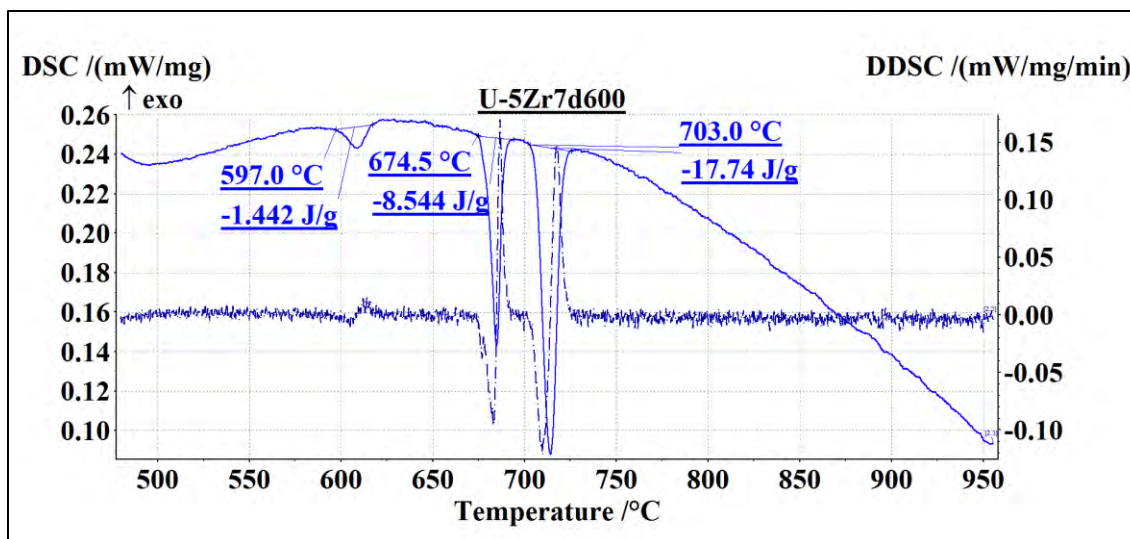
(b) U-5Zr7d600
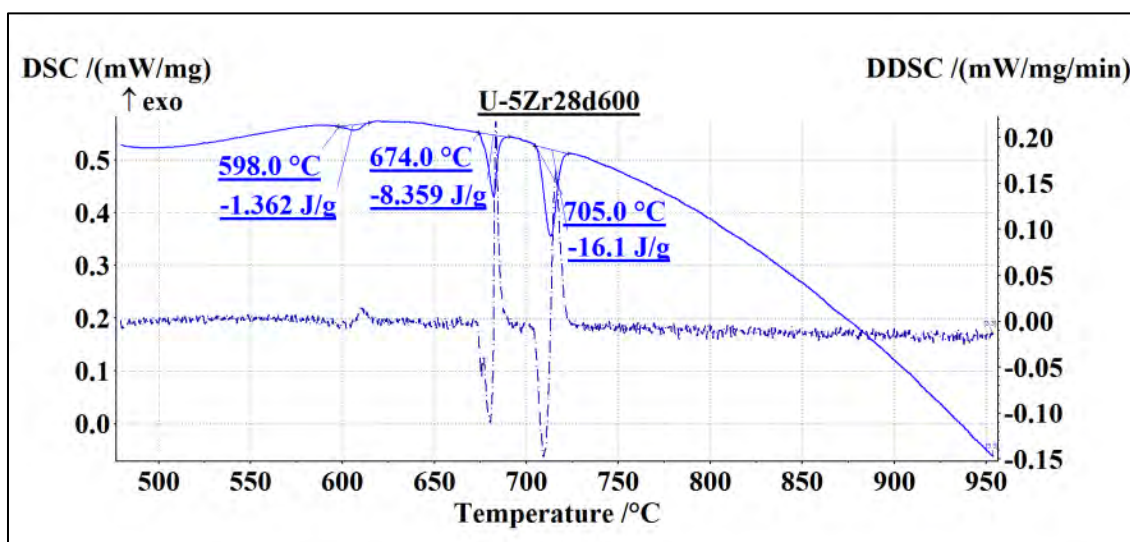
(c) U-5Zr28d600

Figure 4-20: Continued.

119

4.2.3.3 U-10Zr

The DSC heating curves from the annealed U-10Zr alloys are shown in Fig. 4-21. It appears in Fig. 4-21 that number of phase transformations (peaks) in the DSC heating curves from annealed U-10Zr alloys varied with annealing time. However, this was revealed to be due to different composition of each DSC sample of U-10Zr alloy from statistical BSE image analysis. The irrelevance of annealing time to peak number change was assured from disappearance of third peak in 7 day annealed sample, while 28 day annealed sample again exhibited the peak.
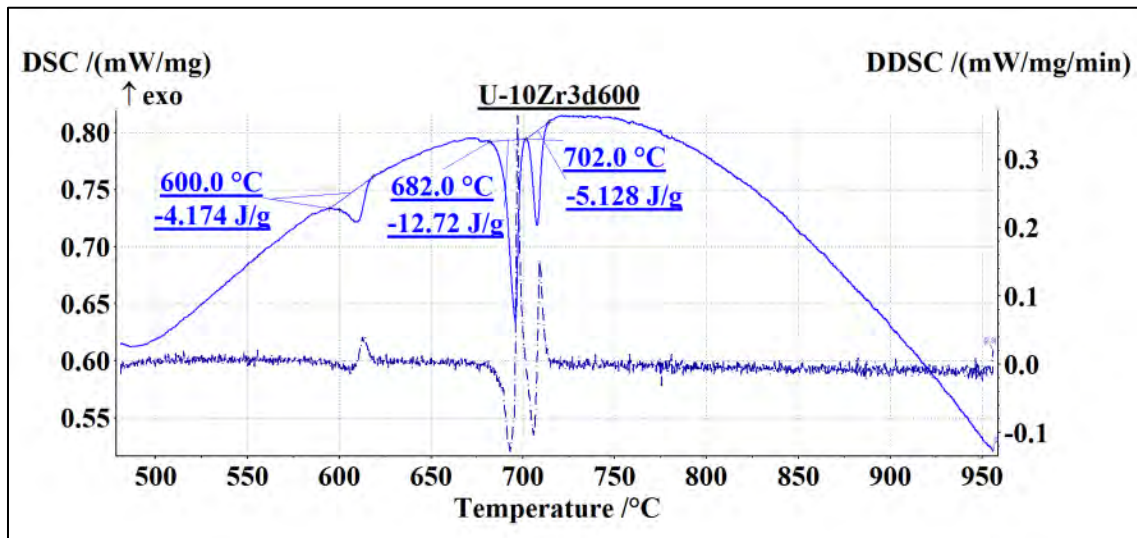
(a) U-10Zr3d600

Figure 4-21: DSC heating curves from annealed U-10Zr alloys.
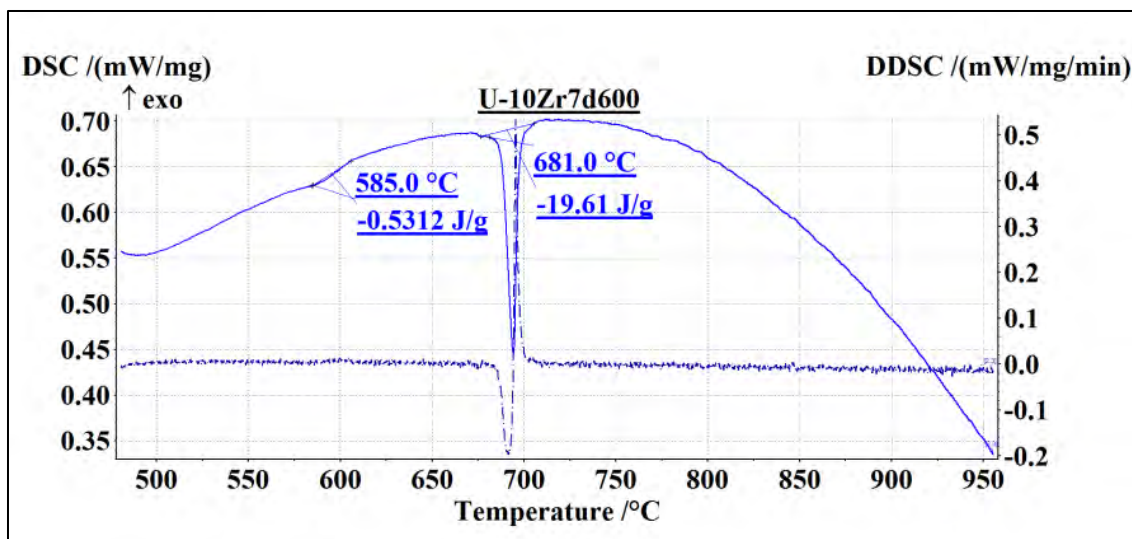
(b) U-10Zr7d600
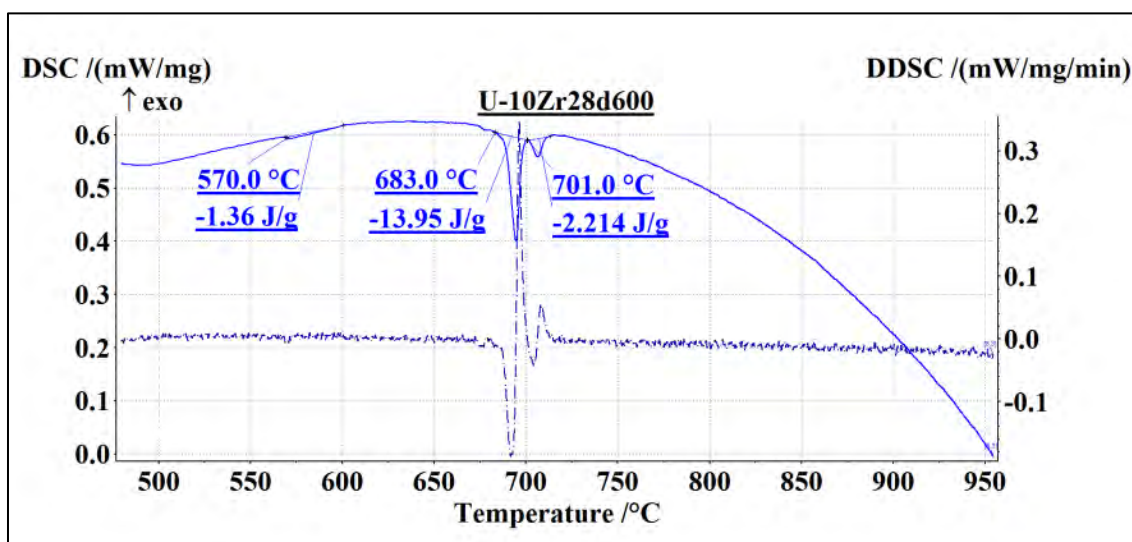
(c) U-10Zr28d600

Figure 4-21: Continued.

4.2.3.4 U-20Zr

The DSC heating curves from the annealed U-20Zr alloys are shown in Fig. 4-22. Most importantly, the third peak was never appeared from U-20Zr alloy, regardless of the alloy thermal history. It is clearly not in accordance with Sheldon's phase diagram. On the contrary, the absence of the third peak can reasonably be explained by adopting Rough's phase diagram, since it was revealed that the presence of the miscibility gap in the phase diagram of U-Zr binary alloy system would not occur the corresponding peak in the DSC curves from the alloys at measurable scale. Further discussion on the results is deferred to Section 5.2.
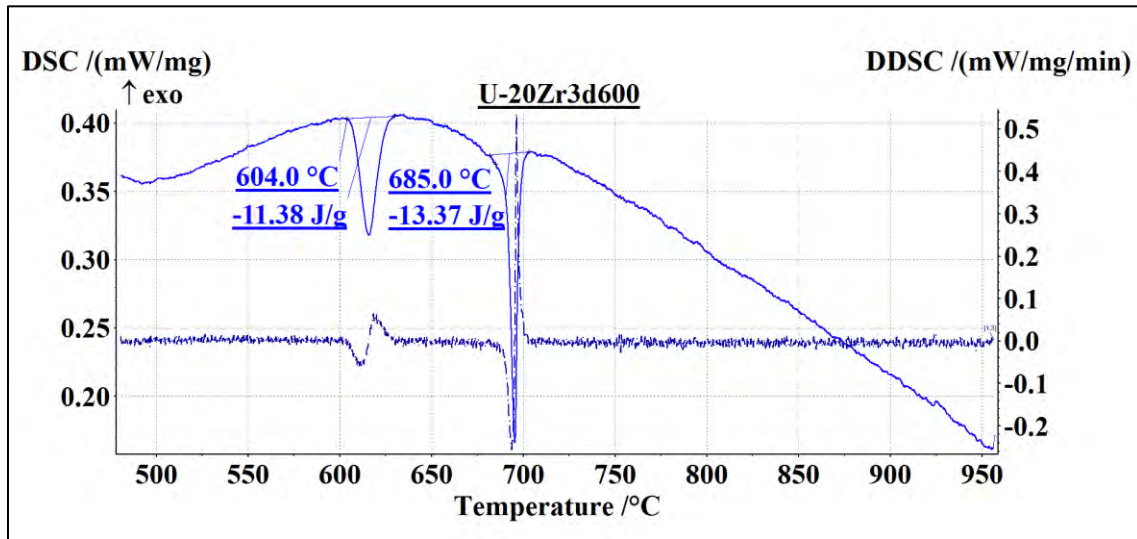
(a) U-20Zr3d600

Figure 4-22: DSC heating curves from annealed U-20Zr alloys.
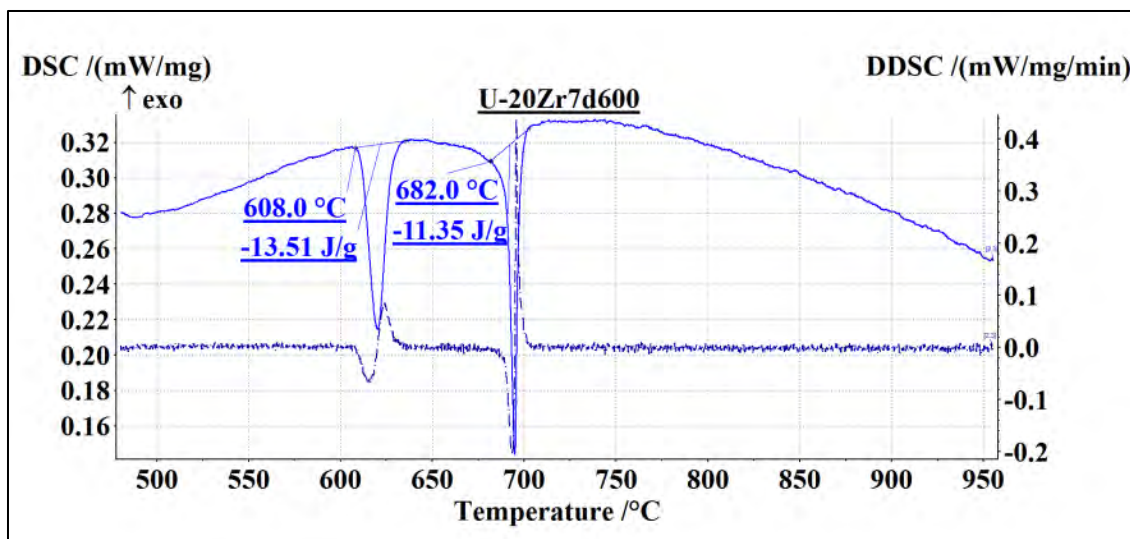
(b) U-20Zr7d600
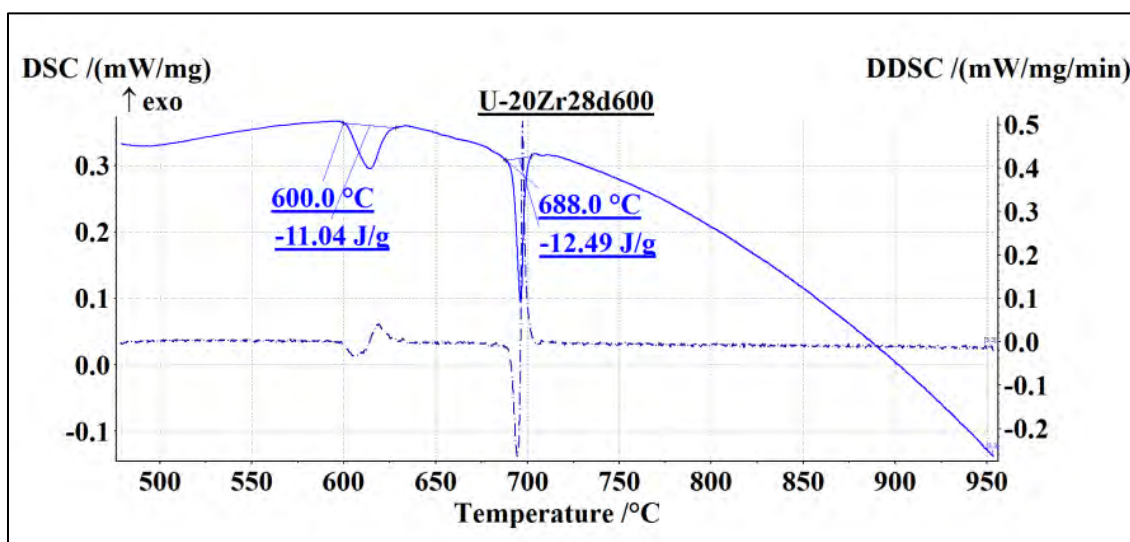
(c) U-20Zr28d600

Figure 4-22: Continued.

4.2.3.5 U-30Zr

The DSC heating curves from the annealed U-30Zr alloys are shown in Fig. 4-23. The U-30Zr alloy exhibit similar behavior with the U-20Zr alloy, except the phase transformation enthalpies. The consistency between the two alloys for the phase transformation temperatures and the number of phase transformations indicates that only two isotherm lines may exist in Zr-rich part of U-Zr binary phase diagram, likewise in Rough's phase diagram. Also, the measured second phase transformation temperatures are exactly matched with Rough's phase diagram given in Fig. 2-3.
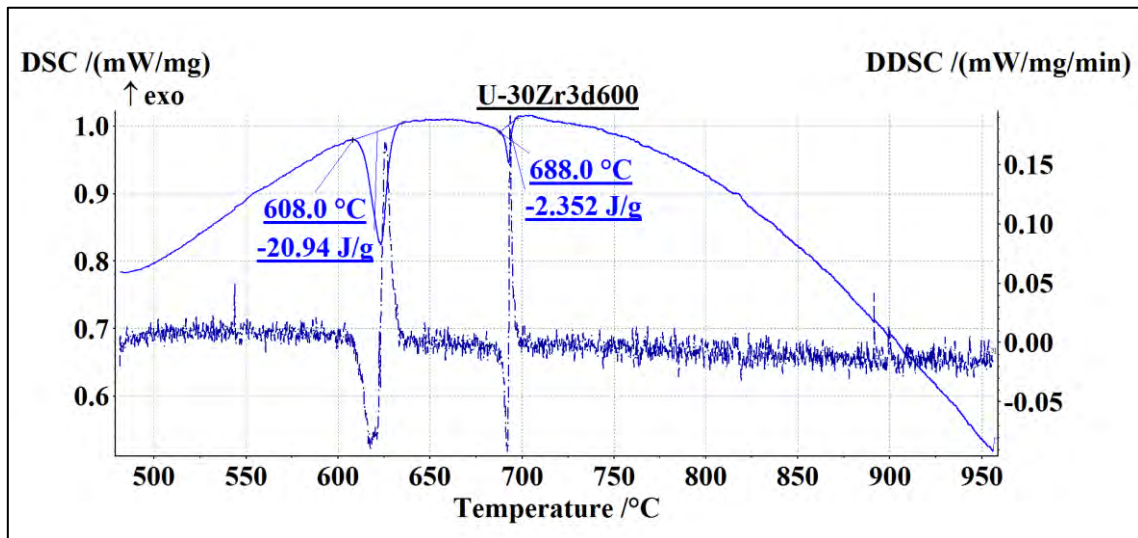
(a) U-30Zr3d600

Figure 4-23: DSC heating curves from annealed U-30Zr alloys.

124
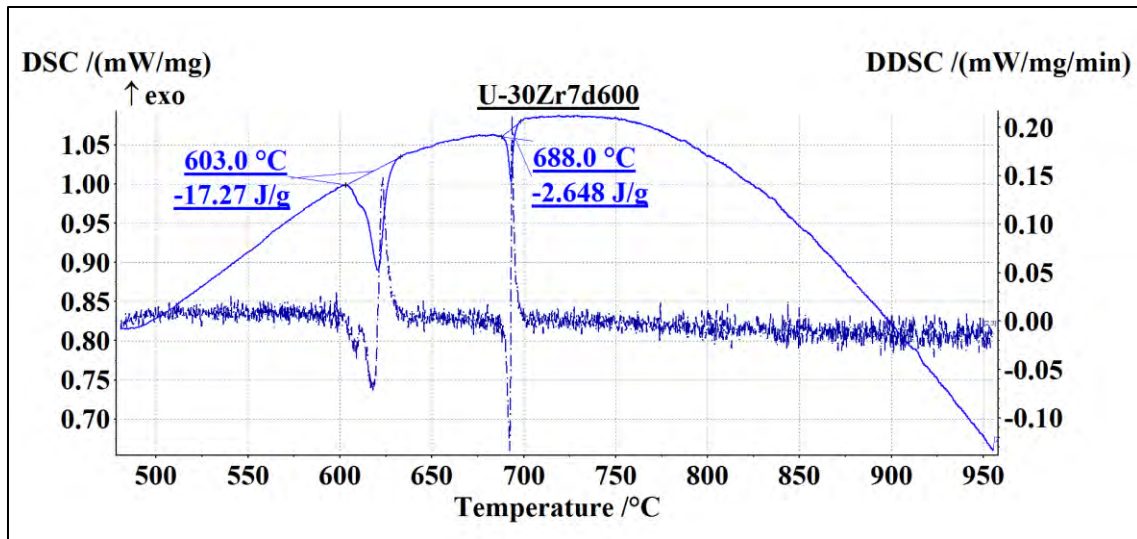
(b) U-30Zr7d600

Figure 4-23: Continued.

4.2.3.6 U-40Zr

The DSC heating curves from the annealed U-40Zr7d600 alloys is shown in Fig. 4-23. The alloy exhibited two phase transformations, although the second peak was significantly shrunk to be almost vanished. This results which separate from U-Zr binary phase diagram was anticipated from the observed microstructure of the annealed U-40Zr alloy shown in Fig. 4-10(d) and (e).
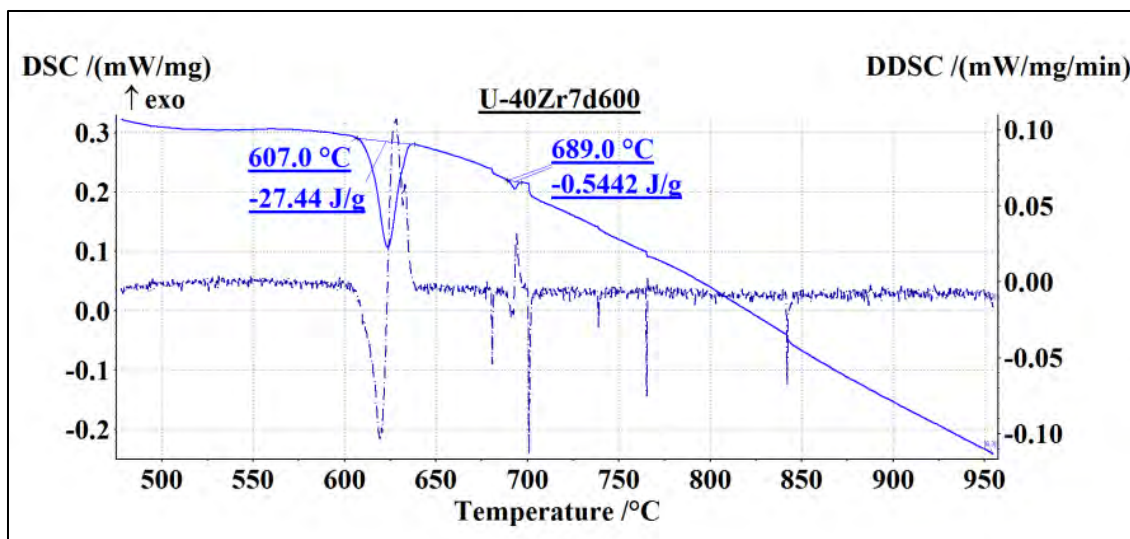
Figure 4-24: DSC heating curve from U-40Zr7d600.

4.2.3.7 U-50Zr

DSC heating curves from U-50Zr alloy are shown in Fig. 4-25. Despite confirmed presence of zirconium precipitates in the EPMA characterization, typical DSC heating curves from the alloy have shown a single peak corresponding to δ-$UZr_2 \rightarrow \gamma$ phase transformation at ~605 °C.
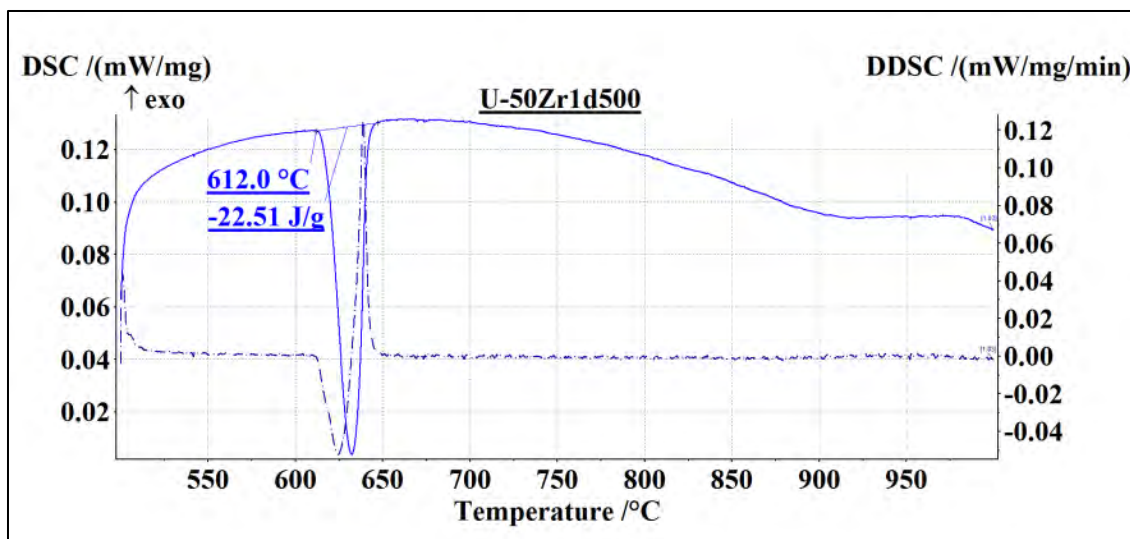
(a) U-50Zr1d500
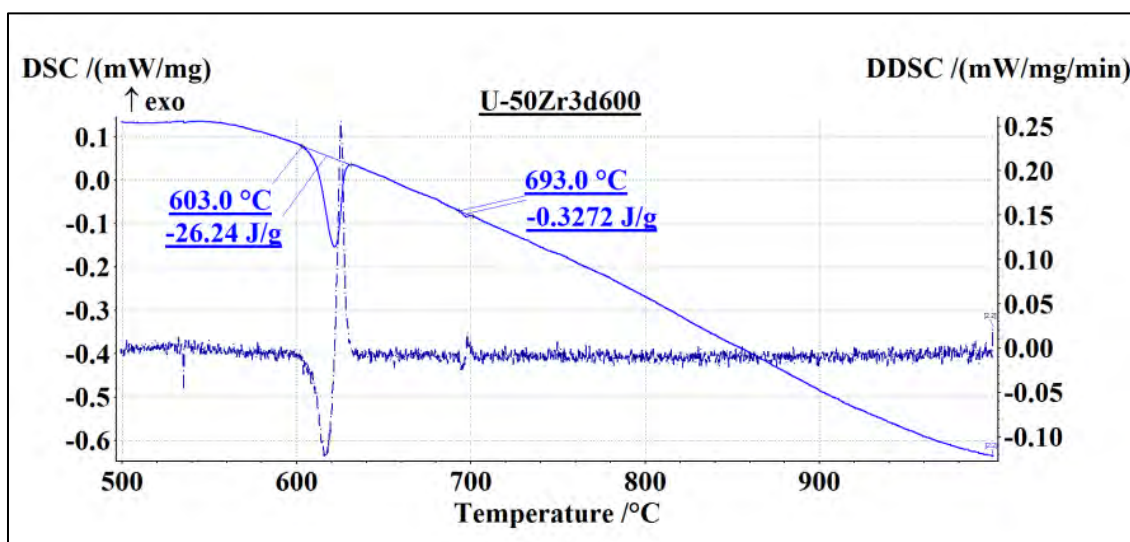
(b) U-50Zr3d600

Figure 4-25: DSC heating curves from annealed U-50Zr alloys.
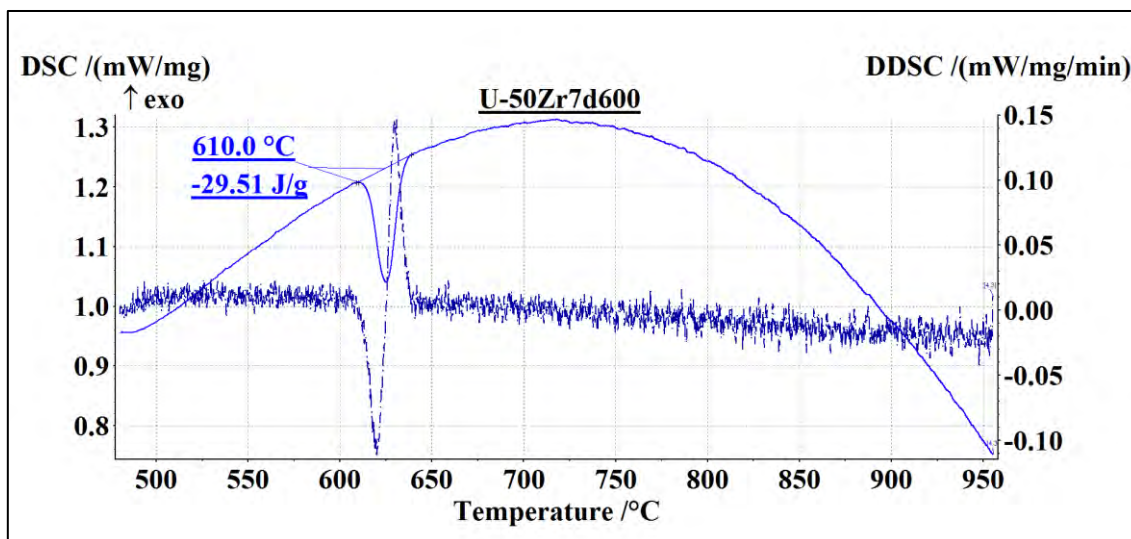
(c) U-50Zr7d600
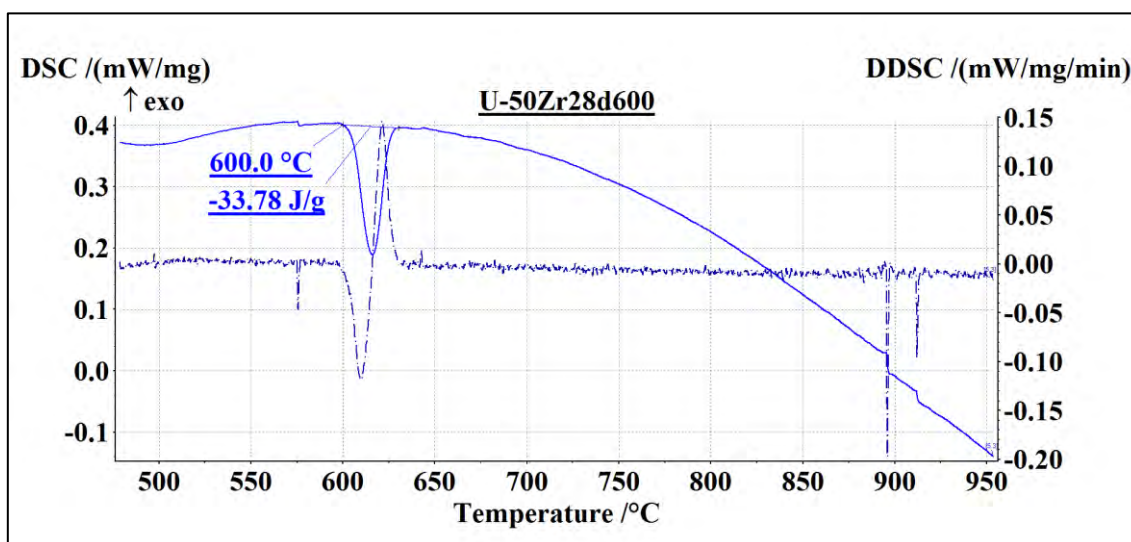
(d) U-50Zr28d600

Figure 4-25: Continued.

128

4.2.4 Transformation Temperatures and Enthalpies

The preceding DSC data curves are representatives from multiple experiments. A comprehensive compilation of the measured transformation temperatures and enthalpies from the first DSC heating curves from U-Zr alloys are listed below for samples annealed for 3, 7, and 28 days [156].

4.2.4.1 U-Zr3d600

Transformation temperatures and enthalpies from 3 day annealed U-Zr alloys at 600 °C (i.e. U-Zr3d600) are given in Table 4-5. The measured enthalpies of each phase transformation were compensated using effective masses of alloy samples at corresponding temperatures of the phase transformation. The effective mass of each alloy at each phase transformation temperature was calculated by assuming that the mass increase simultaneously recorded in TGA was solely due to oxidation of the alloy.

Reference transformation enthalpies for the first transformations of U-Zr alloys, i.e. δ-UZr$_2$ $\rightarrow$ γ_2 phase transformation, were gathered from open literature [128, 157]. A very limited number (sometimes zero) of reference values were available for the alloy compositions under evaluation, especially for the second and the third phase transformations.

Table 4-5: Phase transformation temperatures and enthalpies of U-Zr3d600.

Alloy	No.	Temp. (T_s)	Experimental (ΔH_{exp}) Measured	Experimental (ΔH_{exp}) Compensated		References (ΔH_{ref})	$\dfrac{\Delta H_{exp}}{\Delta H_{ref}}$
		(°C)	(J/g)	(J/g)	(kJ/mol)	(kJ/mol)	(%)
	1	585	0.58	0.61	0.14	0.32 [128]	45
U-2Zr	2	675	9.01	9.59	2.26	-	-
	3	708	17.23	18.49	4.35	-	-
	1	583	2.50	2.67	0.62	0.94 [128]	66
U-5Zr	2	676	8.05	8.78	2.02	-	-
	3	704	15.31	16.81	3.88	-	-
	1	596	3.78	3.84	0.86	1.57 [157]	55
U-10Zr	2	682	12.63	12.94	2.89	1.43 [157]	202
	3	702	5.16	5.30	1.18	0.29 [157]	408
	1	605	11.53	11.78	2.46	-	-
U-20Zr	2	682	13.19	13.55	2.83	-	-
	3	-	-	-	-	-	-
	1	608	21.09	21.09	4.09	3.95 [128]	104
U-30Zr	2	688	2.15	2.15	0.42	-	-
	3	-	-	-	-	-	-
U-50Zr	1	604	30.18	35.52	5.85	5.17 [128]	113

The compensated transformation enthalpies and available corresponding reference values were fairly well matched, except with Matsui *et al*. [157]. However, the Matsui reference values were not directly measured but calculated from heat capacities, which is not as precise as direct measurement. Also, the examined alloy composition at U-20at%Zr for the study was slightly off from the U-10Zr (U-22.48at%Zr) alloy used here.

4.2.4.2 U-Zr7d600

The transformation temperatures and enthalpies measured from U-Zr7d600 samples are given in Table 4-6.

Table 4-6: Phase transformation temperatures and enthalpies of U-Zr7d600.

| Alloy | No. | Temp. (T_s) | Experimental (ΔH_{exp}) | | | References (ΔH_{ref}) | $\dfrac{\Delta H_{exp}}{\Delta H_{ref}}$ |
| | | | Measured | Compensated | | | |
		(°C)	(J/g)	(J/g)	(kJ/mol)	(kJ/mol)	(%)
U-0.1Zr	1	663	10.94	11.06	2.63	2.791 [136]	94
	2	769	17.74	18.11	4.31	4.757 [136]	91
U-2Zr	1	593	0.18	0.18	0.04	0.32 [128]	13
	2	674	9.00	9.17	2.16	-	-
	3	704	17.63	18.02	4.24	-	-
U-5Zr	1	596	1.64	1.66	0.38	0.94 [128]	41
	2	675	8.51	8.70	2.01	-	-
	3	702	17.91	18.35	4.23	-	-
U-10Zr	1	572	2.32	2.33	0.52	1.57 [157]	33
	2	685	20.82	21.00	4.69	1.43 [157]	328
	3	-	-	-	-	0.29 [157]	-
U-20Zr	1	607	13.04	13.11	2.74	-	-
	2	685	13.19	13.30	2.78	-	-
	3	-	-	-	-	-	-
U-30Zr	1	603	17.50	17.53	3.40	3.95 [128]	86
	2	683	3.55	3.56	0.69	-	-
	3	-	-	-	-	-	-
U-40Zr	1	607	27.44	28.22	5.06	5.41 [128]	94
	2	689	0.54	0.57	-	-	-
U-50Zr	1	609	29.64	30.12	4.96	5.17 [128]	96

Note from Table 4-6 that U-0.1Zr is compared to uranium [136]. Also, the U-10Zr alloy data only reveals two transformations, which is not consistent with the data in Table 4-5 or 4-7; the reason for this is that there was a composition variation between the U-10Zr alloy samples that will be discussed in Section 5.1.5. The noted variations appear to have placed the test alloy samples at 3d and 28d on the opposite sides of the monotectoid point in the phase diagram (Fig. 2-2) as compared to the sample used in the 7d anneal.

4.2.4.3 U-Zr28d600

The transformation temperatures and enthalpies of U-Zr28d600 are given in Table 4-7. Note the third transformation of U-10Zr alloy is again evident.

Table 4-7: Phase transformation temperatures and enthalpies of U-Zr28d600.

Alloy	No.	Temp. (T_s)	Enthalpy				
			Experimental (ΔH_{exp})			References (ΔH_{ref})	$\dfrac{\Delta H_{exp}}{\Delta H_{ref}}$
			Measured	Compensated			
		(°C)	(J/g)	(J/g)	(kJ/mol)	(kJ/mol)	(%)
U-2Zr	1	600	0.26	0.26	0.06	0.32 [128]	19
	2	673	9.36	9.47	2.23	-	-
	3	708	15.50	15.76	3.71	-	-
U-5Zr	1	595	2.80	2.84	0.65	0.94 [128]	70
	2	674	8.66	8.85	2.04	-	-
	3	705	16.50	16.96	3.91	-	-
U-10Zr	1	570	1.65	1.67	0.37	1.57 [157]	24
	2	686	11.63	11.93	2.66	1.43 [157]	186
	3	701	4.28	4.39	0.98	0.29 [157]	-
U-20Zr	1	600	12.61	13.08	2.73	-	-
	2	688	14.32	15.04	3.14	-	-
	3	-	-	-	-	-	-
U-50Zr	1	600	34.03	34.37	5.66	5.17 [128]	109

4.3 Theoretical Assessments on Helium Ion-beam Irradiation on U-Zr Alloys

4.3.1 Radiation Damage and Helium Distribution

In preparation for the ion bombardment of U-Zr alloys with helium, the projected ranges and longitudinal straggling of 140 keV helium ions in U-0.1, 10, 20, and 40wt%Zr alloys were estimated by using the Stopping and Range of Ions in Matter (SRIM) [152], as shown in Fig. 4-26.
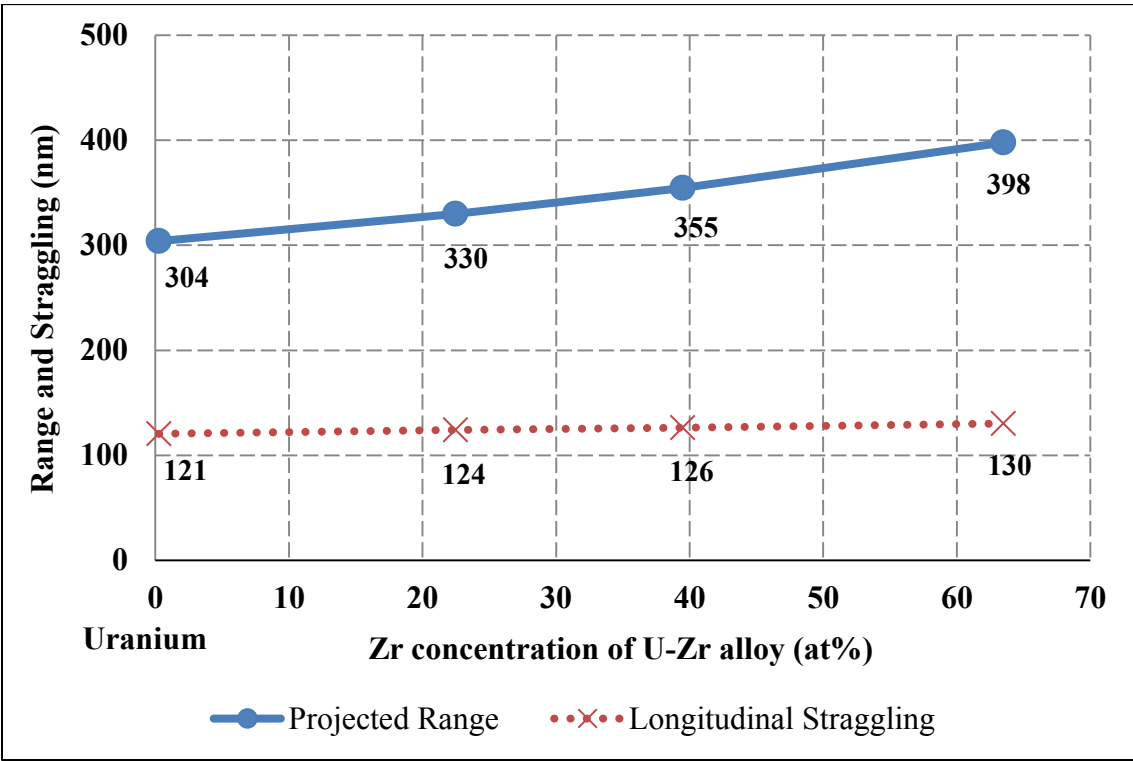
Figure 4-26: Projected ranges and straggling of 140 keV He⁺ ions implanted in U-Zr alloys.
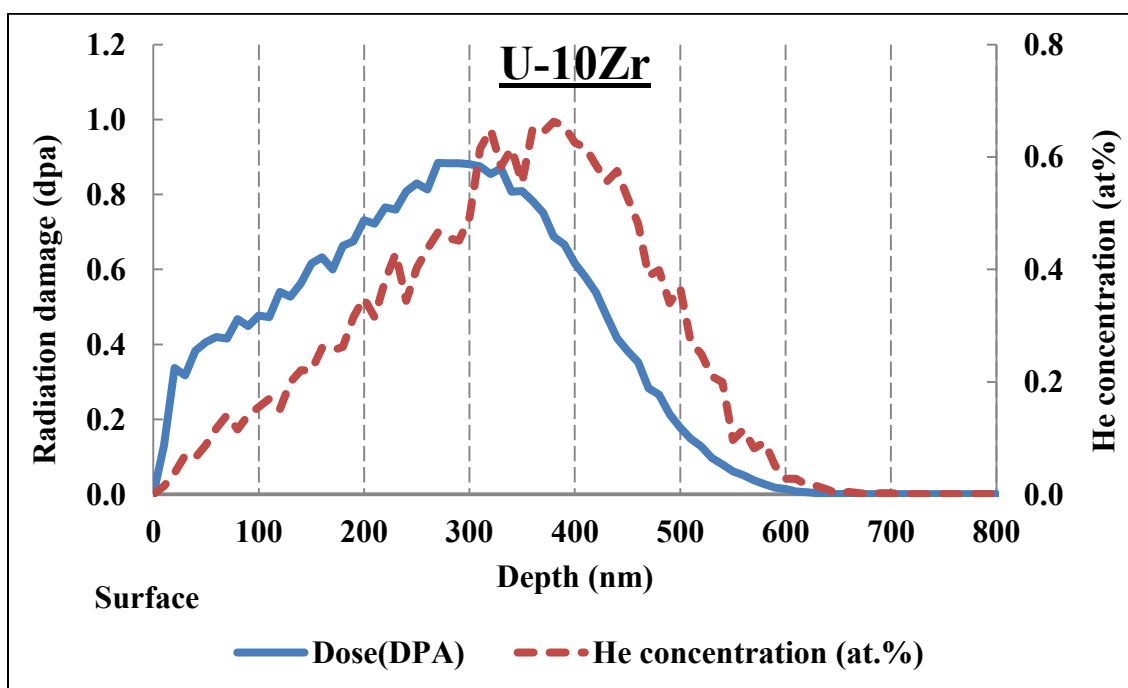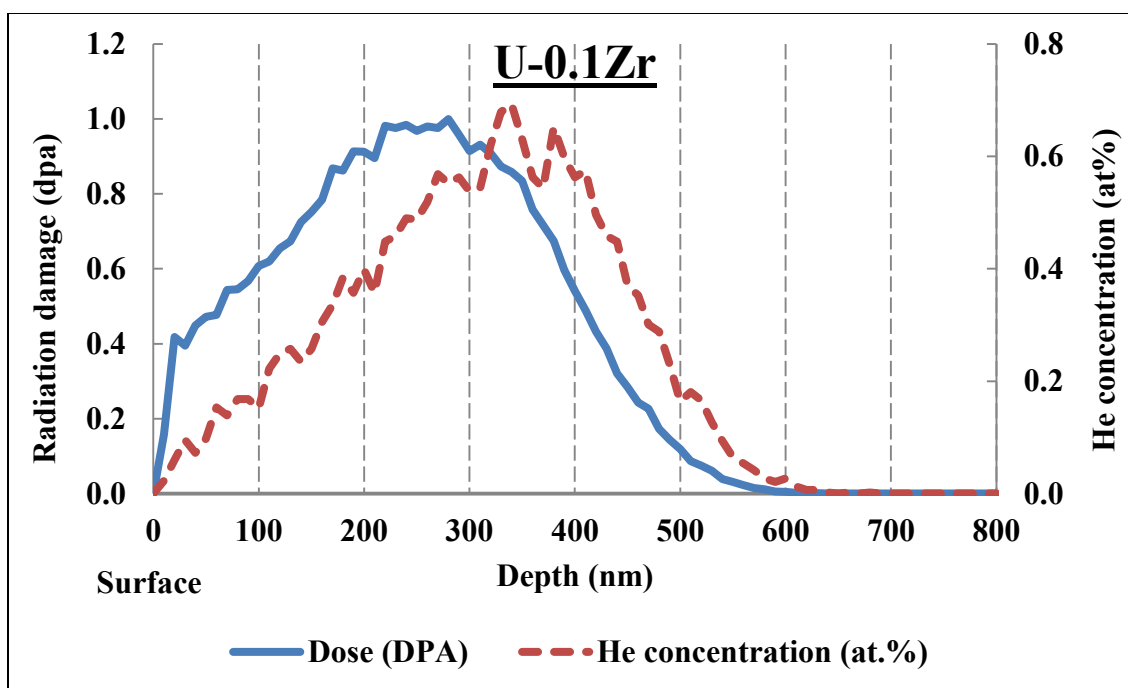
Figure 4-27: SRIM calculated radiation damage and helium distribution induced by reference dose (1 × 10^{16} ions/cm^2) of 140 keV He$^+$ ion-beam irradiation in U-Zr alloys.
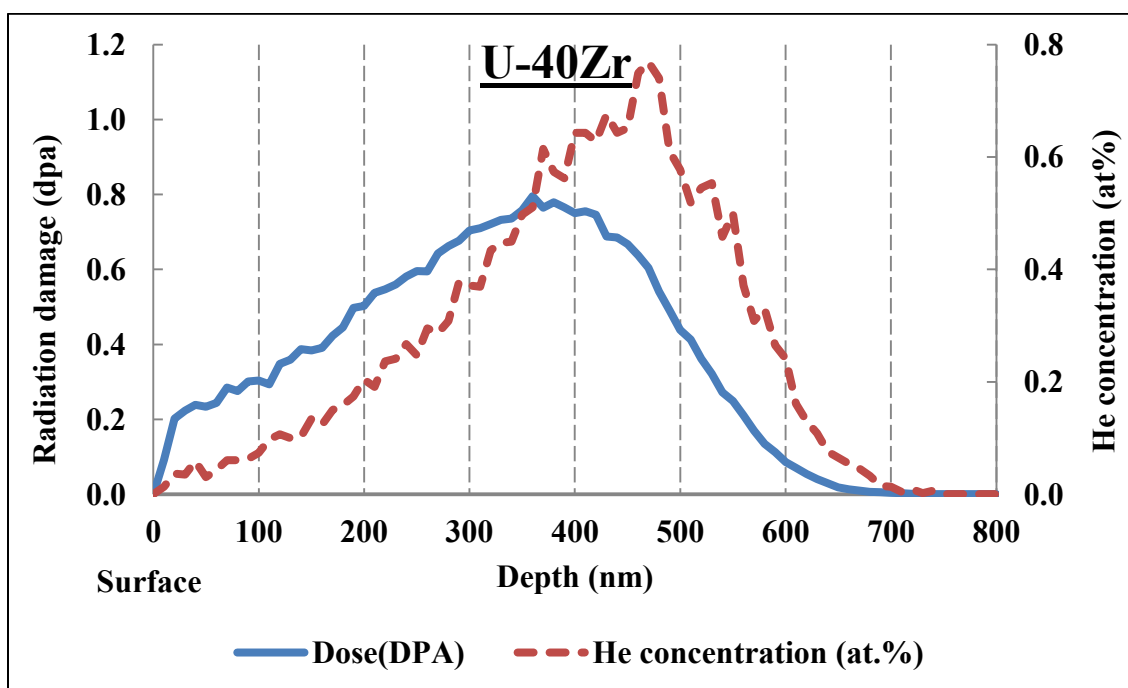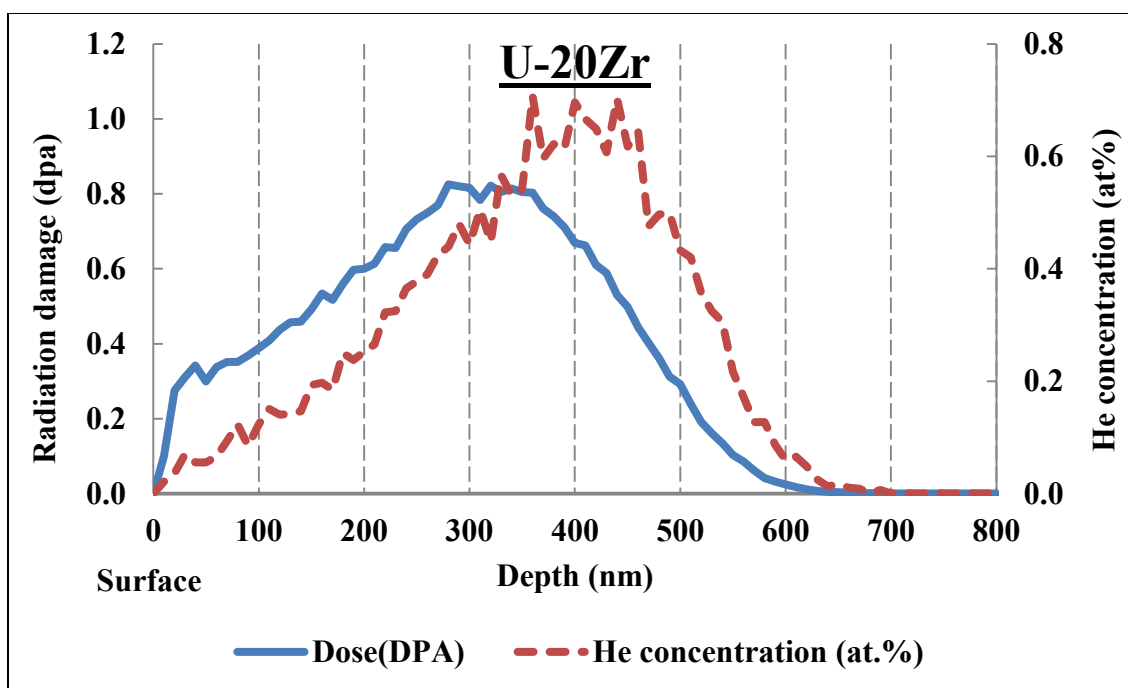
Figure 4-27: Continued.

Figure 4-27 shows that the calculated induced radiation damages and helium distributions within the alloys. The projected range increased with zirconium composition as shown from Fig. 4-26, while the longitudinal straggling is nearly constant. Lateral straggling is omitted from the figure because typical irradiated area (~1 cm × ~1 cm) were over 10^4 times wider than the estimated straggling (~150 nm), comparable to its longitudinal counterpart. The alloy densities suggested by SRIM were accepted as the inputs for the calculations, unavoidably disregarding physical inhomogeneity of the alloys, e.g. solid phases, defect structures, and local composition fluctuation, due to the limitation of the program.

4.3.2 Estimated Alloy Foil Temperature during the Irradiation

U-Zr alloy foils were irradiated in a high vacuum chamber (~10^{-7} Torr) at ambient temperature without external thermal intervention but the foil temperature can be elevated during the irradiation due to energetic ion-beam itself. To estimate maximum temperature of the alloy foil during the irradiation, a simplified 1-D conduction model was considered, assuming that dynamic thermal equilibrium between the energy inflow from high speed ions and outflow through the layer of carbon adhesive tape fixing the alloy foil on the ceramic wall of the vacuum chamber of the accelerator.

The adopted assumptions and premises required to estimate the temperature of alloy foils during the irradiation are listed below.

1. The thermal energy from irradiated helium ions and heat dissipation was in dynamic equilibrium in the U-Zr alloy foils at saturated temperature.

2. The vacuum chamber wall was an infinite reservoir whose temperature was constant at ambient temperature (25 °C).

3. The unknown maximum (saturated) temperature of the foil was constant for entire alloy foil, considering relatively high thermal conductivity [150, 158] of thin (~150 μm) U-Zr alloy foils.

4. Heat dissipation due to conduction through carbon tape was the only mode of cooling for the foil. Air cooling was negligible since the vacuum chamber pressure was maintained extremely low (~10^{-7} Torr) during the irradiation.

5. The alloy foil was parallel to the carbon tape and wall of vacuum chamber.

6. The thicknesses of alloy foil and carbon tape were constant.

7. There was no gap or mechanical stress between the layers of alloy foil, carbon adhesive and chamber wall.

Assuming all above, governing equation for the given system can be given as Equation (4-1).

$$k_{carbon} \cdot \Delta T \cdot t_{carbon} = E_{He} \times \phi_{He} \times A_{beam}, \text{ or } \therefore \Delta T = \frac{E_{He} \times \phi_{He} \times A_{beam}}{k_{carbon} \cdot t_{carbon}} \tag{4-1}$$

where k_{carbon} is the thermal conductivity of carbon (1.7 W/m·K), ΔT is the difference between saturated and ambient (25 °C) temperature, t_{carbon} is the thickness of the carbon adhesive layer (2.5×10^{-4} m), E_{He} is the energy of implanted helium ions (2.243×10^{-14} J), ϕ_{He} is the flux of ion-beam (2.778×10^{12} ions/cm^{2}s), and A_{beam} is the area irradiated (1 cm^2). Given values are either exact or conservatively assumed.

Substituting all parameters, the temperature elevation (ΔT) was estimated as 146.6 °C for a typical U-Zr sample. Therefore, the saturated temperature of alloy foil could be increased up to ~180 °C during irradiation. This calculation is very sensitive to the thickness of carbon adhesive layer and the variation of thermal conductivity of the system, mainly depending on the temperature of carbon adhesive layer and gap conductance between the layers of the alloy foil, carbon adhesive and the chamber wall.

However, it is indicative enough that during the irradiation still the alloy foils were subjected within RT range of U-Zr binary phase diagram (< 617 °C), since extraordinarily conservative assumptions were adopted for the thickness and thermal conductivity of the carbon layer. In addition, *in-situ* heated TEM of two phase U-Zr alloys has confirmed (Sections 4.4.3.1 and 4.4.4.1) that the annealing effect from ion-beam heating was negligible in metallurgical standpoint.

4.4 Nano-scale Characterization and *In-situ* Heating of Irradiated U-Zr Alloys

The U-0.1, 10, 20, 30, 40, and 50Zr alloys were irradiated with He$^+$ ions at fluences ranging from 1×10^{14} ions/cm^2 to 5×10^{16} ions/cm^2 using a 140 keV

accelerator and then examined using a 200 keV TEM, JEOL JEM-2010, as listed in Table 4-8. In particular, U-10Zr and U-20Zr alloys were *in-situ* heated during the TEM observation.

Hereinafter, the shorthand notation used to denote TEM specimens of various dose irradiated as-cast or annealed U-Zr alloys has been expanded from the previous nomenclature to include a means to identify the irradiation history. For instance, U-0.1ZrAi0 stands for the U-0.1wt%Zr (U-0.1Zr) alloy that is as-cast (A) and unirradiated (i0). As another example, U-40ZrHi5 stands for the U-40wt%Zr (U-40Zr) alloy heat-treated (H) (7 days at 600 °C for all annealed specimens for in Table 4-8) and irradiated at the fluence of 5×10^{16} ions/cm^2 (i5). The entire matrix for TEM observation of irradiated U-Zr alloys can be covered by extended usage of the given two examples.

Table 4-8: Experimental matrix for 140keV He$^+$ ion-beam irradiation and TEM.

Alloys	Thermal history	He$^+$ ion-beam irradiation dose ($\times 10^{16}$ ions/cm^2)				
		0	0.01	0.1	1	5
U-0.1Zr	AC	O	-	O	O	O
U-10Zr	AC	-	-	-	O	O (*in-situ* heated)
	7d600	-	-	-	-	O
U-20Zr	AC	-	-	-	-	O (*in-situ* heated)
U-30Zr	7d600	-	-	-	-	O
U-40Zr	AC	O	-	-	-	O
	7d600	-	O	-	O	O
U-50Zr	7d600	-	-	-	-	O

U-30Zr and U-50Zr alloys were excluded from the further observation to avoid duplication of data. As seen in Section 4.1.2, U-30Zr has similar structure with U-20Zr (i.e. δ-UZr$_2$ phase matrix with α-U precipitates) and U-50Zr is similar to U-40Zr (i.e. single δ-UZr$_2$ phase with α-Zr secondary phase precipitates). U-20Zr was chosen over U-30Zr to conduct *in-situ* heated electron diffractometry to further investigate phase transformation behavior of the alloy shown in the DSC observation that was inconsistent with current U-Zr phase diagram (Fig. 2-2). U-40Zr was selected over U-50Zr due to the concern regarding extensive presence of α-Zr precipitates in U-50Zr.

Each U-Zr alloy selected was considered to be representative of each phase structure possible in U-Zr binary system at ambient temperature; U-0.1Zr for single α-U phase including trace amount of zirconium, U-10Zr for α-U phase matrix with δ-UZr$_2$ phase precipitates, U-20Zr for δ-UZr$_2$ phase matrix with α-U phase precipitates and U-40Zr for single δ-UZr$_2$ phase matrix.

4.4.1 U-0.1Zr

4.4.1.1 U-0.1ZrAi0

The unirradiated as-cast U-0.1Zr alloy, U-0.1ZrAi0 following the shorthand notation given above, was examined to be a reference for further TEM observations of irradiated alloys. Two selected BF images obtained from different areas of a specimen of U-0.1ZrAi0 are shown in Fig. 4-28 with inserted corresponding DPs.
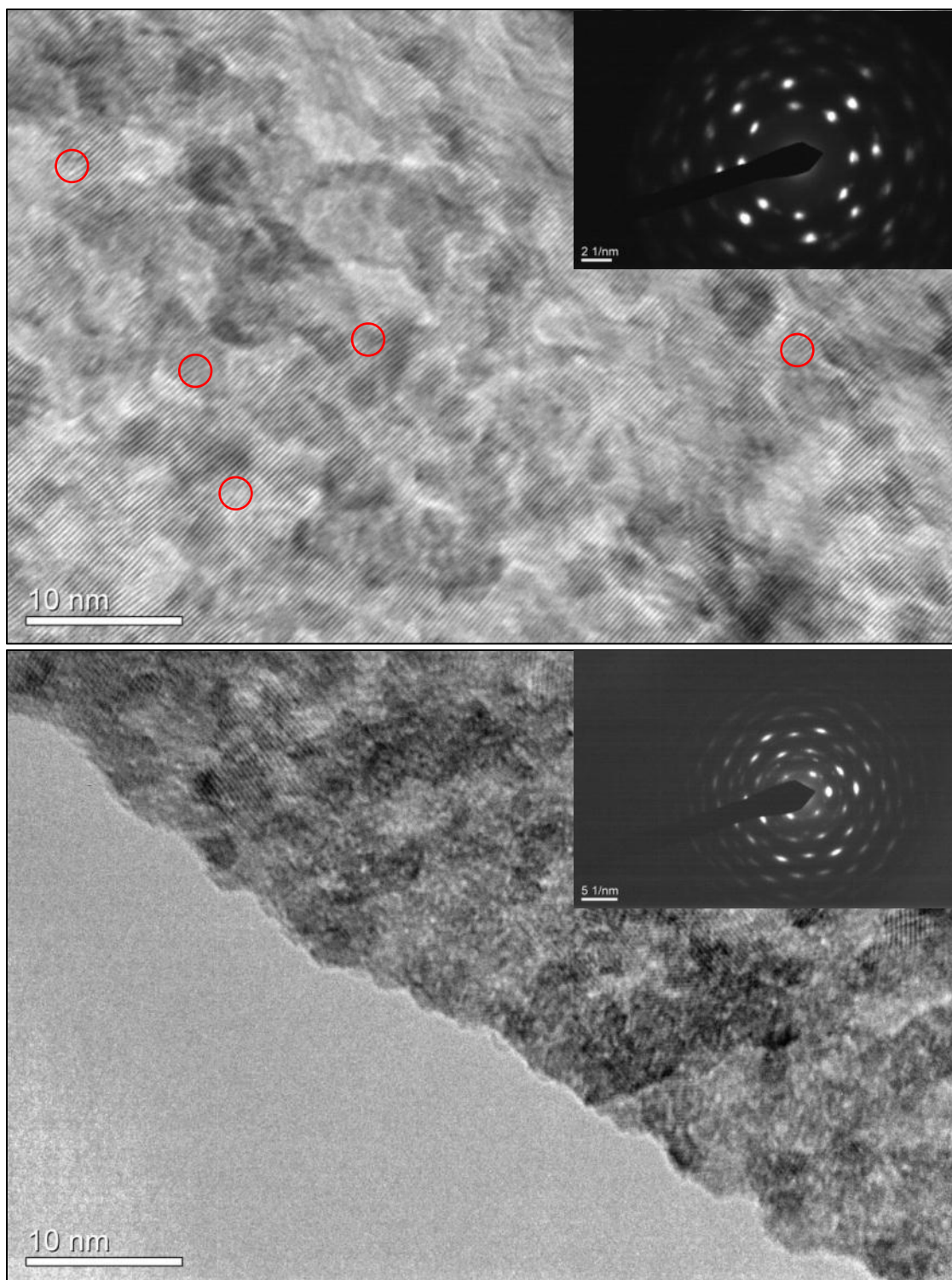
Figure 4-28: Strained single crystal structure of U-0.1ZrAi0.

The inserted DPs indicate that the areas have a single crystal or large grain polycrystalline structure. Numerous edge dislocations (marked with red circles in Fig. 4-28) exist within distinctive atomic crystalline. Circumferentially dispersed diffraction spots in the DP in Fig. 4-28(bottom) could imply strained crystal due to internal stresses. These defect structures were potentially formed during mechanical thinning of sectioned alloy button (> 500 μm thick) to foil (~150 μm thick). Hence, applied mechanical force was decreased for subsequent TEM specimen preparation. In particular, no mechanical force was applied for final polishing using 3, 1, and 0.25 μm diamond suspensions to relieve accumulated mechanical damages.

4.4.1.2 U-0.1ZrAi0.1

Figure 4-29 shows three different types of defect structures and artifacts observed in this specimen. Long straight lines across the BF image in the figure are unavoidable scratches from final polishing of mechanical thinning process that have been further damaged by electropolishing. These scratches were used as an indicator to estimate electropolishing depth on the irradiated side of the alloy foils, since the same type of damage structure on the other side of the specimen ought to be completely removed via intensive electropolishing on the surface carved at least 50 μm thick layer. The micro-scale torus-like shape is likely to be an electropolishing artifact since its dimension exceeds estimated specimen thickness (< ~100 nm) for electron transparency. However, smaller spherical features (< ~50 nm) randomly distributed within and outside the torus

could be helium bubbles [159], but this observation certainly requires further experiments to decisively identify the features. The SAD pattern inserted in the figure indicates that the surface of observed area was significantly oxidized (Section 5.2.5) after the specimen preparation during ~15 min long specimen transfer from the specimen preparation facility to the TEM facility, although the specimen oxidation was mitigated by using a plastic vial filled with acetone as specimen container during the transfer. Final electropolishing in the TEM facility was unfeasible due to the radioactivity of uranium. Some other features observed in the specimen are displayed in Fig. 4-30.
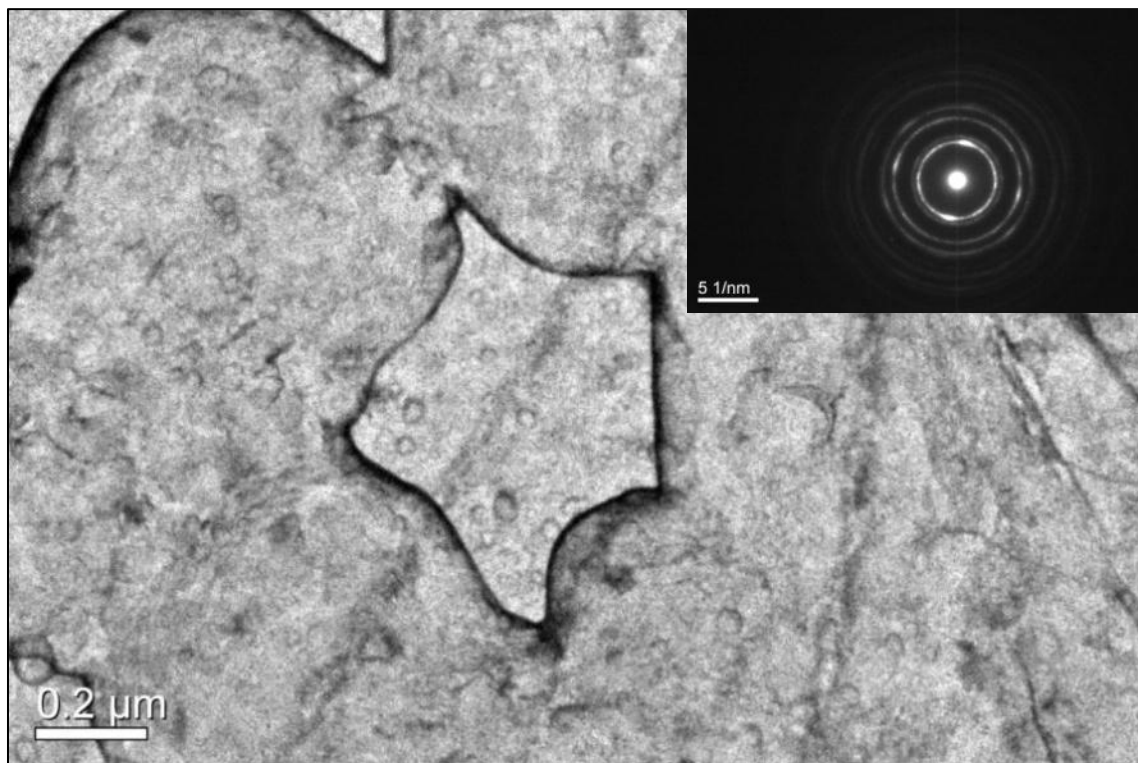
Figure 4-29: Defects and artifacts found from U-0.1ZrAi0.1.
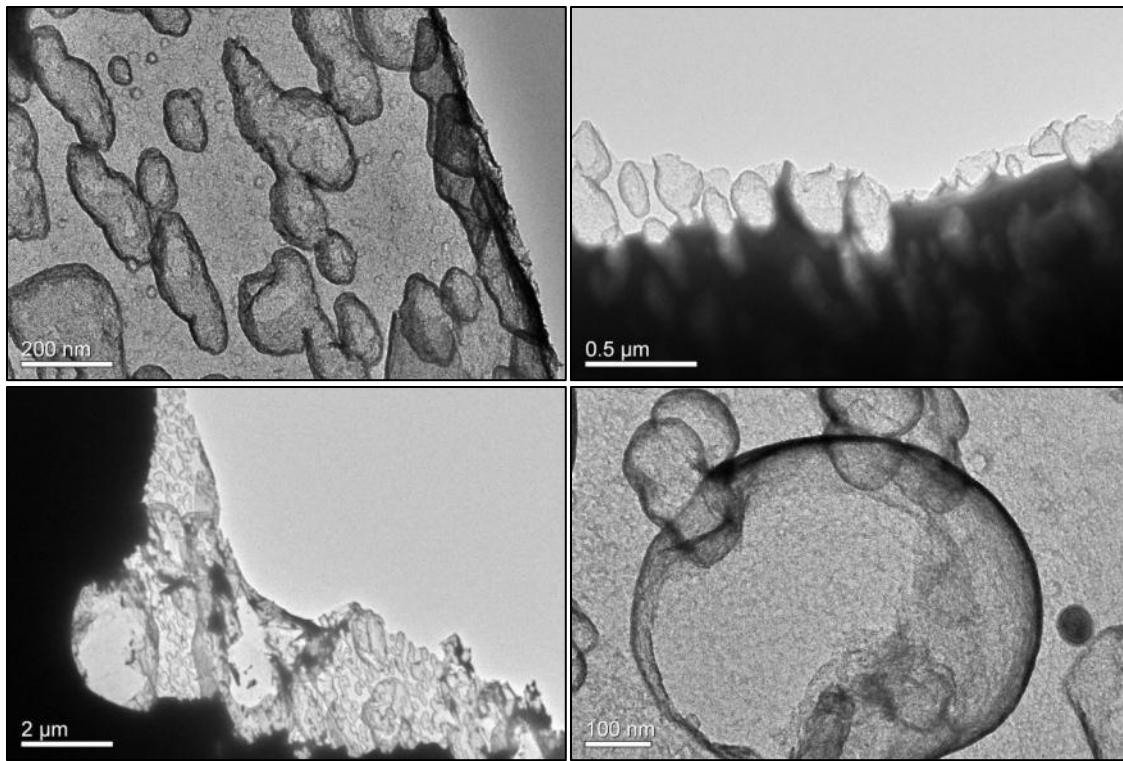
Figure 4-30: Electropolishing artifacts found from U-0.1ZrAi0.1.

Several types of impurities were also found from TEM observation as were from the EPMA characterization. Zirconium dendrites and yttrium oxide are the two most common secondary phases expected from alloy melt-casting process using argon cover gas (with residual levels of nitrogen and oxygen) and yttrium oxide crucibles to contain the metal pieces. It has been experimentally demonstrated many times that zirconium precipitates are stabilized within U-Zr alloys due to nitrogen and oxygen [119, 160, 161].

Secondary phase precipitates are conveniently distinguishable due to their darker contrast. Figure 4-31 shows than the features are thicker than uranium surrounding matrix, which has the highest scattering form factor among all elements in this study,

can be present in the specimen. Preferential thinning of uranium or U-rich phase was consistently observed from all compositions of U-Zr alloys, therefore often distinctively revealing the morphology of zirconium rich phases, i.e. δ-UZr$_2$ phase and zirconium dendrites.
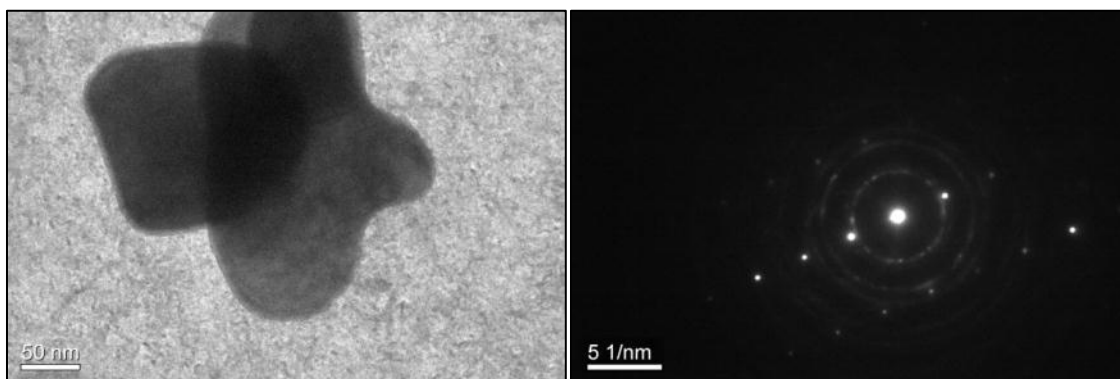
Figure 4-31: Overlapped secondary phase particles found from U-0.1ZrAi0.1.

Figure 4-31(right) shows the single crystal structure of the secondary particles survived from ion-beam irradiation within a polycrystalized uranium medium, regardless of oxidized surface or metallic inside. The ring type DP of polycrystalline UO$_2$ was often incompletely decomposed into highly symmetric hexagonal spot-like DP as shown in Fig. 4-32. Several spot DPs overlapped with the diffraction rings in the figure may be originated from the secondary particles shown in the inserted BF image.
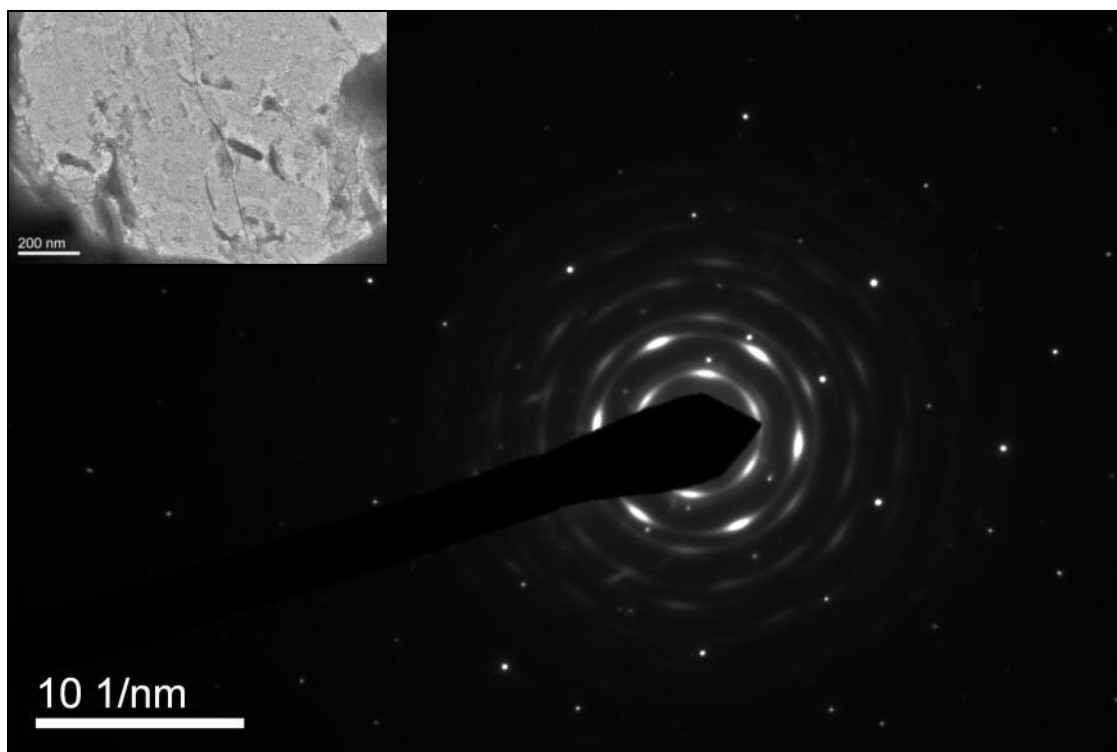
Figure 4-32: Spot-like SAD pattern of U-0.1ZrAi0.1.

4.4.1.3 U-0.1ZrAi1

Randomly oriented nano-grains in an oxidized area of U-0.1ZrAi1 are well shown in Fig. 4-33. Severe radiation damage in this area was also affirmed by the inserted DP which has completely even contrast along circumference for all rings and the significantly diffused center beam haloing the shadow of the needle tip on the TEM viewing screen.
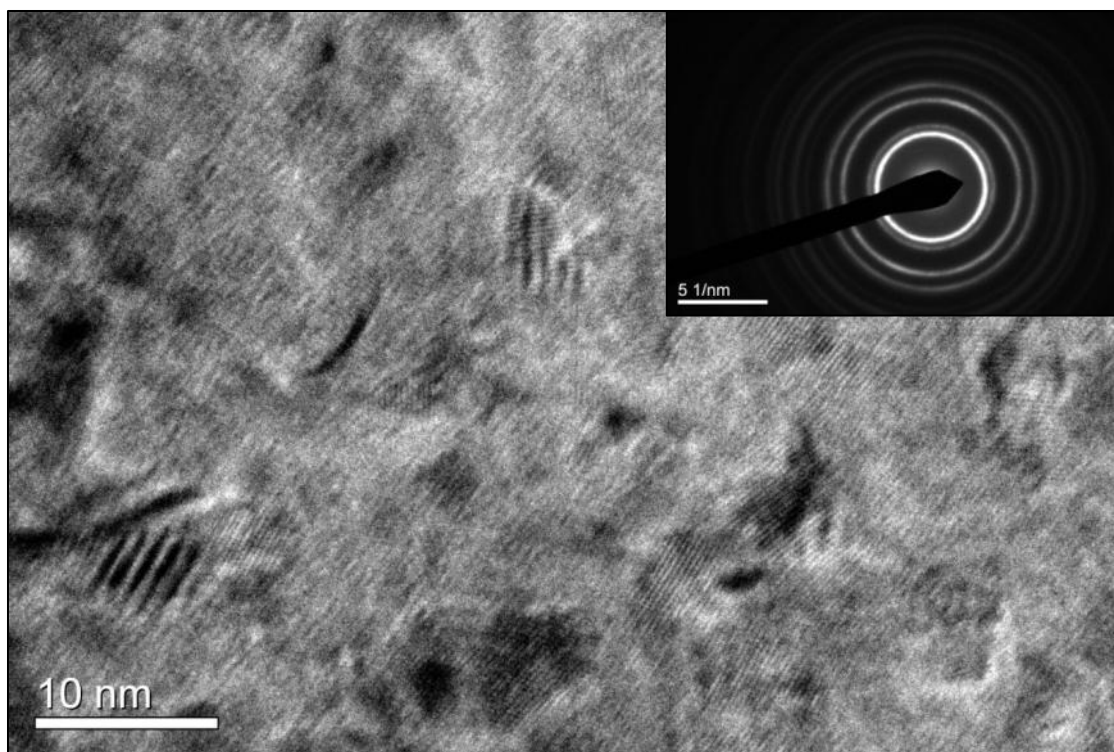
Figure 4-33: Polycrystalline medium found in U-0.1ZrAi1.

Numerous bubbles were occasionally found across several regions of U-0.1ZrAi1 specimens as shown Fig. 4-34. The bubble sizes were often over 100 nm which marginally exceeds the range of scale to be considered as ion-beam irradiation induced helium bubbles, although significantly diffused rings appeared in imposed DP apparently shows the area suffered exorbitant irradiation damage resulted in amorphization.
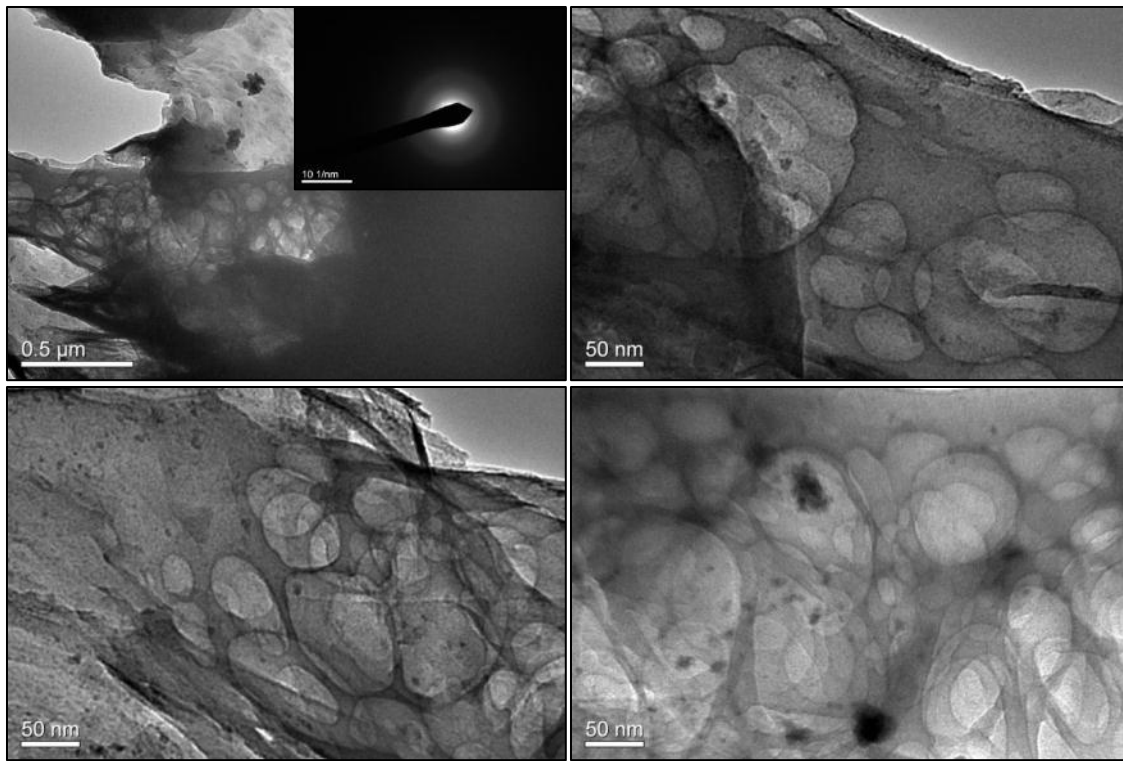
Figure 4-34: Numerous bubbles found from U-0.1ZrAi1.

Figure 4-35 shows four DPs obtained from the area having an yttrium oxide particle. The DPs in the left column indicate a single crystal structure within the particle. However, in the DP at the middle right a bright diffused ring pattern was present, as recorded using the CCD camera, since the brightest spot is blocked. This advent indicates that in the DP at middle right the electron beam diffracted by nano-grained medium was overshadowed by the transmitted electron beam. These ring patterns can be removed from DP by using smaller diffraction aperture as shown in the bottom right. However, the dispersed remnant diffraction spots to some extent indicate the impurity particle was placed on top of alloy bulk, mainly consisting of uranium.
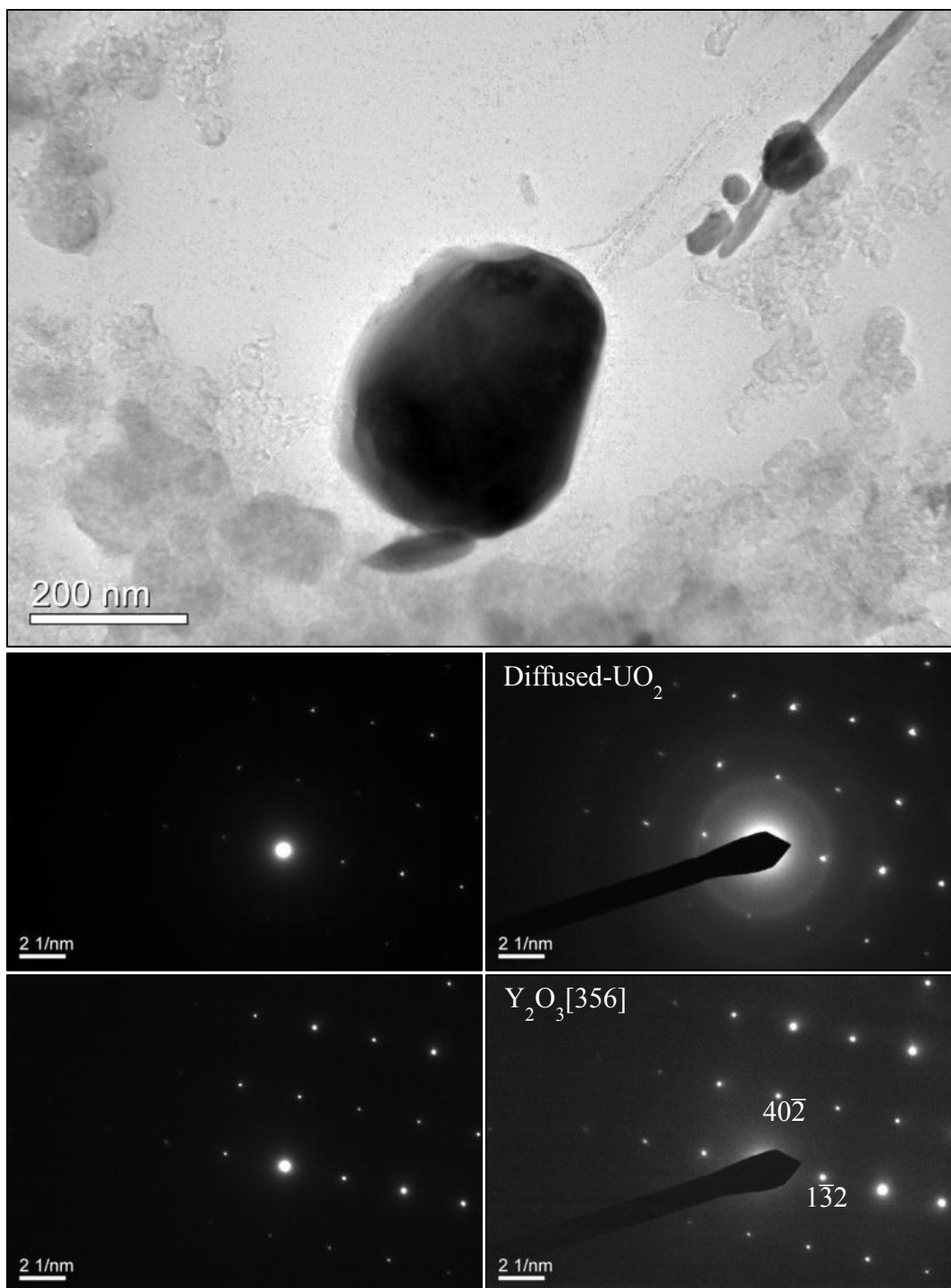
Figure 4-35: Yttrium oxide particle in U-0.1ZrAi1; the DPs were obtained using 50 μm (middle) and 20 μm (bottom) diameter apertures.
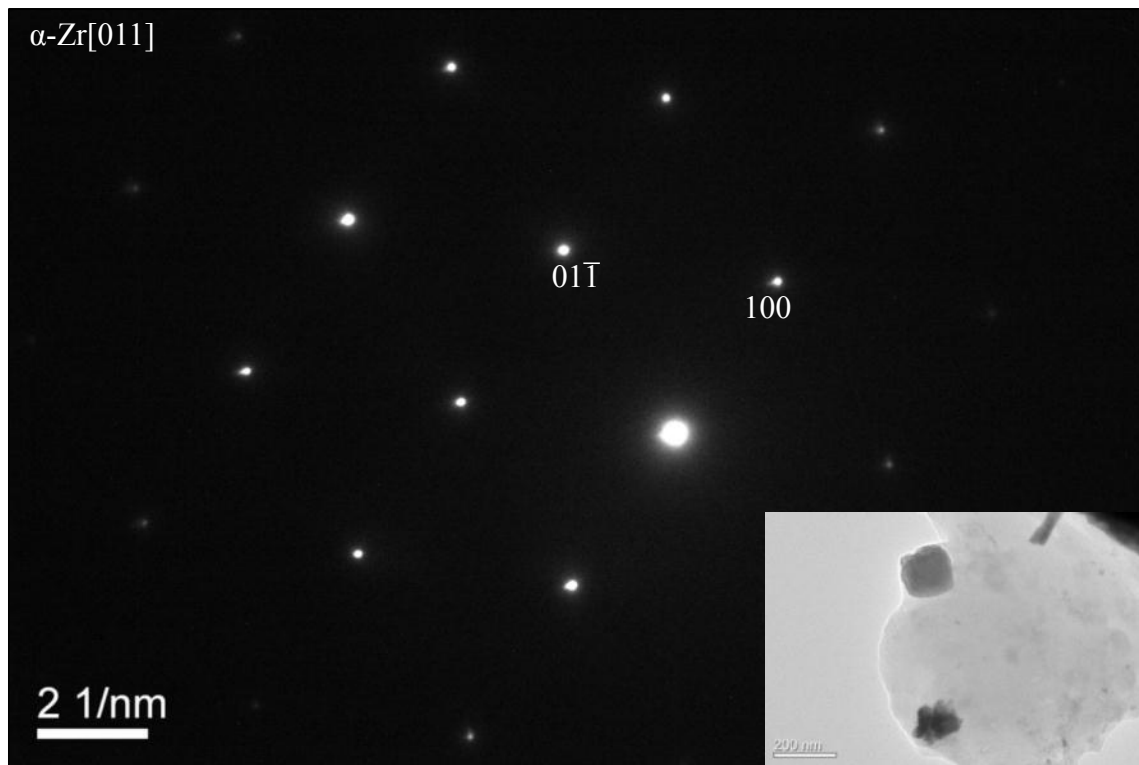
Figure 4-36: Secondary α-Zr phase particle in U-0.1ZrAi1.

The DP from another secondary phase (α-Zr) particle is shown in Fig. 4-36. The diffused ring pattern from the background was excluded by placing the smallest diffraction aperture (10 μm) right on the rounded rectangular particle edged out from the boundary. The DPs of impurities shown in Figs. 4-35 and 4-36 are included for the completeness of the TEM data analysis, even though the impurities were considered as minor features and excluded from the further analysis.

4.4.1.4 U-0.1ZrAi5

Numerous elliptical features (perhaps bubbles polishing artifacts), typically three dimensionally overlapping on each other, were observed from U-0.1ZrAi5, as shown in Fig. 4-37.

The dimensions of these circular features shown in Fig. 4-37 ranged from a few nanometers to ~100 nm diameter. The morphologies are fairly similar to the bubbles observed from U-0.1ZrAi1. Figure 4-38 shows a brighter contrast image of overlapped circular features, which implies the features are less dense than the surrounding medium likely gas bubbles [162, 163].

A critical difference between the features/bubbles found in U-0.1ZrAi1 and U-0.1ZrAi5 was their mobility. The features observed in the highly irradiated alloy (5×10^{16} ions/cm^2) were moving within the specimen and coalescing with each other during observation under a 200 keV electron beam. Moreover, focused electron beam was able to stimulate the bubbles to move in the highly irradiated alloy. In contrast, the features stationed in the lower dose irradiated alloy (1×10^{16} ions/cm^2) and the beam crossover was incapable to activate any mobility in the alloy.
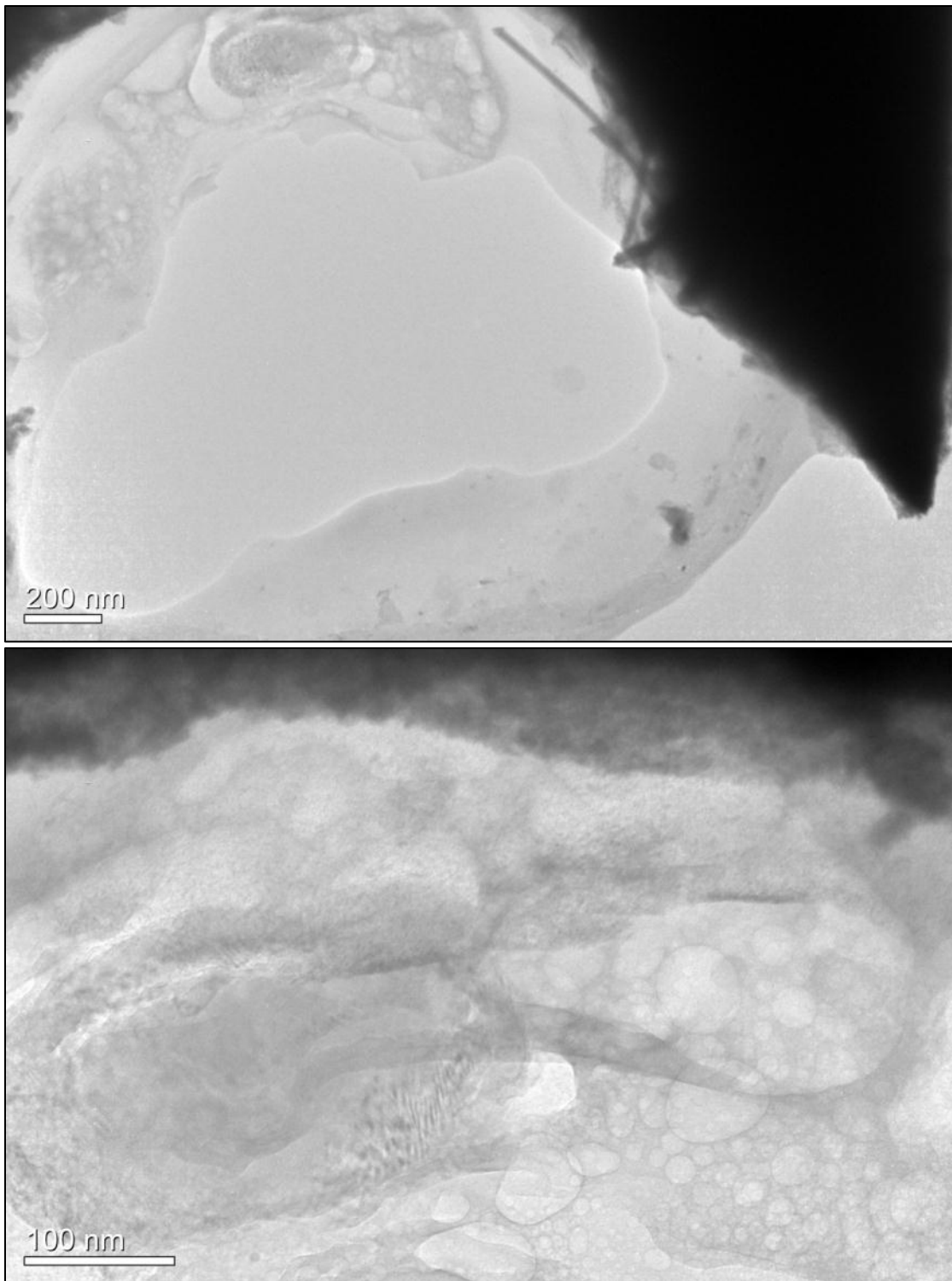
Figure 4-37: Moving and coalescing bubbles found from U-0.1ZrAi5.
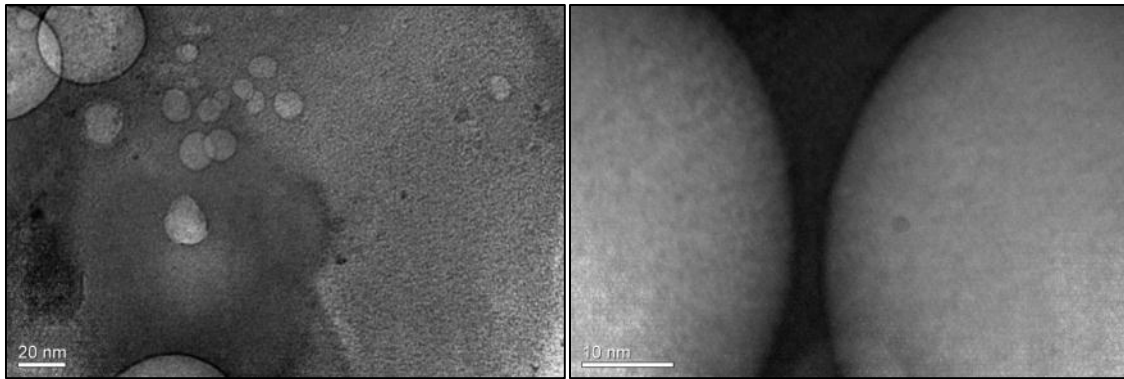
Figure 4-38: Brighter contrasts occurred from overlapped bubbles (left) and two bubbles about to coalesce (right) in U-0.1ZrAi5

The bubble-like features in U-0.1ZrAi5 often disappeared during observation usually, but not necessarily, after growing up to a certain extent ($> \sim 100$ nm) via coalescence. Once bubble started shrinking, it would completely disappear within several seconds. Figure 4-39 shows two BF images of an area having several features, which were consecutively taken with 190 seconds gap. The growth of the larger bubbles are marked using solid ellipses (red) and the distances between the bubbles and the specimen boundary are indicated with dashed arrow (white). Biased surface tension on the largest (78 nm) bubble in Fig. 4-39(b) is evident from its deflected boundary, which matches with the direction of the displacement, away from the specimen boundary.
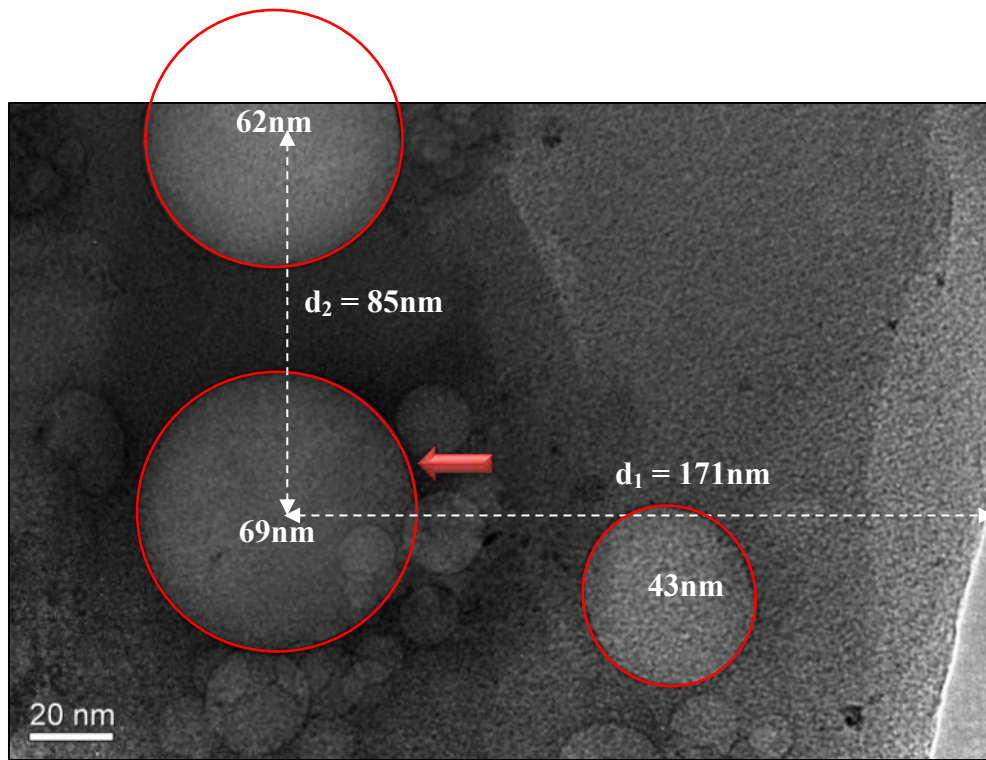
(a) Reference time (0 sec)
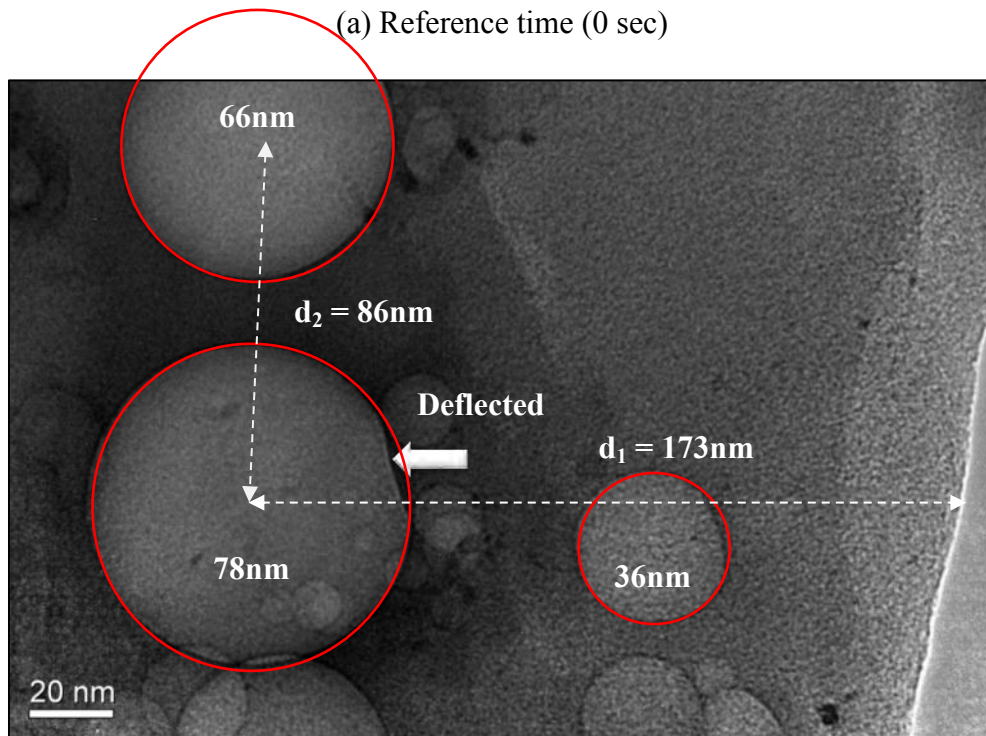
(b) 190 seconds after

Figure 4-39: Consecutive images of mobile bubbles in U-0.1ZrAi5.

4.4.2 U-40Zr

4.4.2.1 U-40ZrAi0

Unirradiated as-cast U-40Zr was examined as the reference for δ-UZr$_2$ phase features, although EPMA characterization on the alloy had revealed the presence of zirconium precipitates (Section 4.1.2.3). The impurity insertion was undetectable using EDS which implies that the level was less than the 0.08 wt% detection limit of the system [164]. Typical BF images and corresponding DPs are shown in Fig. 4-40. From the two DPs inserted on the bottom image, extra nearest spots at non-exact angles in the upper DP image are shown with the needle covering the transmitted electron beam, indicating the area is nearly, but not perfect, single crystal.

Figure 4-41 contrasts two different types of electropolishing artifacts with appropriately thinned featureless area of the alloy. The bottom left image shows redeposited compounds from the electrolyte whereas the area shown in the bottom right has many pitting holes on both sides of the specimen resulted from double side electropolishing. Note that the unirradiated alloy specimens were evenly electropolished from both sides to decrease the curvature of electropolishing dimple. Darker contrasts of specimen boundaries are three dimensionally rolled features of very well-thinned alloy foils, evident from their constant flagging during the observation.
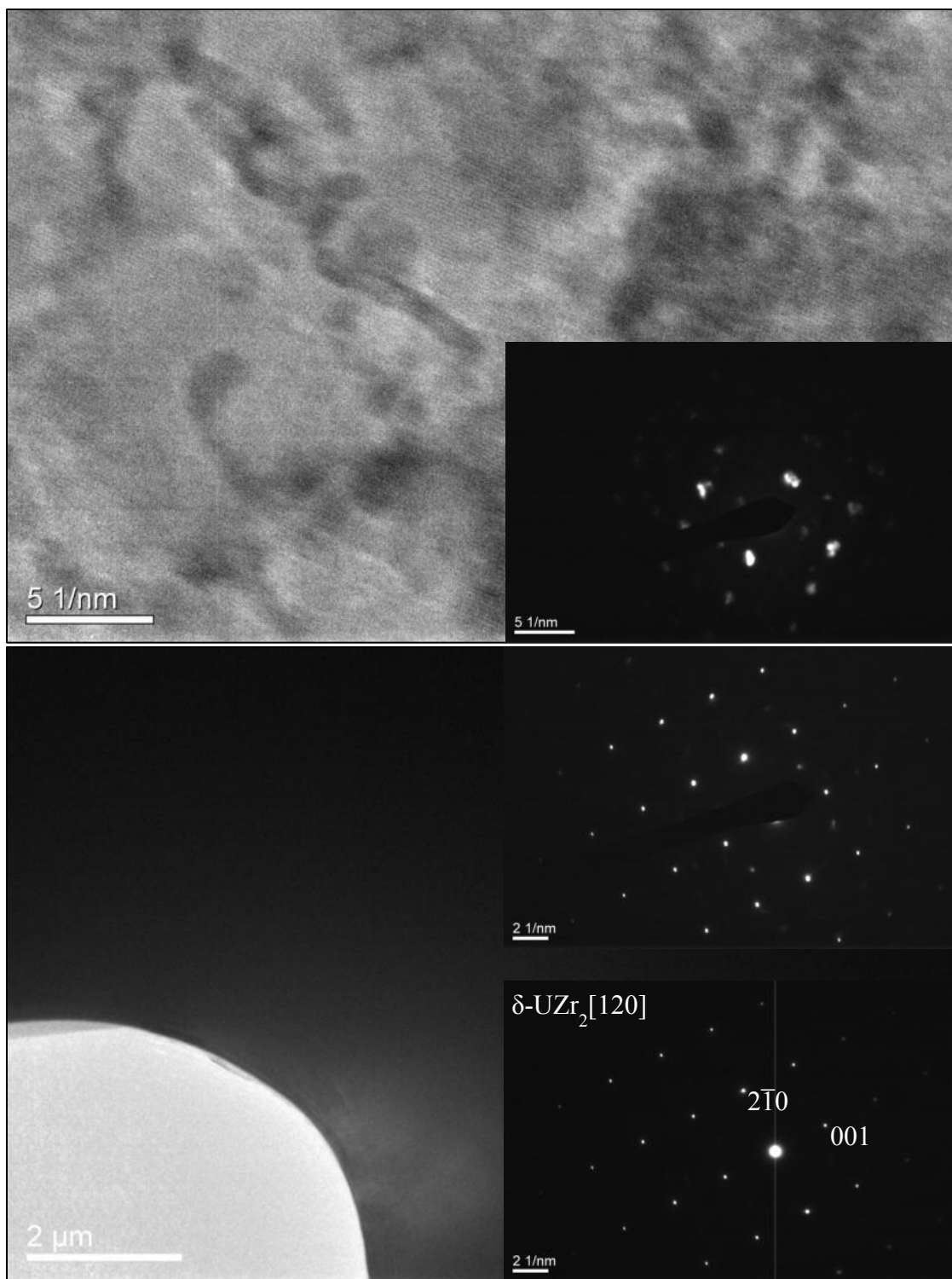
Figure 4-40: Representative near single crystal δ-UZr₂ phase bulk of U-40ZrAi0.
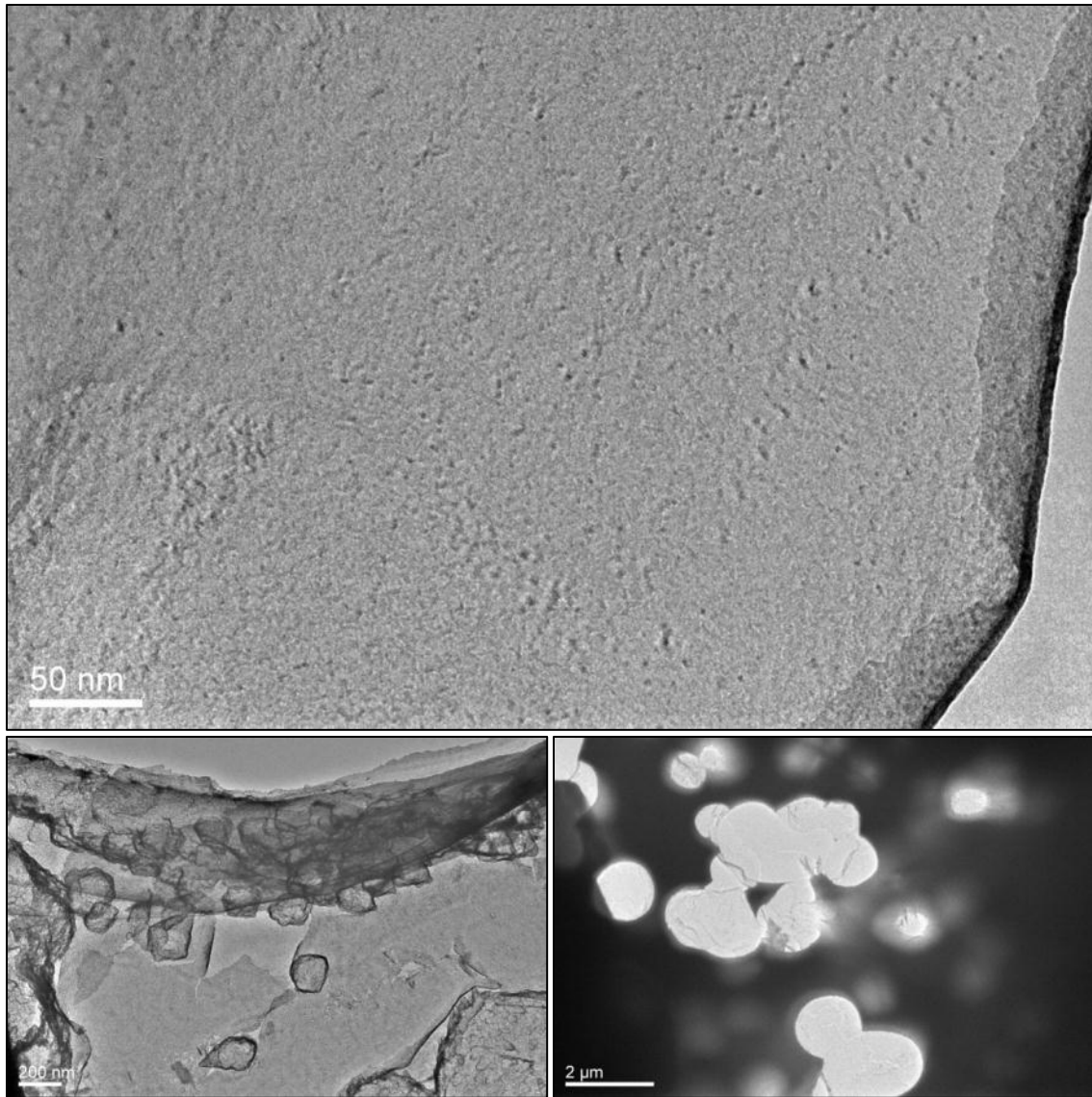
Figure 4-41: Clearly polished area (top) contrasted with two types of electropolishing artifacts (bottom); deposited material (left) and pitting holes (right) in U-40ZrAi0.

4.4.2.2 U-40ZrAi0.01

Mechanically thinned foils (~150 μm) of U-40Zr used to observe etched secondary phase precipitates on its surface. Those precipitates were clearly distinguishable as shown in Fig. 4-42(top), owing to their darker contrast and morphologies matched with the EPMA observation. Scratches produced during mechanical thinning process appeared as long crossing lines, which indicate that very shallow electropolishing was done on the irradiated side of the specimen. The presence of irradiation induced defect structure was ambiguous as shown in Fig. 4-42(bottom), although the inserted DP implies that the grain orientations were randomized due to irradiation. Scattered dark specks (~10 nm) could be suspected as radiation induced defect clusters based on the morphology and their absence from unirradiated alloys.

Figure 4-43 includes a BF image (top) and three DPs from a secondary phase precipitate, taken using stepwisely larger diameter of diffraction apertures; 10 μm (middle left), 20 μm (middle right) and 50 μm (bottom left). In contrast, the bottom right DP was obtained from brighter surrounding adjacent to the precipitate.
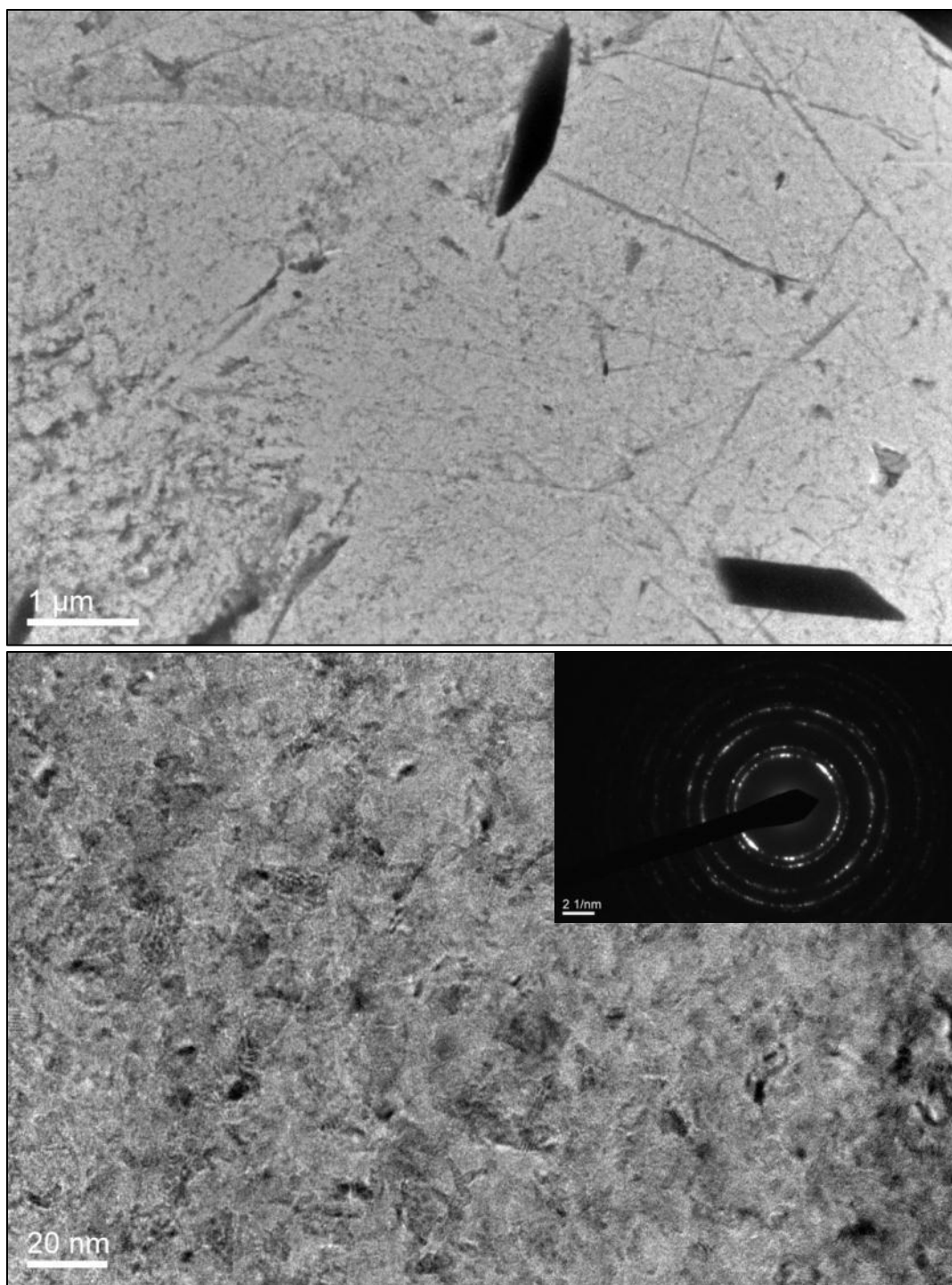
Figure 4-42: Mechanically etched secondary phase precipitates, surviving after shallow electropolishing on the irradiated side of U-40ZrAi0.01.
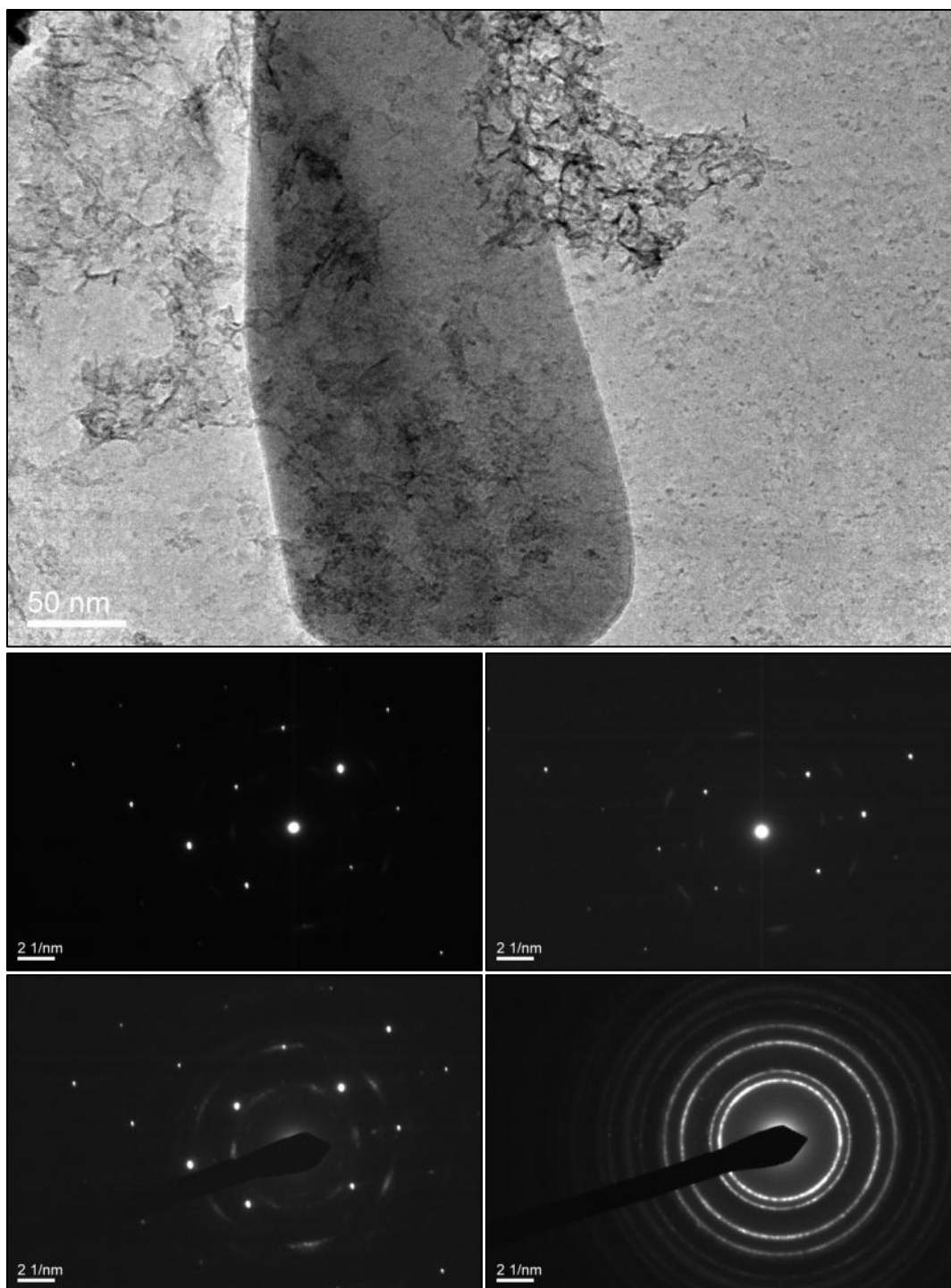
Figure 4-43: Secondary phase particle in U-40ZrAi0.01; BF image (top) and DPs taken using 10 (middle left), 20 (middle right), and 50 μm (bottom left) apertures. (The DP at bottom right was taken from brighter surrounding in the BF image.)

161
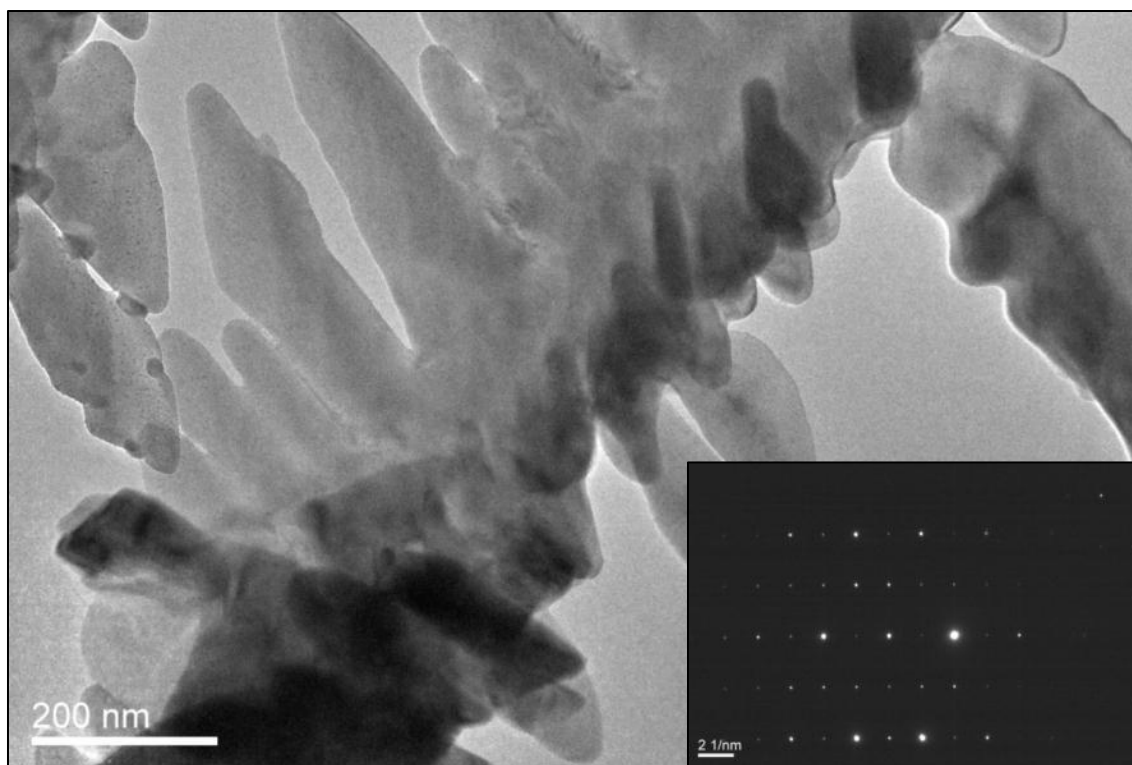
Figure 4-44: Electrochemically exposed zirconium dendrite from U-40ZrAi0.01.

Another type of secondary phase, the zirconium dendrite, is shown in Fig. 4-44. The dendrite was likely nucleated on cooling during the alloy fabrication process; this image is a companion to the EPMA image in Fig. 4-10. It survived after etching away the δ-UZr$_2$ phase matrix during excessive electropolishing, due to its chemical resistance to the electrolyte, in contrast to the independent precipitates distinguished from the matrix phase via preferential mechanical thinning. The dendrites commonly had larger dimensions combining a long primary arm with relatively short secondary arms. Note the darker contrast caused from secondary arms overlapping the primary arms in Fig. 4-44.

4.4.2.3 U-40ZrAi5

In the highly irradiated U-40Zr alloy specimen (U-40ZrAi5), a thin mesh structure was observed constructed with numerous variant hexagonal rings connected to each other (herein after referred as to "hex-mesh" structure). This porous structure has a hole within each hex-ring unit cell having a very fine, straight crystal enclosing the hole as shown in Fig. 4-45(bottom). Two formation mechanisms of the structure may hypothetically be suggested. The simple and trivial explanation could be that this structure is an electropolishing artifact deserves little further evaluation, but the fact that this feature was only observed in highly irradiated (5×10^{16} ions/cm^2) U-40Zr alloys indicates that it may indeed be related to the irradiation of the alloy specimen having single δ-UZr$_2$ phase.

Therefore, an alternative could be that it is a very thin high dose irradiated area that used to have abundant low pressure helium bubbles and empty cavities, since the dimensions of unit hex-rings are fairly even and small and matched with irradiation induced bubbles displayed later in Sections 4.4.2.4 and 4.4.2.5. The extraordinarily thin nature of this area was evident since no DP was obtainable from the area, impeding the element identification of the hex-mesh structure.

Several zirconium dendrites, which constantly had a crystal size over ~1 μm length, were repeatedly found within the U-40Zr alloy. These large crystals could be useful to calibrate the camera length of the TEM. Diffraction patterns of a dendrite at various camera lengths are shown in Fig. 4-46.

163
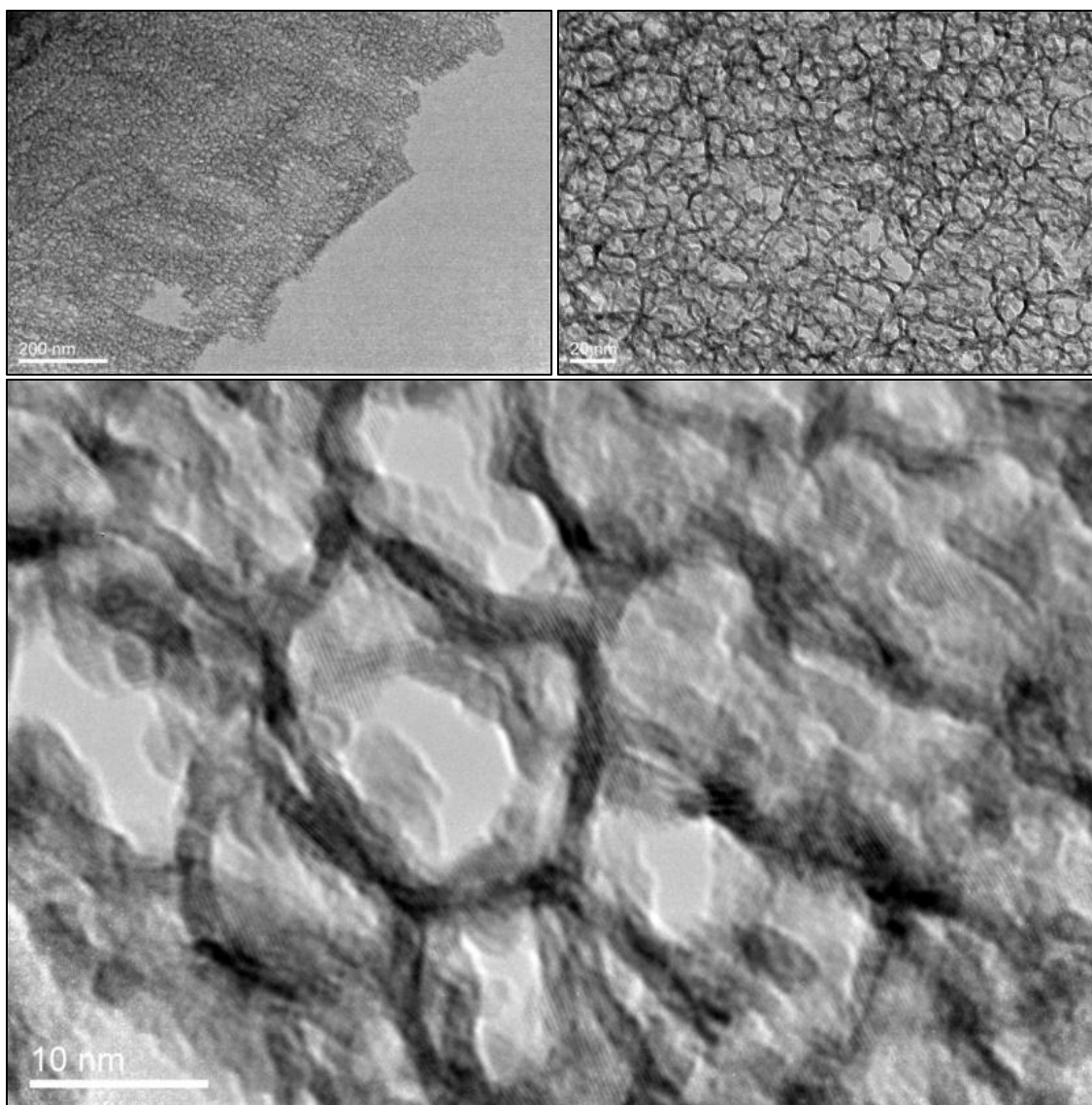
Figure 4-45: A "hex-mesh" structure (very thin porous area having fine crystals) found in U-40ZrAi5.
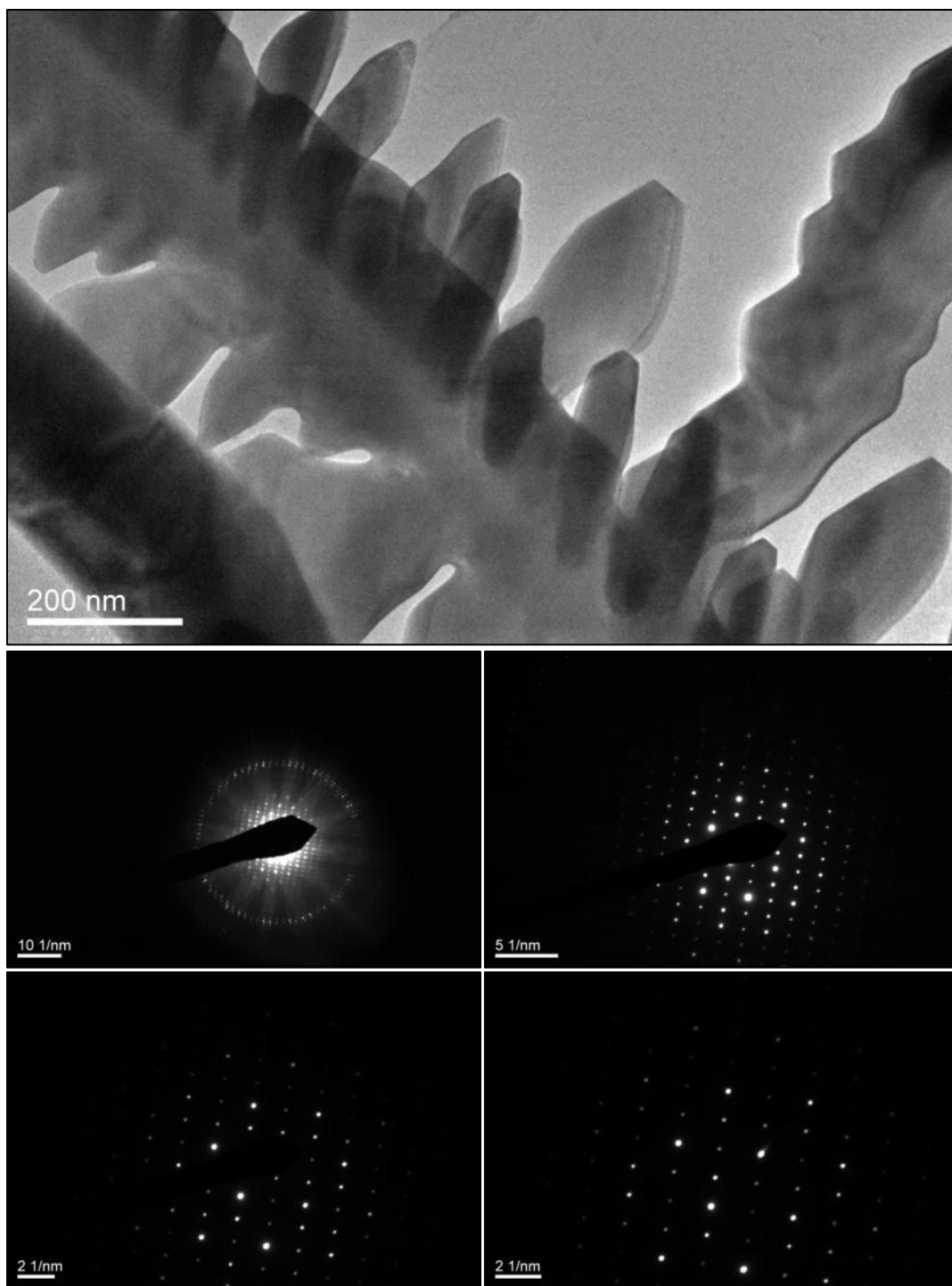
Figure 4-46: DPs of zirconium dendrite in U-40ZrAi5 at various camera lengths, from the top left, 10, 30, 40, 50, 60, 80, 100, 120, 150, and 200 cm.
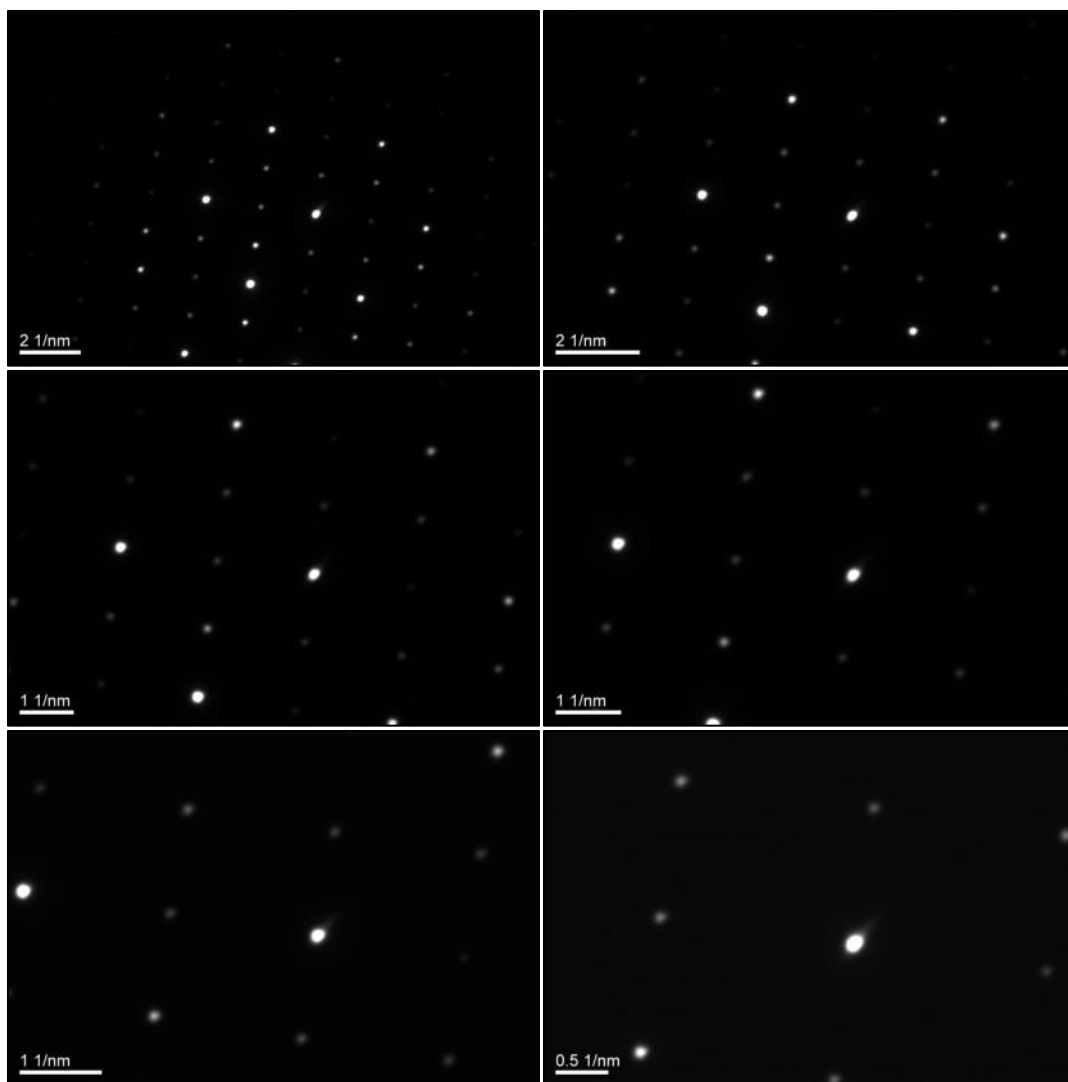
Figure 4-46: Continued.
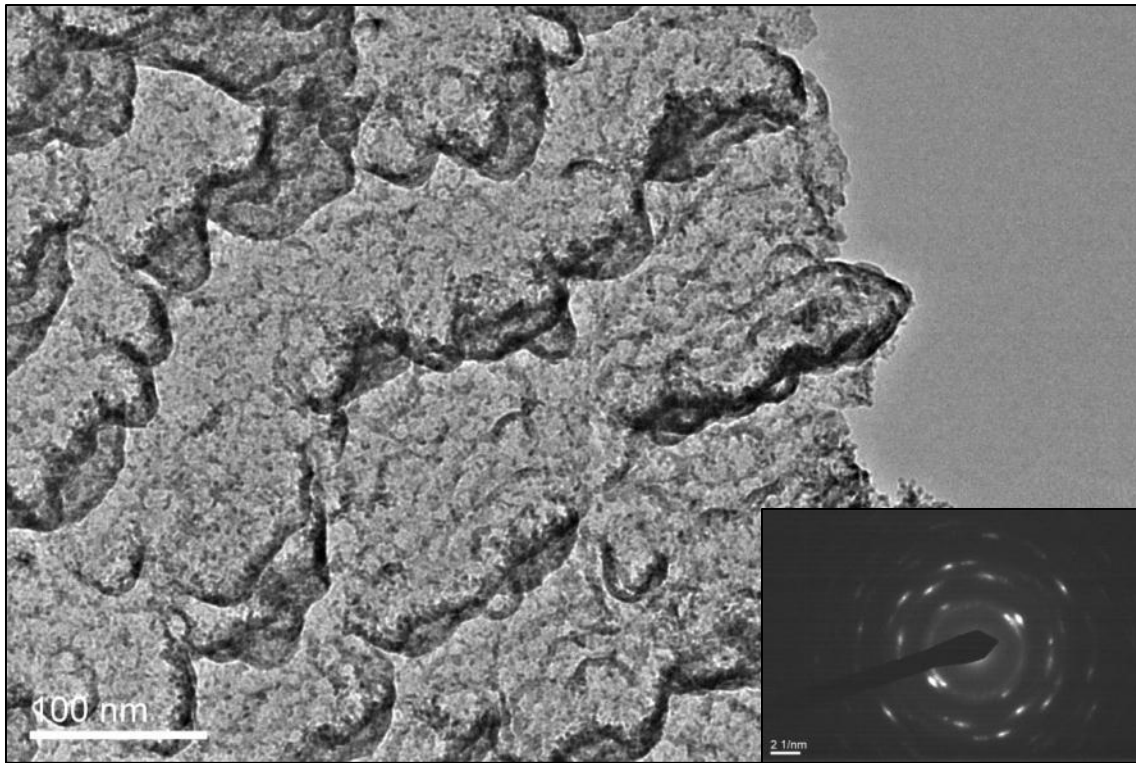
Figure 4-47: Electrochemically contaminated area in U-40ZrAi5.

A representative electropolishing artifact and some secondary phases found from the alloy are displayed in Figs. 4-47 and 4-48. The inserted DP in Fig. 4-47 has elongated spot type ring pattern that implies very little radiation damage but significant potential surface contamination likely caused by redeposition from the electropolishing process.
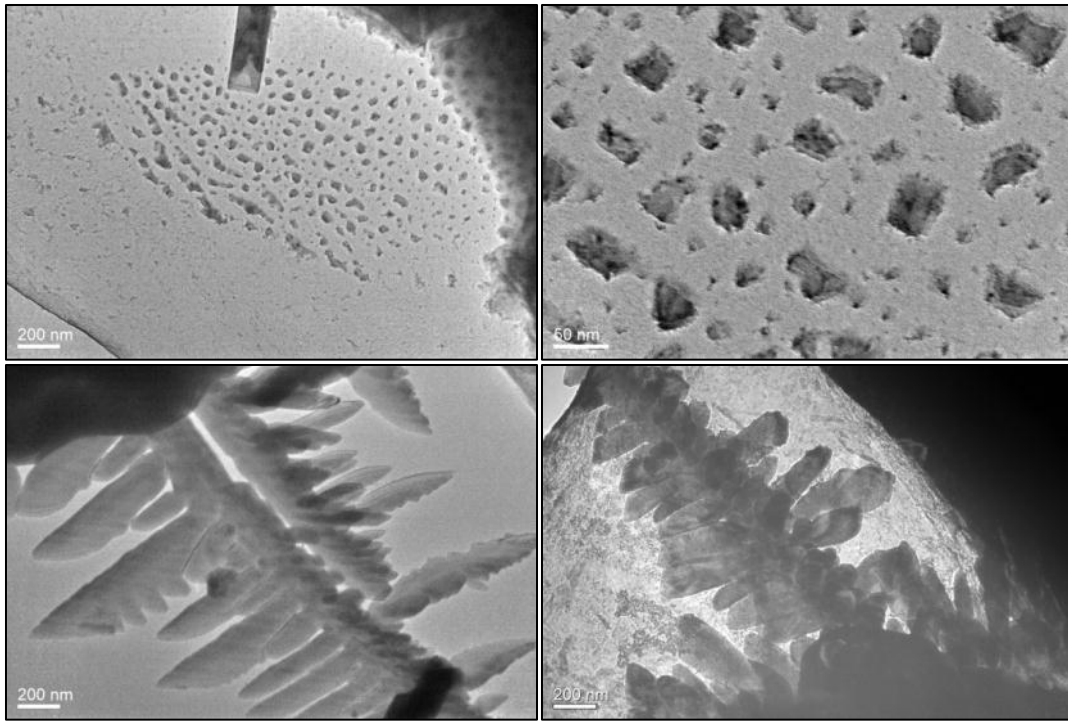
Figure 4-48: Secondary phase particles found within U-40ZrAi5.

4.4.2.4 U-40ZrHi1

Figure 4-49 shows numerous bubbles induced by helium ion-beam irradiation in U-40ZrHi1. Average bubble size and density estimated by TEM image analysis were (6.0 ± 1.5) nm and (250 ± 40) /μm^2, respectively. This feature is apparently vacancy-type defect structure since similar feature was observed as holes from very thin regions of the specimen as shown in the last image of Fig. 4-49. Note bright Fresnel fringes surrounding the holes indicating underfocus [165]. In contrast, darker contrast features are electropolishing artifacts, similar with the ones shown in Fig. 4-41(bottom left) obtained from unirradiated alloy, U-40ZrAi0.
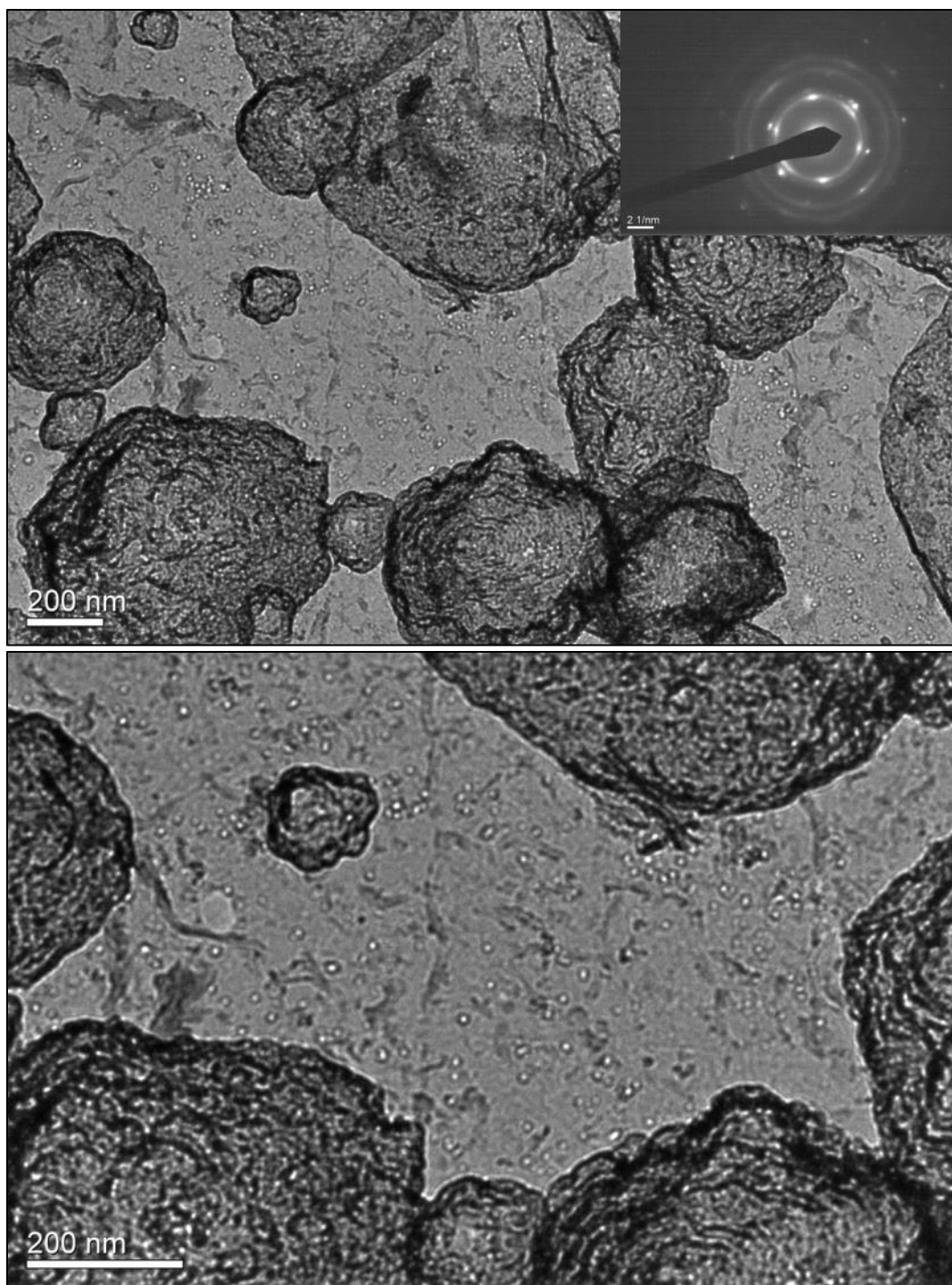
Figure 4-49: Bubbles (brighter dots) induced from 140 keV He$^+$ ion-beam irradiation found in U-40ZrHi1.
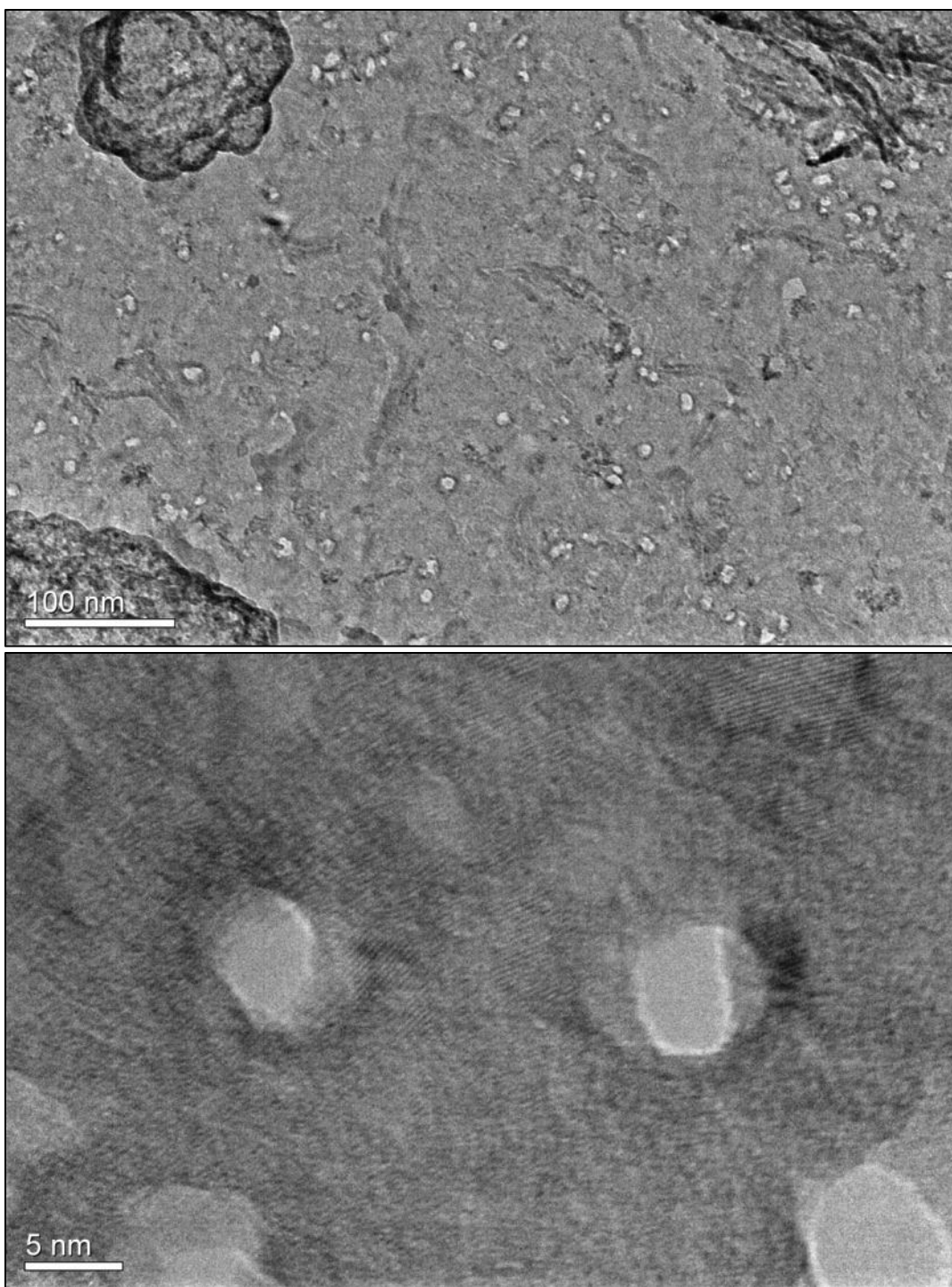
Figure 4-49: Continued.

170
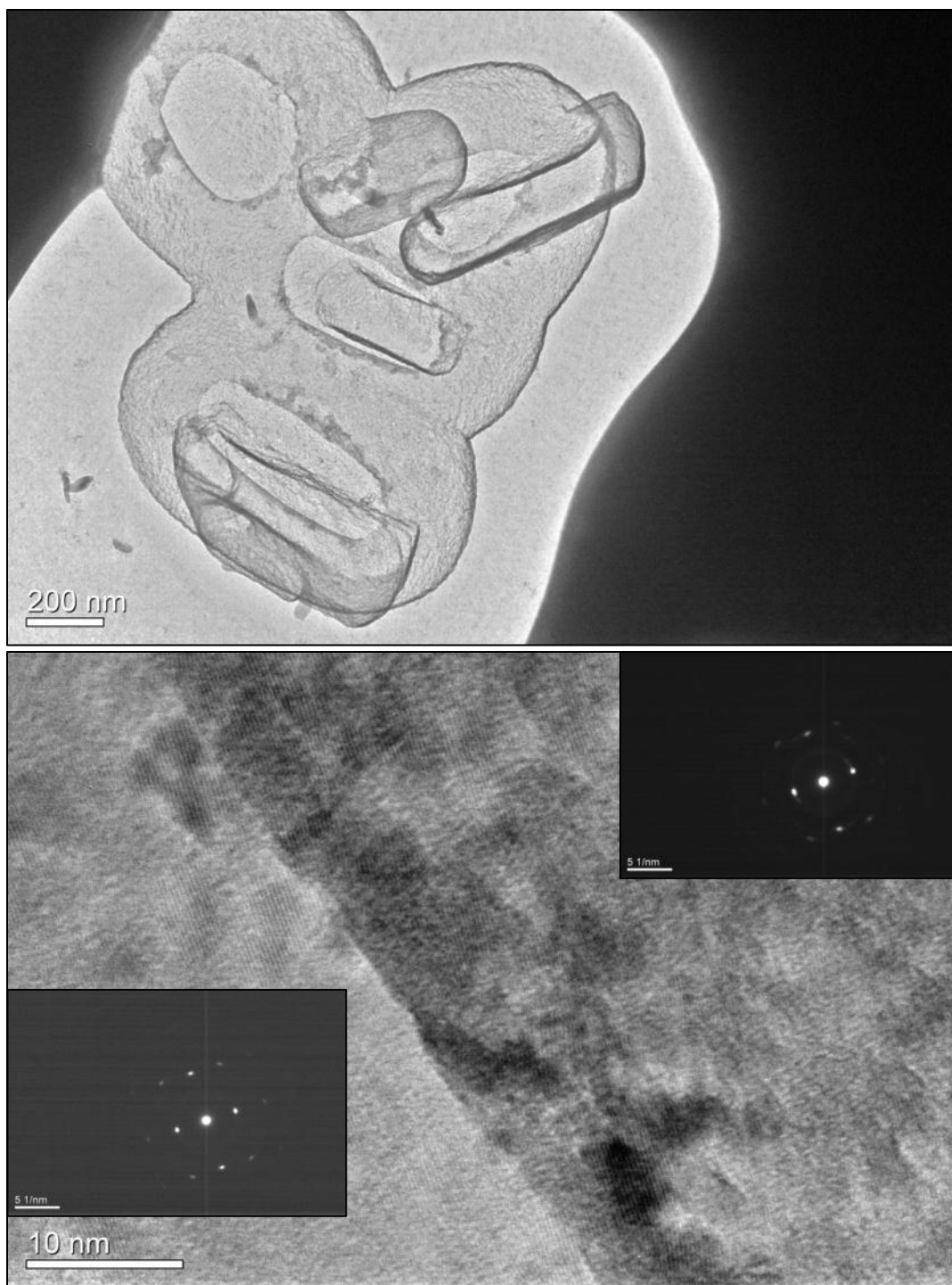
Figure 4-50: Combined-torus shaped electropolishing artifacts found from U-40ZrHi1.
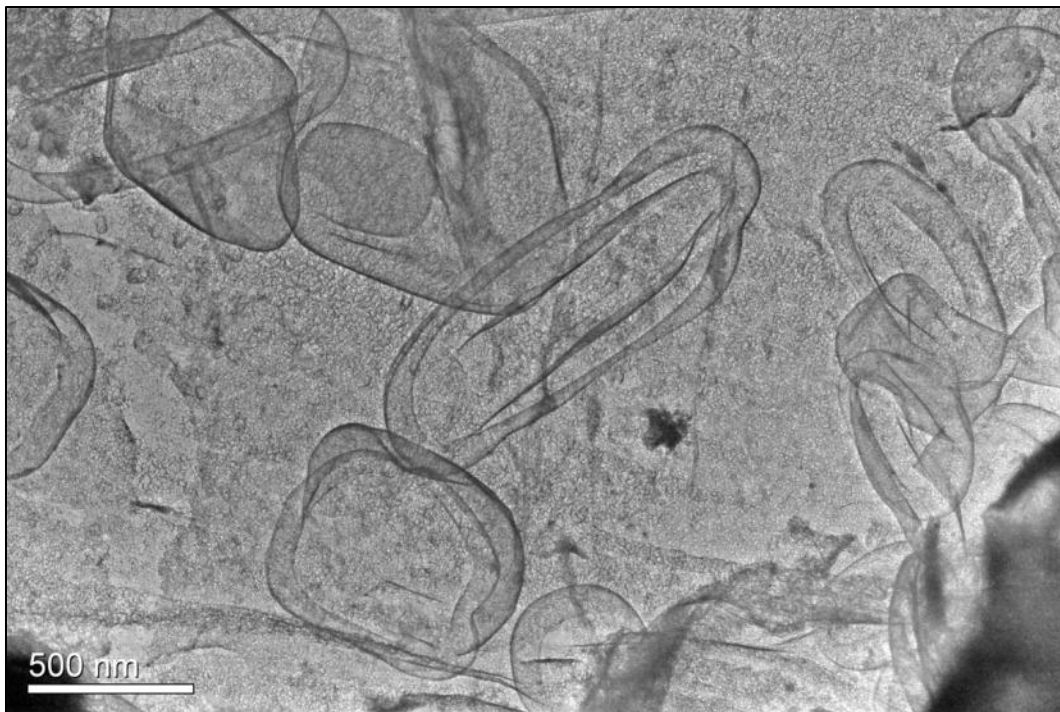
Figure 4-51: Overlapped larger torus-like artifacts found from U-40ZrAi1.

Figures 4-50 and 4-51 show that several other types of defect structures, which were not necessarily formed due to radiation damage, but were rather likely to have originated from electropolishing. The combined tori shown at the top of Fig. 4-50 are over 1 µm large and have comparable contrast with surrounding material. To consider the features as radiation induced vacancy-type defects, one must assume that the thickness of the torus complex is oddly thin compare to the planar dimensions of the features, which certainly exceed the area thickness transparent under 200 keV electrons ($< \sim 100$ nm).
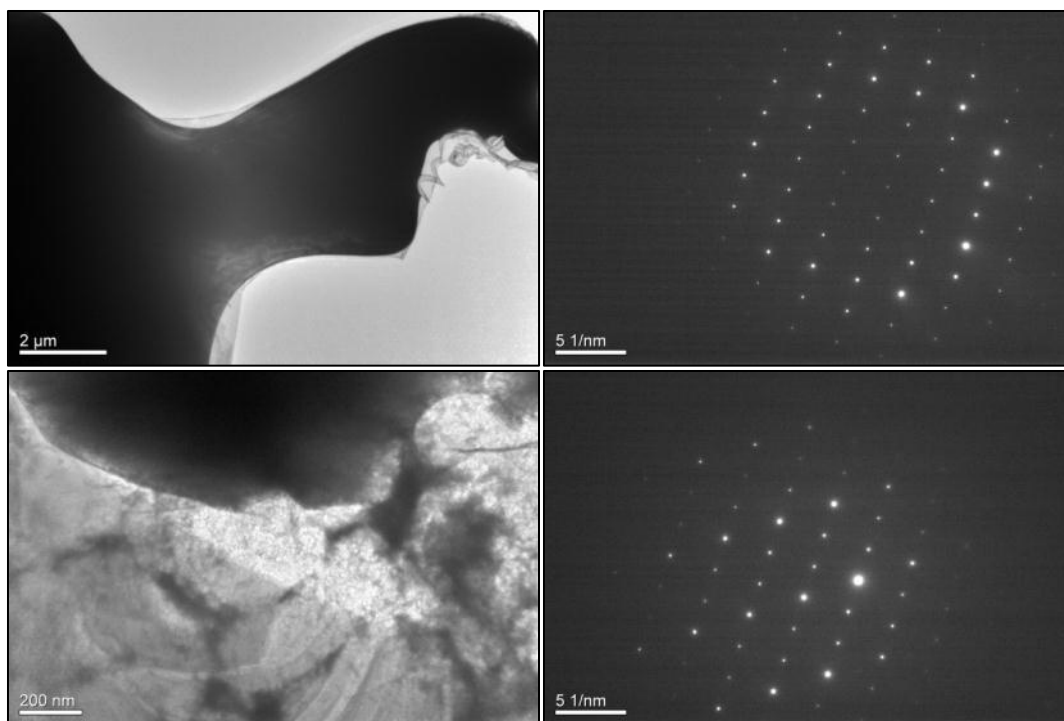
Figure 4-52: DPs (right) of two over-polished regions (left) of U-40ZrHi1.

Even aside from the impractical assumption noted above, similar contrast with background is still unlikely. More definitely, the crystalline nature of the region is vividly continuous and undisturbed by the boundary of the feature as shown in Fig. 4-50(bottom). Also, the DPs taken from in and outside of the torus were spot type patterns without any meaningful difference between them. Another group of torus-like artifacts is shown in Fig. 4-51. These are likely thin layers of redeposited compounds from electropolishing, which can be deduced from darker contrast, occurred from overlapped features. These artifacts indicated local fluctuation of electropolishing conditions caused by improper specimen placement on the electrode, as shown in Fig. 3-5. Specimens were often moving slightly under biased vertical electrolytic jet flow, slightly off from the

center of the specimen. Over-thinning could have been occurred sweeping away entire irradiation damaged layer of local regions. The absence of radiation damage features is evident in Figs. 4-50 and 4-51, showing the artifacts not along with sharp straight lines generated from mechanical thinning of the specimen. Moreover, the DPs obtained from several regions of the alloy imply undamaged atomic crystals as shown in Fig. 4-52.

4.4.2.5 U-40ZrHi5

In the highly irradiated U-40Zr alloy (U-40ZrHi5), numerous bubbles were observed in several regions as shown in Fig. 4-53. Bubbles in the figure have similar morphologies with the bubbles found in U-40ZrHi1. The features were regarded as irradiation induced bubbles because the morphologies and dimensions of the features were fairly identical in both alloys but number densities were proportional to the irradiation doses. Average bubble size and density estimated by TEM image analysis were (5.2 ± 1.2) nm and (1460 ± 30) /μm^2, compared to (6.0 ± 1.5) nm and (250 ± 40) /μm^2 in U-40ZrHi1, respectively.

Figure 4-54 shows that the hex-mesh structure was repeatedly found in U-40ZrHi5, just as it was in U-40ZrAi5. Again, no DP was obtained from the extremely thin area because the diffracted electrons could not generate a recordable intensity. This structure is likely an over-polished region having numerous bubbles. Note the bubbles shown in Fig. 4-53 and the holes inside the hex-rings in Fig. 4-54 resemble each other, both in shapes and dimensions.

174
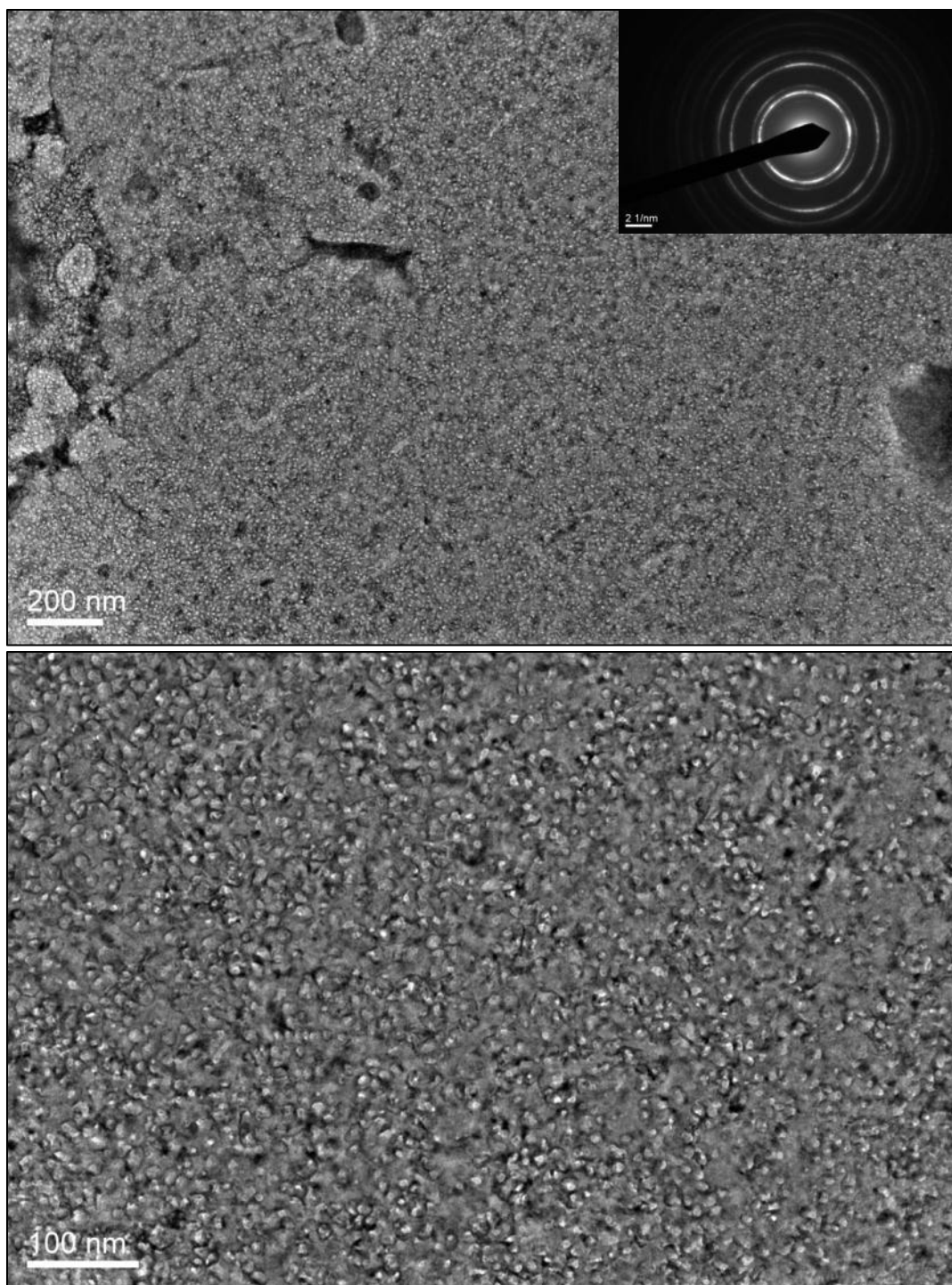
Figure 4-53: Numerous bubbles induced from 140 keV He$^+$ ion-beam irradiation found in U-40ZrHi5.
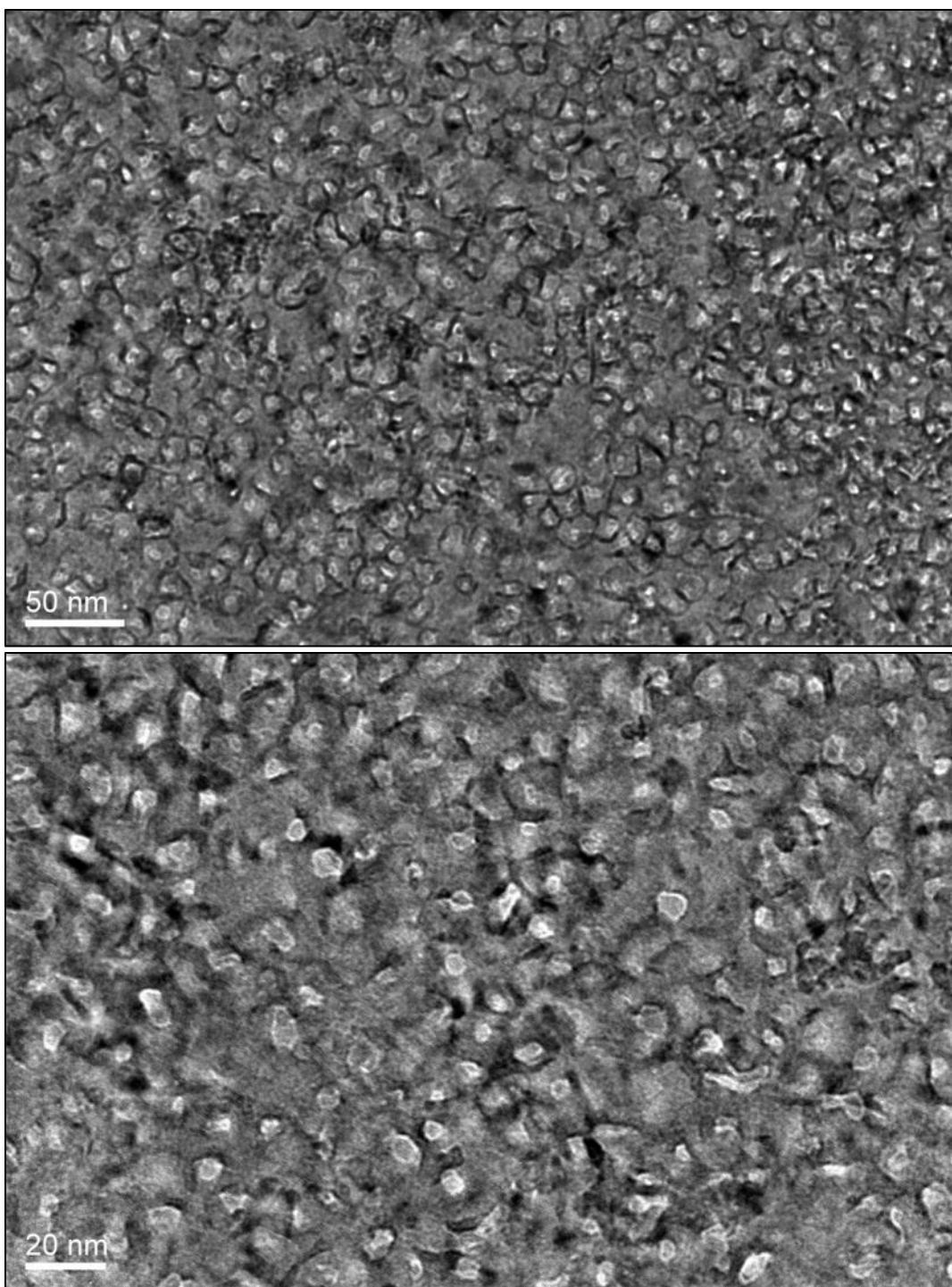
Figure 4-53: Continued.
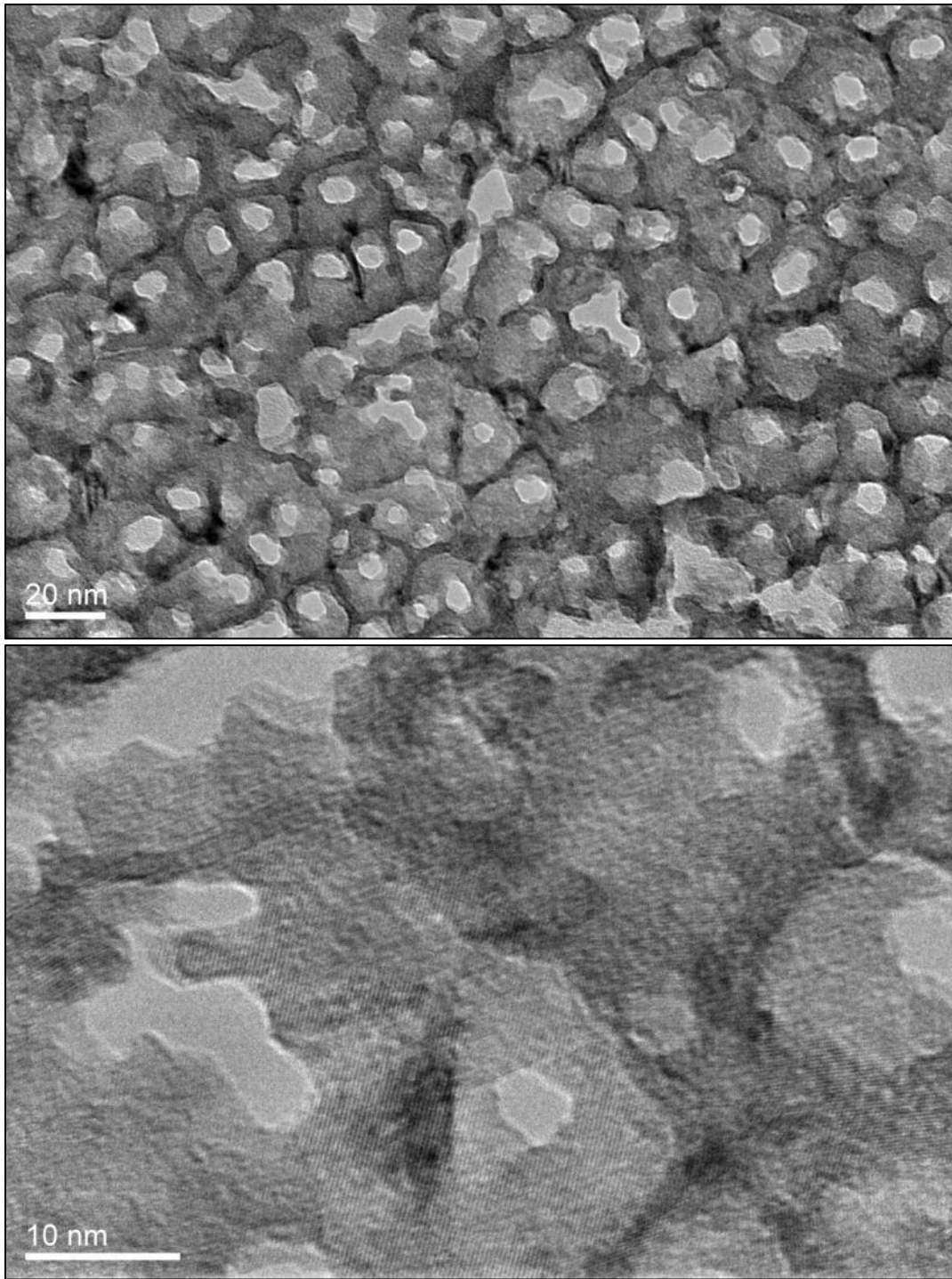
Figure 4-54: Highly porous hex-mesh structure in U-40ZrHi5.

The average size and density of the center holes of the hex-mesh structure estimated from Fig. 4-54(top) are (5.8 ± 1.5) nm and (670 ± 70) /μm^2, respectively, thus the dimension is comparable to the bubble size, (5.2 ± 1.2) nm, while the density is less than half of the bubble density, (1460 ± 30) /μm^2. Therefore, the hex-mesh structure could be considered as an over-polished region having numerous bubbles. In other words, different degree of electropolishing on identical nanostructure of irradiated U-40Zr alloy could yield the two different types of morphologies shown in Figs. 4-53 and 4-54.

The surface morphology of zirconium dendrites was again observed in this alloy as vividly shown in Fig. 4-55(top). Waiving stripes appeared on the surface of several secondary arms of the dendrite that ought to be distinguished from zirconium crystal clearly shown in Fig. 4-55(bottom). The defect-free single crystal is vividly extended over ~2000 nm^2 wide, although the area is supposed to be relatively thicker as an electron transparent area of zirconium than that of uranium-rich phases. The thicker dimension of the dendrite is indicated from the first and second order Laue zones (FOLZ and SOLZ) appeared in the DP in Fig. 4-56(top left) with six Kikuchi lines crossing the center of the zeroth order Laue zone (ZOLZ). Diffraction patterns of U-rich medium have not been exhibited higher order Laue zone (HOLZ).

The presence of zirconium dendrites was unique in U-40Zr alloy among all four compositions of U-Zr alloys (U-0.1, 10, 20, and 40Zr) observed using TEM and it is matched with the EPMA observation shown numerous zirconium precipitates in U-40Zr alloy (Fig. 4-10). The dendrites were also frequently discovered from the alloy during the TEM observation, regardless of the thermal or irradiation history of the alloy.
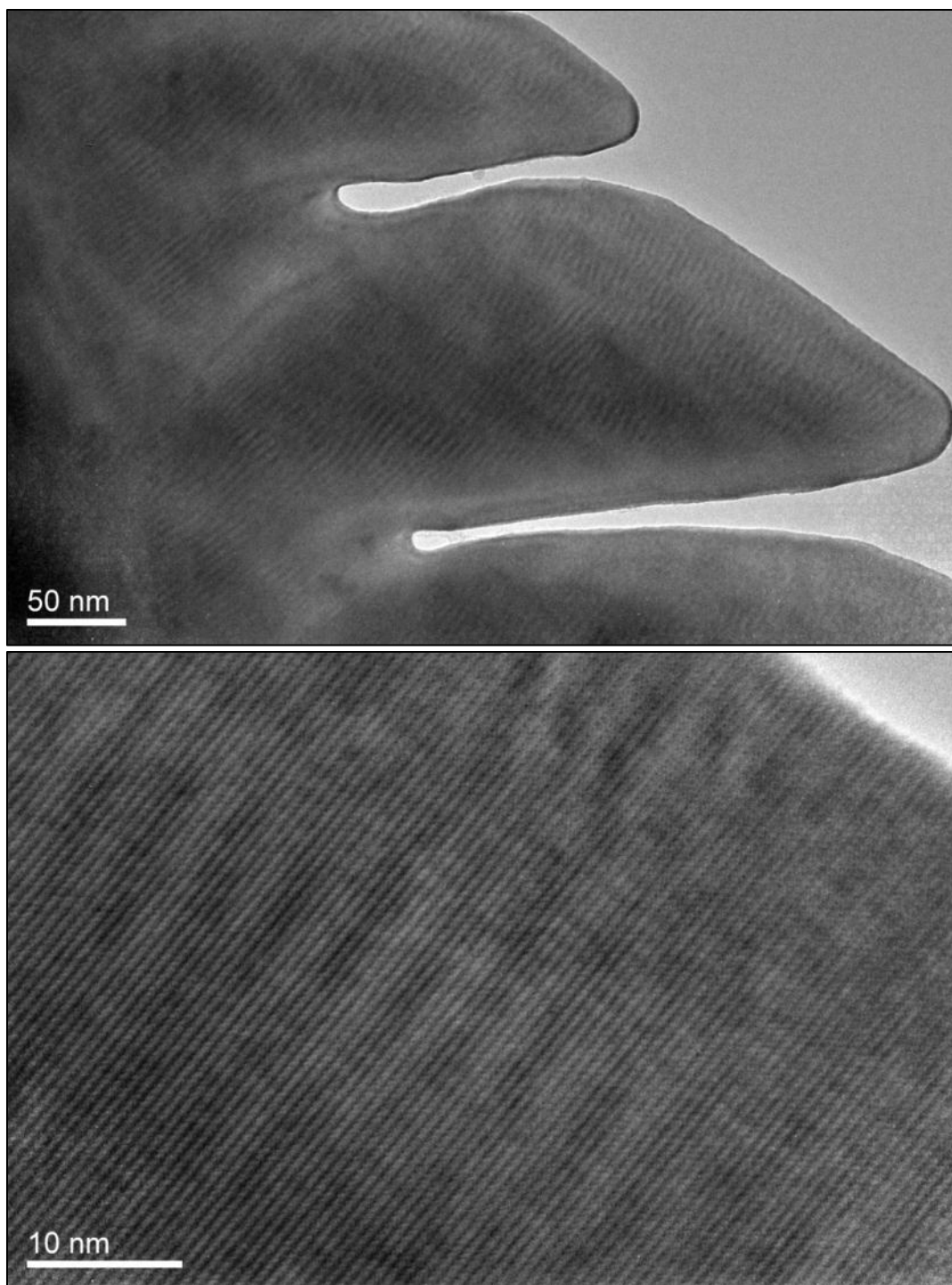
Figure 4-55: Surface morphology (top) and single crystal structure (bottom) of zirconium dendrite in U-40ZrHi5.
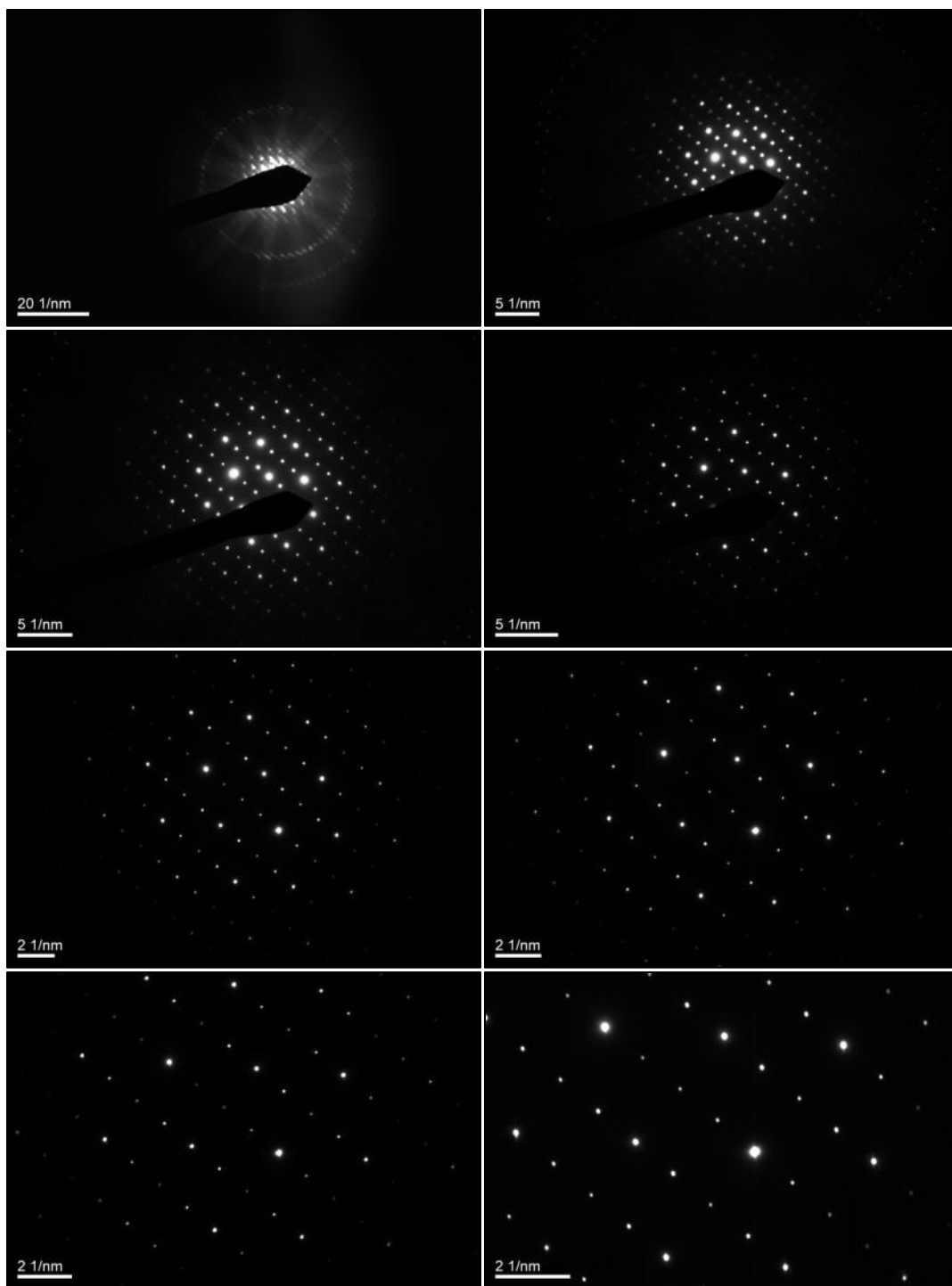
Figure 4-56: DPs of zirconium dendrite in U-40ZrHi5 at various camera lengths, from the top left, 8, 20, 25, 30, 40, 50, 60, and 80 cm.

180

4.4.3 U-10ZrAi5

Electropolishing of the two phase alloys (U-10Zr and U-20Zr) was truly problematic since no electric potential below 40 V was successful to prepare a pure metallic surface. Specimen surfaces were notably oxidized by applying the electric potentials. Oxidation was observed as black debris formed on electropolished surface. The debris was removable using ultrasonic vibrator, however cracking and severe loss of the prepared thinned area was observed. This specimen corrosion was revealed as due to preferential etching of Zr-rich phase precipitates or matrix phase lamellae, depending on alloy composition. Basically, the Zr-rich phase particles or lamellae dissolved more slowly, creating an irregular surface that disturbed the electrolyte flow to be more turbulent. Therefore, the specimen surface was exposed to unstable flow under applied electric potential thus oxidized. Once formed, the oxidized regions incurred additional instability to the flow, which further deteriorated the quality of the alloy specimens.

To resolve the issue, higher voltages ranging from 60 V to 100 V were applied to attempt to match the relative removal rates for two different phases existing in the alloys, δ-UZr$_2$ and α-U. Higher voltages were also beneficial since the specimens can be thinned under relatively uniform condition with a decreased electropolishing time, considering that each specimen was fixed only under hydraulic pressure of vertical downflow of electrolyte other than its own weight. Two regions in U-10ZAi5 prepared applying 100 V are shown in Fig. 4-57. Even higher voltages up to 150 V were tested but perforation was occurred too fast, often less than 10 s.

181
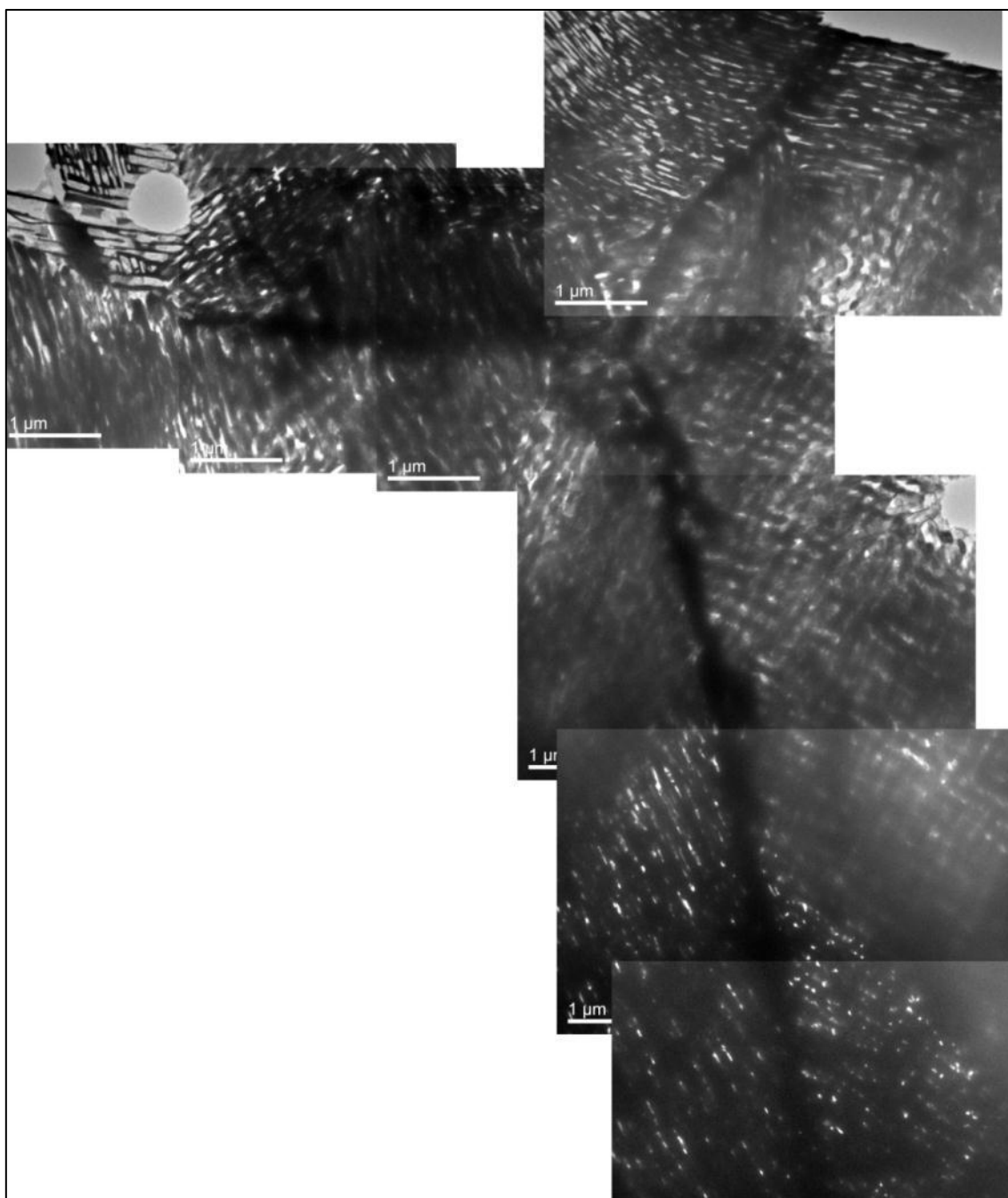
Figure 4-57: Nanostructure of U-10ZrAi5. (Grain boundaries within two phase lamellae structure were electrochemically etched out due to preferential removal of U-rich phase medium.)
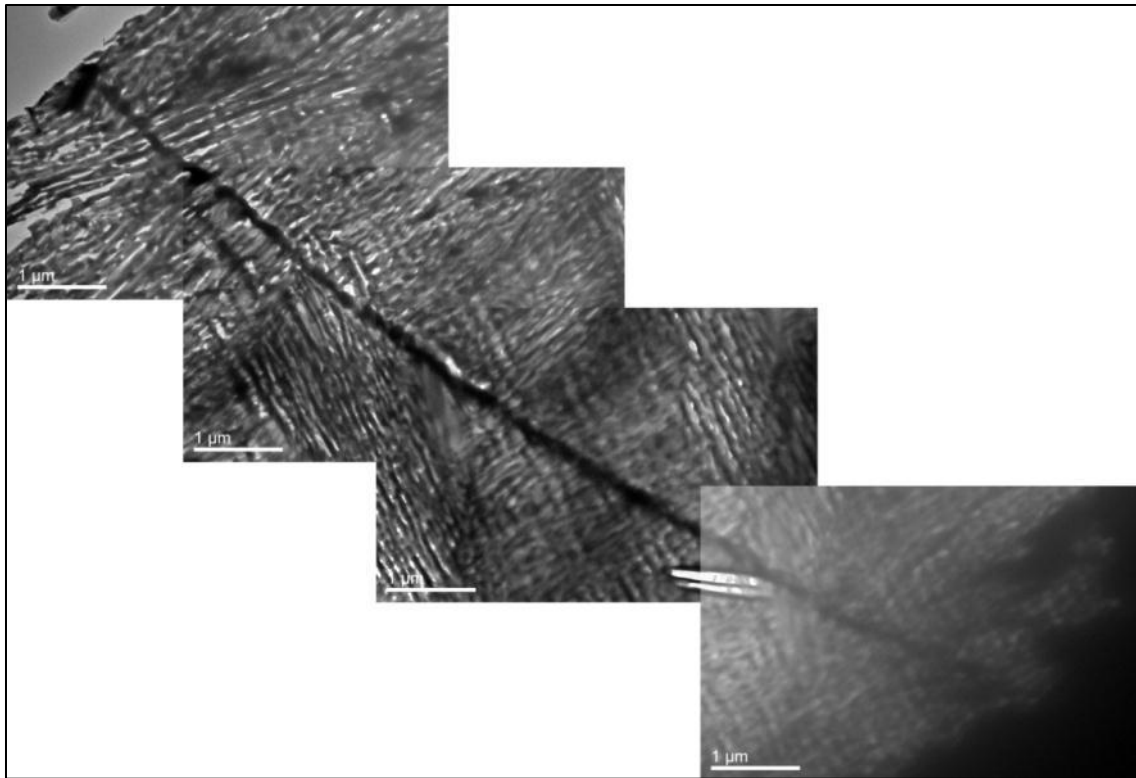
Figure 4-57: Continued.

Observable areas prepared using higher voltages were as large as ~20 μm wide as shown in Fig. 4-57 were extended grain boundary zones are visible. On the other hand, the sizes of electron transparent areas in low voltage prepared specimens were only ~1 μm wide as shown in Fig. 4-58 even though the two phase structure of the alloy is quite visible. However, the two phase lamellae structure of the alloys was not always distinctively contrasted when the area was very thin. Note the specimen boundaries shown in Fig. 4-58 have similar contrasts for both phases in some locations.
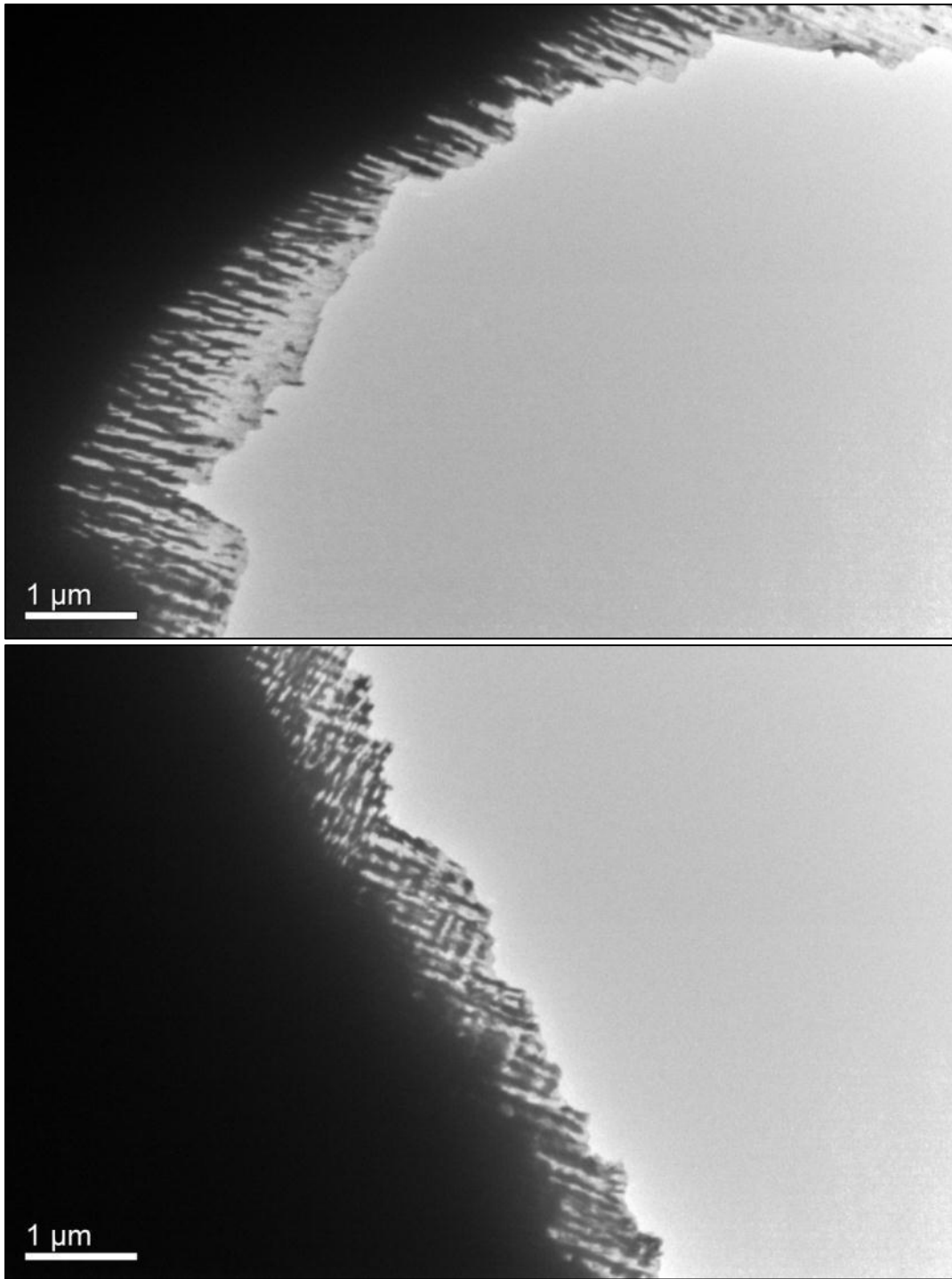
Figure 4-58: Low voltage (40 V) electropolished two phase lamellae structure of U-10ZrAi5.
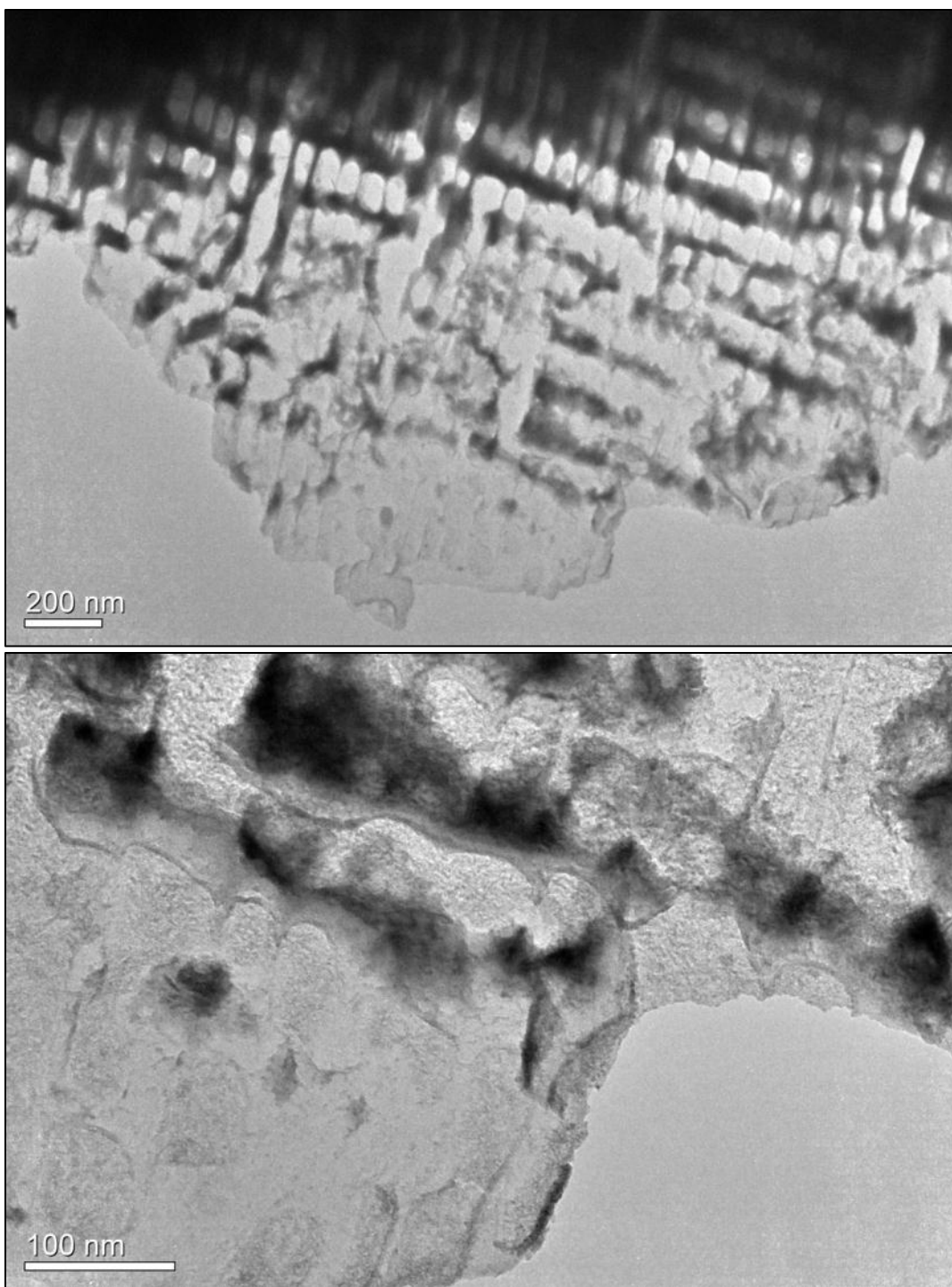
Figure 4-58: Continued.
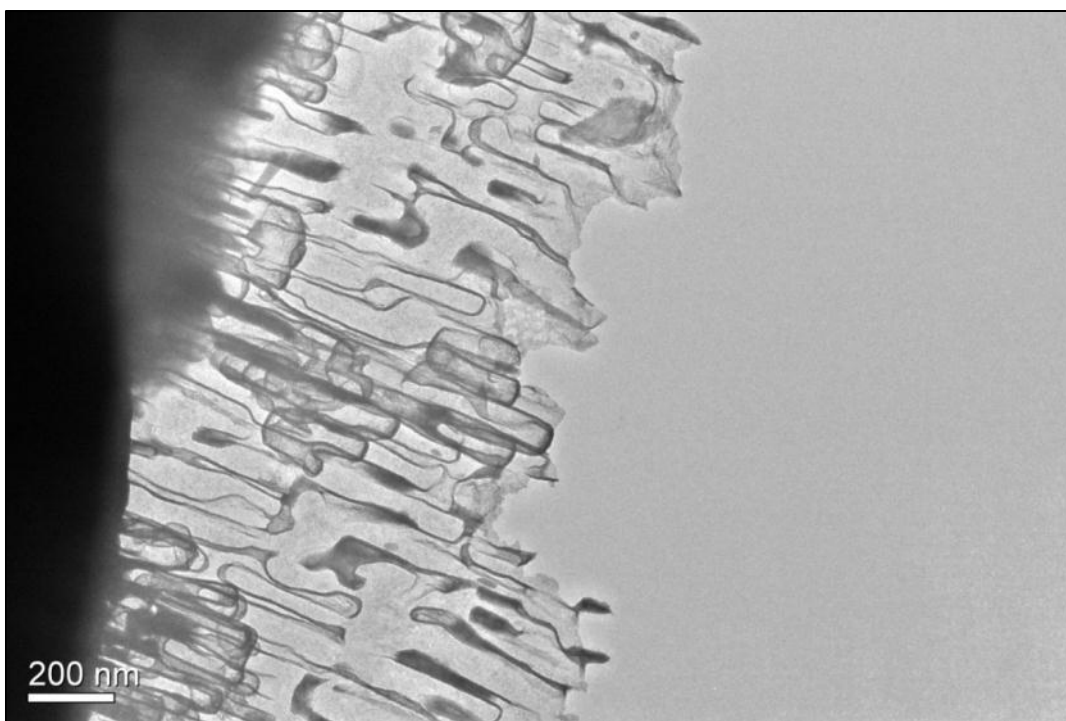
Figure 4-58: Continued.

4.4.3.1 *In-situ* Heating of U-10ZrAi5

A U-10Zr alloy was prepared applying high voltages (> 60 V) to be used for *in-situ* heated experiments using a TEM (JEOL JEM-2010). Bright field images of representative two phase structure of U-10Zr alloy, before and after the heating up to 810 °C, are shown in Fig. 4-59. The inserted DP was obtained at ambient temperature (~25 °C). It should be stressed that the darker precipitates in the figure ought to be δ-UZr_2 phase to be consistent with the lever rule applied on U-Zr binary phase diagram. To confirm this, the composition of the region was estimated as (10.3 ± 0.3) wt% zirconium assuming the darker precipitates are δ-UZr_2 phase. Therefore, darker contrast of δ-UZr_2 than matrix α-U phase indicates thicker nature of Zr-rich phase due to its resistive nature to the electropolishing.

Phase boundaries between the two phases are well shown in Fig. 4-59; the α-U/δ-UZr_2 interphase interfaces are likely coherent allowing only low degree of atomic misfit. The area shown in the figure was over-polished from the irradiated side thus lost radiation damaged layer (i.e. no bubbles). Also, the α-U phase (bright) regions are very thin or completely removed.
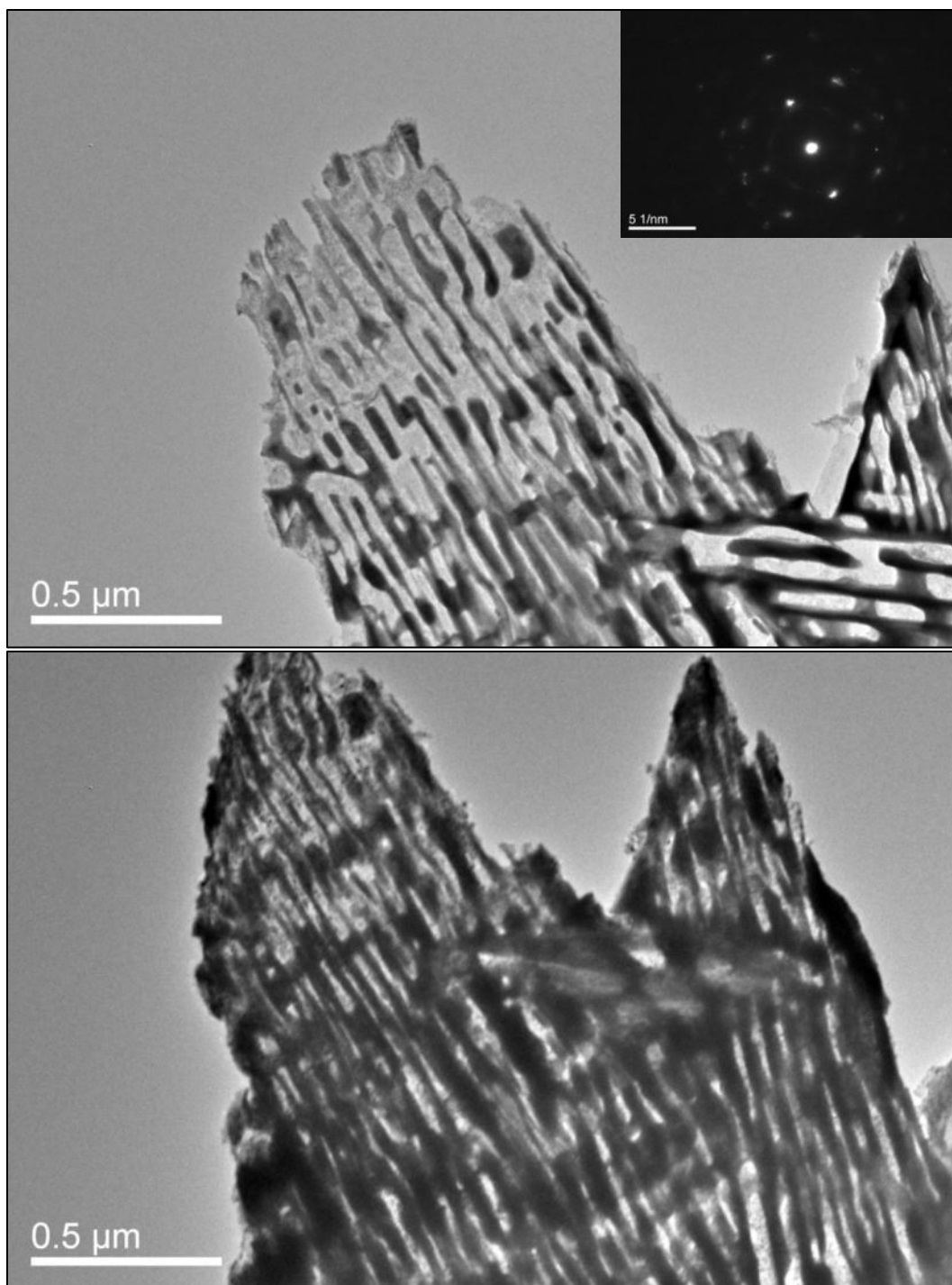
Figure 4-59: Two phase lamellae structure of U-10ZrAi5; before (top) and after (bottom) *in-situ* **heating up to 810 °C.**
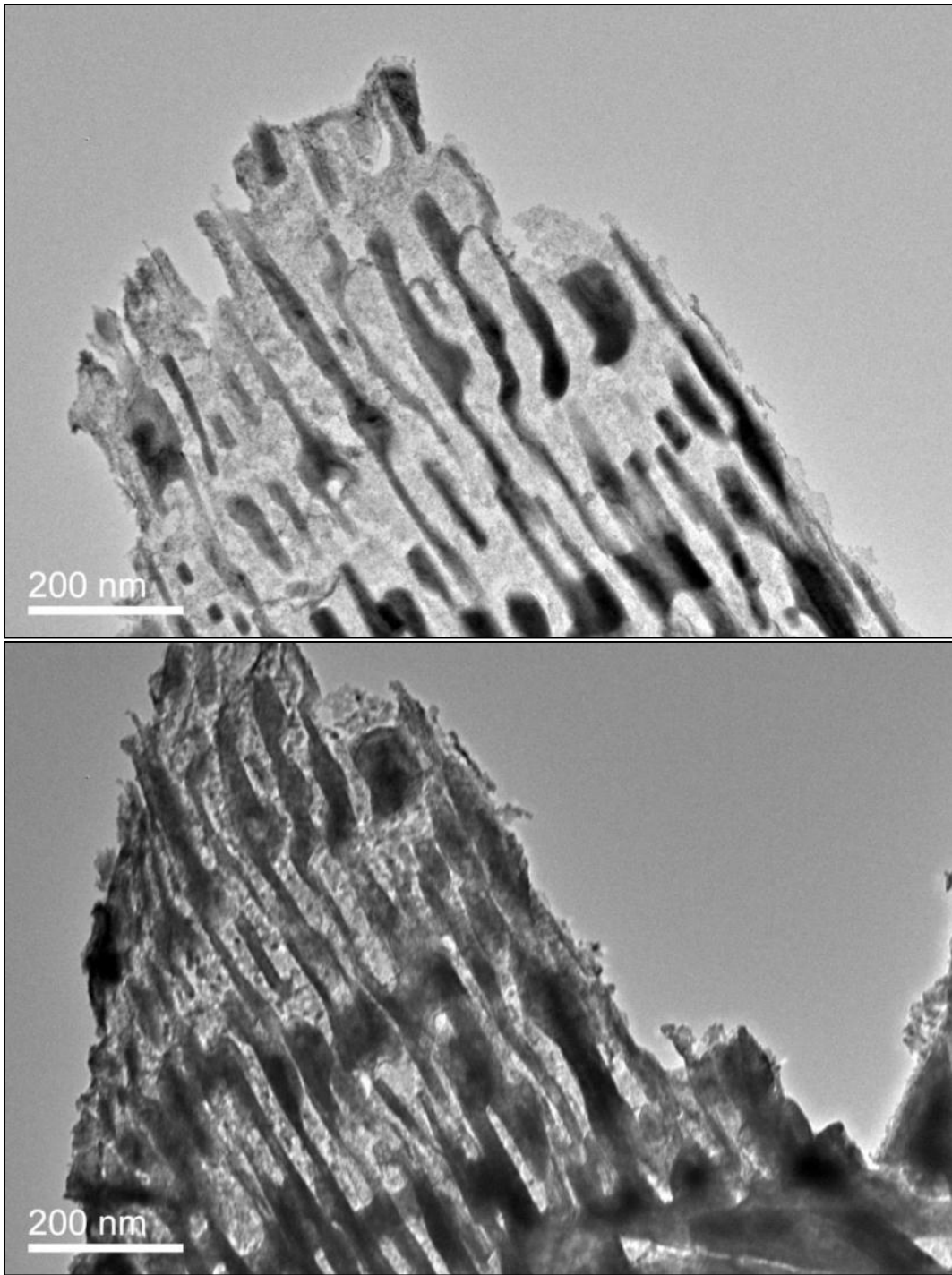
Figure 4-59: Continued.
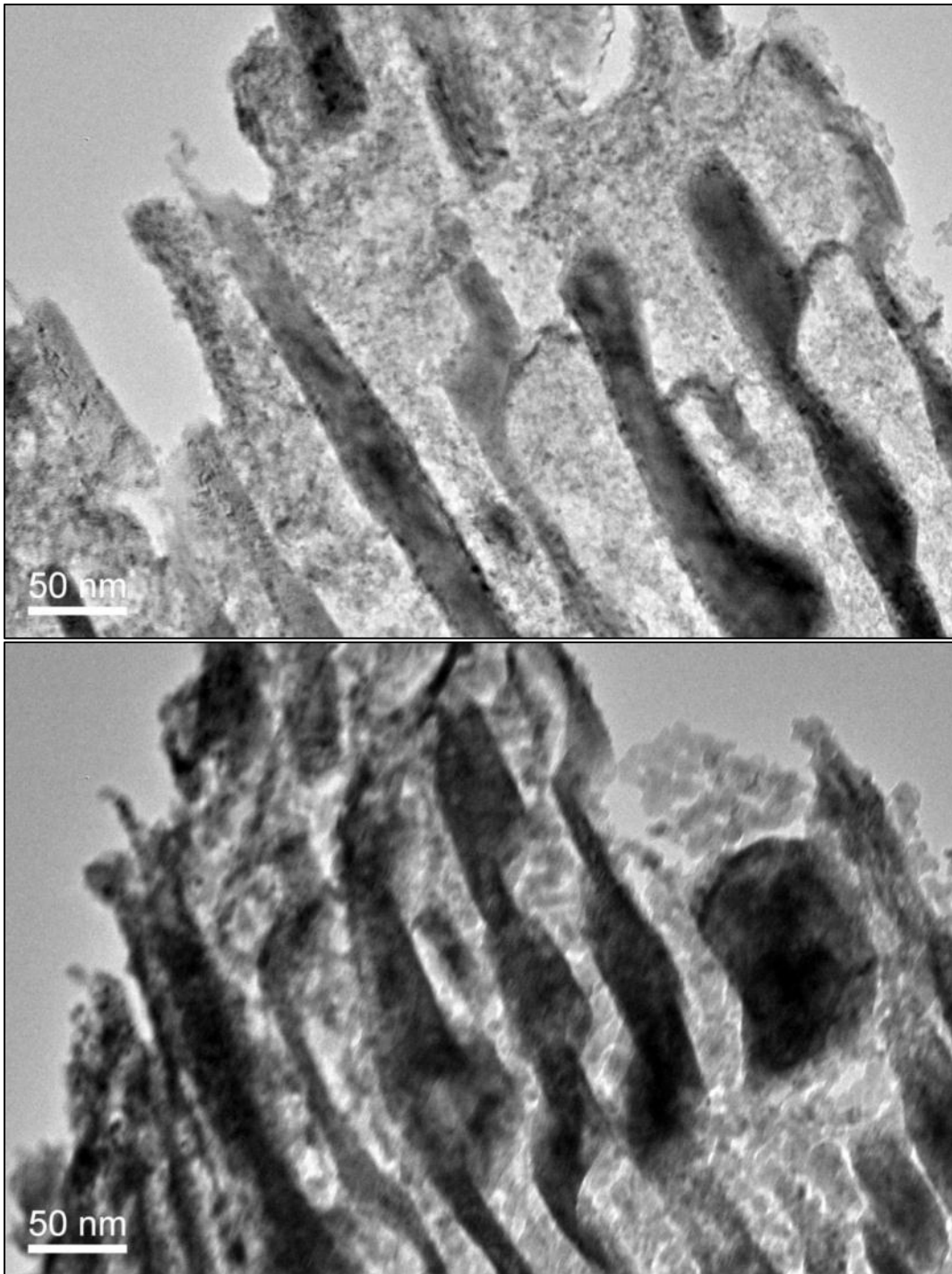
Figure 4-59: Continued.
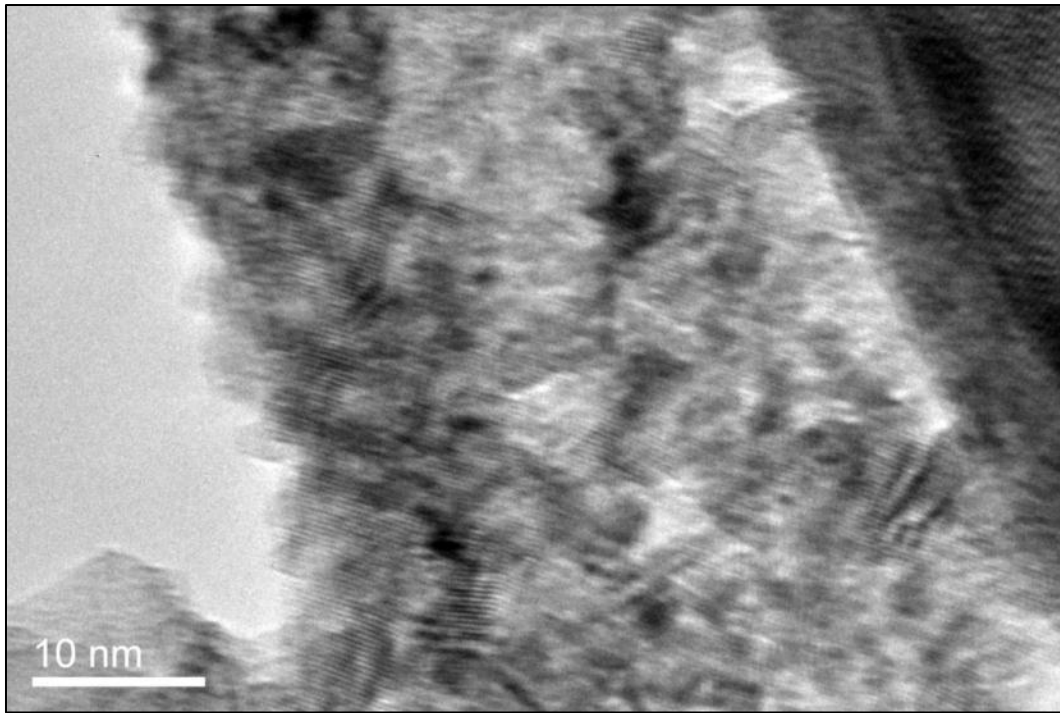
Figure 4-59: Continued.

Another two phase region found in U-10ZrAi5 is shown in Fig. 4-60 and preferential removal of α-U (bright) phase is unmistakable in the figure. The thicker nature of the δ-UZr$_2$ (dark) phase is also evidently shown in Fig. 4-61(top). Although dark fringe on the phase boundary indicates overfocus, the upper (close to electron beam) part of darker precipitates is still in focus while bright lamellae are off from the focus. In the figure, the resilience of the δ-UZr$_2$ phase under electropolishing was reaffirmed from rugged specimen boundary where δ-UZr$_2$ phase precipitates protrude from the fringes of the transparent area. Figure 4-61(bottom) also shows excessively polished α-U phase medium, detached off from adjacent δ-UZr$_2$ phase precipitates.

191
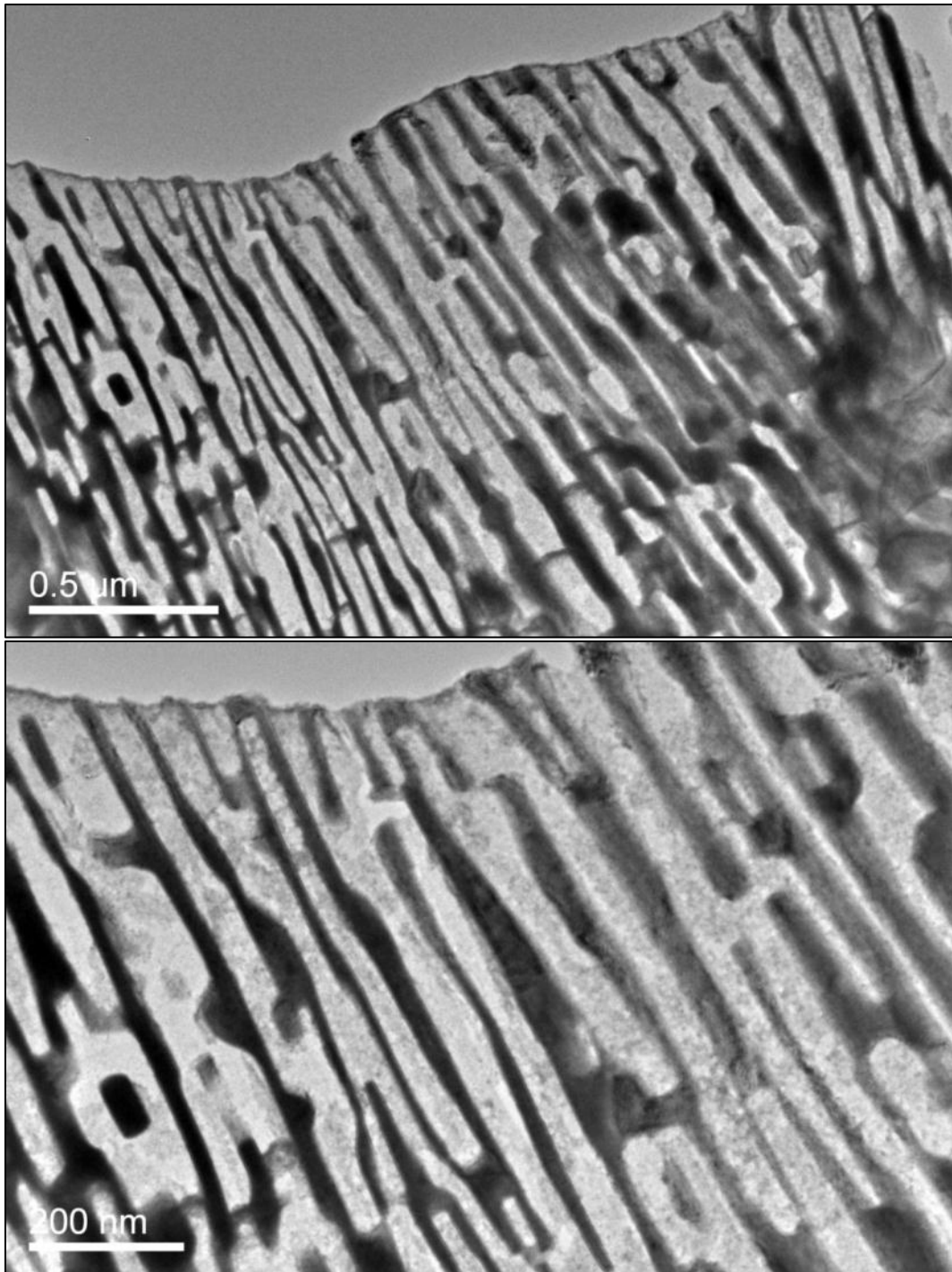
Figure 4-60: As-cast two phase lamellae structure of U-10ZrAi5.
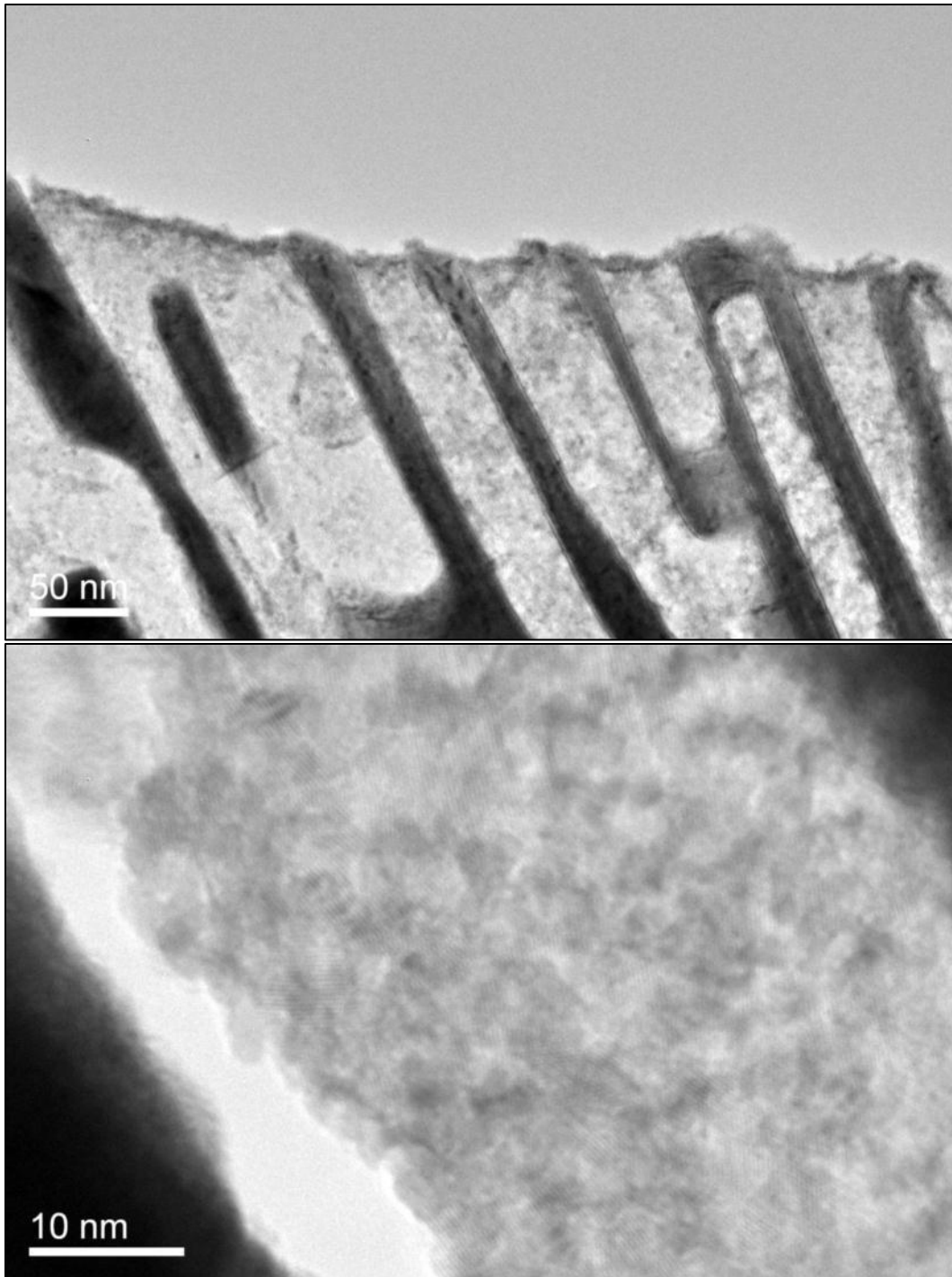
Figure 4-61: Resistive nature of δ-UZr₂ phase to electropolishing shown from U-10ZrAi5.
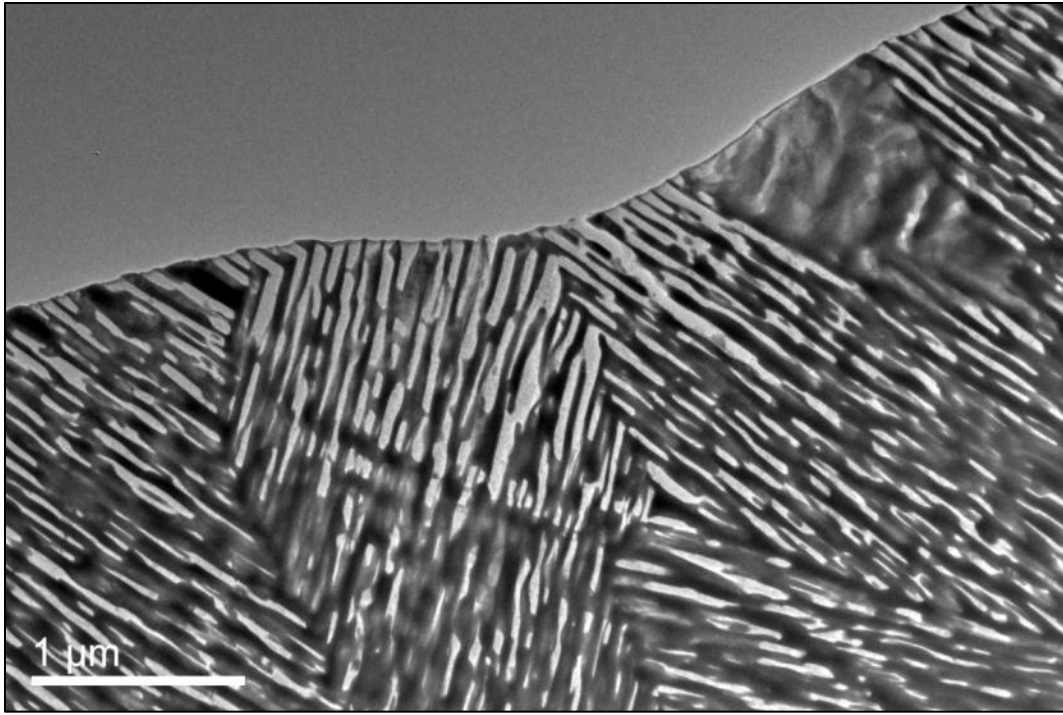
Figure 4-62: Subgrain formation in U-10ZrAi5.

Figure 4-62 shows the coherent nature of the α-U/δ-UZr$_2$ interphase boundary with several subgrains existing within a grain of parent bcc γ phase that were likely formed during the cooling stage of alloy melt-casting. This subgrain formation could be the mechanism for the nearly instant γ phase decomposition observed in Section 4.2 and therefore highlights the infeasibility of quenching the γ phase U-Zr alloys.

An overlapped DP obtained from a translucent area is shown in Fig. 4-63. The displayed area is relatively thick and the overlapped two phase lamellae structure of the area is hinted from indistinct contrast distribution in the figure and the apparent presence of two distinct patterns.

194
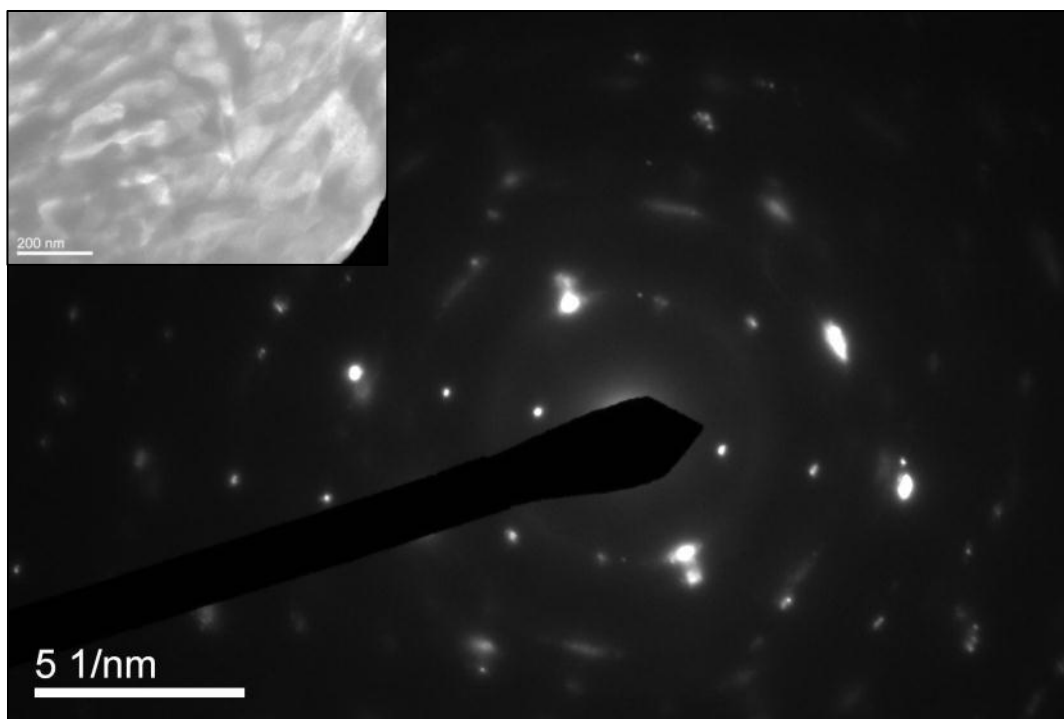
Figure 4-63: SAD pattern of a translucent area in U-10ZrAi5.

Figure 4-64 now shows the culmination of this particular subsection of the research. The images that follow contain a bright field image and a sequence of DPs from that region as the specimen was heated to ~800 °C. During *in-situ* heating TEM of U-10ZrAi5, spot types of DPs were only available from several narrow areas. Moreover, the heated specimen was constantly vibrating at elevated temperatures. As a result, along with temperature increase, it was impractical to keep sequentially imaging spot type DPs of narrow areas using the single tilt heating stage holder. Therefore, ring type DPs were obtained from wide transparent areas at the various temperatures to further investigate the phase transformation behavior of the alloy.
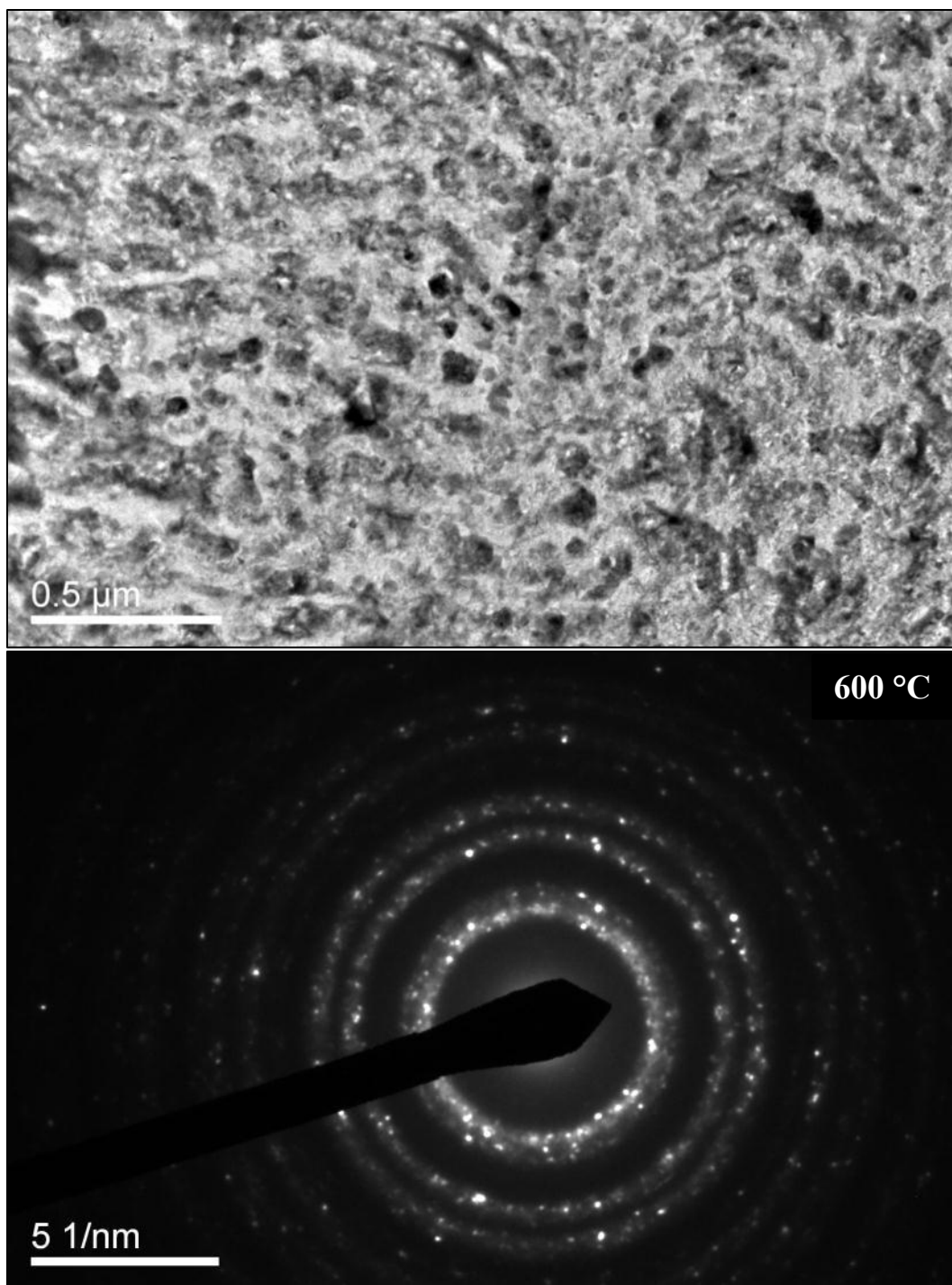
Figure 4-64: DPs of *in-situ* heated U-10ZrAi5, recorded at 600, 610, 615, 620, 640, 650, 665, 670, 675, 685, 693, 700, 710, 720, 730, 743, 758, 773, and 800 °C
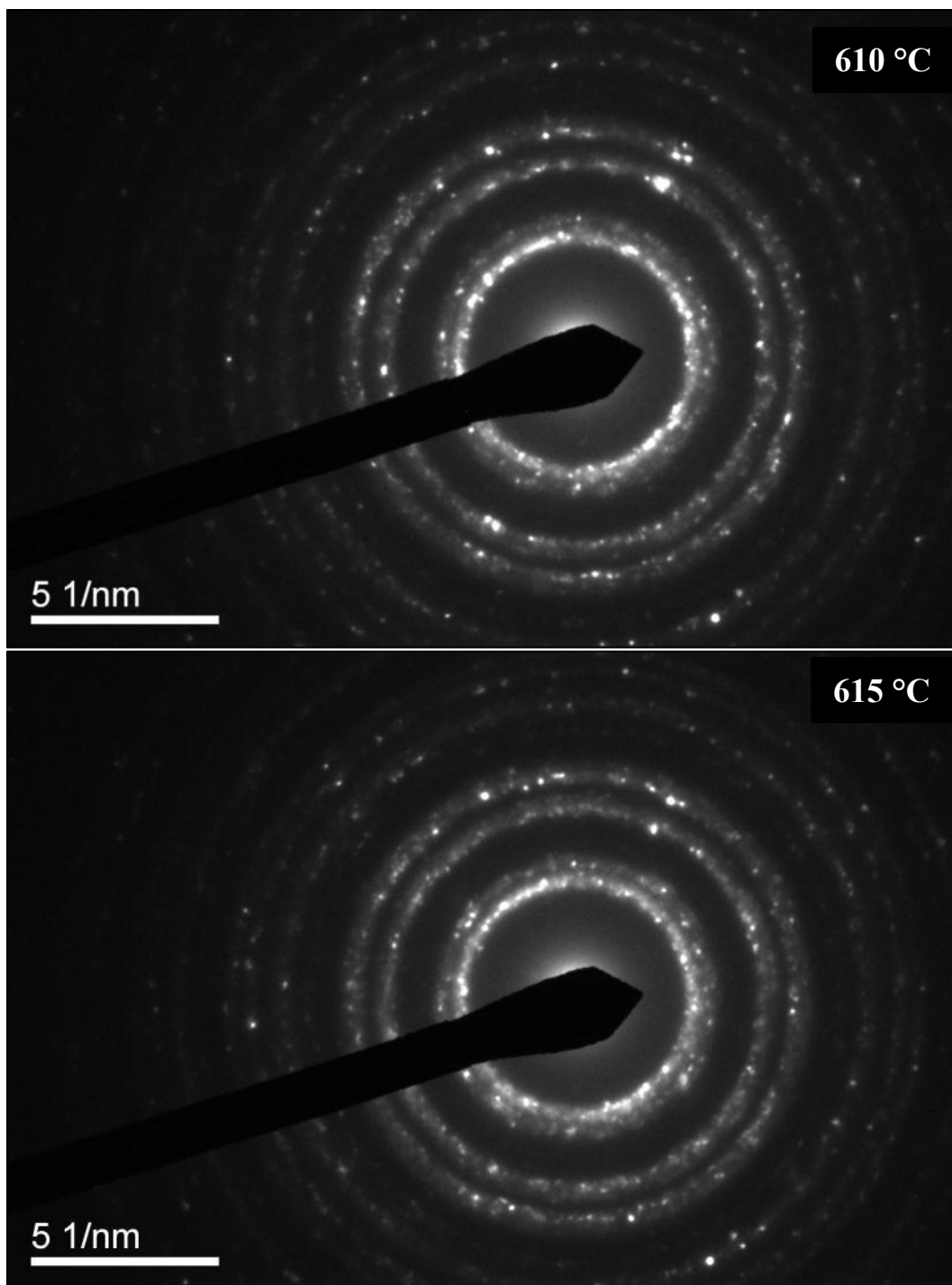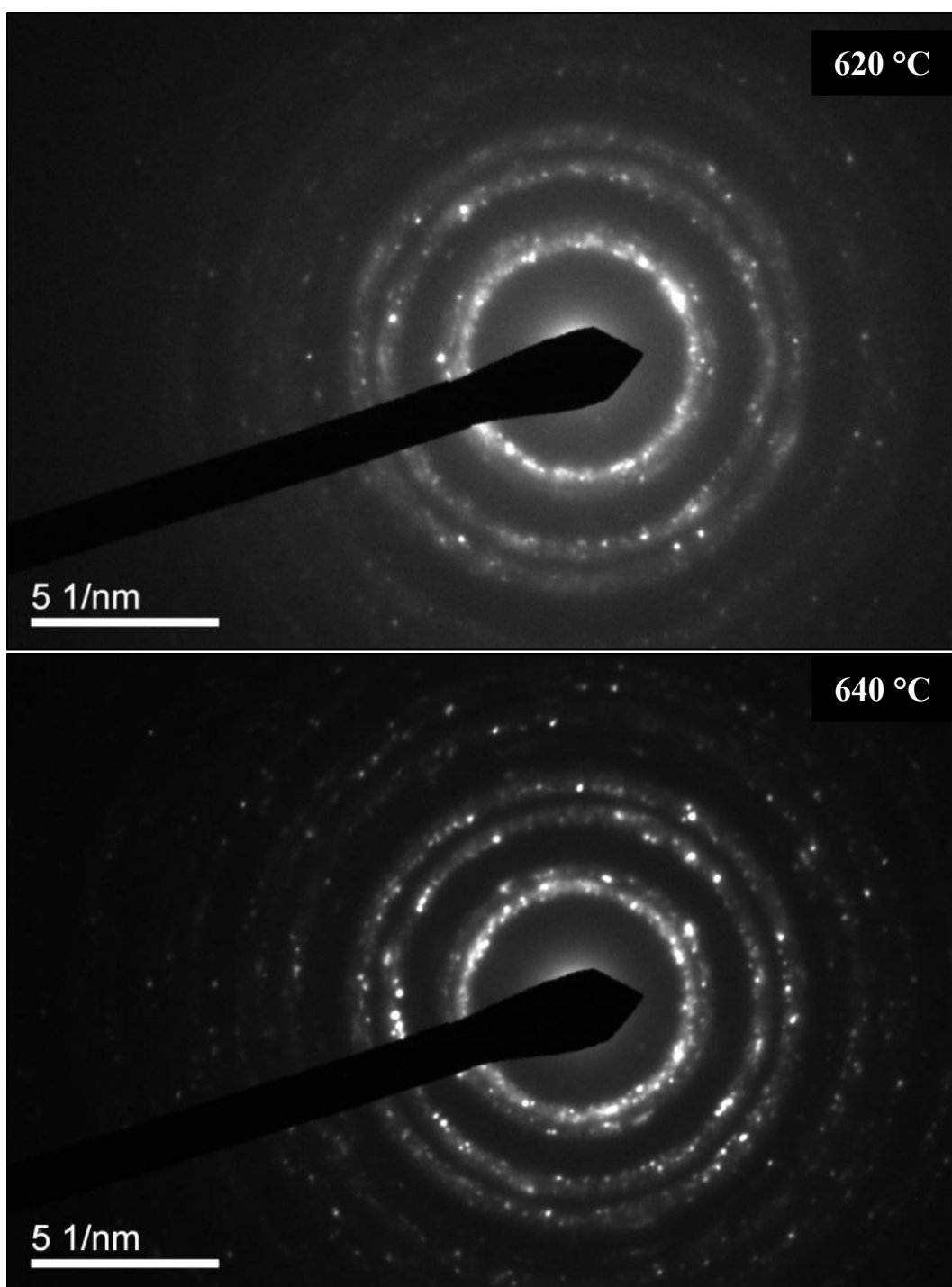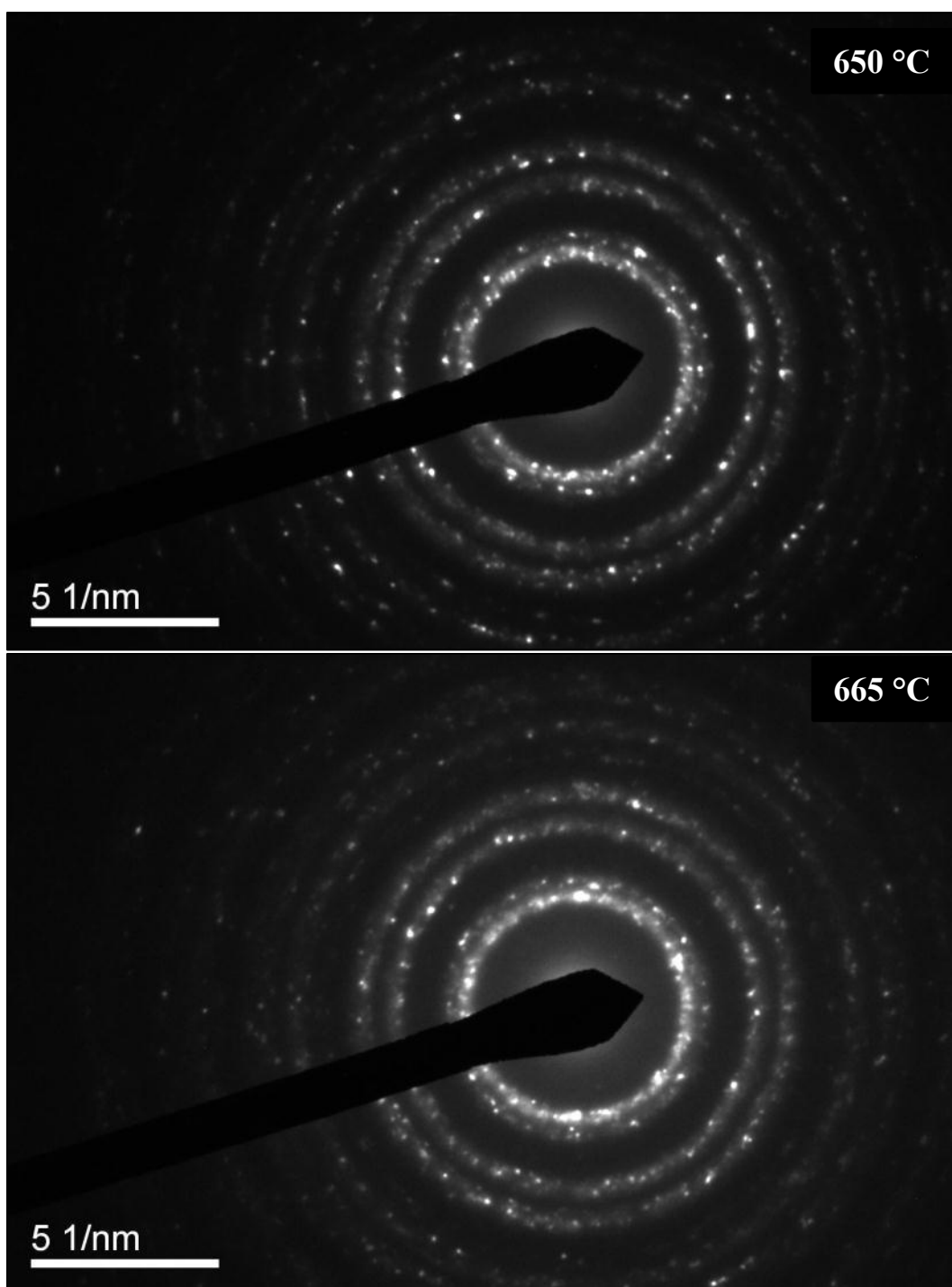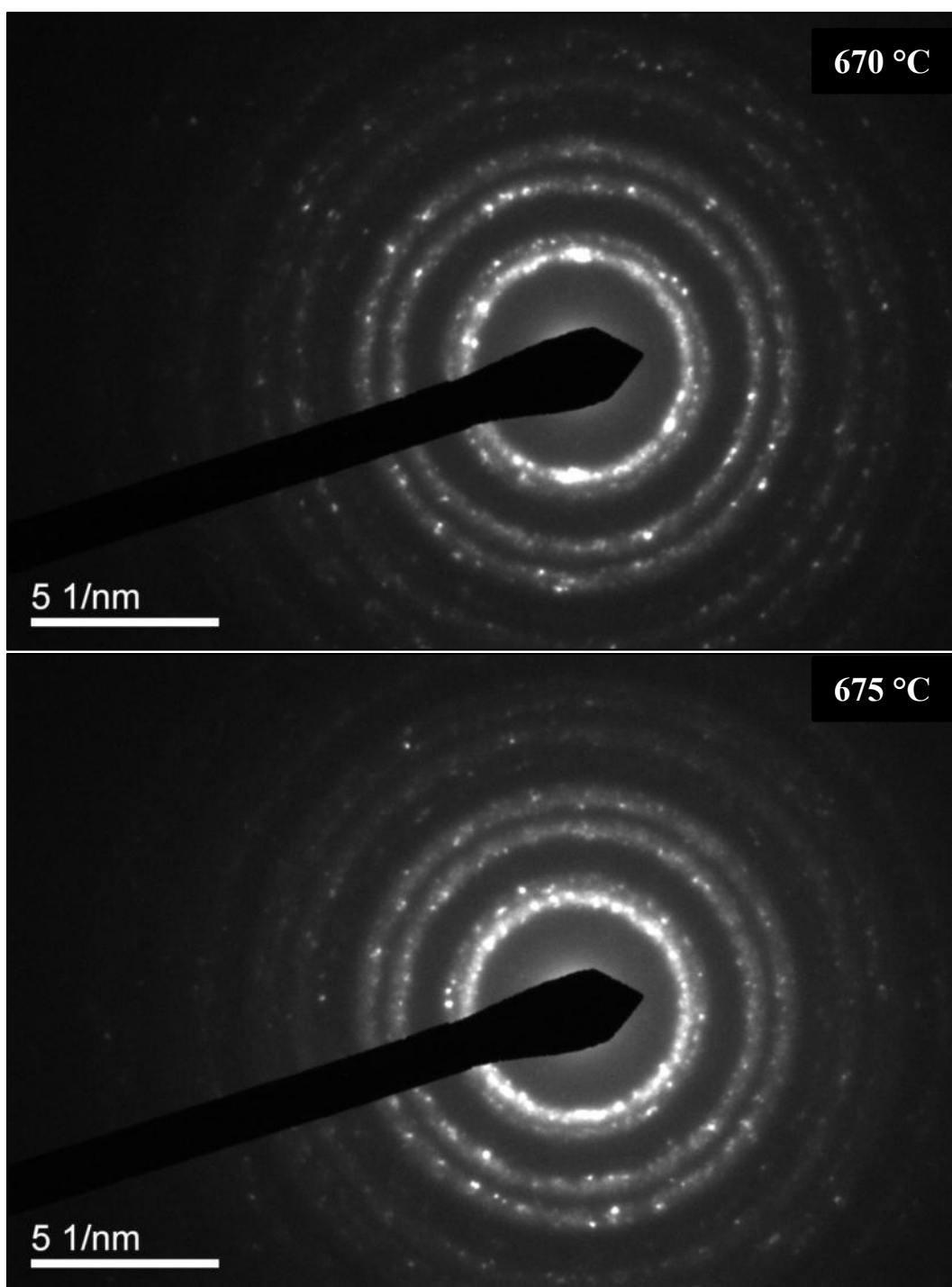
610 °C

5 1/nm

615 °C

5 1/nm

Figure 4-64: Continued.

Figure 4-64: Continued.

650 °C

5 1/nm

665 °C

5 1/nm

Figure 4-64: Continued.

199

670 °C

5 1/nm

675 °C

5 1/nm

Figure 4-64: Continued.

Figure 4-64: Continued.

Figure 4-64: Continued.

Figure 4-64: Continued.

743 °C

5 1/nm

758 °C

5 1/nm
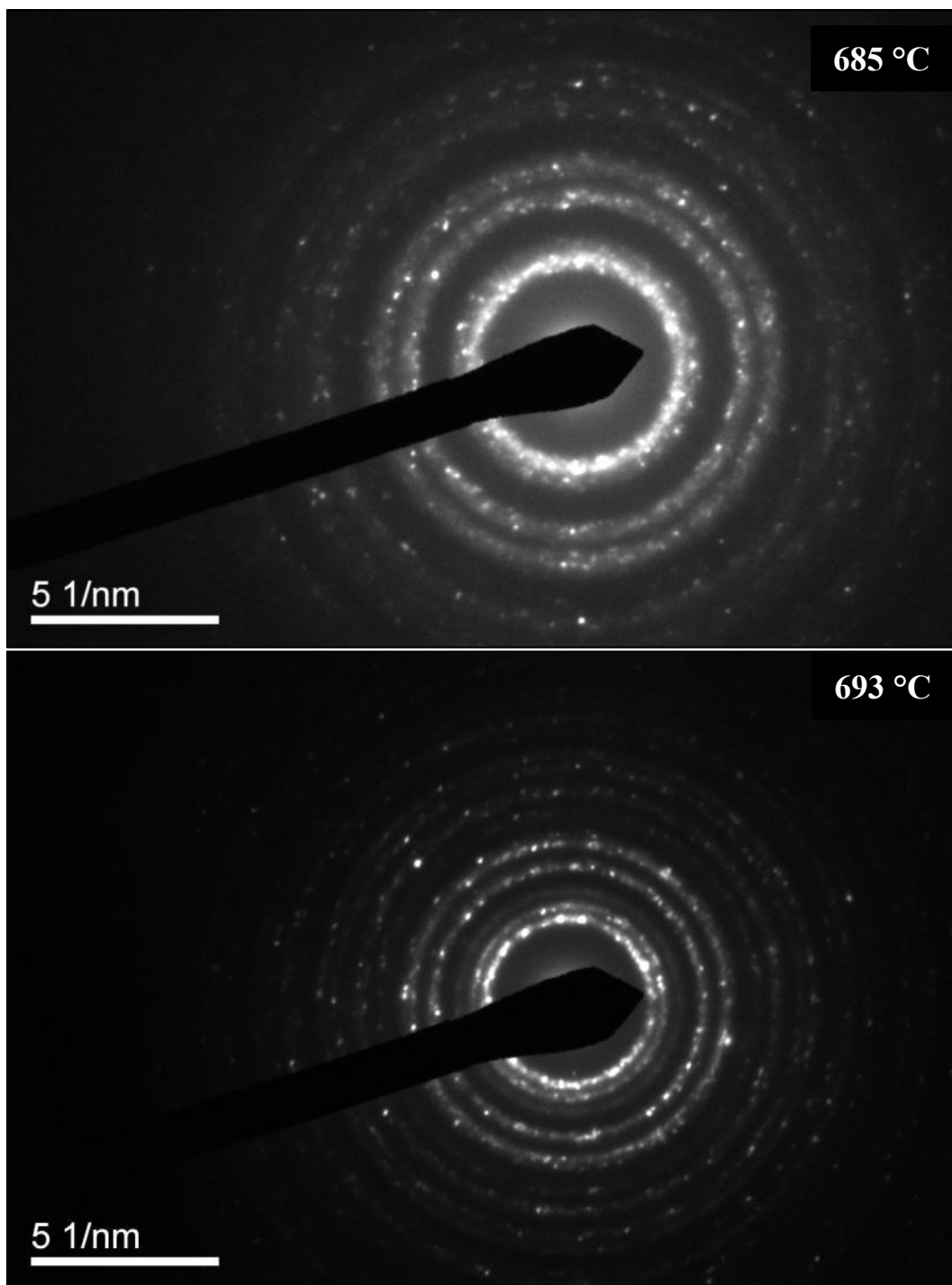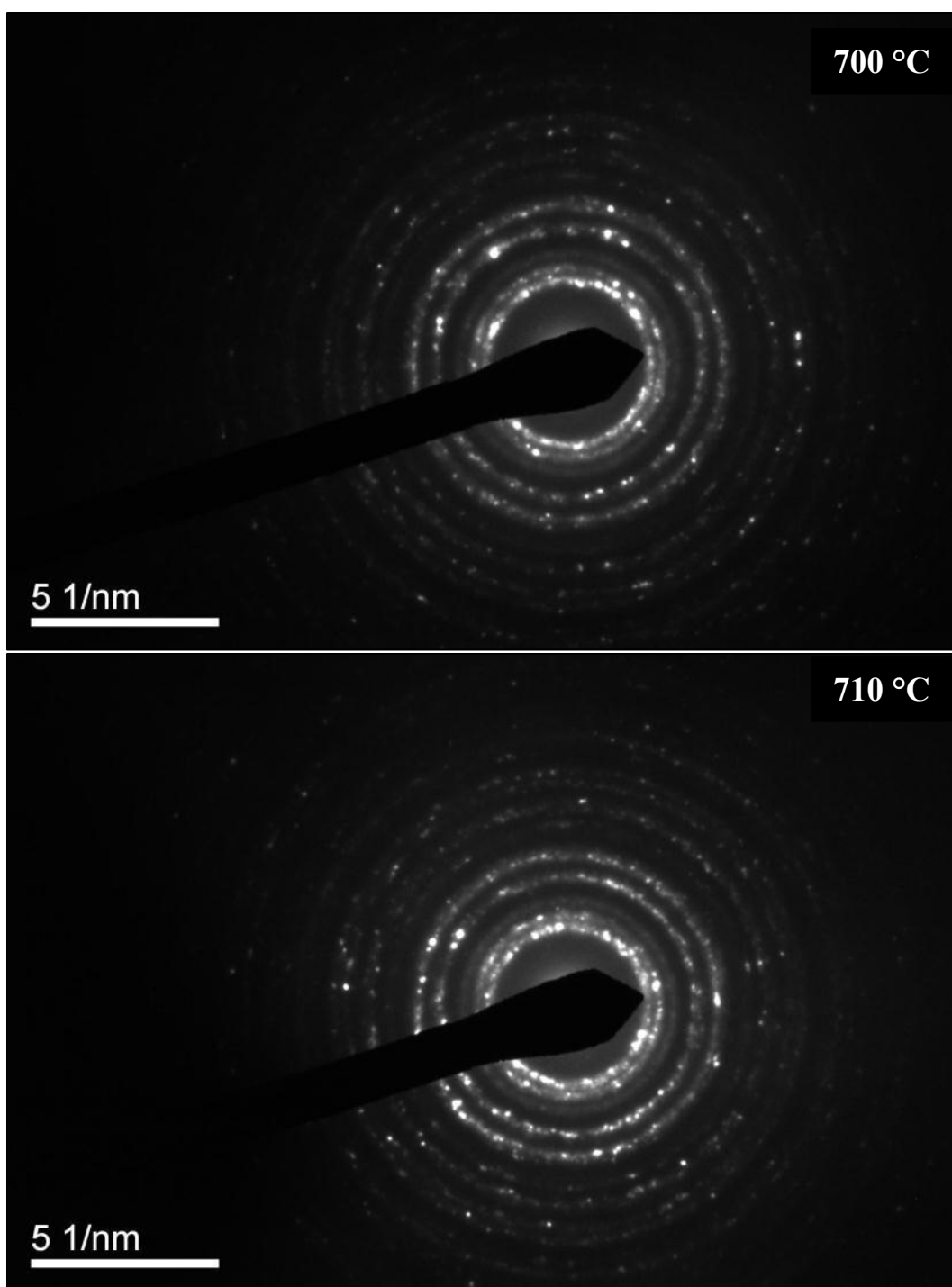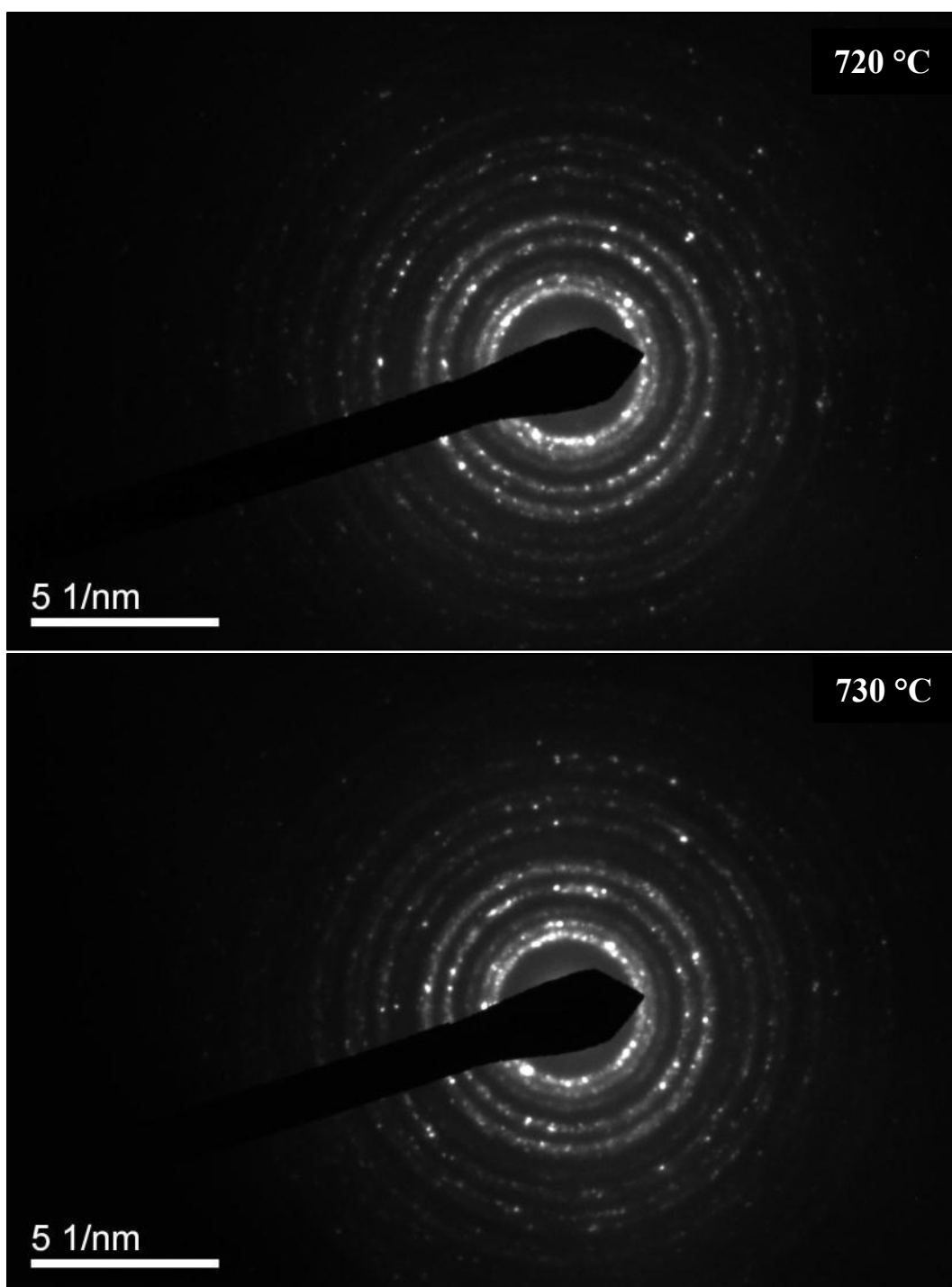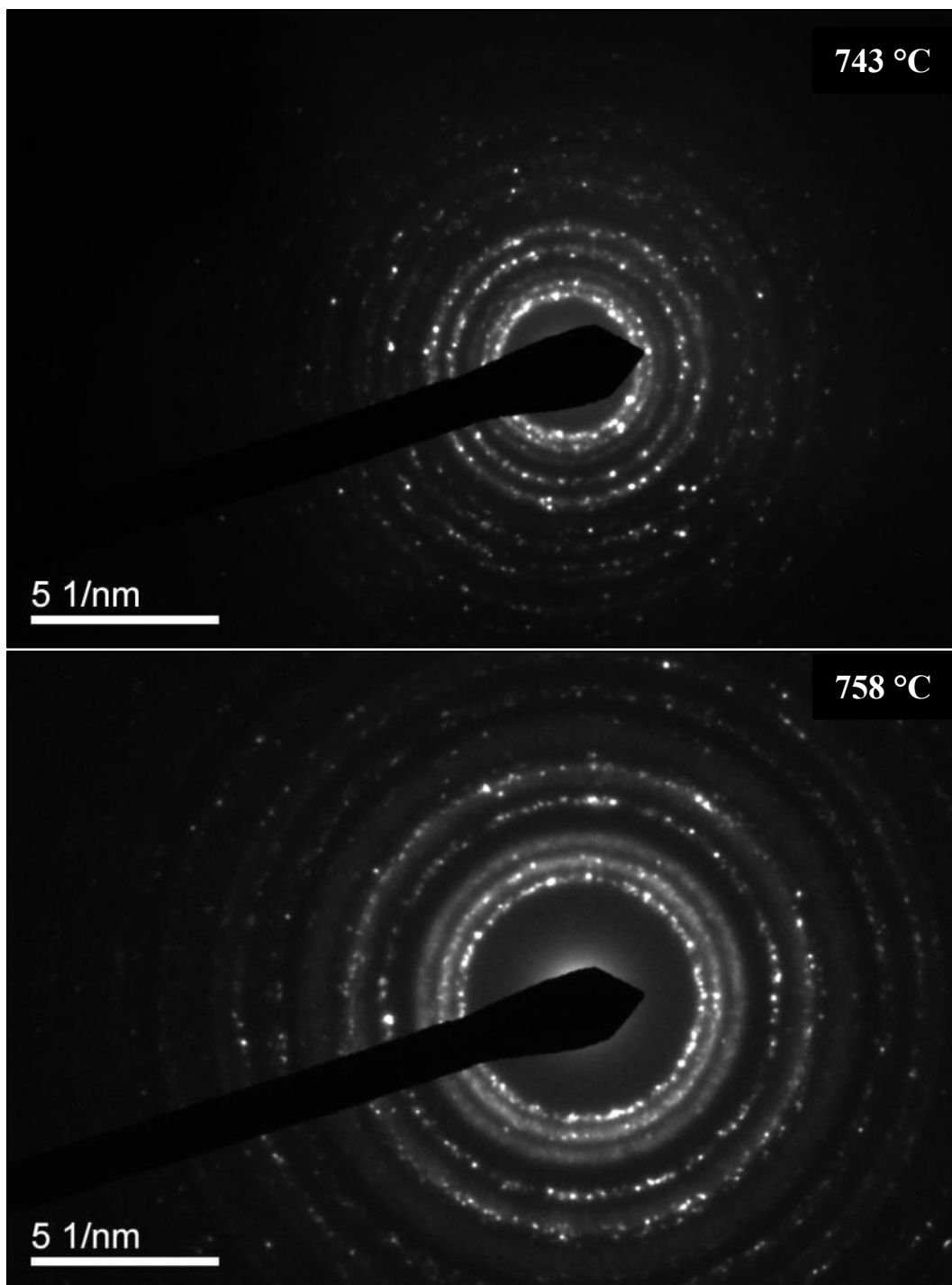
Figure 4-64: Continued.
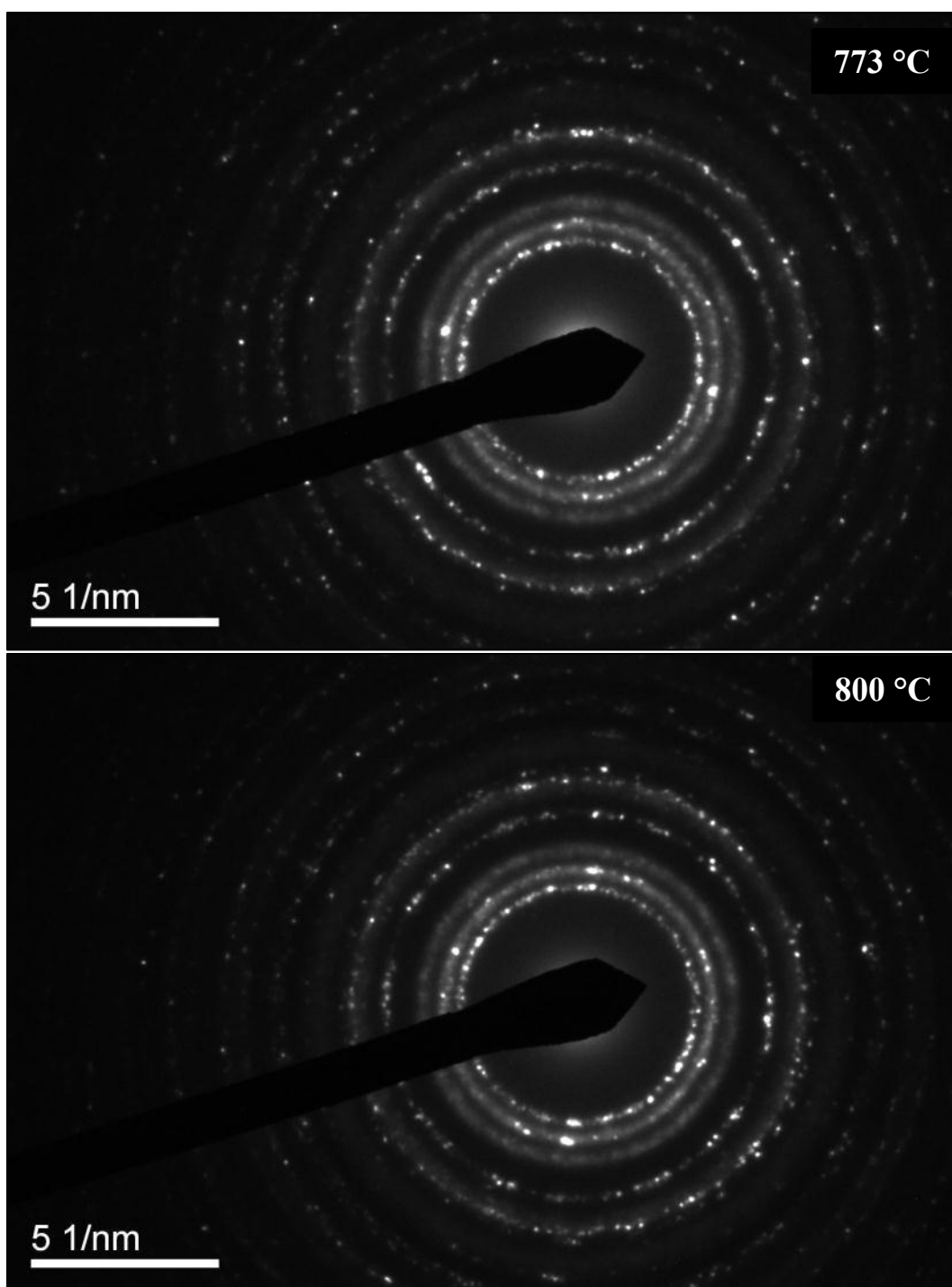
Figure 4-64: Continued.

The sequence of images in Fig. 4-64 contains some remarkable features. One of the more significant features is the evolution of the DP of U-10Zr alloy that begins at 693 °C (p.201). At this temperature, the two adjacent innermost rings in the DPs below the transition temperature quickly evolved into three adjacent innermost rings and this feature remains present in the DPs for all the higher temperatures (> 693 °C). In other words, an extra ring suddenly appears at 693 °C during heating, between the second and the third ring of low temperature DP. However, the other part of the DP do not show notable change along with temperature increase up to 800 °C, meaning the ratios between the diameters of all rings in the DP were maintained, regardless of specimen temperature (Section 5.2.5).

Note that the absolute diameters of the rings in the DPs were significantly affected by electron beam focus under continuing specimen heating. The sequence of DPs in Fig. 4-64 was taken in exact focus only at the temperatures below 610 °C and at 758 °C due to limited time. Off-focus imaging of the DPs can be justified by the fact that only relative ratios between the diameters of each ring in the DPs contain appropriate information of the crystal structure of the region. More specifically, the ratios are the same with the spacing between the atomic planes generating constructive electron interference.

So in the light of the U-Zr phase diagram (Figs. 2-2 and/or 2-3), the DP at 758 °C, which was unchanged during heating from 693 °C to 800 °C, ought to represent the bcc γ phase. In the same manner, the DP at 610 °C, which was unchanging below 693 °C, is supposed to represent (α-U, δ-UZr$_2$) phase mixture. Nevertheless only one transition was

observed from the DP of U-10Zr alloy, the DP of the alloy composition ought to exhibit three transitions to be coincided with Sheldon's phase diagram, corresponding to the phase transformations of 1) δ-UZr$_2$ $\rightarrow$ γ_2 at 617 °C, 2) α-U $\rightarrow$ β-U at 662 °C, 3) β-U $\rightarrow$ γ_1 at 693 °C. It was anticipated that no remarkable change on DP will be observable regarding the miscibility gap in the phase diagram since γ_1 and γ_2 have identical bcc crystal structure with γ phase, except minimal changes in the lattice constants.

A possible hypothesis to explain these observations that could stand with all *in-situ* heated TEM observation is that the observed transition at 693 °C occurred as a result of an α-U $\rightarrow$ γ_1 phase transformation. This would indicate that the existence of the (β-U, γ_2) phase zone might be limited below the zirconium composition of the alloy (< 10 wt%); this would also be consistent with the observations in Section 4.2 as discussed in Section 5.2. This hypothesis is based on two experimental facts that the only transformation temperature observed was 693 °C and that once changed DP was constant up to 800 °C.

Quantitative DP analysis and further discussion on the observation is provided in Section 5.2.5, which further strengthens the suggested hypothesis. It was tentatively concluded from the noted analysis that the primary DPs of the alloy at lower temperature (< 693 °C) were likely representative of the fluorite structure of uranium dioxide (UO$_2$) [166, 167], or solid solution of uranium dioxide and zirconium dioxide (UO$_2$, ZrO$_2$). This oxide formation is expected on the specimen surface and was unavoidable during the transfer of the prepared TEM specimens from the preparation facility to the TEM

facility ~15 min away. This surface oxidation of prepared very thin (< 100 nm) electron transparent areas of the alloy specimens may have been instantly occurred.

Although the presence of surface oxidation was clearly evident from the DP analysis, the analysis also showed that the new third ring that appeared at higher temperatures (> 693 °C) DPs was best matched with γ phase among all the other considerable phases in U-Zr binary alloy system and inserted impurities. In fact, the bcc γ phase was the only considerable candidate possible based on the ratios between the diffraction rings in the DPs, assuming the lower temperature DPs truly do represent UO_2 from surface oxidation.

However, the missing transition of the DP at 617 °C for the phase transformation of δ-UZr_2 → $γ_2$ necessitates further investigation. This could be due to incomplete crystallographic formation of δ-UZr_2 phase in a partially oxidized area although the assessed chemical compositions of the phase from the BF image analysis were in good agreement with the phase diagram. It is important to note that the zirconium composition of $γ_2$ phase at 617 °C is comparable to that of δ-UZr_2 phase. Another considerable explanation is the DP of δ-UZr_2 phase could be fairly well overlapped with that of γ phase. Historically, δ-UZr_2 phase had been misunderstood in X-ray diffraction (XRD) as a bcc crystal structure, which has about three fold larger lattice constant compare to parent bcc γ phase [168]. These results are considered further in Section 5.2.

4.4.4 U-20ZrAi5

This section describes the TEM observation made for the highly-irradiated as-cast U-20Zr alloy. In this case, low voltage (< 60 V) electropolishing was more successful than in U-10Zr alloy, as shown in Fig. 4-65. Differential electrochemical etching and diverse subgrain orientation of two phase lamellae structure of the alloy give rise to the various nanostructures shown in the figure.

A generally bright area including numerous darker particles aligned in a row is shown in Fig. 4-65(first). The darker particles are likely thicker Zr-rich δ-UZr$_2$ phases based on the noted resistive nature of Zr-rich phases to the electropolishing environment and the morphology of the particles. However, the DP superimposed on the image indicates significant oxidation of the area and the presence of zirconium precipitates.

Figure 4-65 also contains an over-polished area at different magnifications to emphasize that the area appeared as one medium in the second image was actually comprised of two overlapped planes where the dark lamellae are vertically separated from bright background with a height difference of some indeterminate extent. Therefore it was impossible to concurrently place the two planes in focus during the observation. Note bright Fresnel fringe surrounding dark lamellae structure in the third image, indicating underfocus. This two-layer structure was due to the electrochemically etched mesh of the Zr-rich δ-UZr$_2$ phase lamellae placed over the other thin electron transparent area.

The complex structure shown in the last image in Fig. 4-65 could be the same lamellae structure shown in the other images, merely oriented in different direction. A subgrain comprises a coherent two phase lamellae which is not exactly parallel to the plane of mechanical thinning that is also the plane of electropolishing which could give rise to this type of images under the transmitting electron beam. Several other regions oriented in various directions with respect to the electron beam have been frequently observed.

Micrometer-scale secondary phase rods were often etched out at low voltage (40 V) prepared U-20Zr alloy specimens, as shown in Fig. 4-66. The inserted DP (top) and DF image (bottom) indicate single crystal structure of the secondary phase rod, which was indexed as yttrium oxide (Y_2O_3). Note the morphology of the secondary phase particles at grain boundaries shown in Fig. 4-7(c).
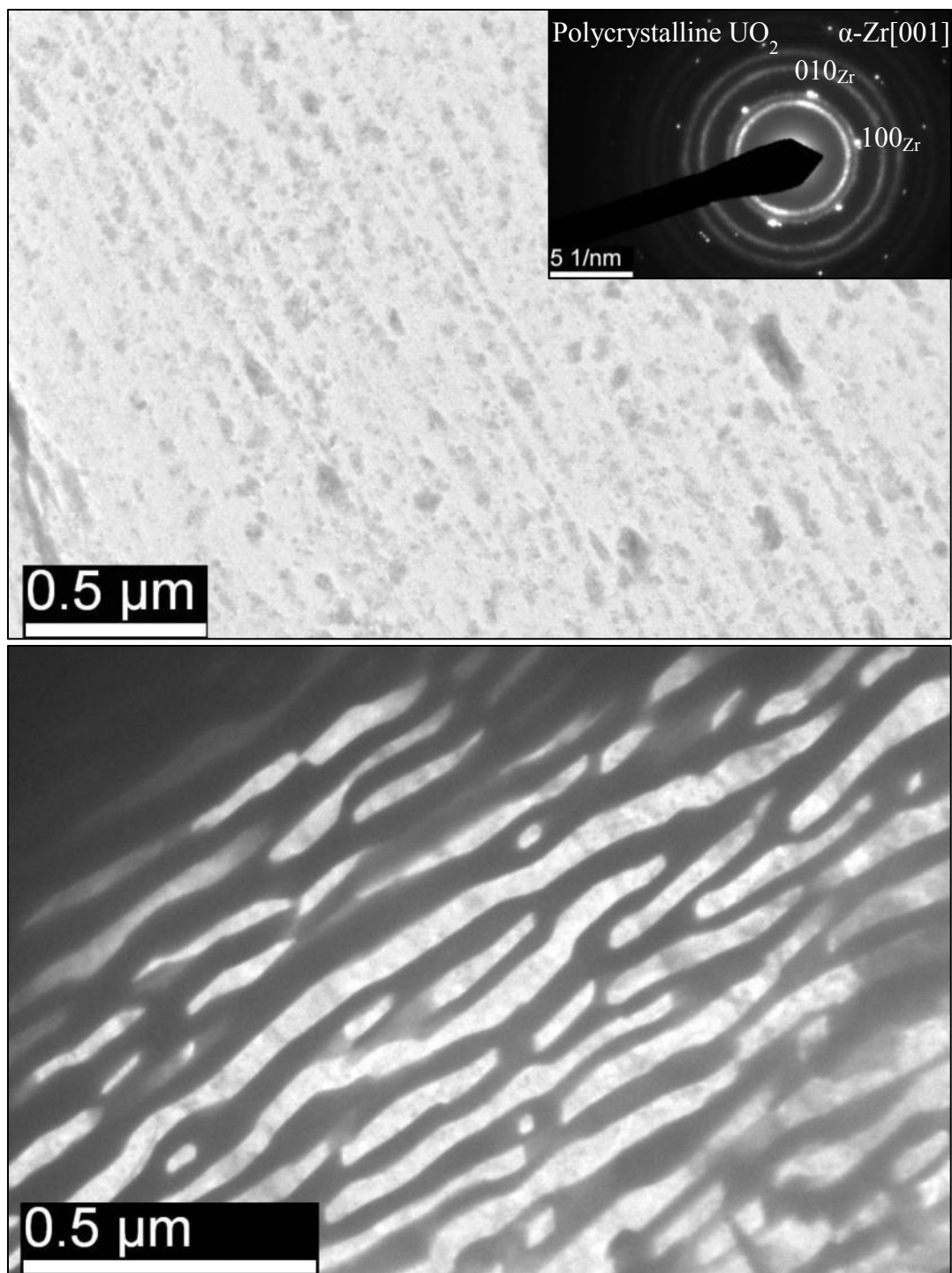
Figure 4-65: As-cast two phase lamellae structure of low voltage (40 V) electropolished U-20ZrAi5.
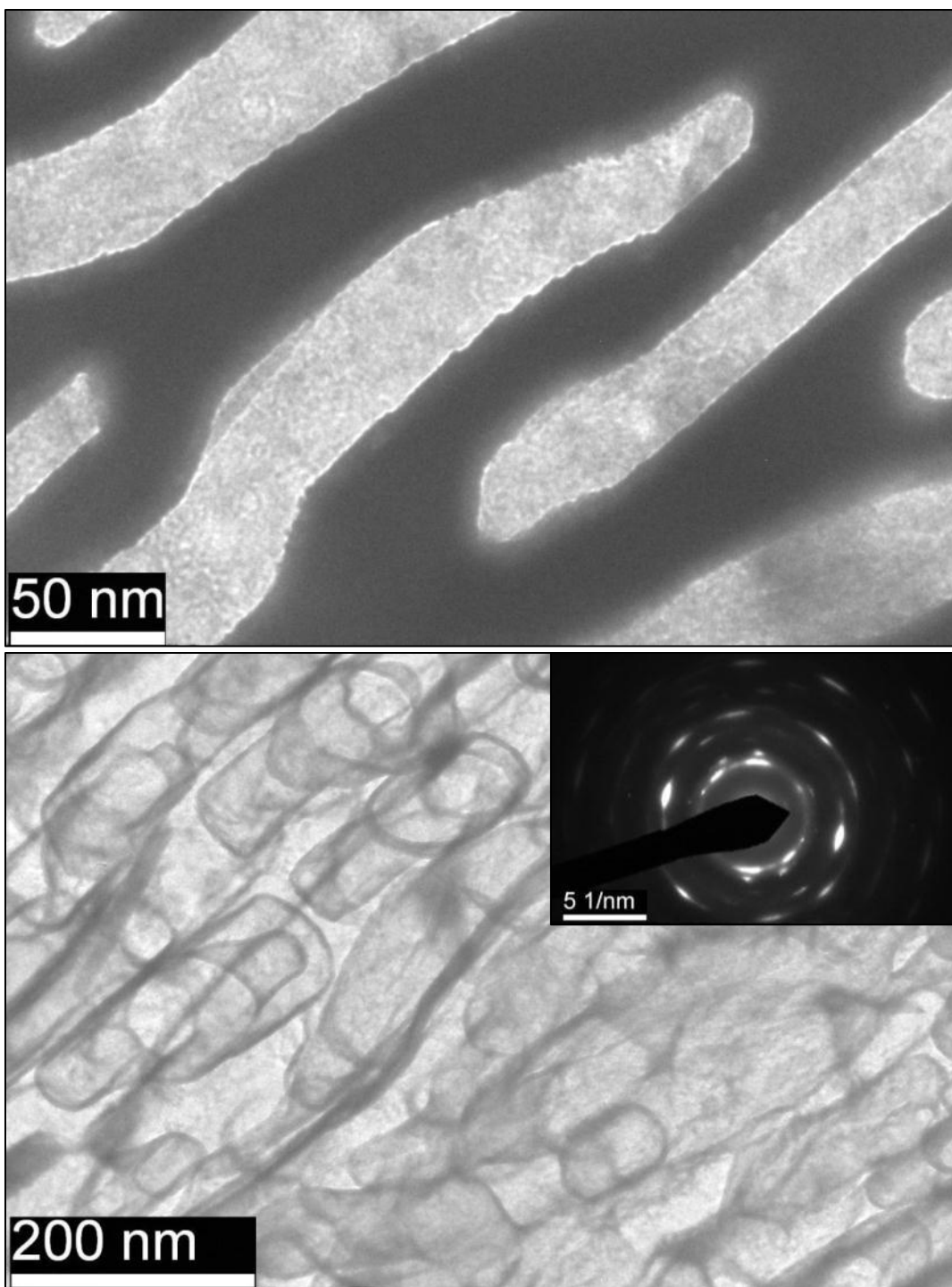
Figure 4-65: Continued.
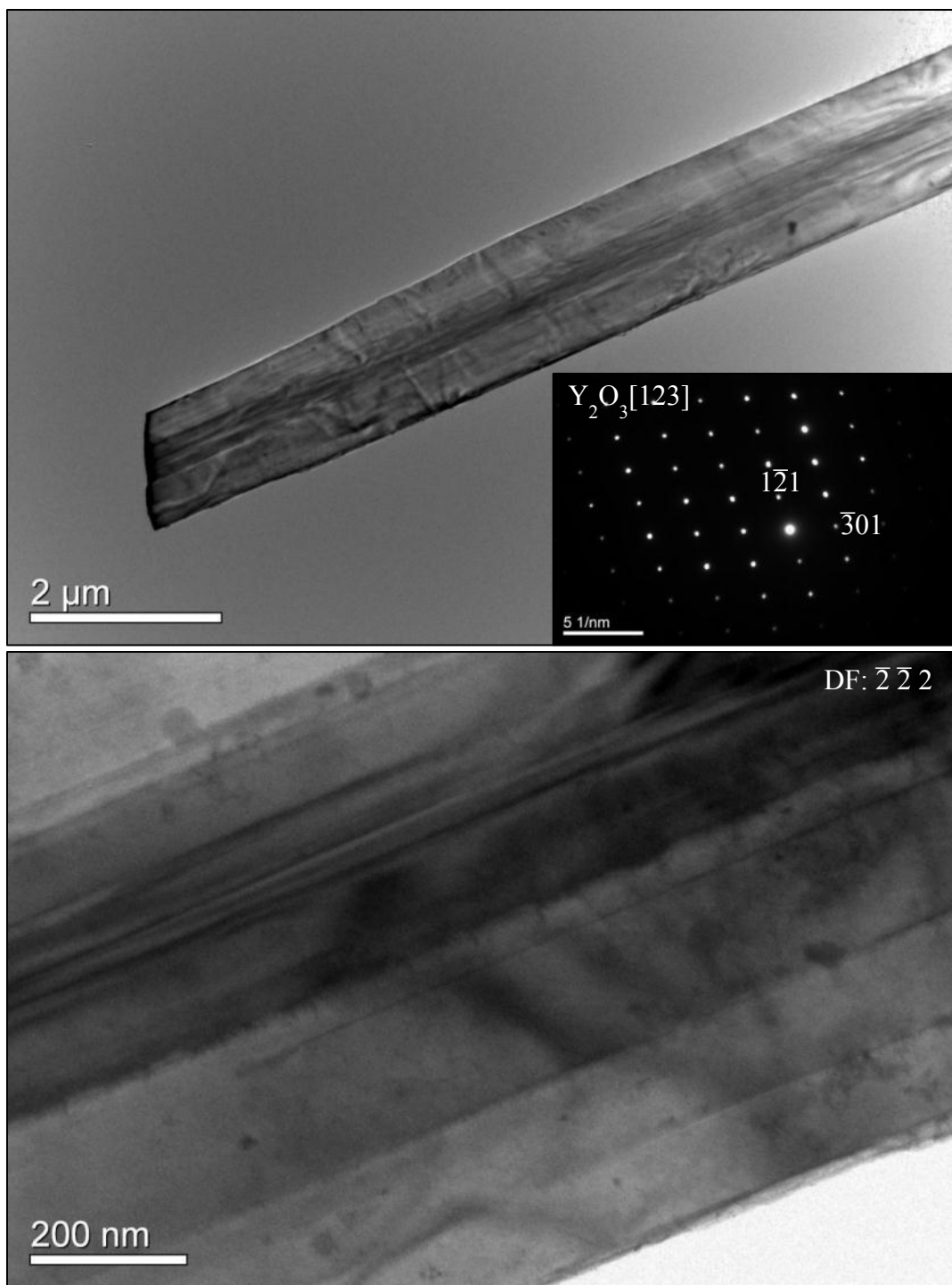
Figure 4-66: Electrochemically etched out yttrium oxide particles from U-20ZrAi5.

As in the U-10Zr alloy specimen, higher voltage (> 60 V) electropolishing remarkably improved the specimen quality of U-20Zr alloy, enabling the clear observation of the two phase lamellae structure of the alloy from numerous wide areas, as shown in Fig. 4-67. Dark precipitates in the figure may have α-U phase. Note that Fig. 4-8 shows enlarged congruous structure of annealed U-20Zr. The estimated zirconium composition of the area was (19.7 ± 0.7) wt% from BF image analysis assuming the dark and bright regions have α-U and δ-UZr$_2$ phase, respectively.

Mass-thickness contrasts are consistent for U-20Zr alloy as shown in Fig. 4-67. In other words, the dense U-rich phase is darker and light Zr-rich phase is brighter, indicating less variation of specimen thickness over the two phase regions than was observed in the U-10Zr alloys. On the contrary, the contrast of the two phases in BF images was reversed in U-10Zr as shown in Figs. 4-59 and 4-62, i.e. darker Zr-rich and brighter U-rich phases, implying U-rich phase matrix were remarkably thinner than Zr-rich precipitates.

The reversed phase contrast in the two alloys can be explained from different electrochemical resistivity of reversed matrix phase of each alloy. For U-20Zr, electrochemically resistive δ-UZr$_2$ phase matrix could protect α-U phase precipitates from preferential over-polishing to form relatively flat specimens. On the other hand, α-U phase matrix of U-10Zr would be uncovered to electrolyte flow, while δ-UZr$_2$ phase precipitates are less eroded to form corrugated electron transparent area corresponding to as-cast two phase lamellae structure of the alloy.
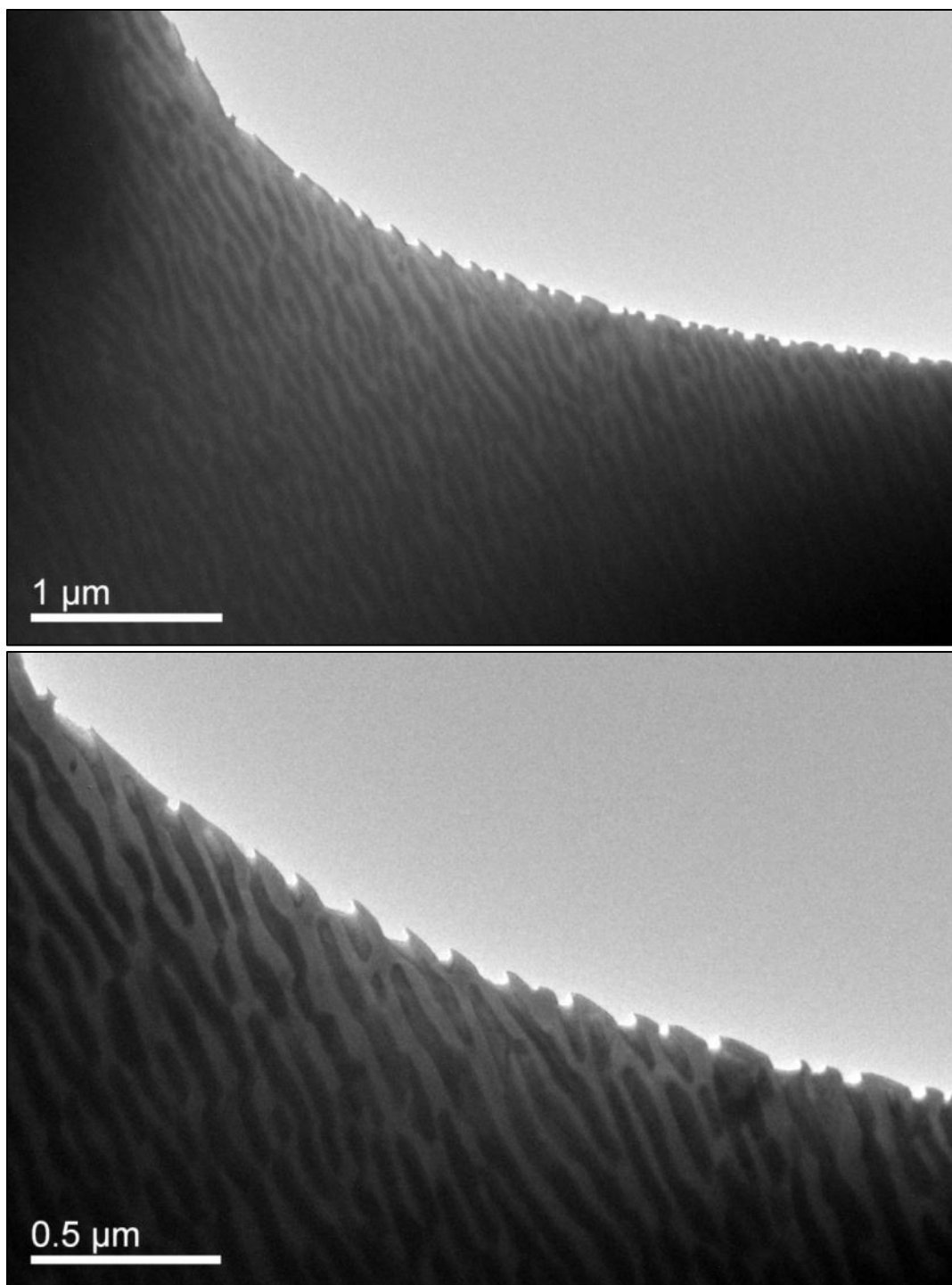
Figure 4-67: As-cast two phase lamellae structure of U-20ZrAi5. (Saw-tooth shaped perforated boundary was due to high voltage (100 V) electropolishing.)
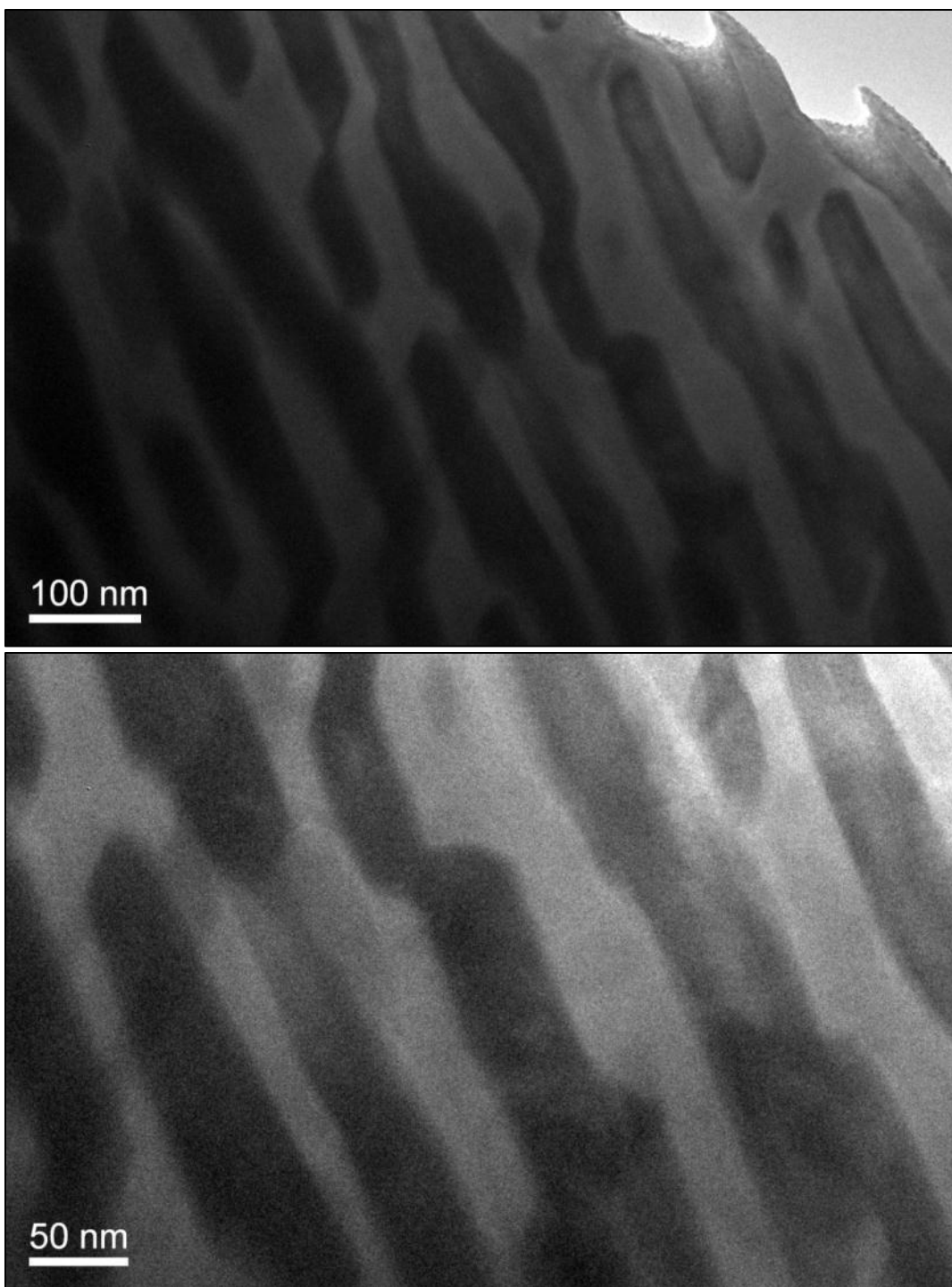
Figure 4-67: Continued.
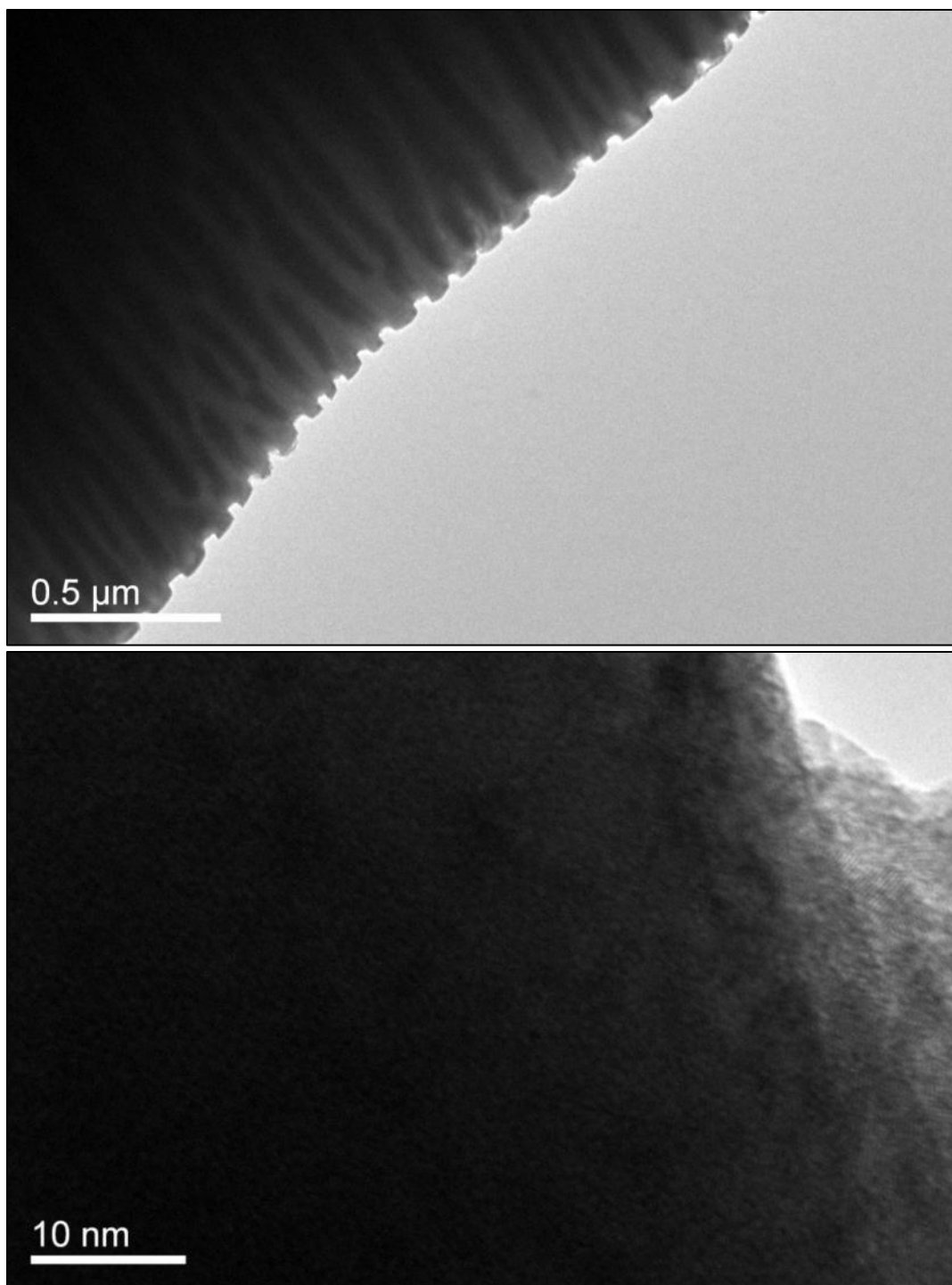
Figure 4-68: Saw-tooth shaped perforated boundary (top) and opaque α-U phase precipitates (bottom) of U-20ZrAi5.
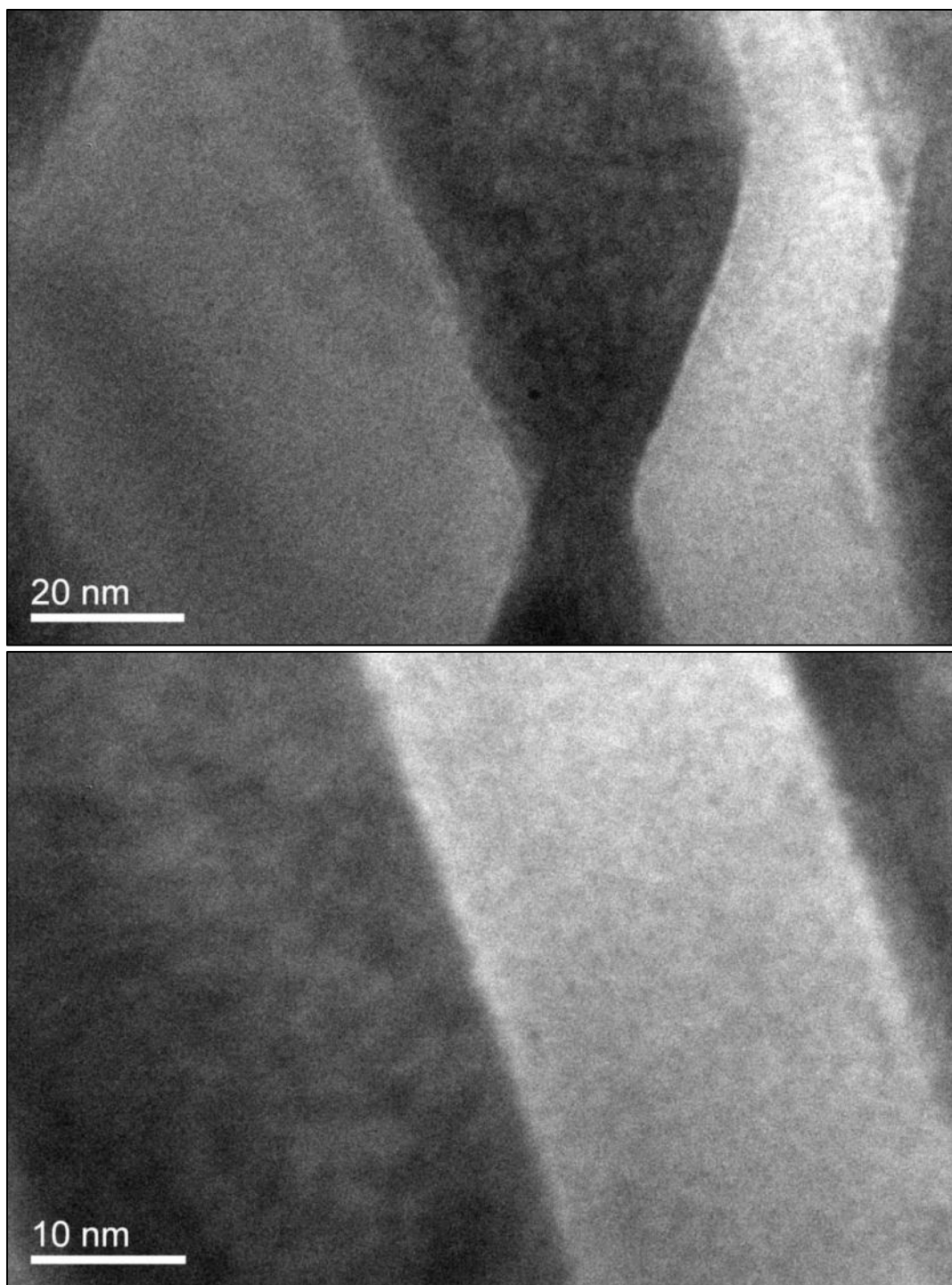
Figure 4-69: Coherent α-U/δ-UZr₂ phase boundaries in U-20ZrAi5.

The saw-tooth shaped perforated boundary shown in Fig. 4-67 is another unique characteristic of high voltage electropolished U-20Zr. The structure may have formed from preferential removal of α-U precipitates. It should be highlighted that each dent on the boundary was unexceptionally decorated with a ripped-off α-U (dark) precipitate while δ-UZr$_2$ phase lamellae formed the outermost periphery. Figure 4-68 shows another area having similar boundary and opacity of α-U phase precipitates, indicating the two areas shown in Figs. 4-67 and 4-68 are relatively thicker than the areas shown in Figs. 4-59 and 4-66. Finally, the coherent nature of the α-U/δ-UZr$_2$ interphase boundaries is visualized in Fig. 4-69.

4.4.4.1 *In-situ* Heating of U-20ZrAi5

The area shown in Fig. 4-67 was tracked and kept in view while the specimen was *in-situ* heated from 25 °C up to 810 °C, cooled down to 597 °C, and then annealed for 20 min. From the BF images shown in Fig. 4-70, three significant observations are possible:

1) The morphology evolution of the regions were nearly instantaneous due to expedited surface diffusion during the phase transformation(s),

2) No notable changes were observed during heating up to 600 °C, and

3) The BF images taken at high temperatures were unavoidably blurred due to thermal vibration of the specimen.

219
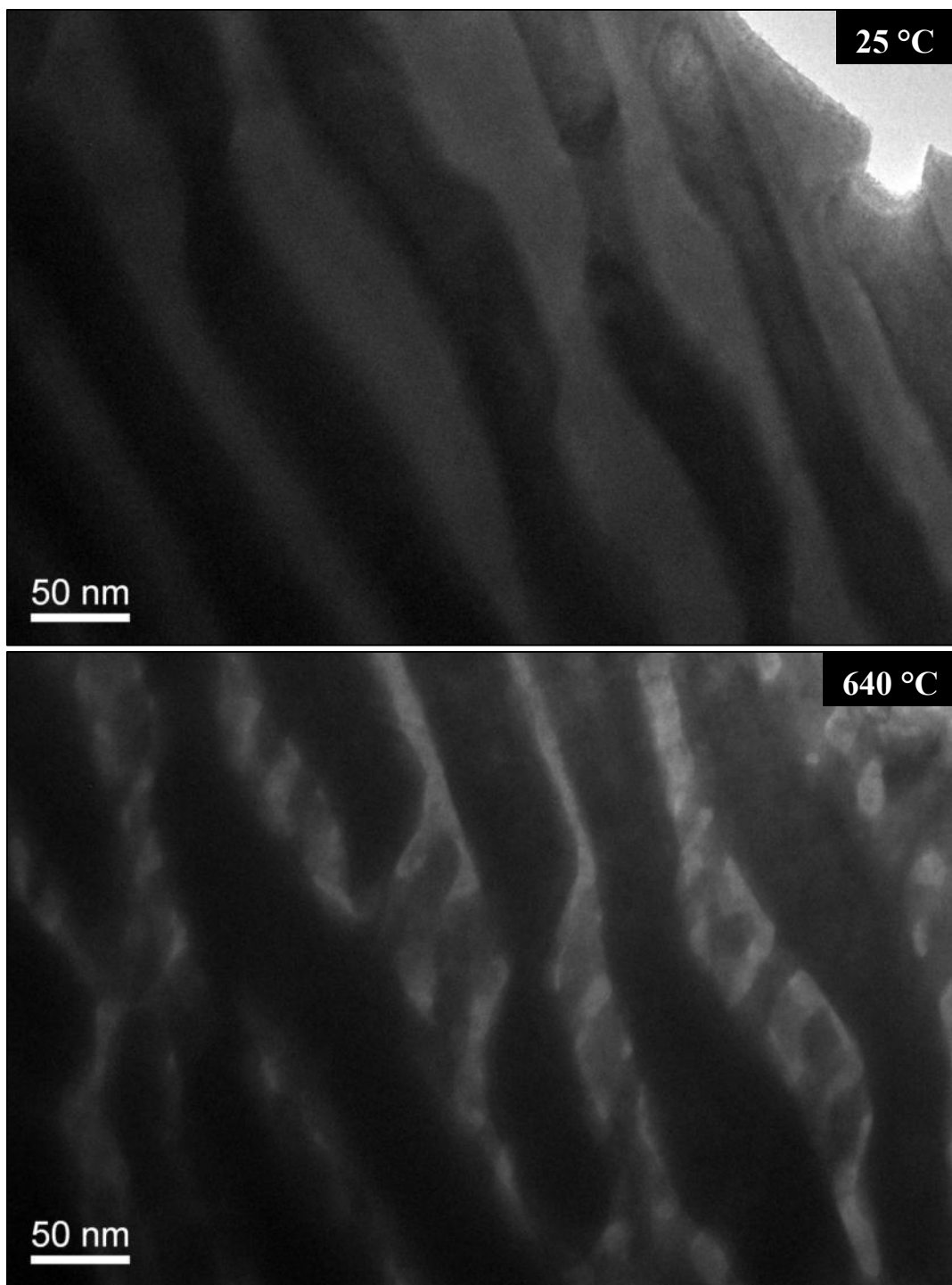
Figure 4-70: Nanostructure evolution of U-20ZrAi5 during *in-situ* heating from 25 °C to 810 °C, cooling down to 597 °C, and annealing at 597 °C for 20 min.
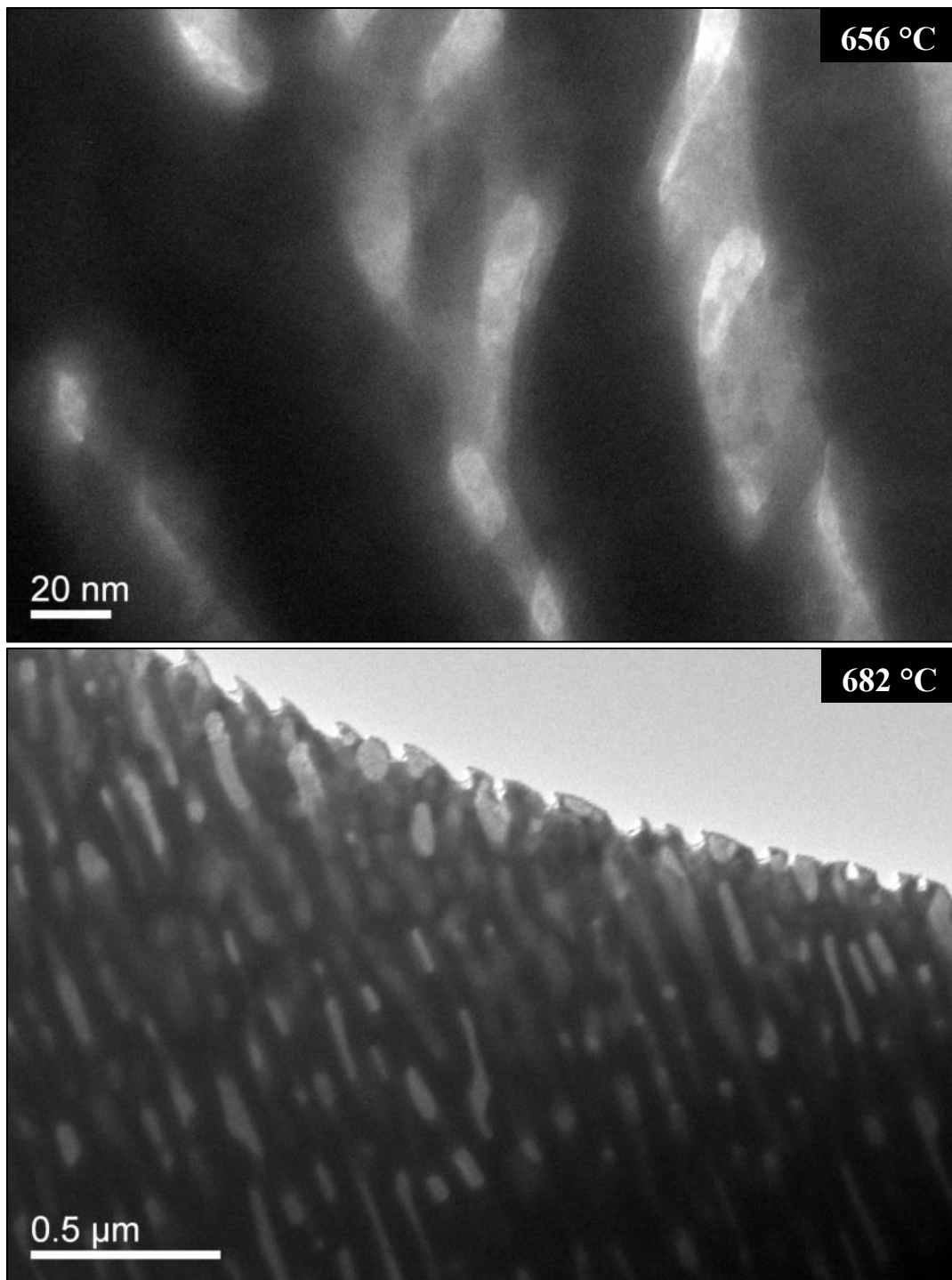
Figure 4-70: Continued.
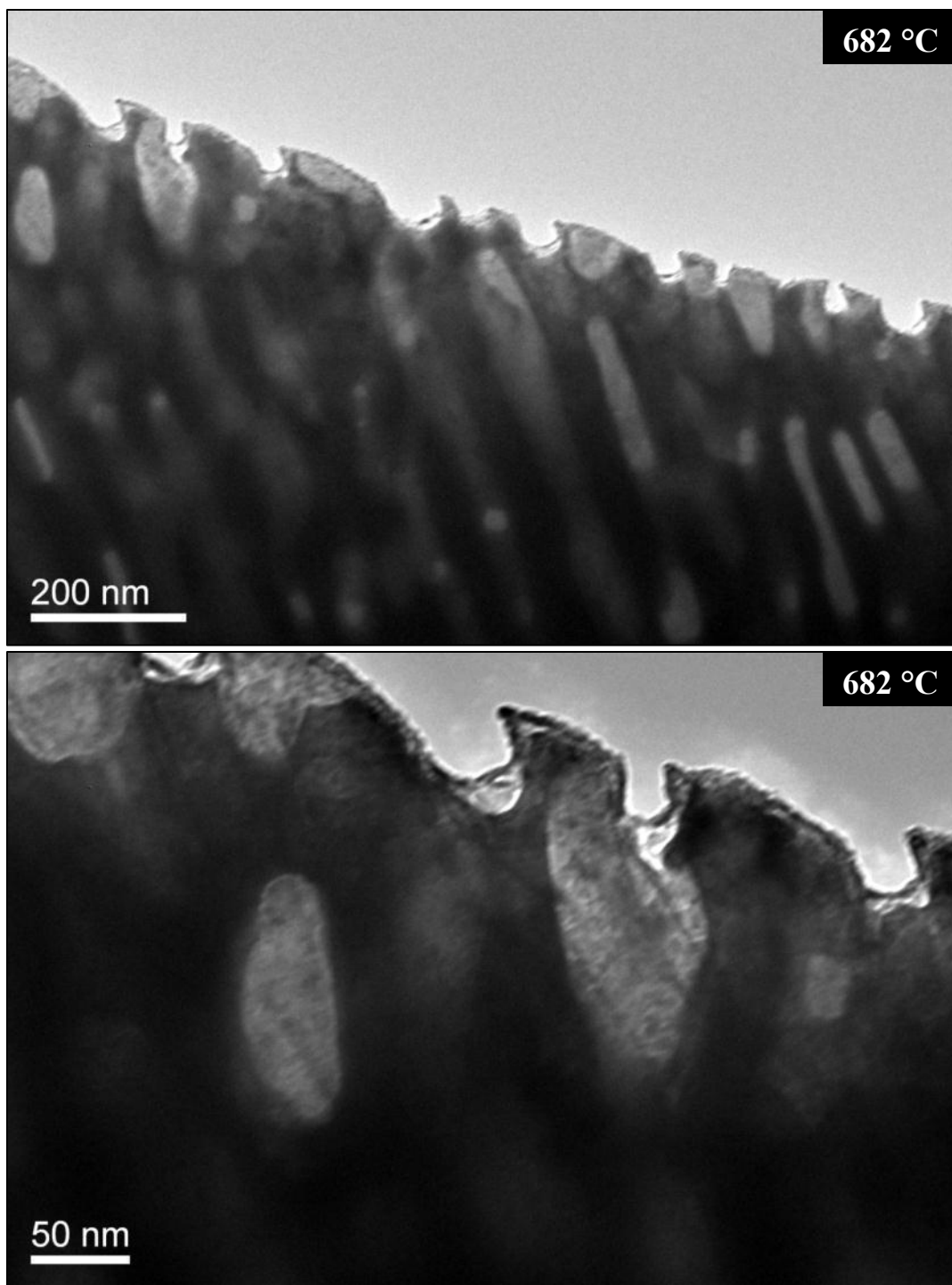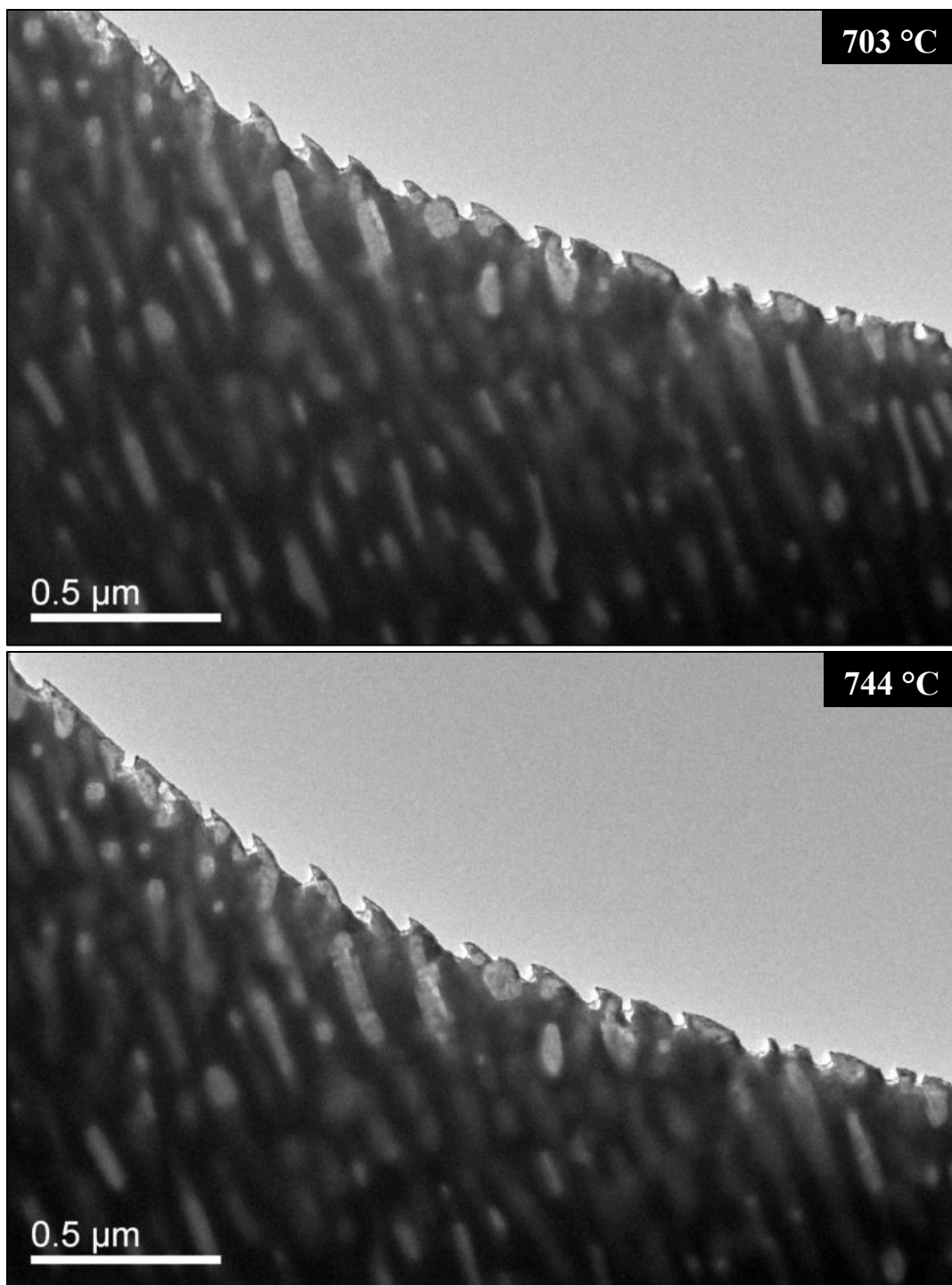
Figure 4-70: Continued.

Figure 4-70: Continued.

Figure 4-70: Continued.

Figure 4-70: Continued.

681 °C (cooling)

0.5 µm

679 °C (cooling)

0.5 µm
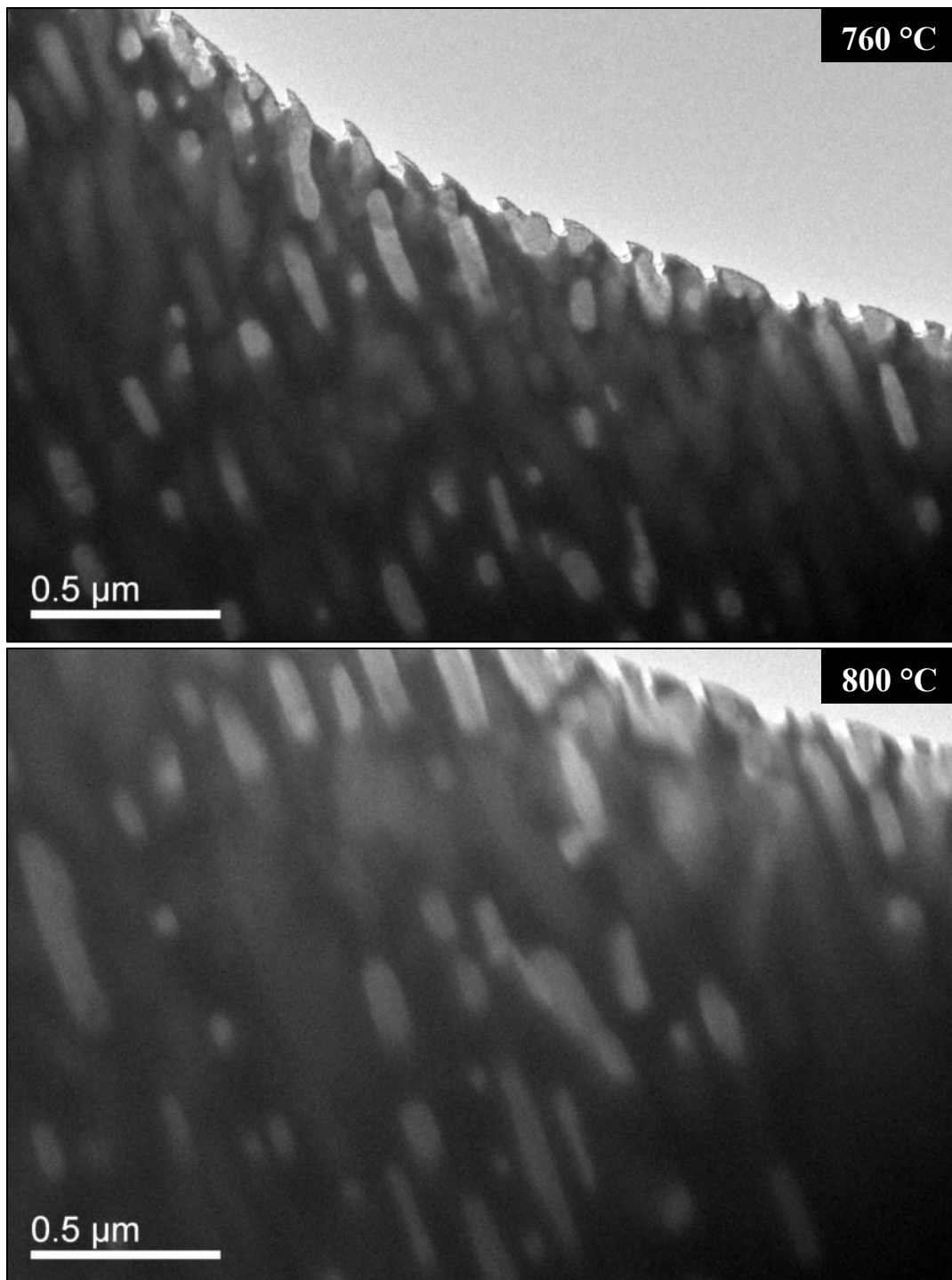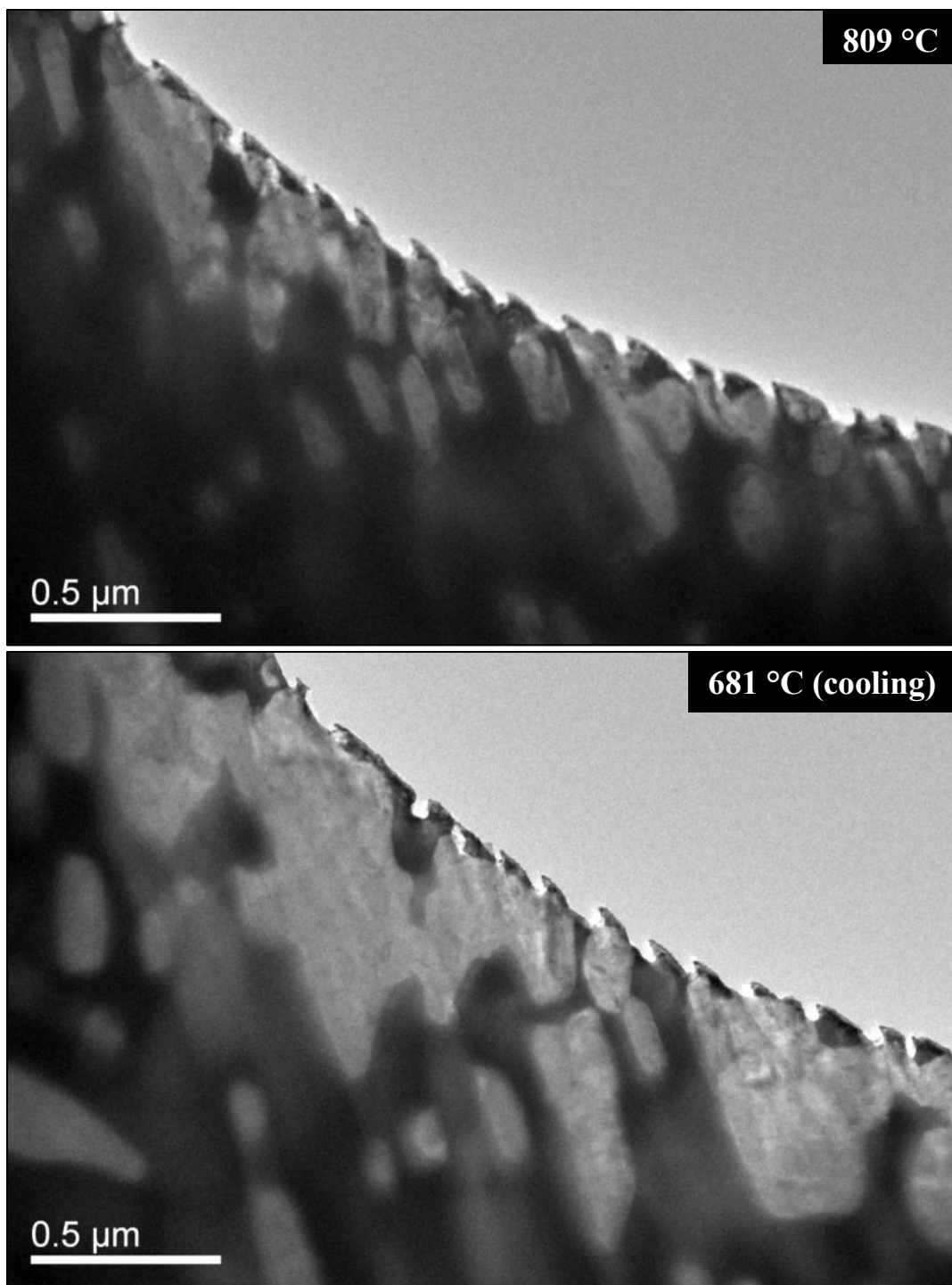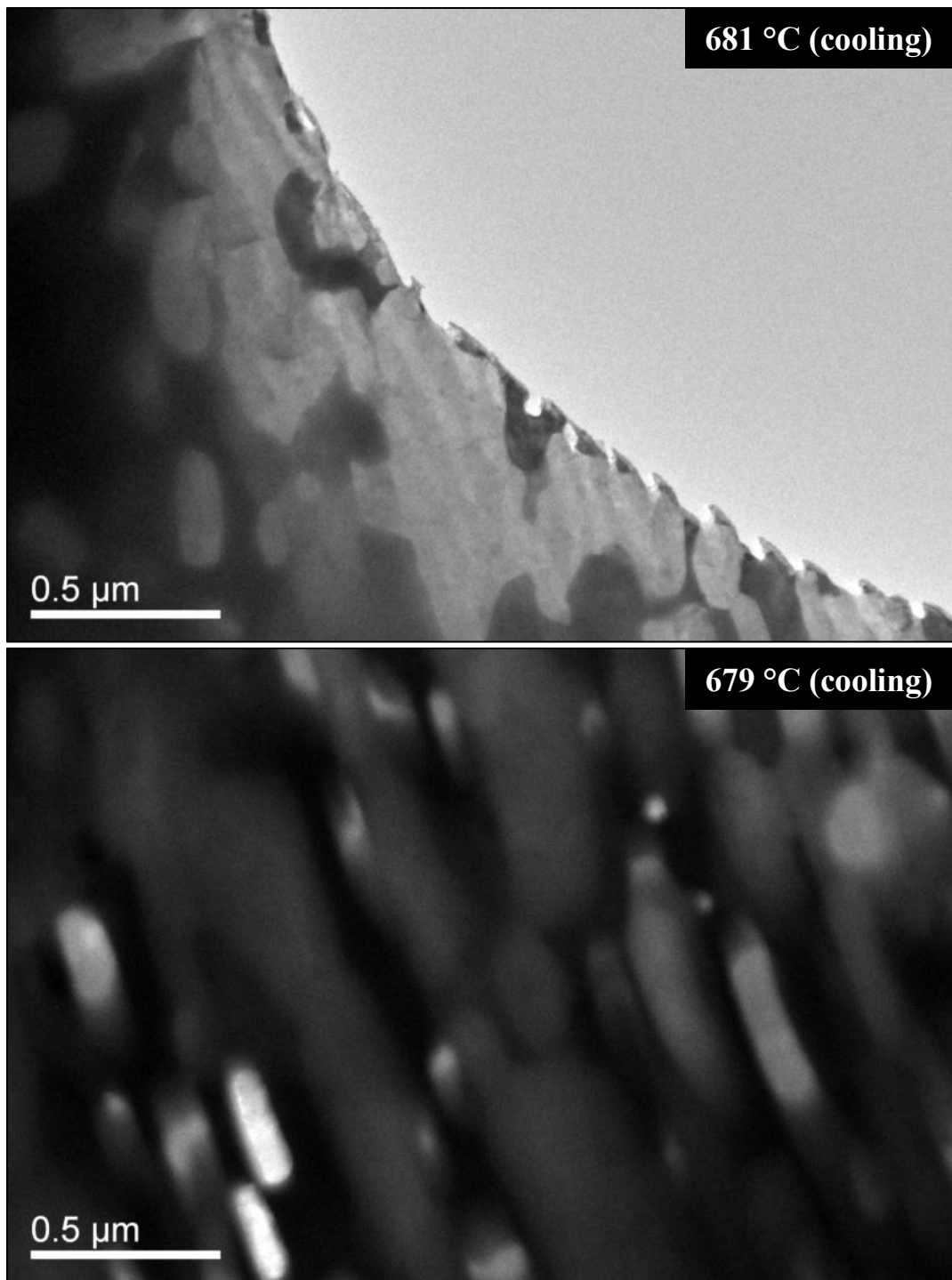
Figure 4-70: Continued.
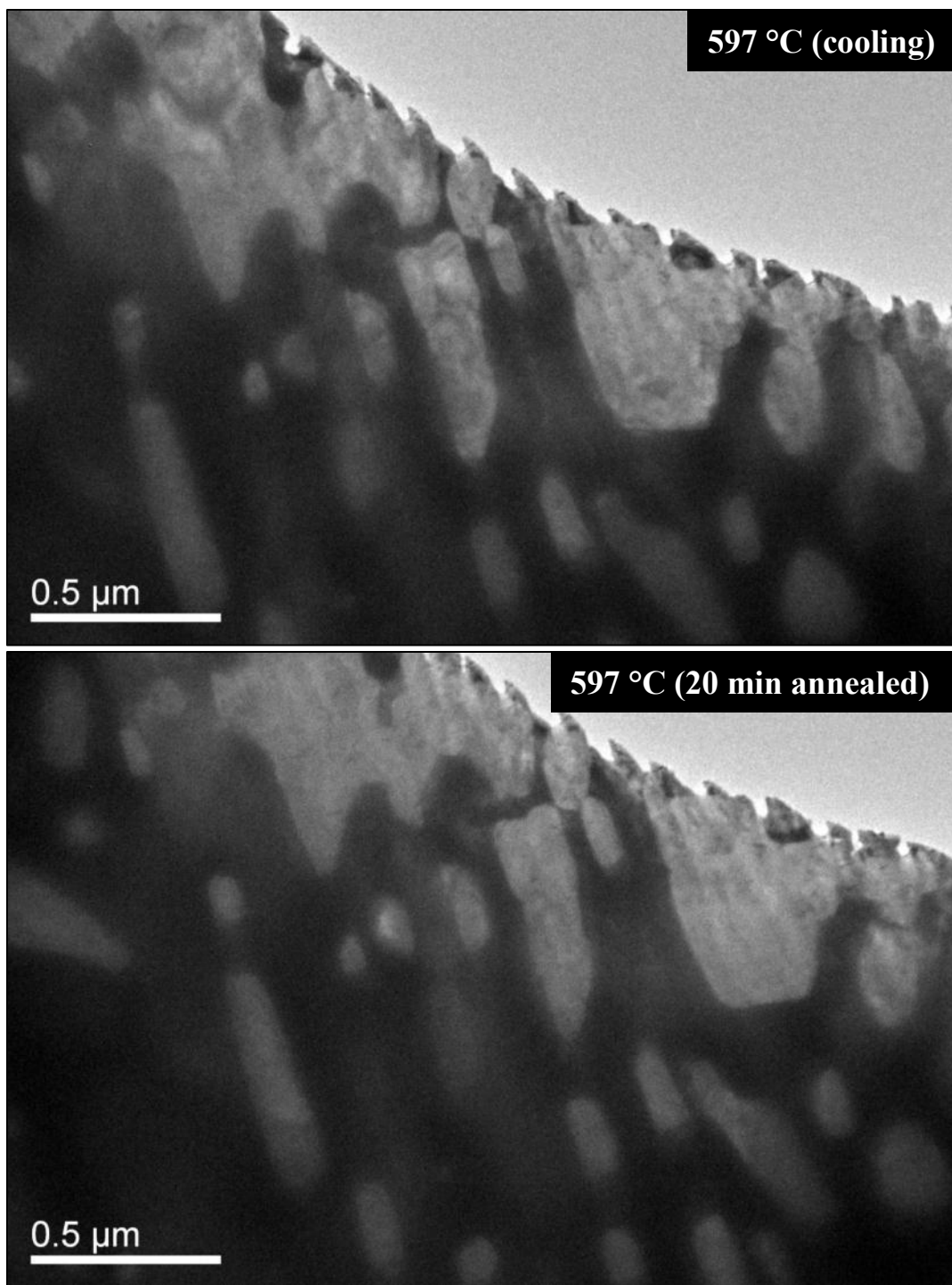
Figure 4-70: Continued.

There is a wealth of information to be gleaned from this remarkable sequence of images. First, the morphology change of U-20Zr alloy during heating was noted to occur above 620 °C, as shown in Fig. 4-70 (640 and 656 °C), may be due to phase transformation driven by uranium diffusion from the dark α-U precipitates into the brighter δ-UZr$_2$ phase matrix to form γ$_2$ phase, since uranium contents in γ$_2$ phase has to be increased along the temperature increase following the phase diagram.

Another noteworthy phenomenon shown in the images was numerous dark bridges formed bridging the two α-U phase precipitates, meaning diffusion of uranium atoms was not uniform at all phase boundary, possible due to nonstoichiometry in the δ-UZr$_2$ phase or the incomplete decomposition of γ phase.

Accelerated diffusion at more elevated temperature (> 680 °C) is visualized in three BF images taken at 682 °C at different magnifications. The contrast variations observed are due to enhanced uranium diffusion into bright phase matrix (formerly δ-UZr$_2$) which implies the local alteration of the composition and/or thickness, which could be driven by δ-UZr$_2$ → γ$_2$ phase transformation following the phase diagram.

The dispersion of the darker phases was continued during further heating the specimen from 682 °C to 809 °C, indicating that the formation of a single γ phase was not instantaneous and necessitated intermediate to long term annealing; this matches with the presence of the miscibility gap of (γ$_1$, γ$_2$) phase in the phase diagram [169].

In the highest temperature images (744 °C to 810 °C), where the specimen is presumed to be fully transformed to the single γ phase, the contrast variations represent remnant thickness variations arising from the electropolishing of the two phase alloy.

228

After heating the specimen up to 810 °C, it was cooled down to 681 °C and the apparent remnant phase boundaries due to still slightly dark U-rich region whose crystal structure is unclear at the temperature. Also, in Fig. 4-70 (681 °C), the presence of newly formed dark phases in the perforated specimen boundary indicates faster surface diffusion of uranium atoms assuming fairly even specimen thickness regardless of local phase, which is reasonable considering lower melting point of uranium.

From the two images taken at 597 °C, before and after the annealing for 20 min, the contrast redistribution was nearly halted, implying that diffusion is sluggish below 600 °C in U-20Zr alloy, maybe due to the lack of phase transformation. Further discussion on the meaning of these results is deferred to Section 5.2.5.

As a final observation, DP imaging was extremely troublesome during the *in-situ* heating of this alloy, not only because of the high temperature but also because two phase structure of the alloy. There were mainly three reasons for the noted difficulty:

1) The functionality of the single tilt heating stage holder was limited and could not readily align the atomic crystal to occur symmetric Ewald construction by placing the crossover of Kikuchi lines on the center of ZOLZ in found DPs,

2) The very thick and therefore opaque α-U precipitates interrupted the diffracted electron beam, and

3) The perpetual motion of the entire alloy specimen subjected to thermal vibration and expansion while heating specimen.

Even so, an attempt to capture the DPs was made and the patterns are presented in Fig. 4-71. The results were less than optimal DP images and analysis was challenged due to the above reasons. Even the best images obtained were not given clear indexing, although the evolution of DP along with temperature change was clearly observed. Overall, securing eccentricity, i.e. placing the specimen in exact focus not to change the focus while tilting the specimen, was impractical for the alloy specimens under constant thermal vibration and expansion, activated surface diffusion and occasional phase transformation, even aside from limited time (6 h) for consecutive usage of the TEM.

A second wide and very thin electron transparent area without distinctive phase contrast was selected for diffractometric study of U-20Zr alloy to provide a set of information comparable to the U-10Zr alloy information in Section 4.4.3.1. Bright field images of the selected area at 25 °C are shown in Fig. 4-72. The more usable ring type DPs were obtained from the wide transparent area at elevated temperatures as shown sequentially in Fig. 4-73.

Since two distinctively bright spots were repeatedly appeared on the innermost ring in the DPs, some DF images were taken utilizing the deflected beam forming one brightest spot at upper part of the innermost ring. The images show numerous white spots spread over entire selected area as shown in Fig. 4-74.
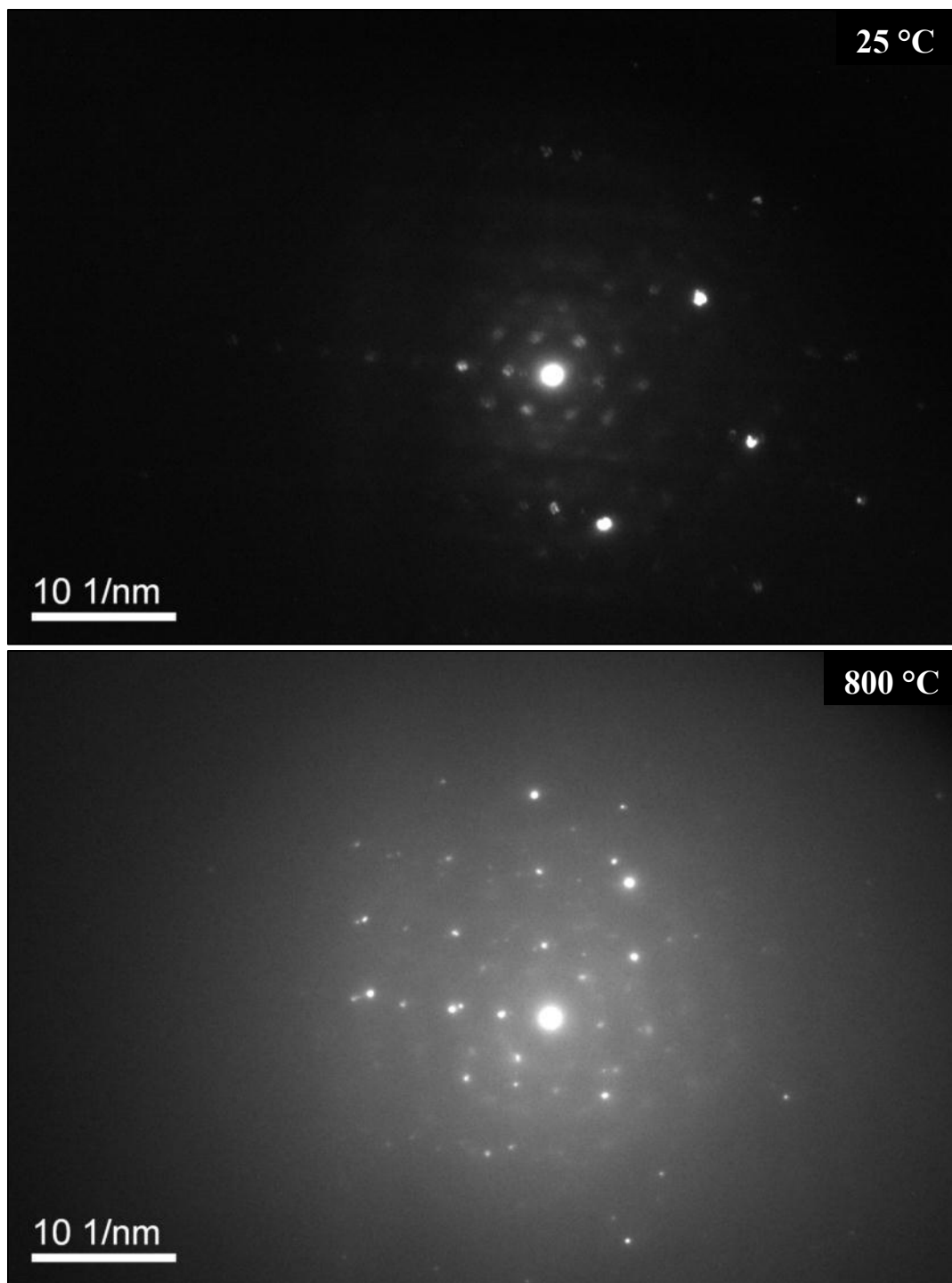
Figure 4-71: DPs of typical two phase lamellae structure of U-20ZrAi5, obtained at 25 and 800 °C during heating, and at 691 °C during cooling from 810 °C.

691 °C (cooling)

5 1/nm
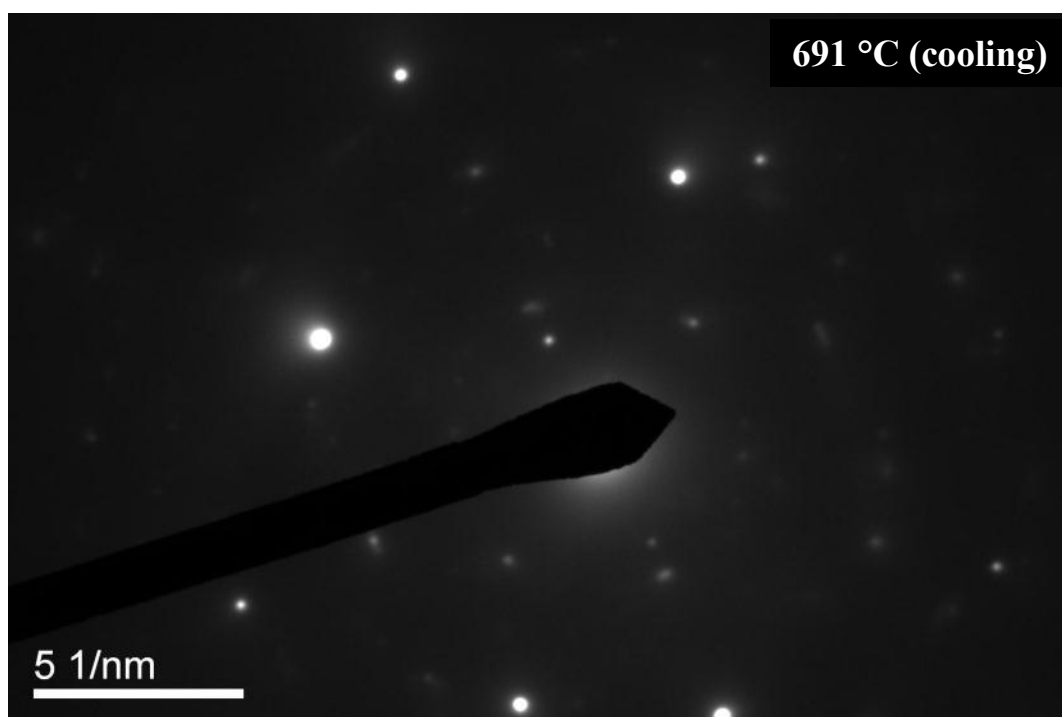
Figure 4-71: Continued.
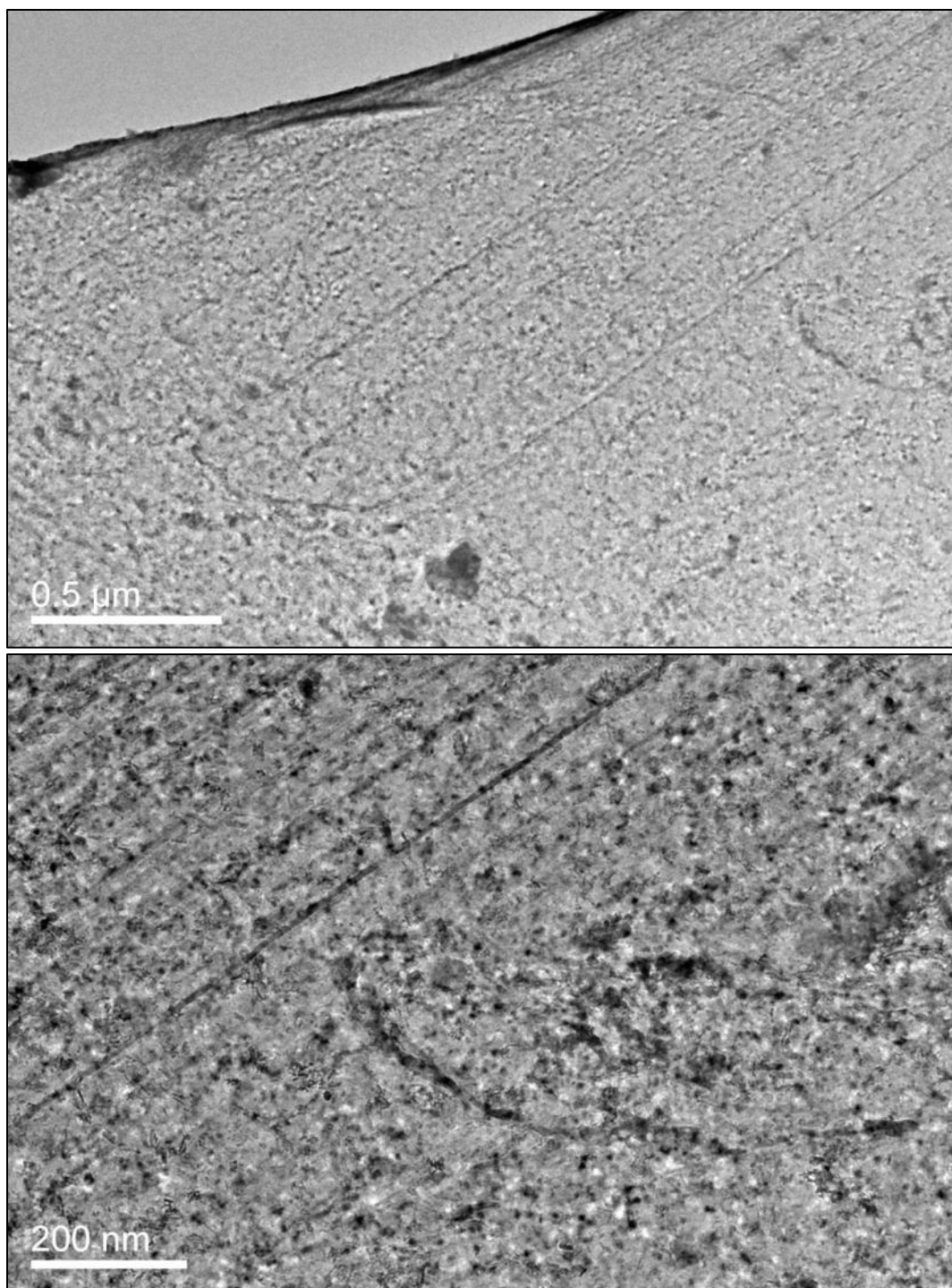
Figure 4-72: Wide transparent area without phase contrast selected for *in-situ* heating electron diffractometry of U-20ZrAi5.
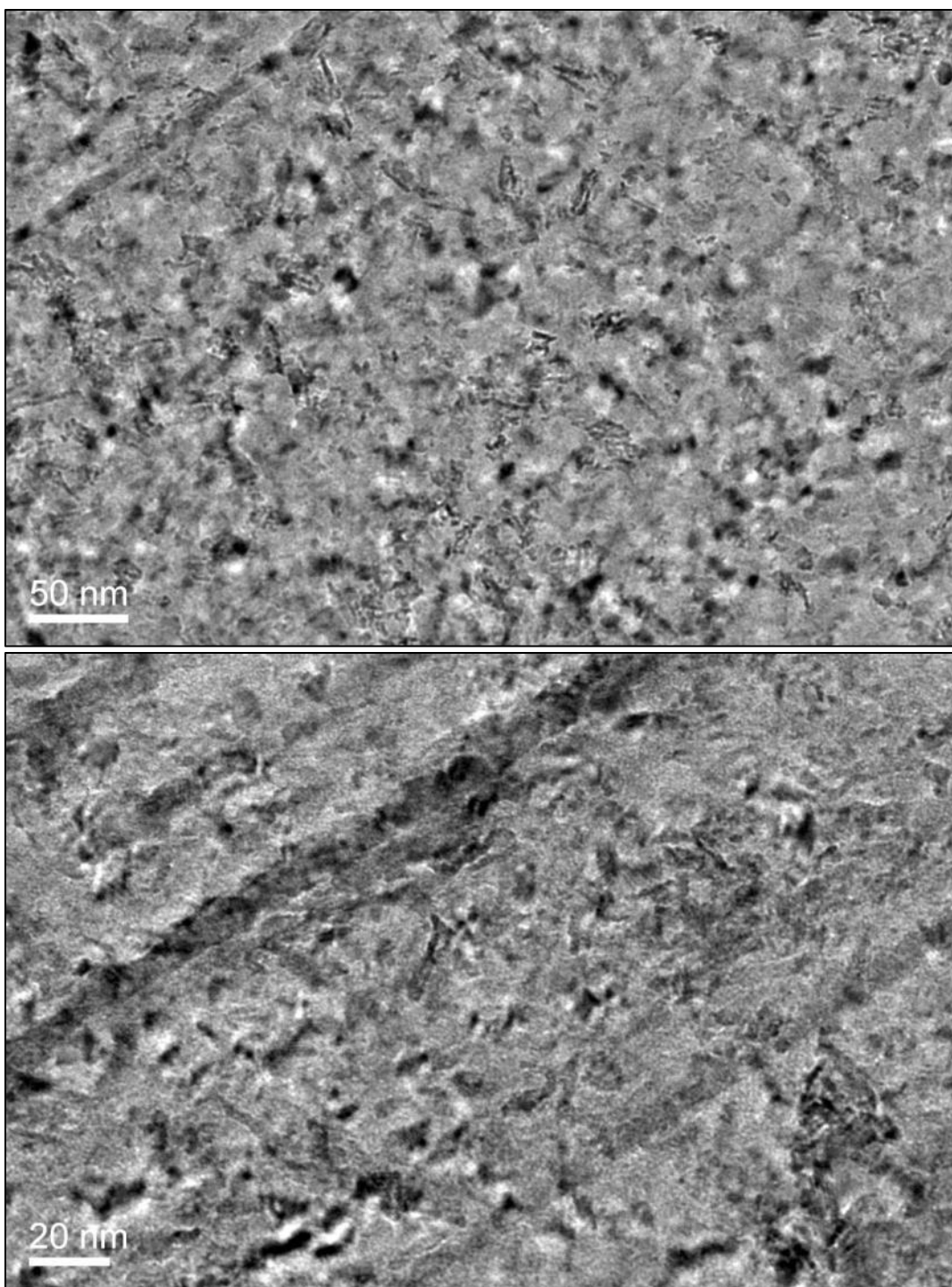
Figure 4-72: Continued.
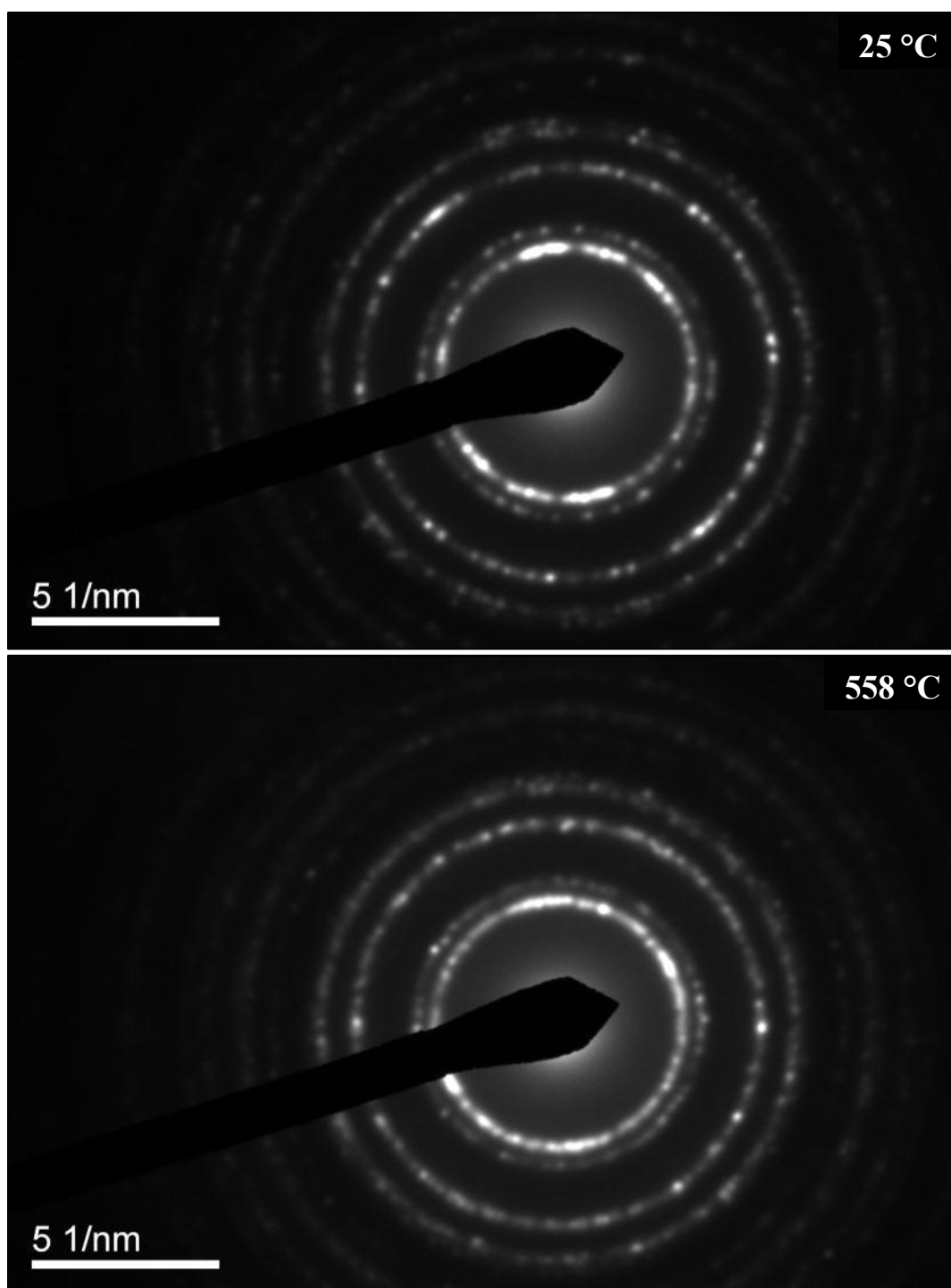
Figure 4-73: DPs of *in-situ* heated U-20ZrAi5, recorded at 25, 558, 590, 600, 618, 627, 640, 656, 670, 681, 812, and 815 °C during heating, at 705 and 690 °C during cooling, and at 690 °C after 20 min annealing.

590 °C

5 1/nm

600 °C

5 1/nm

Figure 4-73: Continued.

618 °C

5 1/nm

627 °C

5 1/nm

Figure 4-73: Continued.

640 °C

5 1/nm

656 °C

5 1/nm

Figure 4-73: Continued.

238

670 °C

5 1/nm

681 °C

5 1/nm

Figure 4-73: Continued.

812 °C

5 1/nm

815 °C

5 1/nm

Figure 4-73: Continued.

705 °C (cooling)

5 1/nm

690 °C (cooling)

5 1/nm
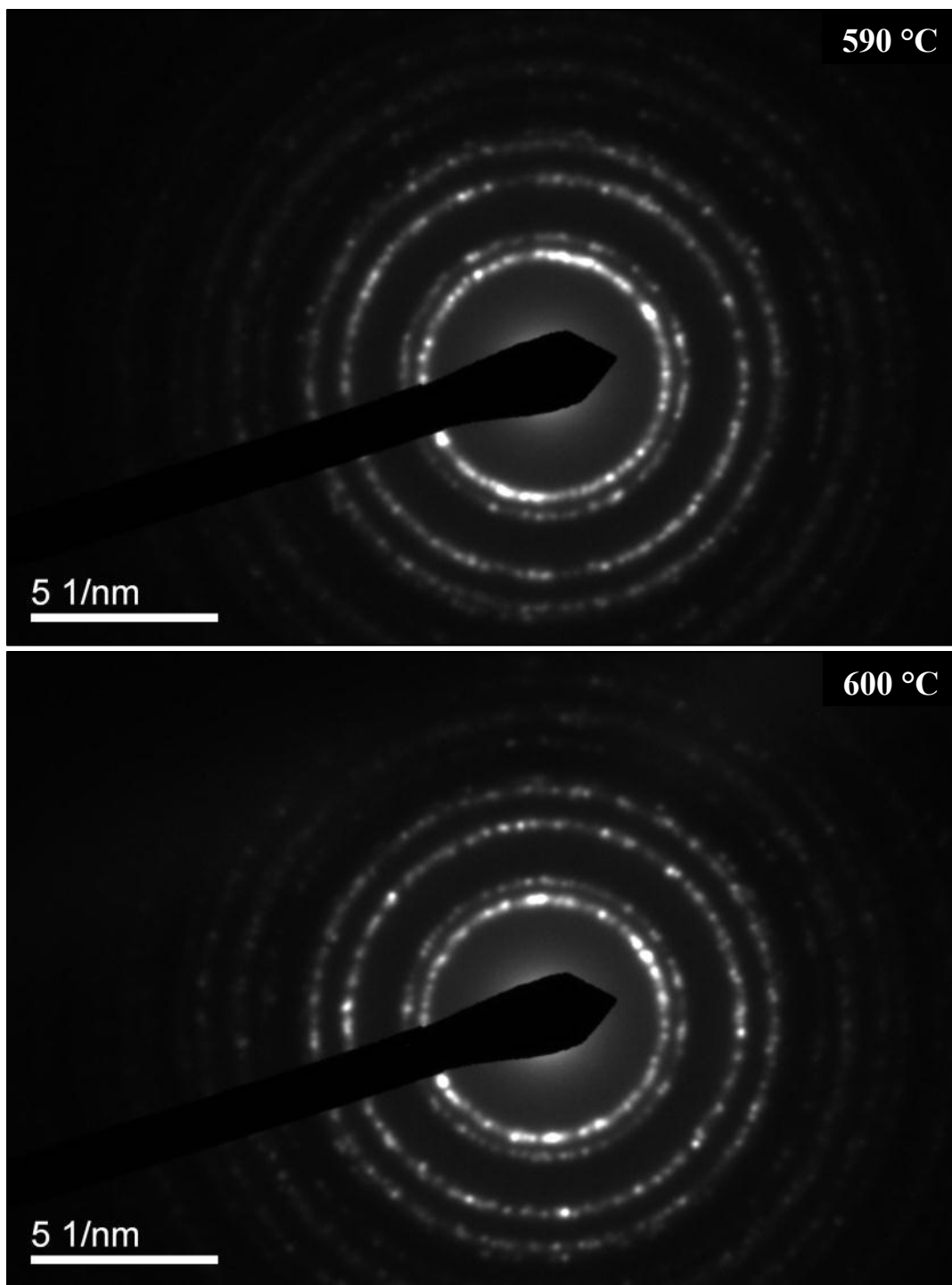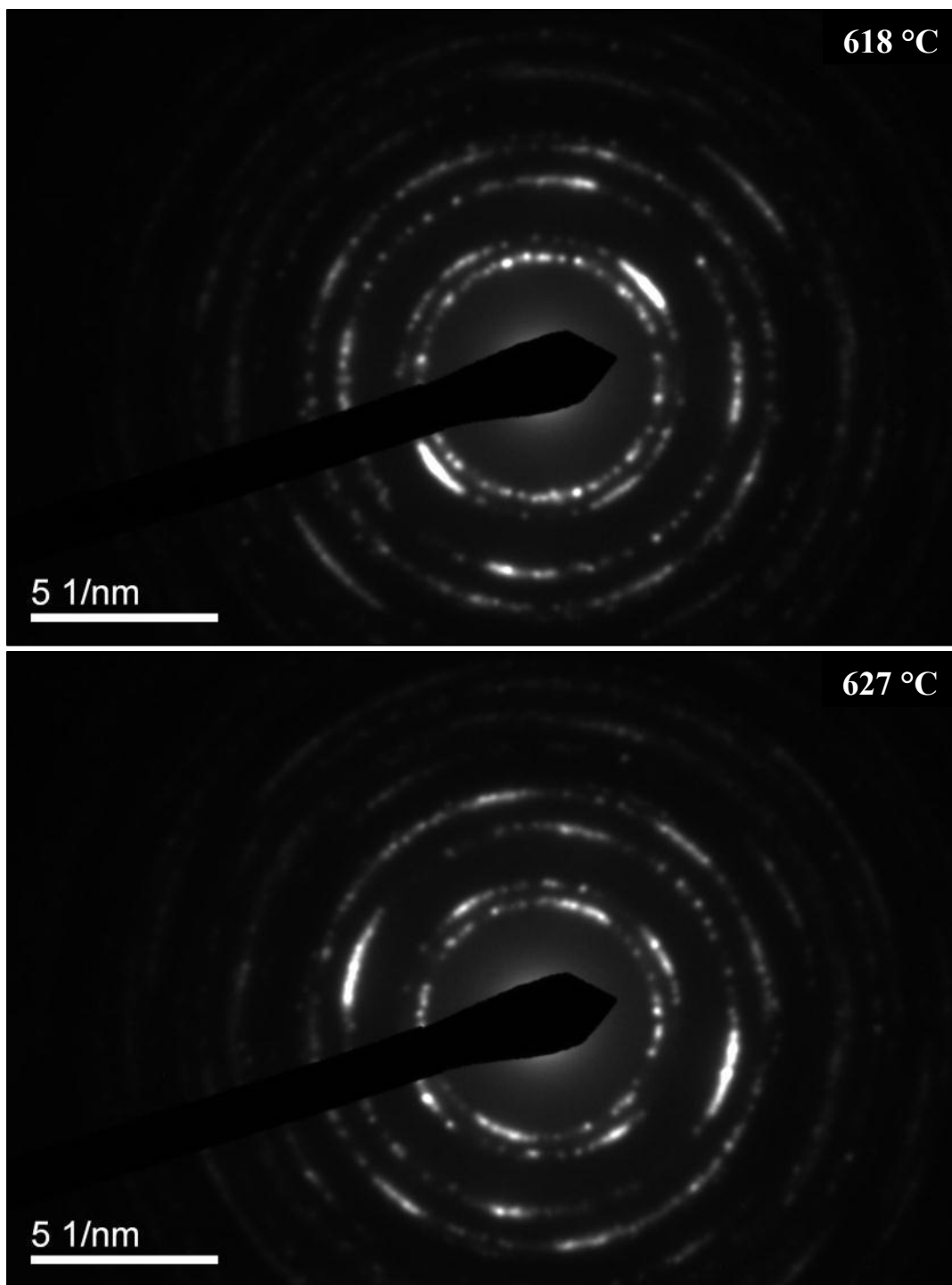
Figure 4-73: Continued.

Figure 4-73: Continued.

Figure 4-73 shows that no notable transition was observed in the DPs from 25 °C to 681 °C. Although the first remarkable change was observed at 690 °C, it was not instantly recorded due to abnormal specimen temperature spiking over 700 °C during imaging. *In-situ* heating experiments were unavoidably implemented along with ongoing phase transformation, adjusting applied voltage for specimen heating to compensate for heat absorption corresponding to phase transformation enthalpy in order for holding the temperature during imaging which was not always successful. However, all DPs taken at 690 °C or above are indistinguishably similar to each other while they differ from the DPs at or below 681 °C, which is exactly identical behavior with that of U-10Zr alloy. The meaning of these data will be discussed further in Section 5.2.5.
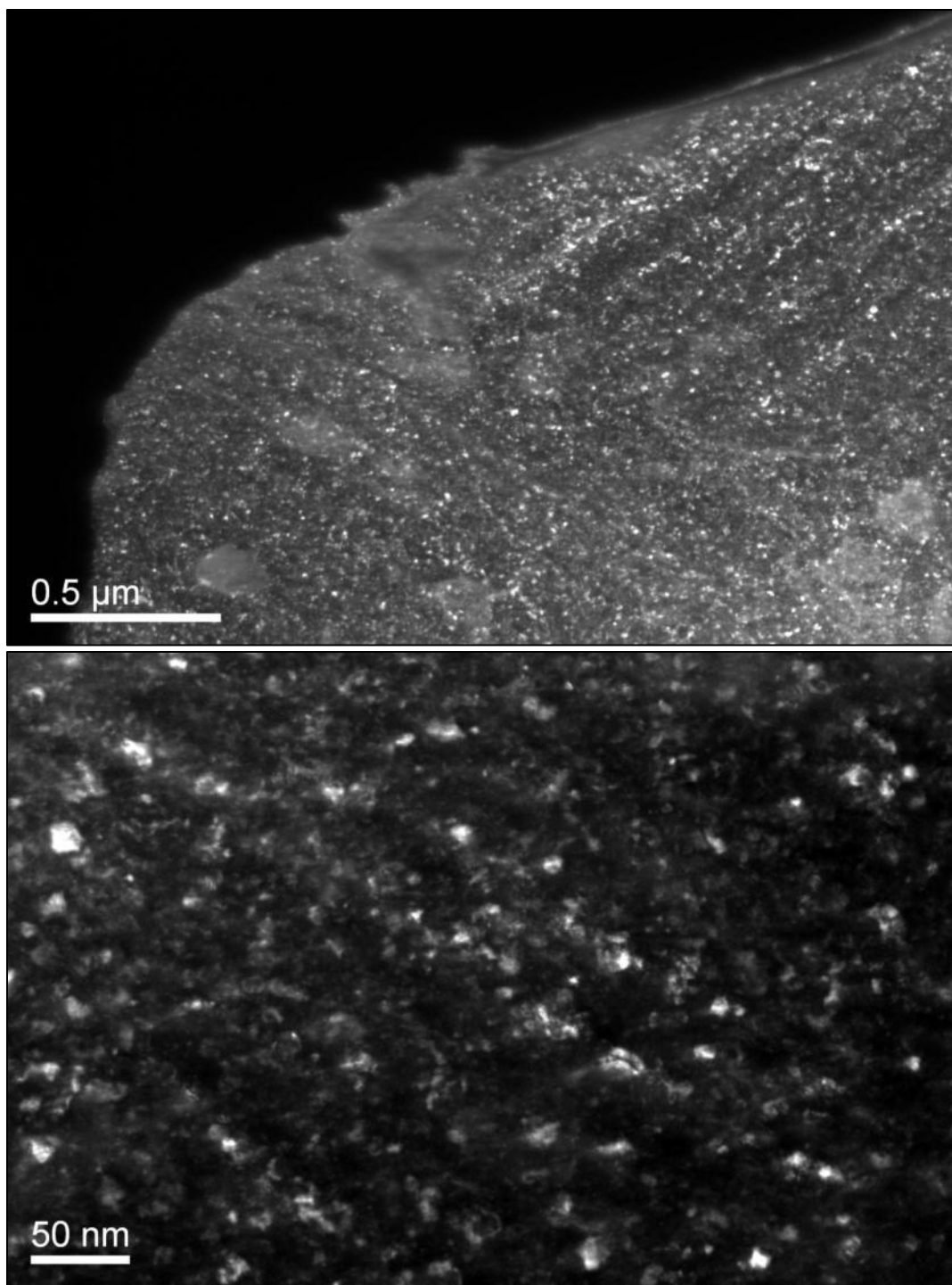
Figure 4-74: DF images of the area used for *in-situ* heating electron diffractometry of U-20ZrAi5.

5. DISCUSSION

The many and varied results in Section 4 arise from the application of a variety of methods and tools toward improving the present understanding of the binary uranium-zirconium alloy system. Many of the data are confirmatory in that they repeat and affirm existing knowledge but significant portions of the data are either first-of-a-kind measurements or contradictory to previous understanding. This section provides a discussion on the meaning of this new body of information as it pertains to the metallurgy of U-Zr alloys (Section 5.1), possible inconsistencies and imperfections in the binary U-Zr phase diagram (Section 5.2), and the behavior of U-Zr alloys under irradiation by helium ion bombardment (Section 5.3)

5.1 Metallurgy of U-Zr Alloys

5.1.1 δ-UZr₂ Phase Formation

Measured compositions of the Zr-rich phase in all U-Zr alloys were consistent with the non-stoichiometric δ-UZr$_2$ phase region given in the U-Zr binary phase diagram. Table 5-1 shows a summary of the measured compositions for the Zr-rich phases. The precipitates in U-2, 5, and 10Zr alloys contained varying amount of zirconium ranging from 61 at% to 69 at% and the Zr-rich matrix phase in U-20, 30, and 40Zr alloys ranged

in composition from 62 at% to 71 at% zirconium. In the U-50Zr, the zirconium content of this phase was found to be increased up to 82 at%.

Table 5-1: WDS measured zirconium compositions of presumptive δ-UZr$_2$ phase.

Alloy	# of spots measured using WDS	Zirconium compositions of presumptive δ-UZr$_2$ phase					
		Min. (at%Zr)	Max. (at%Zr)	Avg. (at%Zr)	1σ (at%Zr)	Avg. (wt%Zr)	1σ (wt%Zr)
U-0.1Zr	-	-	-	-	-	-	-
U-2Zr	2	62.2	65.9	64.0	2.6	40.6	1.0
U-5Zr	3	61.3	68.8	65.1	3.8	41.7	1.5
U-10Zr	11	61.9	67.3	64.9	1.6	41.4	0.6
U-20Zr	5	62.0	70.5	64.6	3.4	41.2	1.3
U-30Zr	6	64.5	70.6	67.0	2.1	43.8	0.8
U-40Zr	5	64.2	65.2	64.7	0.4	41.2	0.1
U-50Zr	29	66.1	81.6	72.4	4.0	50.1	1.6

The morphology and dimensions of the Zr-rich precipitates were characterized and did not show evidence for notable changes for annealing time increase from 3 days to 28 days as shown in Figs. 4-4, 4-5, 4-6, and 4-7. Those precipitates were apparently morphologically and chemically stabilized after 3 days of annealing. This swift formation of the Zr-rich phase is conflicted with some open literatures asserting kinetically very sluggish formation of δ-UZr$_2$ phase [170-173].

The very fine structures observed in the as-cast alloys whose compositions correspond to the (α-U, δ-UZr$_2$) phase zone in the phase diagram, U-2, 5, 10, 20, and

30Zr alloys, were irresolvable using EPMA as described in Section 4.1. However, the TEM characterization on as-cast U-10Zr and U-20Zr alloys revealed that each alloy has a morphologically congruent two phase structure that is consistent with its annealed counterpart as shown in Figs. 4-59, 4-65, and 4-67. In other words, as-cast alloy structures were nearly identical with those of annealed alloys of same composition, except the precipitate dimensions and lamellae spacing.

Bright field TEM image analysis for as-cast two phase U-Zr alloys yielded reasonably matched the actual alloy compositions with intended alloy compositions during melt-casting. The image analysis of Fig. 4-59(top) gives (10.3 $\pm$ 0.3) wt% zirconium for the as-cast U-10Zr alloy. The same method applied to Fig. 4-65(second) gives (19.7 $\pm$ 0.7) wt% zirconium for the as-cast U-20Zr alloy. Thus, the decomposition of single γ phase into the two RT equilibrium phases may be nearly instant (< 2 h), at least in chemical standpoint. The resultant compositions of Zr-rich phase precipitates and matrix were within the existent range of unstoichiometric δ-UZr_2 phase. Also, diffractometry of the as-cast U-10Zr alloy using high resolution transmission electron microscopy (HRTEM) in recent study at Lawrence Livermore National Laboratory (LLNL) also suggests the instant formation of δ-UZr_2 phase [174]; the alloys used for this study were produced with the same equipment and procedures used for this present study so the results are very closely related.

5.1.2 Secondary Phase Formation

Due to the impurities inserted into alloy slugs during casting and annealing, secondary phases composed of oxygen-saturated zirconium and yttrium oxide (Y_2O_3) were found from the observations using EPMA and TEM. However, the DSC-TGA did not show any peaks directly corresponding to the phase transformation of these secondary phases, indicating that they either did not undergo transformations at the temperatures of interest or the mass fractions of those impurity phases were too negligible to be observed by thermophysical measurements.

Although secondary phase effects were practically negligible in EPMA and DSC-TGA, the presence of the impurity particles was considered for nanostructure characterization conducted using TEM, since observable areas prepared utilizing electropolishing of the alloys were relatively narrow (< ~20 μm) compared to the maximum size of the secondary phase particles. However, the discovered impurities were conveniently distinguishable due to their morphology and darker contrasts under TEM as shown in Figs. 4-31, 4-35, 4-36, 4-42(top), 4-43, 4-48(top) and 4-57. Also, it was very helpful for the phase characterization that the typical DPs of the alloy bulk were well known from repeated TEM characterization of various compositions of U-Zr alloys.

There were several cases of reversed mass-contrast in the TEM images in Sections 4.4.3 and 4.4.4 for the U-10Zr and U-20Zr alloys. That is, lower-density phases appeared darker than the uranium phase due to selective electropolishing. The α-U phase

was typically more aggressively etched away leaving thicker δ-UZr$_2$ and/or α-Zr phases and impurity particles. Therefore, these phases and particles were often embossed out from the bulk throughout electropolishing as shown in Figs. 4-44, 4-46, 4-48, 4-55, and 4-66. Typical dimensions and shapes of secondary phase particles shown in the EPMA observation often enabled the handy distinction for the impurity particles on the TEM viewing screen.

For the U-rich region of the U-Zr binary phase diagram, α-Zr phase should not be present, however α-Zr precipitates including trace amount of uranium were frequently observed using EPMA. The formation of the phase precipitates have been repeatedly reported in literature and it is known suspected that the precipitates are stabilized due to the insertion of trace amount of impurities, most importantly nitrogen and oxygen [119, 161], although EDS was incapable to detect those elements from the precipitates. So, in reality, these are impurity-saturated α-Zr phases which are known to maintain their hcp crystal structure without β transformation up to melting above 1900 °C.

The uranium content of the precipitates measured using WDS were (0.7 ± 0.2) at%, which is slightly higher than solubility of uranium in α-Zr phase, 0.4 at% [127, 141], this is likely due to an artifact arising from electron reactions invading the U-rich surroundings. The densities of the precipitates were particularly high in single δ-UZr$_2$ phase composition alloys, i.e. U-40Zr and U-50Zr alloys. The presence of the phase precipitates in the alloys were concentrated, but not limited, at grain boundary.

Zirconium precipitates were frequently revealed and protruding from electropolished TEM specimens of U-40Zr alloy, owing to the electrochemical

resistance of the element. Observed α-Zr precipitates in TEM can be categorized as two types. One is trapezoidal precipitates having darker contrast, which were commonly found within alloy bulk as shown in Fig. 4-42(top). The other type is dendritic with many secondary and tertiary branching arms from the primary arm. The zirconium dendrites were repeatedly etched out from perforated TEM specimen boundary as shown in Figs. 4-44, 4-46(top) and 4-48(bottom). Contrast of the dendrites was similar with the bulk. However the dendrite contrast can be drastically changed by tilting the specimen since it commonly has a single crystal as shown in Fig. 4-55.

Zirconium dendrite protrusion from the bulk of U-40Zr alloy was consistent with preferential etching of Zr-rich matrix phase of U-20Zr alloy. The presumptive δ-UZr$_2$ phase matrix of the as-cast U-20Zr alloy also exhibited higher resistance to the electropolishing compare to α-U phase as shown in Figs. 4-65, 4-67, and 4-68. Therefore, SAD patterns of thicker zirconium dendrites commonly have Higher Order Laue Zones (HOLZ), typically up to the second order, as shown in Figs. 4-46 and 4-56. Defect free single crystal structures of the dendrites were often found from irradiated U-Zr alloys at the highest dose as shown in Fig. 4-46, suggesting that zirconium is more irradiation tolerant than α-U or δ-UZr$_2$ phase. The dendritic form of the α-Zr phase was rarely found in two phase alloys, U-10Zr and U-20Zr, where the EPMA confirmed less formation of zirconium dendrite than in single δ-UZr$_2$ phase alloys, U-40Zr and U-50Zr.

5.1.3 Grain Boundary Effects

Nucleation of the bcc γ phase from cooling molten mixtures of alloys was anticipated to occur with solid secondary phase precipitates having higher melting points than U-Zr alloys. Therefore secondary phase precipitates were often found as continuously aligned along with grain boundaries in as-cast U-Zr alloys as shown in Figs. 4-10 and 4-11. A grain boundary filled with secondary phase precipitates can be formed from solid secondary phase particles suspended in liquid phase U-Zr until γ phase grains grow to finally adjoin other grains. This type of grain boundary feature was often observed in as-cast U-10Zr alloy. Figure 4-57 shows ~20 μm long etched out grain boundaries visualized in the two combined images constructed using several BF images each. Higher electrochemical resistivity of secondary phase is evident from the figure.

Parent γ phase grain boundaries filled with δ-UZr$_2$ phase lamellae were commonly found in annealed U-10Zr alloy as shown in Fig. 4-7. Preferential formation of δ-UZr$_2$ phase at grain boundaries might be due to lower density of the phase and expedited grain boundary diffusion. Excess free energy near grain boundary can be minimized by utilizing misfits between the grains to place newly formed voluminous phases, e.g. δ-UZr$_2$ phase in this case. This hypothesis is strengthened by referring the morphologies of annealed U-20Zr and U-30Zr alloys (Figs. 4-8 and 4-9), not shown any distinguishable grain boundary because grain boundaries in the alloys were preferentially filled with formed δ-UZr$_2$ phase, being indistinguishable with δ-UZr$_2$ phase matrix of the Zr-rich U-Zr alloys.

250

Similar mechanism are likely to be responsible for zirconium precipitate formation along grain boundary in as-cast single δ-UZr$_2$ phase alloys, U-40Zr and U-50Zr, as shown in Fig. 4-10. Impurity induced α-Zr phase nucleation can be accelerated by grain boundary diffusion synergistically combined with higher impurity concentration at grain boundary. Therefore, short-term (~1 h) cooling during melt-casting could be enough to mark major portion of grain boundary with α-Zr precipitate.

5.1.4 δ-UZr$_2$ Phase Decomposition

The uranium-rich phase haloing α-Zr precipitates was often found in the EPMA of annealed U-40Zr and U-50Zr alloys as shown in Figs. 4-10 and 4-11. Measured zirconium composition of the phase was fluctuated within ~1 at% to ~10 at%, depending on the dimension of the phase region. Considering the phase was sandwiched between δ-UZr$_2$ and α-Zr phases, the measured zirconium compositions were likely exaggerated. Therefore the phase was concluded to be α-U since the minimum zirconium contents were corresponding to the solubility limit of zirconium in α-U phase.

The presence of α-U phase in the single δ-UZr$_2$ phase U-40Zr and U-50Zr alloys is not consistent with the U-Zr binary phase diagram and was likely due to δ-UZr$_2$ phase decomposition into α-Zr phase precipitates fixed by impurities, e.g. oxygen or nitrogen. Activated diffusion of impurities in α-Zr phase precipitates during annealing could decompose neighboring δ-UZr$_2$ phase matrix. The susceptible nature of δ-UZr$_2$ phase to

251

impurity insertion decomposed into α-U and α-Zr phases is well known from literatures [123, 161].

This decomposition of δ-UZr$_2$ to α-U and α-Zr was clearly evident in single δ-UZr$_2$ phase U-Zr alloys, but not in other compositions of alloys including α-U phase. Independently formed α-U phase precipitates, apart from zirconium precipitates, were found in U-40Zr alloy as shown in Fig. 4-10(e). Formation of α-U phase is inconsistent with U-Zr binary phase diagram might be due to zirconium lean matrix of the alloy whose effective composition could be below the low end of unstoichiometric δ-UZr$_2$ phase zone in the phase diagram because secondary phase precipitates isolated zirconium.

5.1.5 Estimation of Cast Alloy Compositions Utilizing Image Analysis

Melt-cast U-Zr alloy compositions were first confirmed by measuring wide bulk areas of the annealed alloys using WDS, which was successful for single phase alloys as shown in Table 5-1. However due to inhomogeneous two phase structures of the other annealed alloys, U-2, 5, 10, 20, and 30Zr, the measured compositions were often unreliably fluctuated. Also, zirconium depletion from the alloy bulk was a complication due to the secondary α-Zr phase formation discussed in Section 5.1.2. Therefore the cast alloy compositions were estimated by measuring the composition (by WDS) and area fractions of the two primary phases, α-U and δ-UZr$_2$, from more than ten binary BSE images of annealed alloys; a typical binary image of annealed U-10Zr alloy is shown in

Fig. 5-1. It was calculated as the sum of the products of average area fraction and zirconium solubility of each phase. The estimated compositions of two phase U-Zr alloys are listed in Table 5-2.
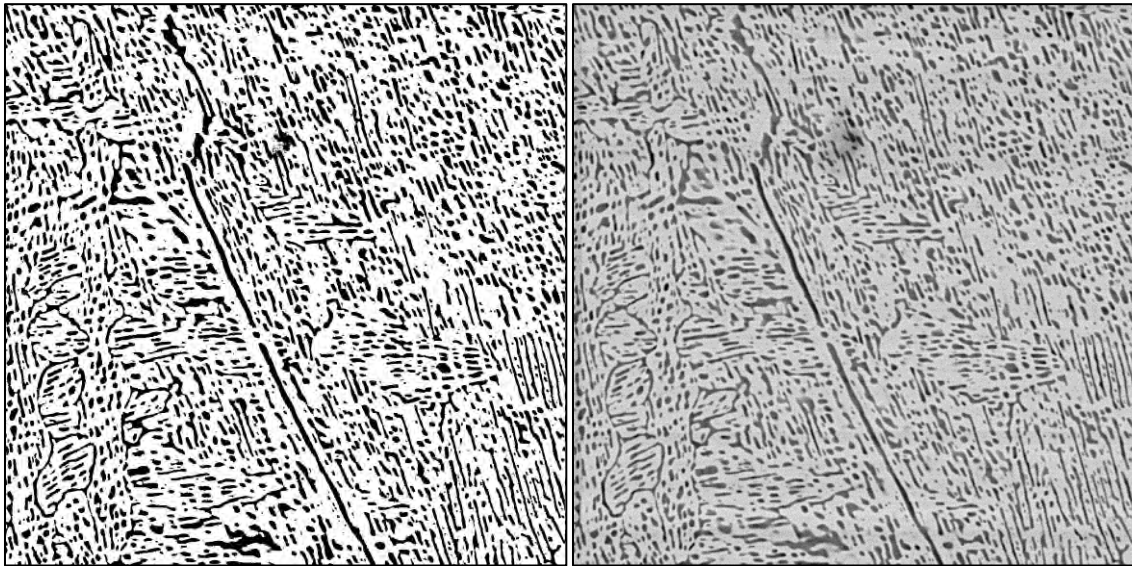
Figure 5-1: Binary (left) and the original BSE (right) images of U-10Zr1d600 (3000X); the binary image was generated using ImageJ (NIH) to estimate the composition of the two phase U-Zr alloy after annealing. (Note the absence of scale bar in the images in comparison to Fig. 4-7(e).)

Table 5-2: Compositions of the annealed two phase U-Zr alloys estimated from BSE image analysis using ImageJ (NIH).

Alloy		Zirconium compositions of two phase U-Zr alloys				
		# of BSE images analyzed	Avg. (wt%Zr)	1σ (wt%Zr)	Avg. (at%Zr)	1σ (at%Zr)
U-2Zr		23	2.6	0.3	6.5	0.7
U-5Zr		62	5.4	0.6	13.0	1.4
U-10Zr	3d600 (DSC)	10	7.8	0.7	18.1	1.4
	7d600 (DSC)	10	10.3	0.6	23.1	1.2
	Total	56	8.3	1.2	19.1	2.4
U-20Zr		21	18.5	1.5	37.2	2.3
U-30Zr		50	23.8	1.6	44.9	2.2

The calculated zirconium compositions of U-10Zr and U-20Zr alloys were slightly lower than the intended compositions established by the masses originally charged into the melt crucibles. This decrease is reasonable considering 1) the secondary impurity-saturated α-Zr phase precipitates were seldom counted in the BSE image analysis of two phase alloys and 2) the low end zirconium composition (63 at%) of δ-UZr_2 phase in Sheldon's phase diagram was adopted to calculate the alloy compositions, although measured zirconium composition of the Zr-rich phase were consistently higher than the theoretical value, as shown in Table 5-1.

Particularly significant zirconium loss from U-30Zr was due to partial non-melting that occurred during the melt-casting of the alloy. Unmelted zirconium chunks were discovered from the EPMA characterization as shown in Appendix C.1. However, the notation for the alloy was unchanged for internal consistency. This is likely to be

responsible for the relatively large discrepancy in the experimental transformation enthalpies of the U-30Zr from theoretical values estimated from the two U-Zr phase diagrams, as discussed in Section 5.2.4.

Table 5-2 shows three compositions especially for U-10Zr due to the importance of the alloy for the discussion on U-Zr binary phase diagram given in Section 5.2. The U-10Zr alloy compositions were estimated for each of the different time-annealed DSC samples of U-10Zr alloy. The 3d600(DSC) and 7d600(DSC), are given in the upper two rows. The composition given in the third row is the average of all BSE images of the alloy including the DSC samples. Recall that adjacent pieces of the same alloy button given the DSC samples were substituted for the DSC samples to give necessary BSE images for the analysis, since once DSC thermal cycled alloy sample cannot be utilized for the image analysis due to excessive secondary phase particles formed during DSC measurement.

5.2 U-Zr Binary Phase Diagram

5.2.1 Critical Review on Current Phase Diagram

There have been extensive recent efforts in the construction of the U-Zr binary phase diagram using thermodynamic calculative methods and data measurements [175-180], however, basically no paradigm shift was made in the basic features of the diagram after Sheldon and Peterson [127]. Sheldon's phase diagram was constructed based on the

selected experimental data and there were some notable conflicts in the data set. One notable point is that published Sheldon's phase diagram does not show any experimental data supporting the existence of the isotherm line at 662 °C splitting the (α-U, γ_2) and the (β-U, γ_2) phase zones as shown in Fig. 2-2.

This isotherm line was mandated by adopting eutectoid decomposition of β-U into (α-U, γ_2) phase. This feature was first suggested by the measurement of phase transformation temperatures using dilatometry, although several compositions of U-Zr alloys exhibited no phase transformation at 662 °C during heating [131]. This temperature was measured by dilatometry only once during cooling where hysteresis may significantly alter the measured transformation temperature, which was self-evident in the study. Another study was also used to support the isotherm utilizing differential thermal analysis (DTA) to observe phase transformations [135]. However, the published DTA data does not confirm the transformation at 662 °C due to poor resolution of the method.

On the other hand, the older phase diagram by Rough's (Fig. 2-3) adopted peritectoid formation of α-U from (β-U, γ_1) phase. Therefore phase transformation temperatures of α-U to β-U were increased along with zirconium contents matched with experimental data [134]. Also, wide (β-U, γ_2) phase zone is absent from the phase diagram and narrow (α-U, γ_1) phase zone is appeared as shown in Fig. 2-3 [124].

5.2.2 Number of Phase Transformation

The single most distinctive differences between the two U-Zr binary phase diagrams (Figs. 2-2 and 2-3) when it comes to the DSC-TGA experiments are the expected numbers of phase transformation for two alloy compositions, i.e. U-10Zr and U-20Zr. The anticipated phase transformation numbers for the selected U-Zr alloy compositions in this study are listed in Table 5-3. Note that 'broad' in parentheses following after the number in the table indicates that the alloy should exhibit relatively broadened peak for the last phase transformation at the highest temperature in the first DSC heating curve. This broadening corresponds to the non-isotherm curved boundary between the two phase zone and the single γ phase zone as the curved boundary will appear a continuous phase transformation over an extended time.

Table 5-3: Theoretical number of phase transformations following the two phase diagrams of U-Zr binary alloy system.

Alloy		U-2Zr	U-5Zr	U-10Zr	U-20Zr	U-30Zr	U-50Zr
# of phase trans-formation	Rough	3 (broad)	3	2	2	2	1
	Sheldon	3 (broad)	3	3	3	2 (broad)	1

The U-10Zr alloy could exhibit two different phase transformation behavior due to position of monotectoid invariant point, sensitively depending on impurity

concentration in the system [131, 141]. It is also possible that the bulk of the melt-cast U-10Zr alloy has effectively low zirconium composition below monotectoid invariant point due to compositional drift in the alloy slug and zirconium depletion as the α-Zr phase precipitates. This was, in fact observed in the U-10Zr DSC results in Section 4.2 that indicate two and three transitions, depending on the impurity level and the actual phase compositions reported in Table 5-2.

It is evident from Table 5-3 that U-20Zr is another key composition to referee that DSC measurements follow which phase diagram, based on the number of solid phase transformations, i.e. the number of peaks in DSC heating curve, aside from the transformation temperatures or enthalpies. DSC heating curves from U-Zr7d600 and U-Zr28d600 are collectively shown in Fig. 5-2 [156].

Figures 4-22 and 5-2 shows the first DSC heating curves from all annealed U-20Zr samples exhibiting only two phase transformation peaks, clearly not in accordance with Sheldon's phase diagram. In addition, the last peaks of all annealed U-30Zr shown in Figs. 4-23 and 5-2(a) were not broadened but were clearly diminished in contrast to all the other peaks. Note from Fig. 5-2 that the last peaks of annealed U-2Zr were clearly wider than the counterparts of other U-Zr alloys as expected in Table 5-3. Moreover, only two peaks were observed from the DSC heating curve of U-10Zr7d600, which must have three peaks following Sheldon's phase diagram. However, three peaks were obtained from U-10Zr3d600 and U-10Zr28d600. Figure 5-3 highlights this improbable behavior of different time annealed U-10Zr alloy samples. Note U-10Zr28d600 is

intentionally omitted from the figure since it is simply a duplication of U-10Zr3d600 in the context of given the figure.

It is important to note from Figs. 5-2 and 5-3 that phase transformation behavior of U-10Zr28d600 is almost identical with that of U-10Zr3d600. Therefore variant phase transformation behavior of U-10Zr alloy was not likely due to different annealing time period. Since this dramatic change was unlikely occurred in the same composition alloy samples and U-10Zr alloy is close to the monotectoid invariant point in U-Zr phase diagram, axial zirconium composition alteration within 14 mm high melt-cast slug of U-10Zr alloy was suspected to be the cause for the abnormality. Therefore, as noted in Section 5.1.5, the actual compositions of the DSC samples of U-10Zr alloy were estimated utilizing BSE image analysis as shown in Table 5-2. Note all BSE images were taken from the remained pieces of the identical alloy buttons yielded the DSC samples.
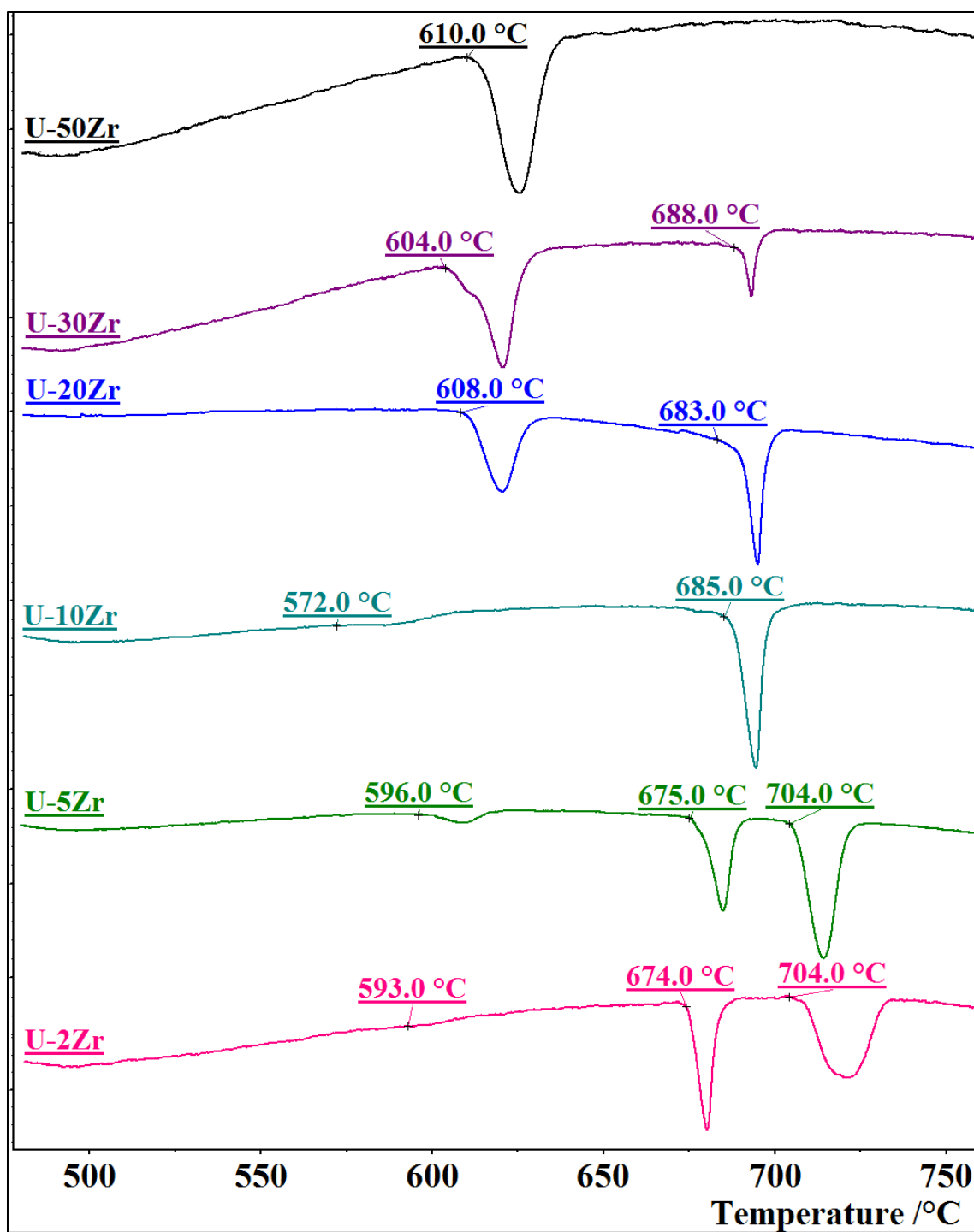
(a) DSC curves from U-Zr7d600 (ordinate is not to scale)

Figure 5-2: DSC heating curves from U-Zr7d600 and U-Zr28d600.
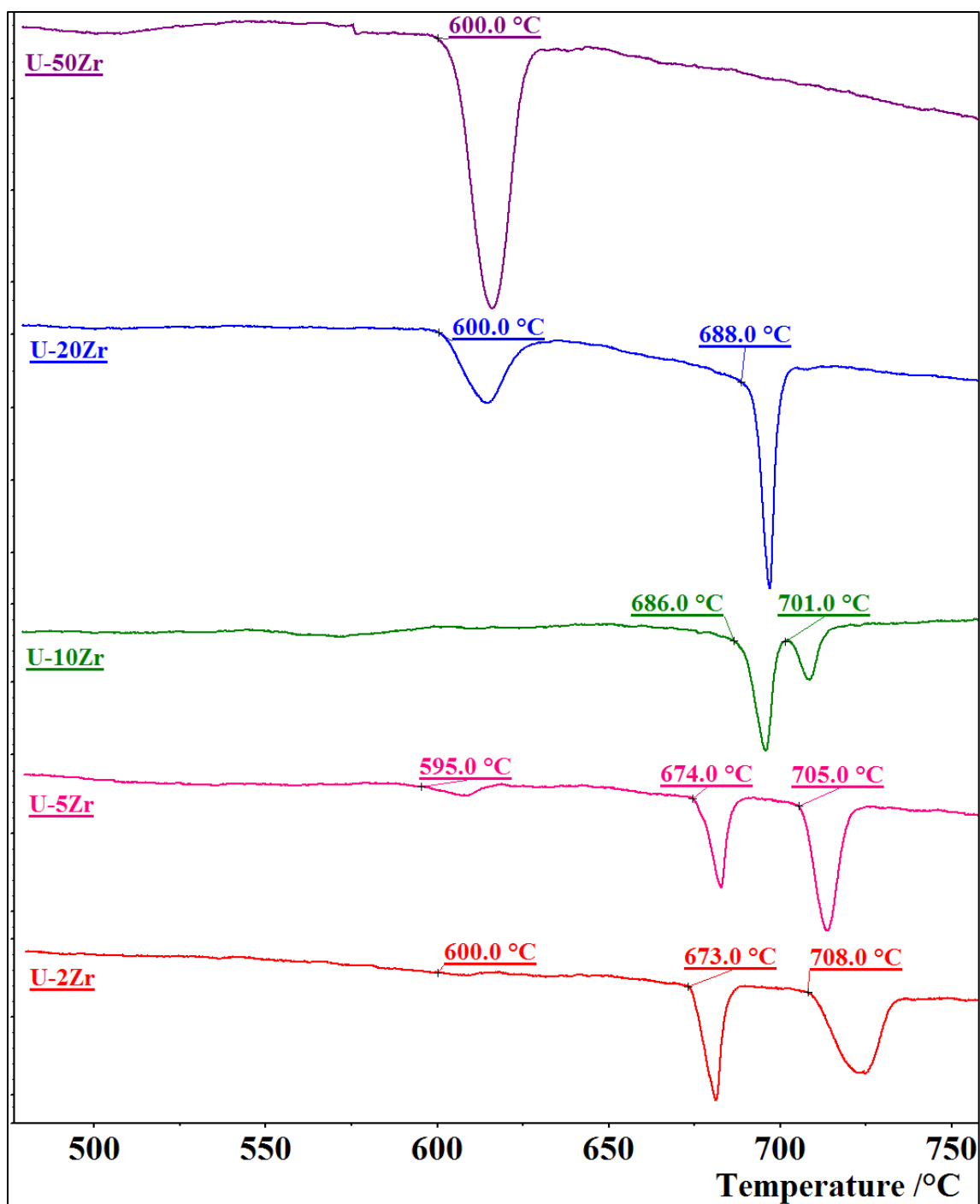
(b) DSC heating curves from U-Zr28d600 (ordinate is not to scale)

Figure 5-2: Continued.
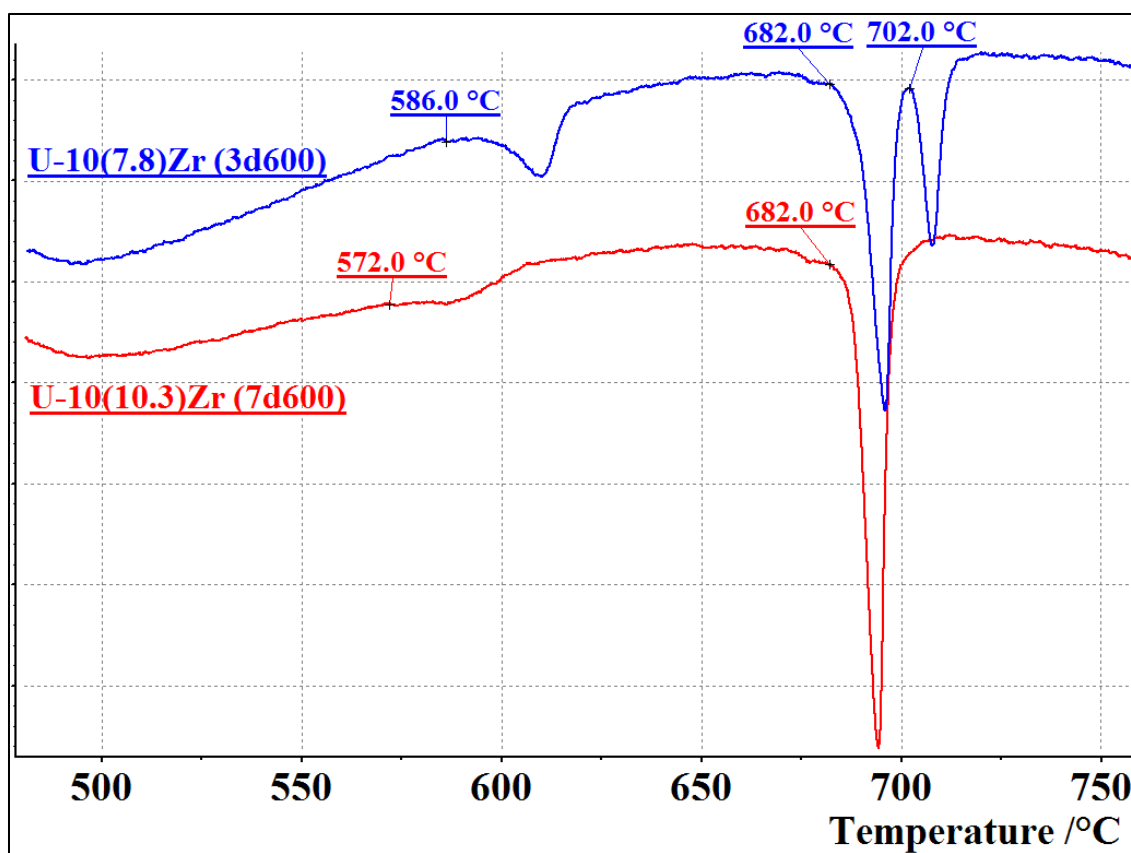
Figure 5-3: Variant phase transformation behavior of U-10Zr alloys.

The estimated zirconium compositions of the DSC samples for U-10Zr3d600 and U-10Zr7d600 were (7.8 ± 0.7) wt% and (10.3 ± 0.6) wt%, respectively, as given in Fig. 5-3. Following the analysis, U-10Zr3d600 was considerably close to experimentally reported highest zirconium composition of the monotectoid invariant point, 16 at% (6.8 wt%) [141]. Note that reported positions of the invariant point will vary along with the degree of impurity insertion. The most intuitive way to explain this result is that 1) the (β-U, γ_2) phase zone should not exist over 10 wt% zirconium in U-Zr phase diagram as

in Rough's phase diagram and 2) monotectoid invariant point may need to be positioned approximately between 7.8 wt% and 10.3 wt% in U-Zr phase diagram.

5.2.3 Phase Transformation Temperatures

The theoretical phase transformation temperatures from the two phase diagrams are shown in Table 5-4. In contrast, Table 5-5 shows experimentally measured phase transformation temperatures of annealed U-Zr alloys using DSC. It needs to be highlighted that the phase transformation responsible for each temperature is different for the two U-Zr phase diagrams in Table 5-4.

Phase transformations from Rough's phase diagram are adopted in Table 5-5 because the phase diagram was apparently preferred by the experimental data. More specifically, only two transformations were observed from U-10Zr7d600 and U-20Zr alloys. Anomalous behavior of U-10Zr3d600 and U-10Zr7d600 is again highlighted in the table and estimated compositions of the DSC samples are given in the last column.

Discrepancies between experimental and theoretical transformation temperatures are less stressed in Tables 5-4 and 5-5, since those could be sensitively influenced by various experimental conditions, e.g. heating rate, purge gas flow rate, and instrument calibration. However, measured transformation temperatures were significantly better matched with Rough's phase diagram, regardless of alloy composition and annealing period. Some important alloy compositions and transformation temperatures are emphasized in bold and underlined in Tables 5-4 and 5-5. Also, note that the

monotectoid construct in U-Zr binary phase diagram may be incorrect as well since Table 5-5 tends to show two isotherms; one at ~675 °C for U-2Zr and U-5Zr alloys, and a second at ~685 °C for U-10, 20, 30, and 40Zr alloys.

Table 5-4: Theoretical phase transformation temperatures in U-Zr phase diagrams.

	Alloy	Peak 1 (°C) $(\alpha, \delta) \rightarrow (\alpha, \gamma_2)$	Peak 2 (°C) $(\alpha, \gamma_2) \rightarrow (\beta, \gamma_2)$	Peak 3 (°C) $(\beta, \gamma_2) \rightarrow (\beta, \gamma_1)$
Sheldon	U-2Zr	617	662	693 (broad)
	U-5, <u>10, 20Zr</u>	**<u>617</u>**	**<u>662</u>**	**<u>693</u>**
	U-30Zr	617	**<u>662 (broad)</u>**	-
	U-50Zr	~610	-	-
	Alloy	Peak 1 (°C) $(\alpha, \delta) \rightarrow (\alpha, \gamma_2)$	Peak 2 (°C) $(\alpha, \gamma_2) \rightarrow (\alpha, \gamma_1)$	Peak 3 (°C) $(\alpha, \gamma_1) \rightarrow (\beta, \gamma_1)$
Rough	U-2Zr	~610	685	~705 (broad)
	U-5Zr	~610	685	~705
	<u>U-10, 20Zr</u>	**<u>~610</u>**	**<u>685</u>**	-
	U-30Zr	~610	**685**	-
	U-50Zr	~605	-	-

Table 5-5: DSC measured phase transformation temperatures of annealed U-Zr alloys.

Alloy		Peak 1 (°C) $(\alpha, \delta) \rightarrow (\alpha, \gamma_2)$	Peak 2 (°C) $(\alpha, \gamma_2) \rightarrow (\alpha, \gamma_1)$	Peak 3 (°C) $(\alpha, \gamma_1) \rightarrow (\beta, \gamma_1)$	Est. Comp.
U-2Zr	3d600	585	**675**	710 (broad)	U-2.6Zr
	7d600	593	**674**	708 (broad)	U-2.5Zr
U-5Zr	3d600	583	**676**	704 (narrow)	U-5.3Zr
	7d600	600	**675**	704 (narrow)	U-5.6Zr
U-10Zr	**3d600**	596	**683 (connected)**	**702 (connected)**	**U-7.8Zr**
	7d600	585	**686 (merged)**	-	**U-10.3Zr**
U-20Zr	3d600	605	682	-	U-18.5Zr
	7d600	608	683	-	U-18.5Zr
U-30Zr	3d600	608	688	-	U-24.2Zr
	7d600	604	686	-	U-23.7Zr
U-40Zr	7d600	607	(689)	-	-
U-50Zr	3d600	604	-	-	-
	7d600	609	-	-	-

5.2.4 Phase Transformation Enthalpy Analysis

Hypothetical transformation enthalpies of U-Zr alloys were calculated for the two types of U-Zr binary phase diagrams. Theoretically estimated enthalpies were compared to corresponding experimental values measured using DSC-TGA. In order for calculating phase transformation enthalpies, inevitable assumptions accepted are as follows.

- 1) Molar phase transformation enthalpies are conserved.

  ■ Molar phase transformation enthalpies of α-U → β-U and β-U → γ phase reactions per mole are conserved regardless of alloy composition change, i.e. $\Delta H_{\alpha \to \beta} = 2.791$kJ/mol and $\Delta H_{\beta \to \gamma} = 4.757$kJ/mol [136].

  ■ It was experimentally proven, from the measured enthalpies of uranium and U-0.1Zr alloy given in Tables 4-4 and 4-6, that the presence of trace amount of zirconium near solubility limits in α-U and β-U phases does not significantly affect phase transformation enthalpies. Marginally larger transformation enthalpies of U-0.1Zr alloy may be due to oxidation resistance.

- 2) Molar enthalpy of direct phase transformation of α-U → γ phase is assumed as the sum of $\Delta H_{\alpha \to \beta}$ and $\Delta H_{\beta \to \gamma}$.

  ■ Direct measure of $\Delta H_{\alpha \to \gamma}$ is fundamentally impossible because pure elemental uranium does not exhibit the phase transformation, therefore adopting this assumption is unavoidable. Thus, $\Delta H_{\alpha \to \gamma} = 7.548$kJ/mol.

With the assumptions above, all peaks from DSC heating curves from U-Zr alloys may be compared to theoretical enthalpies for each phase transformation anticipated from each U-Zr phase diagram. Each theoretical phase transformation enthalpy was calculated using Equation (5-1) as the total sum of the products of the

266

molar phase fractions of the alloys undergone the phase transformation and the molar enthalpies of the phase transformation.

$$\Delta H_n = \sum_{i=\alpha,\beta,\delta} \left(\sum_{j=\beta,\gamma} \Delta H_{i \to j} \times X_i \right) \tag{5-1}$$

where ΔH_n is total phase transformation enthalpy for n^{th} phase transformation (n = 1, 2, and 3, the smaller n indicates the lower temperature phase transformation as used in Tables 4-5, 4-6, and 4-7), and. X_i is the molar fraction of the phase which undergone the phase transformation at the given temperature, respectively.

Note that the entire portion of alloy is not necessarily simultaneously subjected to phase transformation, which means the grand sum of X_i need not be unity for all the cases. Also, all three bcc phases, γ_1, γ_2 and γ, are regarded to be an equivalent phase, since reported phase transformation enthalpy of (γ_1, γ_2) $\to \gamma$ was only ~6 % of the smallest phase transformation enthalpy of the system [157]. Phase transformations into any bcc phase should give rise to equal phase transformation enthalpy, assuming all the other conditions for the transformation are the same.

Equation (5-1) can be rewritten in an explicit form by considering only allowed transformations in the system following the phase diagrams.

$$\Delta H_n = \Delta H_{\delta \to \gamma} \cdot X_\delta + \Delta H_{\alpha \to \beta} \cdot X_\alpha + \Delta H_{\alpha \to \gamma} \cdot X_\alpha + \Delta H_{\beta \to \gamma} \cdot X_\beta \tag{5-2}$$
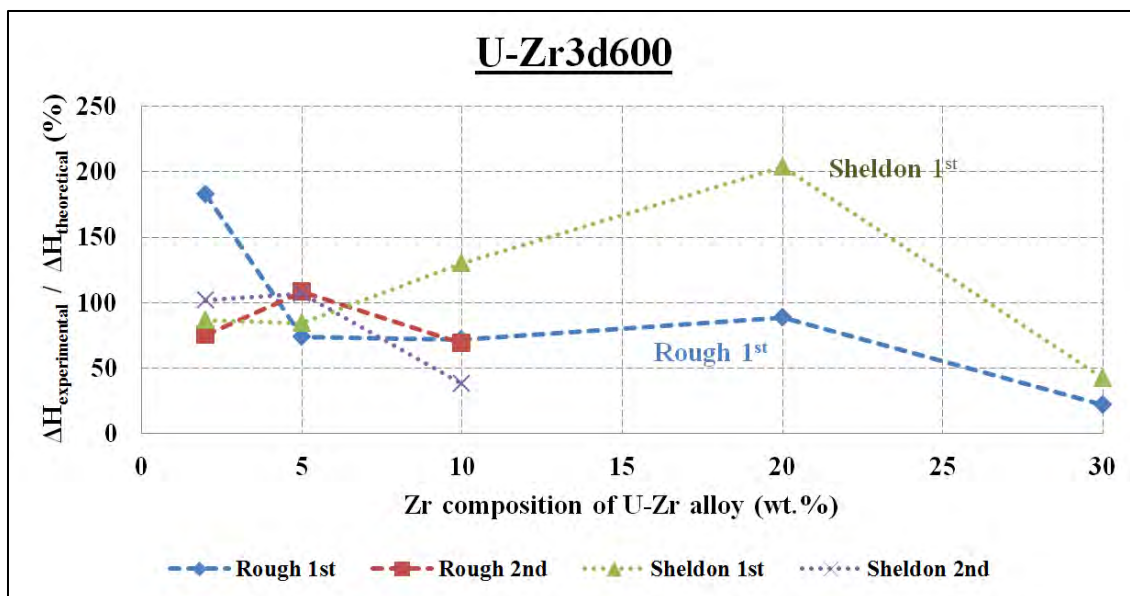
(a) U-Zr3d600
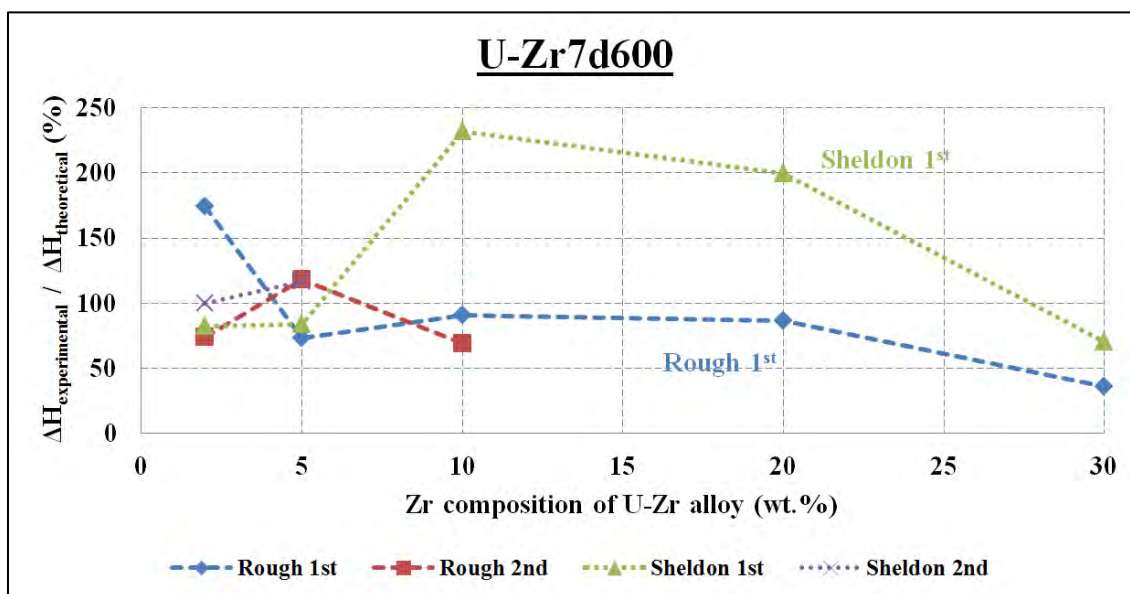
(b) U-Zr7d600

Figure 5-4: Comparison between the DSC-TGA measured experimental phase transformation enthalpies and the theoretical phase transformation enthalpies predicted from the two different types of U-Zr binary phase diagrams.

The fractions of experimental phase transformation enthalpies to theoretically calculated phase transformation enthalpies using Equation (5-2) were already given in Tables 4-4, 4-5, 4-6, and 4-7 for annealed U-Zr alloys. Figure 5-4 graphically shows which phase diagram is more consistent with experimental phase transformation enthalpies measured using DSC-TGA. Each point in the figure indicates the proportionality between the experimental enthalpy and the calculated theoretical enthalpy. Therefore the proximity of the point on the graph to the hypothetical line at 100% indicates the better fit between the experimental data and the phase diagram predictions.

From the comparison in Fig. 5-4, Rough's phase diagram apparently shows better agreement with the experimental data, except for U-2Zr, while the data from Sheldon's diagram repeatedly hover near the 200% line, meaning measured enthalpies are over two fold larger than theoretical enthalpies calculated based on Sheldon's phase diagram. This large offset is apparently due to the additional isotherm line at 662 °C, splitting single phase transformation of α-U → γ phase into two phase transformations of α-U → β-U and β-U → γ phase, therefore decreasing the theoretical phase transformation enthalpies for Zr-rich U-Zr alloys.

5.2.5 In-situ Heating Electron Diffractometry

The DSC-TGA results do not coincide with Sheldon's phase diagram in the standpoint of 1) number of phase transformations of U-10Zr and U-20Zr alloys, 2) phase transformation temperatures of all compositions of U-Zr alloys, and 3) the phase transformation enthalpy analysis.

Therefore, more authentic experimental evidences were desired to strengthen the hypothesis, which the (β, γ_2) phase field is absent from Zr-rich (> 10 wt%) part of U-Zr phase diagram, particularly considering Sheldon's phase diagram have been near constitutionally referred over the last two decades.

Therefore SAD patterns of as-cast U-10Zr and U-20Zr alloys irradiated at 5×10^{16} ions/cm^2 (U-10ZrAi5 and U-20ZrAi5) were sequentially obtained at various temperatures ranging from 25 °C to 815 °C during *in-situ* heated TEM as shown in Figs. 4-64 and 4-73. The compositions of U-Zr alloys were selected, in part, due to inconsistent behaviors of the alloys with Sheldon's phase diagram. The as-cast thermal history and relatively high dose irradiation were chosen to polycrystalize the alloys which already had smaller phase precipitates and narrow lamellae.

Further, the microstructure dimensions of annealed two phase U-Zr alloys observed in the EPMA were comparable or larger than the widest electron transparent area prepared utilizing single jet electropolisher in the TEM observation. Thus, entire observable area could undesirably have single phase, either α-U or δ-UZr$_2$. Also, instant adjustment of atomic crystal alignment toward incident electron beam was unfeasible

270

since only single tilt heating stage specimen holder was accessible for the experiments. These limitations in combination with thermal expansion and vibration of the specimen at elevated temperatures mandated discarding the idea to obtain spot type DPs from single crystal regions. Therefore, the fine-grained polycrystalline as-cast specimens were preferred to obtain the ring type DPs after ion-beam irradiating the alloys.

For both of U-10Zr and U-20Zr alloy, the only notable change in the DP of each alloy was occurred at ~690 ℃. The SAD patterns of the alloys obtained at some representative temperatures for each phase region in U-Zr binary phase diagram are contrasted in Fig. 5-5; for U-10Zr alloy, 615 °C for (α-U, δ-UZr$_2$) phase, 693 °C for (γ_1, γ_2) phase, and 800 °C for single γ phase, and for U-20Zr alloy, 600 °C for (α-U, δ-UZr$_2$) phase, 690 °C for (γ_1, γ_2) phase, and 815 °C for single γ phase.

However, DP indexing shown in Table 5-6 indicated that the observed DPs below 690 °C were mainly obtained from either UO$_2$ or UO$_2$-ZrO$_2$, which does not have any crystallographic phase transformation up to ~1400 °C [181-187]. Considering all potential constituents of U-Zr alloy TEM specimen, the newly appeared ring in the DPs obtained above ~690 °C was best matched to the diffraction from the (110) planes of the γ phase of U-Zr binary alloy system. Referred crystallographic data for the analysis are summarized in Table 5-7.
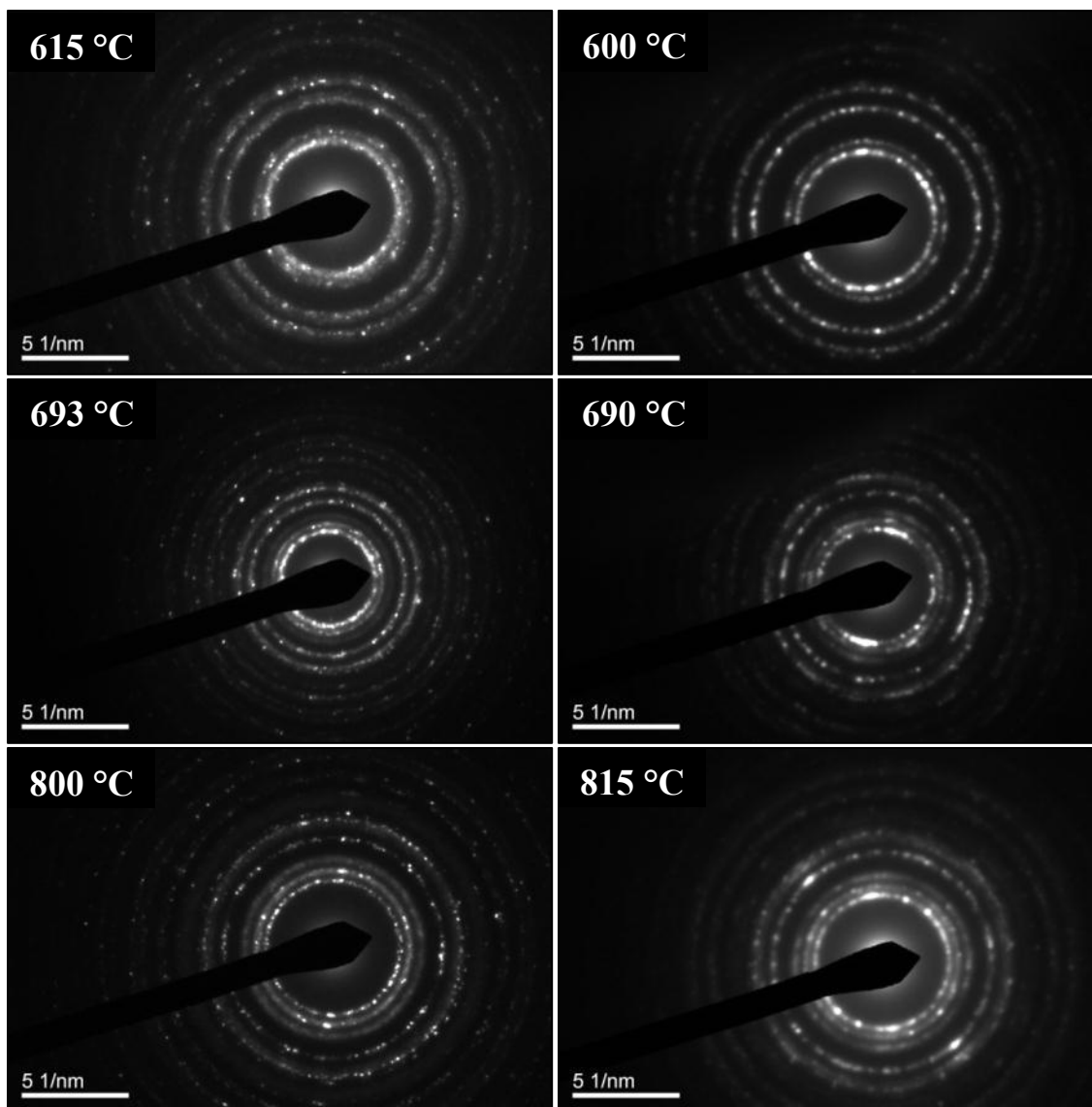
(a) U-10ZrAi5 at 615, 693, and 800 °C   (b) U-20ZrAi5 at 600, 690, and 815 °C

Figure 5-5: Evolution of DPs of U-10ZrAi5 (left) and U-20ZrAi5 (right) at elevated temperatures. Only one notable transition occurred at 693 and 690 °C for each alloy. (Given DPs are all selectively duplicated from Figs. 4-64 and 4-74.)

Table 5-6: Indexing of representative electron diffraction patterns of U-Zr alloys

Phase	Temp.	Diameters (1/nm) and ratios of diffraction rings in reciprocal space of DPs										Comment
(α-U, δ-UZr$_2$)	< ~605 °C [124]	Diameter (1/nm)	4.04	4.60	6.48	6.82	7.92	8.77	10.26	11.22	-	Candidate phase mixture for RT
		Ratio/ α-U(001)	1.00	1.14	1.61	1.69	1.96	2.17	2.54	2.78	-	
γ phase	> ~605 °C [124]	Diameter (1/nm)	-	-	8.00	11.32	-	13.86	-	17.90	19.60	Reasonably matched with all DPs at high temperatures (> 690 °C)
		Ratio/ UO$_2$ (111)	-	-	**1.26**	1.79	-	2.19	-	2.83	3.10	
		Diffracting planes	-	-	**γ(110)**	γ(200)	-	γ(211)	-	γ(301)	γ(222)	
UO$_2$ or (UO$_2$, ZrO$_2$)	< ~1400 °C [185]	Diameter (1/nm)	6.33	7.31	-	10.34	12.13	14.63	15.93	17.90	19.00	Consistently matched with the most DPs at RT
		Ratio/ UO$_2$(111)	**1.00**	**1.15**	**-**	**1.63**	**1.91**	**2.31**	**2.52**	**2.83**	**3.00**	
		Diffracting planes	**(111)**	**(200)**	**-**	**(220)**	**(311)**	**(400)**	**(331)**	**(422)**	**(333)**	
Alloy (Fig.)	**Temp.**	**Diffraction ring**	**1st**	**2nd**	**(HT)**	**3rd**	**4th**	**5th**	**6th**	**7th**	**8th**	**Presumptive phase**
U-0.1ZrAi1 (Fig. 4-33)	25 °C	Diameter (1/nm)	6.03	6.96	-	9.82	11.56	13.98	15.28	17.04	18.02	UO$_2$
		Ratio/ UO$_2$(111)	**1.00**	**1.15**	**-**	**1.63**	**1.92**	**2.32**	**2.53**	**2.82**	**2.99**	
U-10ZrAi5 (Fig. 4-64)	610 °C	Diameter (1/nm)	6.30	7.22	-	10.13	11.86	14.19	15.52	17.32	18.37	UO$_2$ or (UO$_2$, ZrO$_2$)
		Ratio/ UO$_2$(111)	**1.00**	**1.15**	**-**	**1.61**	**1.88**	**2.25**	**2.46**	**2.75**	**2.92**	
	758 °C	Diameter (1/nm)	6.45	7.34	8.42	10.41	12.31	-	16.10	18.15	19.26	UO$_2$ + γ phase
		Ratio/ UO$_2$(111)	**1.00**	**1.14**	**1.31**	**1.61**	**1.91**	**-**	**2.50**	**2.81**	**2.99**	
U-20ZrAi5 (Fig. 4-73)	670 °C	Diameter (1/nm)	6.34	7.43	-	10.40	12.31	14.72	16.10	18.15	-	UO$_2$ or (UO$_2$, ZrO$_2$)
		Ratio/ UO$_2$(111)	**1.00**	**1.17**	**-**	**1.64**	**1.94**	**2.32**	**2.54**	**2.86**	**-**	
	690 °C	Diameter (1/nm)	5.39	6.12	7.01	8.74	10.25	12.36	13.65	15.23	16.16	UO$_2$ + γ phase
		Ratio/ UO$_2$(111)	**1.00**	**1.14**	**1.30**	**1.62**	**1.90**	**2.29**	**2.53**	**2.83**	**3.00**	
U-40ZrAi0.01 (Fig. 4-43)	25 °C	Diameter (1/nm)	6.48	7.46	-	10.57	12.40	14.96	16.36	18.25	19.37	UO$_2$ or (UO$_2$, ZrO$_2$)
		Ratio/ UO$_2$(111)	**1.00**	**1.15**	**-**	**1.63**	**1.91**	**2.31**	**2.53**	**2.82**	**2.99**	

Table 5-7: Crystallographic information of potential constituents of TEM specimens of melt-cast U-Zr alloys [188-193].

System	T_s (°C)	Phase	Crystal structure		Lattice parameter		
			Lattice type	Centered	a	b	c
U	RT	α-U	Orthorhombic	C	2.8539	5.8678	4.9554
	669	β-U	Tetragonal	Primitive	10.7589	-	5.6531
	776	γ-U	Cubic	Body	3.5335	-	-
Zr	RT	α-Zr	Hexagonal	Primitive	3.2317	-	5.1476
	863	β-Zr	Cubic	Body	3.5878	-	-
U-Zr	RT	δ-UZr$_2$	Hexagonal	Primitive	5.025	-	3.086
	693	γ$_1$	Cubic	Body	3.5424	-	-
	617	γ$_2$	Cubic	Body	3.5674	-	-
UO$_2$		-	Cubic	Face	5.47	-	-
ZrO$_2$		-	Cubic	Face	5.143	-	-
Y$_2$O$_3$		-	Cubic	Body	10.604	-	-

It is highly unlikely that the new diffraction ring appeared in high temperature DPs of U-10Zr and U-20Zr alloys was due to intensified surface effects for thin TEM specimens of the U-Zr alloys. It is suspected that surface oxide layer rather protected an inner metallic area, given the transition behavior of the DPs of U-10Zr and U-20Zr alloys, almost exactly matched with the prediction from Rough's phase diagram. Thus, these results from *in-situ* heated electron diffractometry of U-Zr alloys are consistently agreed with the DSC-TGA measurements and were also in agreement with Rough's phase diagram.

5.3 Radiation Induced Structural Evolution

5.3.1 Polycrystallization and Amorphization

Bright field images and SAD patterns of unirradiated U-0.1Zr and U-40Zr alloys clearly indicated large crystalline structures, as shown in Figs. 4-28 and 4-40, which was reasonable, considering that the observed grain sizes of the alloys using EPMA ranged from 20 μm to 1000 μm as shown in Section 4.1 and the ~0.5 μm wide area contributing to SAD pattern construction.

It is apparent from the inserted DPs in Figs. 4-29, 4-33 and 4-34 that sequential polycrystallization of the as-cast U-0.1Zr alloy irradiated at three different doses, i.e. 0.1, 1, and 5×10^{16} ions/cm^2, was qualitatively proportional to the irradiation doses. A spot DP of U-0.1ZrAi0 shown in Fig. 4-28 was transitioning into a ring pattern of U-0.1ZrAi0.1 in Figs. 4-29 and 4-32. Further, a perfect ring pattern appeared for U-0.1ZrAi1, as shown in Fig. 4-33. Finally, a diffused ring pattern was obtained from the highest dose irradiated alloy shown in Fig. 4-34, indicating that the polycrystalline medium at intermediate doses was eventually transforming into an amorphous structure.

Similar evolution was observed in irradiated U-40Zr alloy. Spot type DPs from unirradiated U-40Zr alloy are shown in Fig. 4-40. U-40ZrAi0.01 exhibited an intermediate ring pattern, as in the same dose irradiated as-cast U-0.1Zr alloy, shown in Fig. 4-42. However, diffused ring type was not obtained from U-40Zr alloy irradiated even at the highest dose.

Bright field images of irradiated U-Zr alloys also indicated crystallographic transition of unirradiated as-cast large grains that appeared to be similar to a single crystal for the narrow electron transparent area in the TEM specimens of the alloys. Representative nano-grained regions having many number of atomic crystals oriented in various directions toward electron beam are given in Figs. 4-33 and 4-54.

Often, crystalline features disappeared from some electron transparent areas, even at highest magnification (1,500,000X) available in the TEM. This crystallographic opacity was assumed as due to severe polycrystallization or amorphization. Large crystalline regions found in highly irradiated alloys were regarded as over-polished areas from irradiated side of the specimen. Clear spot pattern DPs obtained from those over-polished areas are shown in Fig. 4-52

5.3.2 Electropolishing Artifacts

Various features suspected to be electropolishing artifacts were unwantedly found from irradiated alloys, as shown in Figs. 4-30, 4-47, and 4-51. Therefore, unirradiated alloys were also examined to give the references. Figure 4-41(bottom) clearly shows two typical types of artifacts, 1) redeposited compounds likely made of resolved specimen and the electrolyte constituents and 2) pitting holes due to over-voltage electropolishing.

Structures resembling these artifacts were therefore excluded from further analysis, however a troublesome situation arose when presumptively irradiation induced